Search for Proton Emission in ^{54}Ni and Multi-Nucleon Transfer Reactions in the Actinide Region

Inaugural-Dissertation
zur
Erlangung des Doktorgrades
der Mathematisch-Naturwissenschaftlichen Fakultät
der Universität zu Köln

vorgelegt von
Kerstin Geibel
aus Düsseldorf

Köln 2012

Vorsitzender der Prüfungskommission:	Prof. Dr. C. Kiefer
Gutachter:	Prof. Dr. P. Reiter Prof. Dr. A. Zilges
Tag der mündlichen Prüfung:	15. Juni 2012

Abstract

The first part of the thesis presents the investigation of fusion-evaporation reactions in order to verify one-proton emission from the isomeric 10^+ state in the proton rich nucleus ^{54}Ni. Between the years 2006 and 2009 a series of experimental studies were performed at the Tandem accelerator in the Institut für Kernphysik (IKP), University of Cologne. These experiments used fusion-evaporation reactions to populate ^{54}Ni via the two-neutron-evaporation channel of the compound nucleus ^{56}Ni. The cross section for the population of the ground state of ^{54}Ni was predicted to be in orders of microbarn. This required special care with respect to the sensitivity of the experimental setup, which consisted of a double-sided silicon-strip detector (DSSSD), a neutron-detector array and HPGe detectors. In two experiments the excitation functions of the reactions (^{32}S+^{24}Mg) and (^{28}Si+^{28}Si) were determined to find the optimal experimental conditions for the population of ^{54}Ni. A final experiment employed a ^{28}Si beam at an energy of 70 MeV, impinging on a ^{28}Si target. With a complex analysis it is possible to obtain a background-free energy spectrum of the DSSSD. An upper cross section limit for the population of the 10^+ state in ^{54}Ni is established at $\sigma(^{54}Ni(10^+)) \leq (13.9 \pm 7.8)$ nbarn.

In the second part of the thesis the population of actinide nuclei by multi-nucleon transfer reactions is investigated. Two experiments, performed in 2007 and 2008 at the CLARA-PRISMA setup at the Laboratori Nazionali di Legnaro, are analyzed with respect to the target-like reaction products. In both experiments ^{238}U was used as target. A ^{70}Zn beam with 460 MeV and a ^{136}Xe beam with 926 MeV, respectively, impinged on the target, inducing transfer reactions. Kinematic correlations between the reaction partners are used to obtain information on the unobserved target-like reaction products by the analysis of the beam-like particles identified with the PRISMA spectrometer. γ spectra from neutron-rich actinide nuclei are obtained with the CLARA array. An extension of the ground-state rotational band in ^{240}U up to the 18^+ state is achieved. The level and transition energies as well as the moments of inertia are compared with theoretical predictions. Based on cross section distributions for various reaction channels the perspectives and limitations for in-beam γ spectroscopy with this experimental method in the actinide region are discussed.

Zusammenfassung

Im Mittelpunkt des ersten Teils dieser Arbeit steht die Untersuchung der Protonenemission aus dem isomeren 10^+-Zustand des protonenreichen Kerns ^{54}Ni. In den Jahren 2006 bis 2009 wurde am Tandembeschleuniger des Instituts für Kernphysik der Universität zu Köln eine Serie von Experimenten durchgeführt, die dem Nachweis dieses seltenen Zerfalls dienen sollten. Ziel war es, mittels Fusions-Verdampfungsreaktionen, ^{54}Ni über den Zwei-Neutronen-Evaporationskanal des Compound-Kerns ^{56}Ni zu populieren.
Der berechnete Wirkungsquerschnitt für die Population des Grundzustands von ^{54}Ni liegt im Mircrobarn-Bereich. Dies stellte besondere Anforderungen an die Sensitivität des experimentellen Aufbaus, zu dessen Bestandteilen ein segmentierter Siliziumzähler (DSSSD), ein Array von Neutrondetektoren und mehrere HPGe-Detektoren zählen. Um die optimalen Reaktionspartner und eine geeignete Strahlenergie zu bestimmen, wurden zwei Experimente zur Messung der Anregungsfunktion für die Reaktionen (^{32}S+^{24}Mg) und (^{28}Si+^{28}Si) durchgeführt. Das finale Experiment verwendete eine Fusions-Verdampfungsreaktion mit einem ^{28}Si-Target und einem ^{28}Si-Strahl bei einer Strahlenergie von 70 MeV. Durch eine aufwendige Analyse ist es möglich, ein untergrundfreies Energiespektrum des DSSSDs zu erhalten. Eine obere Grenze des Wirkungsquerschnittes für die Population des 10^+-Zustands von ^{54}Ni wird mit $\sigma(^{54}Ni(10^+)) \leq (13.9 \pm 7.8)$ nbarn angegeben.

Im zweiten Teil der Arbeit wird die Population neutronenreicher Aktinidenkerne mittels Multi-Nukleon-Transfer Reaktionen untersucht. Dazu wurden zwei Experimente, die in den Jahren 2007 und 2008 am CLARA-PRISMA-Aufbau am Laboratori Nazionali di Legnaro stattfanden, im Hinblick auf die targetähnlichen Reaktionspartner analysiert. Das Targetmaterial ^{238}U wurde im ersten Experiment von einem ^{70}Zn-Strahl bei einer Strahlenergie von 460 MeV und im zweiten Experiment mit einem ^{136}Xe-Strahl von 926 MeV beschossen. Mit Hilfe der Teilchenidentifikation der strahlähnlichen Reaktionspartner in PRISMA ist es möglich, Rückschlüsse auf die targetähnlichen Reaktionsprodukte zu ziehen. Auf diese Weise werden die CLARA-γ-Spektren der neutronenreichen Aktinidenkernen selektiert und analysiert. Insbesondere die Untersuchung von neutronenreichen Uranisotopen ist aufschlussreich. Die Grundzustandsbande von ^{240}U kann um drei bislang unbekannte Übergänge bis zum 18^+-Zustand erweitert werden. Niveauenergien, Übergangsenergien und Trägheitsmomente werden mit theoretischen Vorhersagen verglichen. Anhand der vorliegenden Wirkungsquerschnitte werden die Möglichkeiten und Grenzen der neuartigen, experimentellen Methode für die Aktinidenkerne diskutiert.

Contents

Abbreviations

ADC	**A**nalog **D**igital **C**onverter
AGATA	**A**dvanced **GA**mma **T**racking **A**rray
CF	**C**omplete **F**usion
CLARA	**CL**over **AR**r**A**y
DANTE	**D**etector **A**rray for multi-**N**ucleon **T**ransfer **E**jectiles
DIC	**D**eep **I**nelastic **C**ollision
DSSSD	**D**ouble-**S**ided **S**ilicon-**S**trip **D**etector
FRS	**FR**agment **S**eparator
GANIL	**G**rand **A**ccélérateur **N**ational d'**I**ons **L**ourds
GSI	**G**esellschaft für **S**chwer**I**onenforschung
HFB	**H**artree–**F**ock–**B**ogolyubov
HORUS	**H**igh efficiency **O**bservatory For γ-**R**ay **U**nique **S**pectroscopy
IAS	**I**sobaric **A**nalogue **S**tates
INFN	**I**stitute **N**azionale di **F**isica **N**ucleare
IKP	**I**nstitut für **K**ern**P**hysik
JAEA	**J**apan **A**tomic **E**nergy **A**gency
LNL	**L**aboratori **N**azionali di **L**egnaro
MCP	**M**icro **C**hannel **P**late
MED	**M**irror **E**nergy **D**ifferences
MNT	**M**ulti **N**ucleon **T**ransfer
MoI	**M**oment **o**f **I**nertia
MWPPAC	**M**ulti **W**ire **P**arallel **P**lates **A**valanche **C**ounter
NIB	**N**uclear **I**sospin **B**reaking
PPAC	**P**arallel **P**lates **A**valanche **C**ounter
QEC	**Q**uasi **E**lastic **C**ollision
RDT	**R**ecoil **D**ecay **T**agging
RISING	**R**are **IS**otope **IN**vesti**G**ations
SF	**S**ymmetric **F**ission
SHIP	**S**eparator for **H**eavy **I**on Reaction **P**roducts
TDC	**T**ime **D**igital **C**onverter
VAMOS	**VA**riable **MO**de **S**pectrometer

Part I.

Search for Proton Emission in ^{54}Ni

Introduction

Excited isomeric states and the level scheme of ^{54}Ni were subject of an experiment during the stopped-beam campaign of the RISING project at the GSI (Gesellschaft für Schwerionenforschung)in Darmstadt in the year 2006. Beside the measurement of the level scheme up to an isomeric state of a 10^+ level (with $\tau = 218(4)$ ns) an indirect evidence for a proton emission from the proton-rich ^{54}Ni was discovered: The de-excitation from the $9/2^-$ state to the ground state in ^{53}Co was detected in coincidence with ^{54}Ni. The direct detection of this proton emission was not possible because the experimental setup did not include detectors for light and low-energy particles like protons emitted from the target position.

The direct observation of the expected proton emission out of the isomeric 10^+ level in ^{54}Ni motivated an experiment at the Tandem accelerator at the Institut für Kernphysik (IKP) in Cologne. The experimental setup utilized a highly-segmented silicon-strip detector for proton detection, five neutron detectors and several HPGe detectors. The experimental configuration was installed, tested and optimized in several steps. A first production experiment was performed and analyzed as part of the diploma thesis [37]. In contrast to the GSI measurement, where a fragmentation reaction at relativistic energies had been employed, the Cologne experiment was based on a fusion-evaporation reaction between a ^{32}S beam and a ^{24}Mg target at a beam energy of 90 MeV. The feasibility of the setup was unambiguously demonstrated. However, a beam-correlated background contribution prevented detection of rare proton decay at this stage of the experiment. After several experimental improvements had been applied the experiment was repeated and analyzed as part of the diploma thesis [101] in 2008.

Despite the improvements the expected proton decay of ^{54}Ni was not detected because of some background contributions due to a high beam current and oxygen reactions. The latter was caused by reactions of the beam with an oxygen layer on the Mg target, which as alkaline earth metal is easily oxidized. Moreover, it was not obvious whether the isomeric level is sufficiently populated via the chosen fusion-evaporation reaction. In order to figure out the best conditions to populate the ^{54}Ni nuclei new experiments were performed at various beam energies and different beam-target combinations were used. The total cross section to populate the rare ^{54}Ni-end channel was calculated to be in the microbarn region. Two experiments were performed: first the measurement of the excitation functions for the reactions (^{32}S+^{24}Mg) at beam energies of 82, 85, 90 and 95 MeV and (^{28}Si+^{28}Si) at beam energies of 66, 70, 74 and 80 MeV. The results of these experiments are presented in this work. As an achievement of this studies a final production experiment was performed, employing a pulsed ^{28}Si beam at 70 MeV on a

^{28}Si target. In 2009 the final beam time was accomplished including all improvements. The analysis of this experiment yielded an upper cross section limit for the emission of a proton from the isomeric 10^+ state of ^{54}Ni. These results are also subject of the first part of this thesis.

1. Physics Motivation

1.1. One-Proton Emission

Already at the beginning of the last century proton radioactivity was discussed without any knowledge about the constituents of nuclei. This kind of phenomenon was simply called: H-rays [68]. It was not until the 1960s that the first theoretical predictions for cases of proton radioactivity were made by Goldanskii [41]. Especially for isotopes at the proton drip line, he predicted the emission of one proton for a nucleus of odd Z, whereas for nuclei with even Z two-proton radioactivity was foreseen [8].

It is important to distinguish between direct proton emission and beta-delayed proton emission: Beta-delayed proton emission concerns the emission of a proton out of a highly-excited nuclear state which has been populated by a $\beta+$ decay. This proton emission can be followed by another proton emission from the populated unstable energy level. In the case of a direct proton decay no preceding $\beta+$ decay occurs. The first case of a direct proton emission was observed in 1970 by Cerny et al. [15, 16]. An isomeric $19/2^-$ state in $^{53}\mathrm{Co}^m$ with a lifetime of $(247 \pm 15)\,\mathrm{ms}$ emitted a proton with an energy of $(1.59 \pm 0.03)\,\mathrm{MeV}$ into the ground state of ^{52}Fe . After this striking discovery many observations of proton emission in other nuclei were expected. However, only in 1981 the first observation of proton emission from the ground state of ^{151}Lu was found in an experiment with the velocity filter SHIP at GSI by S. Hofmann et al. [47]. In the following years about 30 examples of proton emitters could be discovered. All proton emitting nuclei are characterized by an odd atomic number. For even-Z nuclei the pairing energy must be considered to cause additional hindrance. For this reason the detection of a proton decay out of ^{54}Ni, an even-even nucleus, would be even especially interesting. With this ^{54}Ni experiment proton emission is investigated in the vicinity of the pioneering work for $^{53}\mathrm{Co}^m$.

A necessary condition for the emission of protons is a positive Q value [48].

$$Q_P = (M_{Z+1} - M_Z - m_p - m_e) \cdot c^2 > 0 \tag{1.1}$$

with M_{Z+1} mass of the parent nucleus, M_Z mass of the daughter nucleus, m_p proton mass and m_e electron mass.
The decay constant λ for proton emission is theoretically factorized in the following way:

$$\lambda = \frac{ln2}{T_{1/2}} = \nu \times P \tag{1.2}$$

with $T_{1/2}$ the half-life, ν, the frequency factor and P, the transmission factor, which contains the Gamow factor:

$$P = P_{jl} = e^{-2G_{jl}} \tag{1.3}$$

It is

$$G_{jl} = \sqrt{\frac{2m}{\hbar^2}} \int_{R_{in}}^{R_{out}} (V_{jl}(r) + V_{Coul}(r) + V_l(r) - Q_{P,nucl})^{1/2} dr \tag{1.4}$$

with $V_{jl}(r)$ the nucleus potential, $V_{Coul}(r)$ the Coulomb potential and $V_l(r)$ the centrifugal potential. The integration is performed across the energetically inhibited area of the nuclear potential with an excited proton in a quasi-bound state. The calculation of proton emission is very similar to the description of the alpha decay. However, the preformation of an α particle is not relevant and proton emission does not depend on this feature.
For long half-lives proton emission competes with β^+ decay [8]. The half-life is strongly related to the available decay energy. Figure 1.1 shows the half-life of proton emitters as a function of the decay energy for different Z, estimated with spherical barrier-penetration calculations and angular momentum transfer $l = 0$. This figure shows the

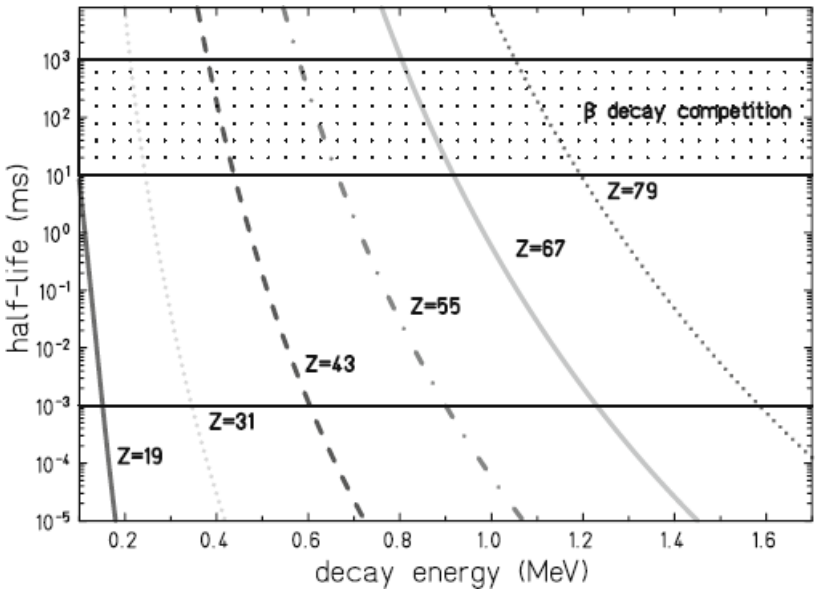

Figure 1.1.: *Calculated half-lives for proton emitters as a function of the decay energy. The upper horizontal lines mark where the competition with the β^+ decay sets in, the lower line indicates the limit of the experimentally accessible half-lives (figure taken from reference [8]).*

window where the proton emission is favorable and should be detectable. The upper

limit is given by the hatched area, which is the region of typical β-decay half-lives and the lower line is the limit of experimentally accessible half-lives. The window is smaller for lighter ions than for heavier ones. This explains why ground-state proton emitter for nuclei lighter than $A = 100$ have not been discovered yet.
Besides the investigation of the proton-emission process by itself, this kind of radioactivity turned out to be a versatile experimental tool to investigate the preceding γ transitions of the proton emitting nuclei. These experiments are based on the very sensitive recoil decay tagging technique (RDT). Herewith it is possible to correlate the interesting γ transitions from the population of the proton-emitting state and the delayed proton-emission events. A very selective tool for γ-ray spectroscopy at the drip line is given which enables spectroscopy of rare reaction channels by reduction of tremendous background contribution. The idea of the RDT method is to implant the recoiling nuclei after compound nucleus reactions into a highly-segmented double-sided silicon-strip detector (DSSSD) [75]. The adjacent proton decay is correlated with the implantation event by the identical DSSSD position. The prompt coincidence between γ rays and implantation makes it possible to tag the γ transitions and to select the emitting parent nuclei at the production target [106]. By this means it is possible to study the nuclei at the proton drip line with very small reaction cross sections which are typically many orders of magnitude lower than other reaction channels or background processes. With this method a wealth of new insights about the very neutron deficient nuclei could be gathered. Improvements in the development of position-sensitive silicon-detectors in the beginning of the 1990s together with the RDT method enabled the investigation of the nuclei at the proton drip line. In case of highly-efficient γ-detector arrays like GAMMASPHERE at the production target and powerful mass separators like the Argonne fragment mass separators, very small production cross sections down to 100 nanobarn are achieved to detect the interesting transitions [8].

1.2. Two-Proton Emission

Due to the fact that ^{54}Ni is an even-even nucleus the emission of two protons is also possible. Two-proton emission from the ground state of a neutron-deficient nucleus with even Z was, as mentioned above, first described by Goldanskii [41]. He predicted two scenarios: the decay process could take place either as the emission of a correlated ^{2}He cluster or as the simultaneous emission of two independent protons.
The simultaneous emission of two protons is only favored when the sequential emission of the protons is forbidden. This is possible for the mass region A=40-50. Here, additional energy from the pairing effect makes the possible two-proton emitter with even Z lighter than the one-proton-emitting daughter nucleus with odd Z. Hence, one-proton emission is forbidden and only simultaneous two-proton emission is possible.
The first evidence for the two-proton emission was discovered in ^{45}Fe with two different experiments in 2002 at GANIL (Grand Accélérateur National d'Ions Lourds), Caen, France,[40] and at GSI (Gesellschaft für Schwerionenforschung), Darmstadt, Ger-

many, [76]. In both experiments ^{45}Fe was produced via fragmentation of a ^{58}Ni beam on a Be target (GSI) or a Ni target (GANIL).
The selected ^{45}Fe particles were implanted in a silicon detector, where the two-proton emission took place. In the case of the GSI experiment four events of this emission with an energy of (1.1 ± 0.1) MeV were found. The GANIL experiment measured 12 decays with an energy of (1.14 ± 0.04) MeV. Additionally, the half-life could be determined in both experiments as $T_{1/2} = (4.7^{+3.4}_{-1.4})$ ms [40] and $T_{1/2} = (3.2^{+2.6}_{-1.0})$ ms [76].

1.3. Physics Case of ^{54}Ni

Nickel isotopes are interesting for the investigation of three doubly-magic isotopes and a shell closure at the proton drip line - ^{48}Ni denotes the proton drip line - as well as for the investigation of *I*sobaric *A*nalogue *S*tates (IAS) in the $f_{\frac{7}{2}}$ shell.
The simplest case for an isobaric multiplet is a pair of mirror nuclei, which contains a nucleus with a number of protons and a number of neutrons that are mutually interchanged in comparison with the other nucleus, like the pair $^{54}_{28}\mathrm{Ni}_{26}$ and $^{54}_{26}\mathrm{Fe}_{28}$.
The total binding energy difference between the two partners of a multiplet with isospin T transformed through exchange of k protons with k neutrons, also called *C*oulomb *D*isplacement *E*nergy (CDE) [7], is given by

$$\mathrm{CDE}(T, T_Z) = M_{(T,T_Z)} - M_{(T,T_{Z+k})} + k\Delta_{nH} \tag{1.5}$$

with M as the atomic mass, Δ_{nH} as the neutron–hydrogen atomic mass difference and T_z as the isospin projection for the larger-Z isobar.
The Coulomb field has the main influence on the mass shifts and hence on the CDE between isobaric nuclei of orders of hundreds of keV up to several MeV. Other isospin breaking effects, for example deriving from nuclear interaction, are expected to be small.
The energy differences of the *excited* states in mirror nuclei are named *M*irror *E*nergy *D*ifferences (MED) and are defined as [7]

$$\mathrm{MED}_{J,T} = E_{J,T,T_z=-T} - E_{J,T,T_z=T} \tag{1.6}$$

where typically the lowest isospin-partner states are compared i.e. $T = |T_z|$. By studying the MED, the strong influence of the Coulomb field is canceled because the ground states of the nuclei are normalized to zero excitation energy. Then the observable energy differences are rather small: In the $f_{\frac{7}{2}}$ shell the MEDs are in the typical range of tens of keV reaching rarely hundred keV and the other isospin-breaking effects become as important as the Coulomb ones.
The $f_{\frac{7}{2}}$ shell between the doubly-magic nuclei ^{40}Ca and ^{56}Ni is particular because here the isospin-breaking effects due to nuclear interaction could be identified uniquely and are clearly more pronounced than displacement energies [33]).
An isomeric 10^+ state in ^{54}Fe [58] with a lifetime of $\tau \approx 525(10)$ ns had been known since a long time. Hence from theoretical predictions an analog state in the mirror nucleus ^{54}Ni was expected. Gadea et al. [33] investigated ^{54}Ni up to the first 6^+ state and the results were compared with the IAS in the isobars ^{54}Co as well as ^{54}Fe and with the states in the cross-conjugate symmetric nuclei of mass A=42. As a result of an experiment at the Gesellschaft für Schwerionenforschung (GSI) in 2006 the level scheme of ^{54}Ni from Gadea et al. [33] was extended to higher levels. Further insights into the nuclear isospin-breaking effects have been obtained [84, 49]. For this experiment a^{58}Ni beam with an energy of 550 MeV/u produced by the SIS synchrotron was fragmented in ^{9}Be target with a thickness of $1\frac{\mathrm{g}}{\mathrm{cm}}$. By means of the $B\rho - \Delta E - B\rho$ technique the fragments were selected in the FRS (FRagment Separator)[38]. After a flight time of 350 ns through the FRS the identified secondary ions ^{51,52}Fe, ^{52,53}Co and ^{53,54,55}Ni were

stopped in a ^{9}Be plate with a thickness of 4 mm. This ^{9}Be plate was surrounded by 15 Euroball cluster detectors measuring the γ rays of delayed, isomeric de-excitation. In 60 hours beam time 4.8×10^{6} ^{54}Ni particles could be implanted and identified. It was possible to identify an isomeric 10^{+} state in ^{54}Ni which is corresponding to the 10^{+} state in ^{54}Fe and has a lifetime of $\tau = 218(4)$ ns. Rudolph et al. [84] established an extended level scheme for ^{54}Ni as it is shown in figure 1.2.

Coincidence gating proved that the measured isomeric γ rays are part of a single

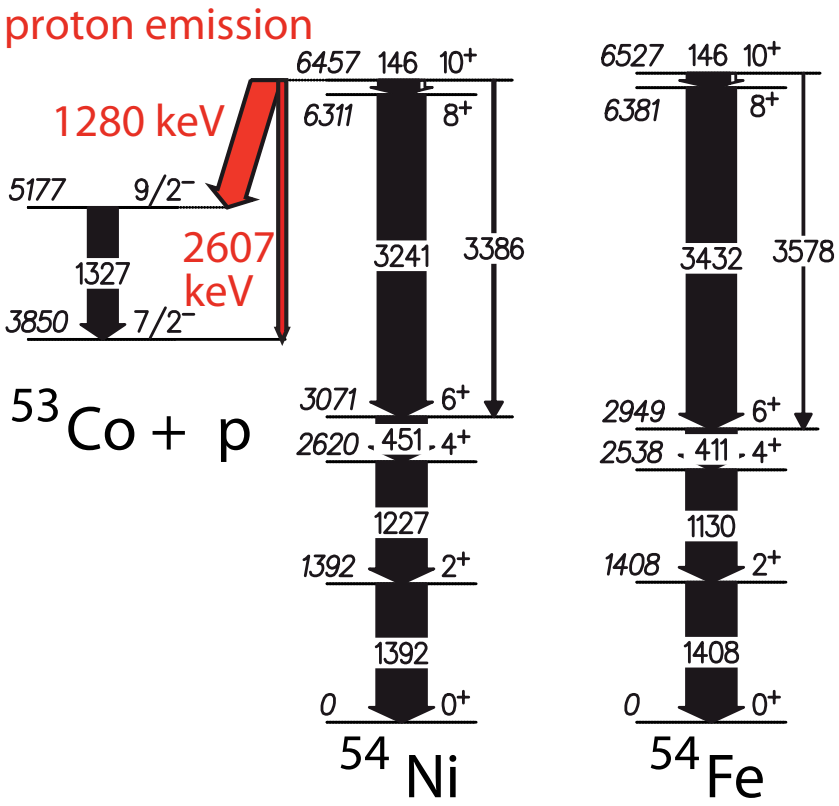

Figure 1.2.: *The resulting level scheme for ^{54}Ni up the 10^{+} state from the work of Rudolph et al. [84]. The possible proton decay from the isomeric level into the first excited state in ^{53}Co is indicated but was not observed directly via its proton decay. For comparison the relevant transitions of the mirror nucleus ^{54}Fe are also shown (figure taken from reference [84]).*

sequence from one γ-ray cascade. However, one peak with a transition energy of 1327.3(4) keV could not be explained to be in coincidence with the other transitions. The 1327.3(4) keV transitions do not belong to the ^{54}Ni level scheme. Because the transitions were unambiguously gated on Z=28 γ rays with this energy could only be emitted from an excited an isomeric Ni state. The assumption that the 1327.3(4) keV line was produced by other isotopes than ^{54}Ni, like ^{53}Ni or ^{55}Ni, is discarded: the

measured cross section for ^{53}Ni was too low to explain the peak intensity, whereas ^{55}Ni has no isomeric state, which could be proven by gating on the transition to the ground state. Other secondary nuclear reactions from other places of the experiment were excluded because the resulting cross section was also too low in comparison to the measured γ-ray intensity.
Consequently the 1327.3(4) keV energy had to originate from a reaction populating excited states in ^{54}Ni. A plausible explanation would be the decay of the isomeric 10^+ state in ^{54}Ni via proton emission into the first excited state ($\frac{9}{2}^-$) in the neighboring ^{53}Co nucleus. Then the proton energy would be expected at 1280 keV. The emission of γ-ray transitions of 1327.3(4) keV energy has been explained by the transition energies from the known ($\frac{9}{2}^-$) state to the ground state. As indicated in section 1.1 this kind of proton emission out of an even Z-nucleus, where the pairing energy has to be considered, would be very striking and interesting. Moreover theoretically not only the proton emission into the first excited state but also a direct proton transition into the ground state can be expected. In this case the proton would have an energy of 2607 keV. Even the two-proton emission from ^{54}Ni to ^{52}Fe is possible. At this point several interesting questions remained open and could not be pursued with the technique and the experimental setup at GSI. Here no particle detectors were included and the predicted proton emission could not be measured directly. These results motivated an experiment at the 10 MV FN Van-de-Graaff Tandem accelerator in the Institut für Kernphysik (IKP), Cologne, which intended to measure the direct proton from the isomeric 10^+ state in ^{54}Ni employing a new detector setup, comprising a DSSSD particle detector together with a neutron-detector array and HPGe detectors for γ-ray spectroscopy.

2. Concept, Realization and Improvements of the Experimental Setup

For the direct observation of the proton emission from the 10^+-state of ^{54}Ni a dedicated experimental setup was constructed at the L 45 beam line at the 10 MV FN Van-de-Graaff Tandem accelerator at the Institut für Kernphysik (IKP) in Cologne.
During 2006 and 2009 the experiment was installed and improved. Section 2.2 explains this progress with the different experimental features in detail. First the general experimental principle is described.

2.1. Main Ideas and the Experimental Concept

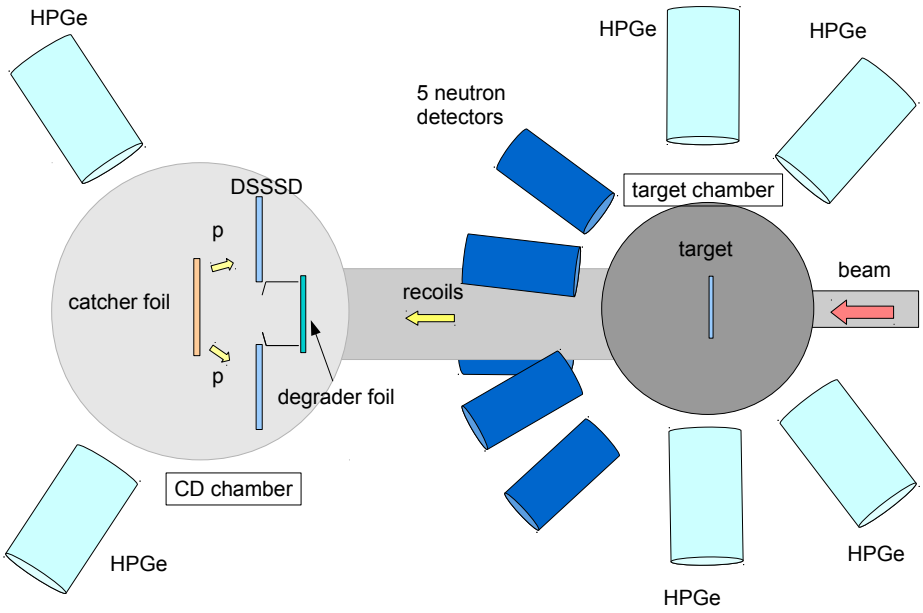

Figure 2.1.: *Setup of the ^{54}Ni experiment with a two-chamber system. The beam, coming from the right, interacts with the target in the first chamber. The recoils move through the DSSSD, are decelerated by a degrader foil and implanted into the catcher foil.*

The basic idea of the experiment is to populate ^{56}Ni compound nuclei by fusion evaporation. The rare two-neutron-evaporation channel of ^{56}Ni populates the interesting ^{54}Ni, which is supposed to emit a proton from the isomeric 10^+ state.
A two-chamber setup is used. In the first chamber (target chamber) the beam, delivered by the Tandem, interacts with the target nuclei. Around this target chamber ancillary detectors are mounted to monitor the reaction channels: several High Purity Germanium (HPGe) detectors, and the neutron-detector array, consisting of five NORDBALL detectors [46].

Due to the half-life of the 10^+ state of ^{54}Ni of $T_{1/2} = 152(4)$ ns and due to the high velocity of the recoils most of the proton emission is not expected in the target chamber. Therefore a second chamber (CD chamber) is placed 30 cm downstream the beam line. At the entrance of this chamber the particles first pass a degrader foil, which decreases the velocity of the recoils to an appropriate value. Just behind the degrader foil, protected against the beam, the core of the experiment, the double-sided-silicon-strip-detector (DSSSD), is located. It is CD-shaped (see figure 2.2), and the recoils as well as the remaining beam particles move through the detector hole in the center of the DSSSD. Behind the detector a target wheel is pivoted, which contains two apertures for beam focussing and, most importantly, the catcher foil. After passing the degrader foil the ^{54}Ni nuclei have a convenient kinetic energy to be stopped and implanted in this catcher foil. When proton emission out of ^{54}Ni at rest takes place, the protons can be emitted backwards out of the catcher foil and into the DSSSD. Around the CD chamber some more HPGe detectors are placed to inspect isomeric γ decays.

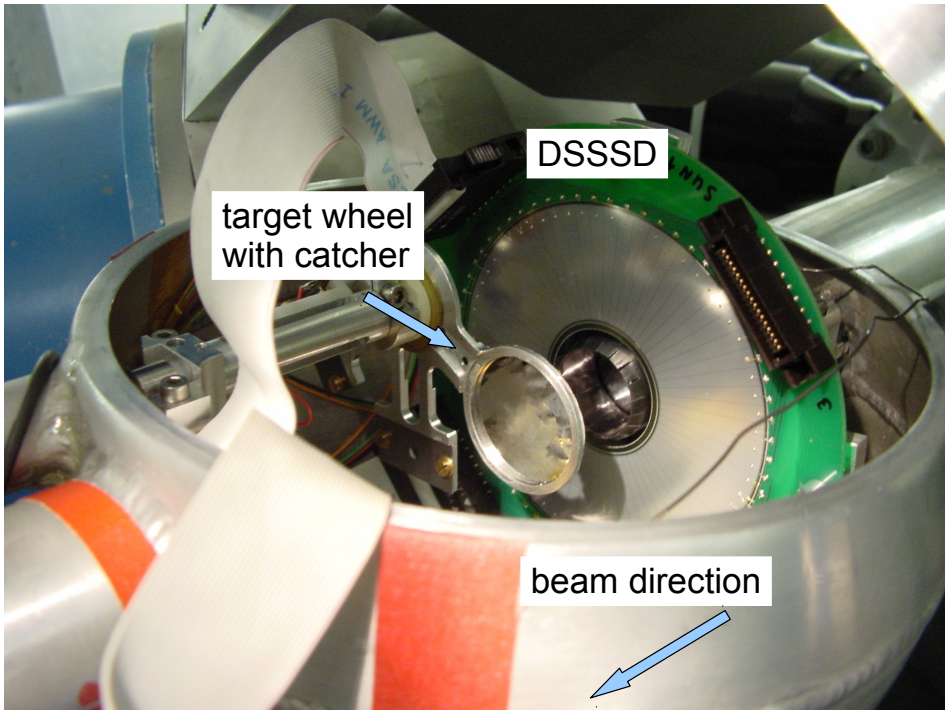

Figure 2.2.: *CD chamber, the beam coming from the right passes the detector through its hole in the center, where the degrader foil is placed. Then it hits the catcher foil, which is together with some focussing apertures mounted on a target wheel.*

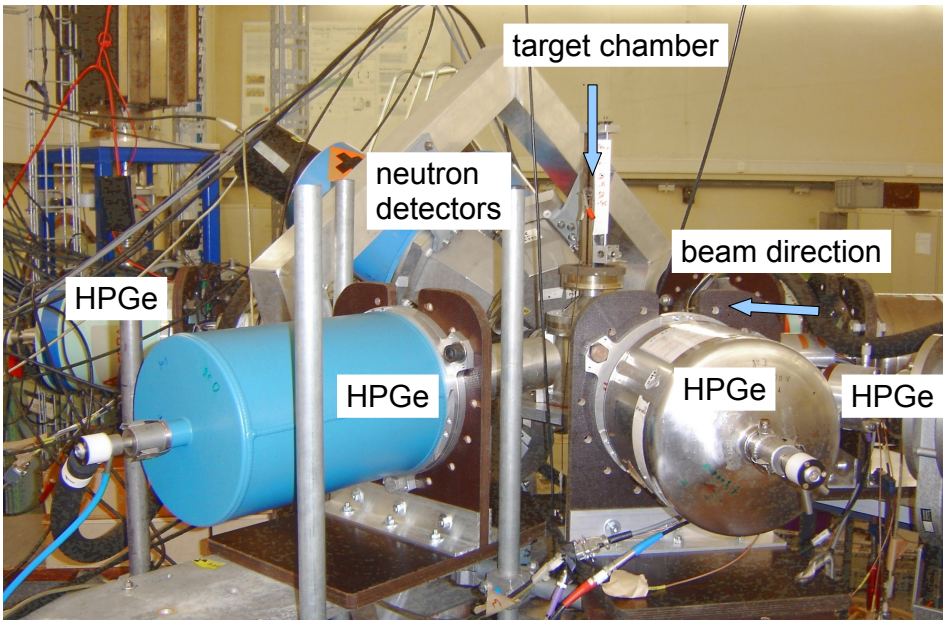

Figure 2.3.: *The target chamber of the ^{54}Ni experiment, surrounded by 4 HPGe detectors. Neutron detectors are directed to the target chamber, placed in backward direction.*

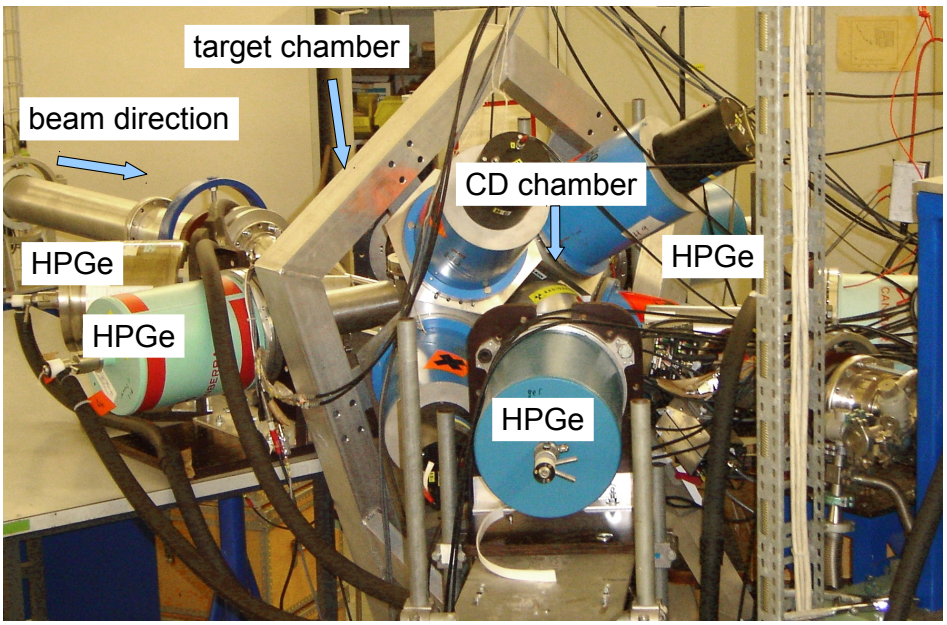

Figure 2.4.: *^{54}Ni experiment with view onto the closed CD chamber. In front sits one of the HPGe detectors.*

2.2. Realization of the First Experimental Setup

Between 2005 and 2009 the experimental setup was developed, tested and and several experiments were performed and improved. In table 2.1 an overview of the different experiments with the features of the experimental setups is listed.

Table 2.1.: *Overview of the different experiments between 2006 and 2009 at the IKP, Cologne, with the aim to detect proton emission out of ^{54}Ni.*

	1st. experiment Diploma thesis K. Geibel	2nd.experiment Diploma thesis A. Wendt	excitation measurement $^{32}S+^{24}Mg$	excitation measurement $^{28}Si+^{28}Si$	3rd. experiment
beam	^{32}S	^{32}S	^{32}S	^{28}Si	^{28}Si
beam energy in MeV	90	90 (pulsed)	82,85,90,95	66,70,75,80	70 (pulsed)
target	^{24}Mg	^{24}Mg	^{24}Mg	^{28}Si	^{28}Si
catcher material	Ni	Al	--------	--------	Al
DSSSD	√	√	--------	--------	√
HPGe-detector	1 at target 1 at CD chamber	1 triple at target, 2 triple at CD chamber	4 at target	Horus-array	4 at target, 2 at CD chamber
neutron detector	5 Nordball detectors	5 Nordball detectors	5 Nordball detectors	--------	5 Nordball detectors

The construction of the beam line and a first experiment which took place in 2006 was part of the diploma thesis of K. Geibel [37]. In this experiment it was the aim to populate ^{54}Ni with a fusion-evaporation reaction of a ^{32}S beam with 90 MeV and a ^{24}Mg target. It turned out that a high beam-correlated background in the spectra of the DSSSD made it impossible to isolate the signal deriving from the proton emission. In this experiment a Ni foil was used as catcher material to stop the compound nucleus ^{56}Ni as efficiently as possible. As an improvement a lighter catcher material than Ni was suggested in order to suppress the backscattering of primary beam particles from the catcher foil to the DSSSD.
An upgraded experiment, which was performed and analysed in the diploma thesis of A. Wendt [101], worked with Al as light catcher material and with a pulsed ^{32}S beam

(pulse length = 80 ns, $\tau = 400$ ns) at 90 MeV instead of a continuous beam. Between two beam pulses the emission of the proton out of an isomeric state should be measurable without any background of scattered, prompt particles from the beam. During the analysis a correction for the DSSSD-energy spectra was developed (see also section 4.5-2), which considers the energy loss of a charged particle (like the particles of the triple-alpha source and the emitted proton) in the passive layers of the DSSSD. An upper limit for the cross section for the population of the 10^+ state of ^{54}Ni could be determined as $\sigma(^{54}\mathrm{Ni}(10^+)) \leq (101.7 \pm 37.2)$ nbarn.
One of the main problems of these two experiments was the oxidation of the Mg target, which led to objectionable reactions. Recoils from the fusion-evaporation reaction (^{32}S+^{16}O) contributed to the γ-ray spectra.
The resulting upper cross section $\sigma(^{54}\mathrm{Ni}(10^+))$ and the undesired oxygen reactions made it necessary to find an improved, alternative experimental setup. To figure out which experimental setup yields the best population for the reaction channels of interest two further experiments were performed. The beam energy for the two fusion-evaporation reactions (^{32}S+^{24}Mg) and (^{28}Si+^{28}Si) was varied. The details and the results of both experiments are described in the two following sections 3.1 and 3.2.

3. Excitation Function Measurements

3.1. The (^{32}S+^{24}Mg) Reaction

In June 2008 an experiment was performed to analyze the γ-ray spectra following the fusion- evaporation reaction (^{32}S+^{24}Mg) at the four different beam energies 82 MeV, 85 MeV, 90 MeV and 95 MeV (at a charge state of 9^+), delivered by the 10 MV FN Van-de-Graaff Tandem accelerator. The experiment took place at the setup, which is described in section 2.1. Additionally to the five neutron detectors, 4 HPGe detectors were mounted around the target chamber. The DSSSD and the HPGe detectors around the CD chamber were not in use during this experiment. The thickness of the ^{24}Mg target was $0.43\frac{mg}{cm^2}$. The effective beam time for a beam energy of 82 MeV lasted 41 h 34 min, for 85 MeV it was 26 h 32 min, for an energy of 90 MeV it took 24 h 25 min and the beam time for a beam energy of 95 MeV it was 16 h 7 min.
Two trigger conditions were used. The first trigger condition was a coincidence of two HPGe-γ signals, the second trigger condition required the coincidence of a neutron and a γ signal to be sensitive to the neutron-evaporation channel.
The aim of the analysis was to compare the population of the different reaction channels. As parameters for the normalization of the spectra the information of the beam time length, the beam current, the rate of the data acquisition or the size of data files were considered. Another way to compare the γ spectra was the normalization to the Compton background of the symmetrized γ-γ matrices. By this means the normalization factors for the γ spectra with the condition of a γ-γ trigger as well as for the γ spectra with a neutron-γ trigger were calculated with the program TV [95]. The two kinds of normalization factor can vary because with different beam energies also the evaporation probability and evaporation angle for neutrons and hence the probability for the detection of a neutron differs.

Figures 3.1 to 3.4 show the normalized γ spectra generated with the γ-γ trigger for the four beam energies: in yellow for a beam energy of 82 MeV, in green for 85 MeV, in red for 90 MeV and the blue spectrum is for 95 MeV. In figures 3.5 and 3.8 the normalized γ spectra for the four beam energies with the condition of the neutron-γ trigger are illustrated.

The γ spectra are analyzed with the program TV [95]. The peak energies, the intensities and the assigned transitions are listed (without normalization factor) in tables 3.1 and 3.2 .

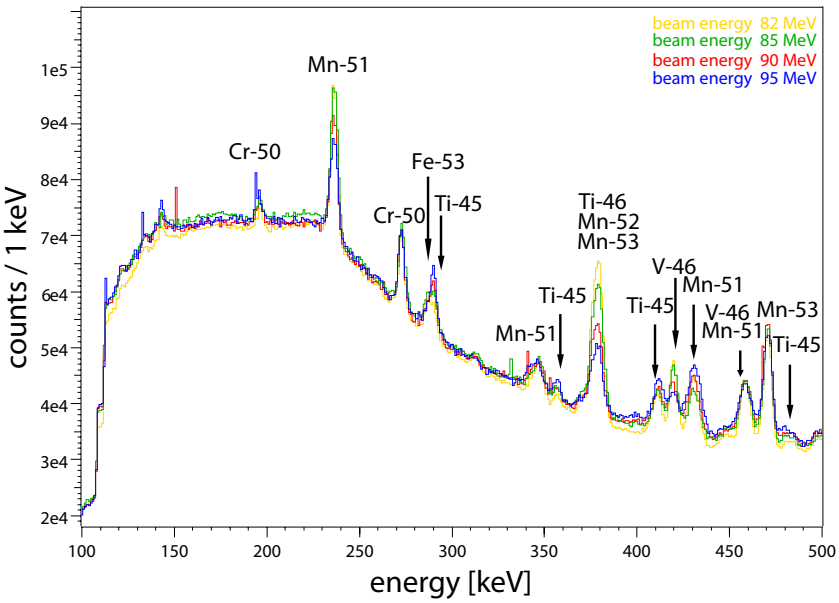

Figure 3.1.: *γ spectrum (100-500 keV) for the (^{32}S+^{24}Mg) reaction at a beam energy of 82 MeV (yellow), 85 MeV (green), 90 MeV (red) and 95 MeV (blue), obtained with a γ-γ trigger.*

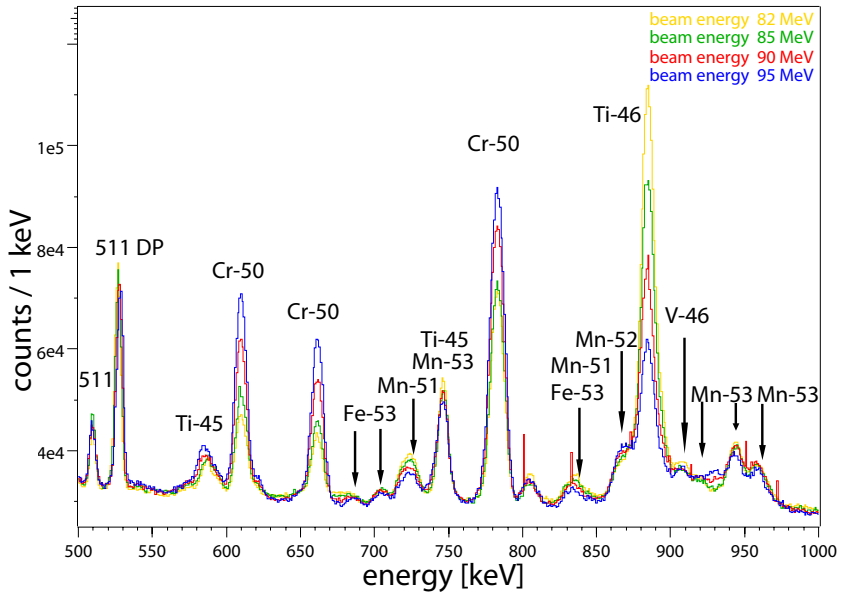

Figure 3.2.: *γ spectrum (500-1000 keV) for the (^{32}S+^{24}Mg) reaction, obtained with a γ-γ trigger.*

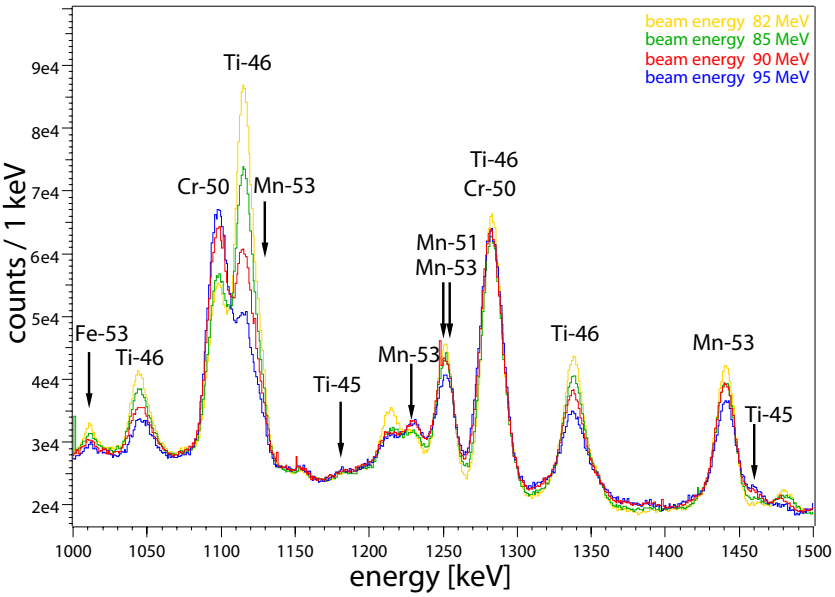

Figure 3.3.: *γ spectrum (1000-1500 keV) for the (^{32}S+^{24}Mg) reaction, obtained with a γ-γ trigger.*

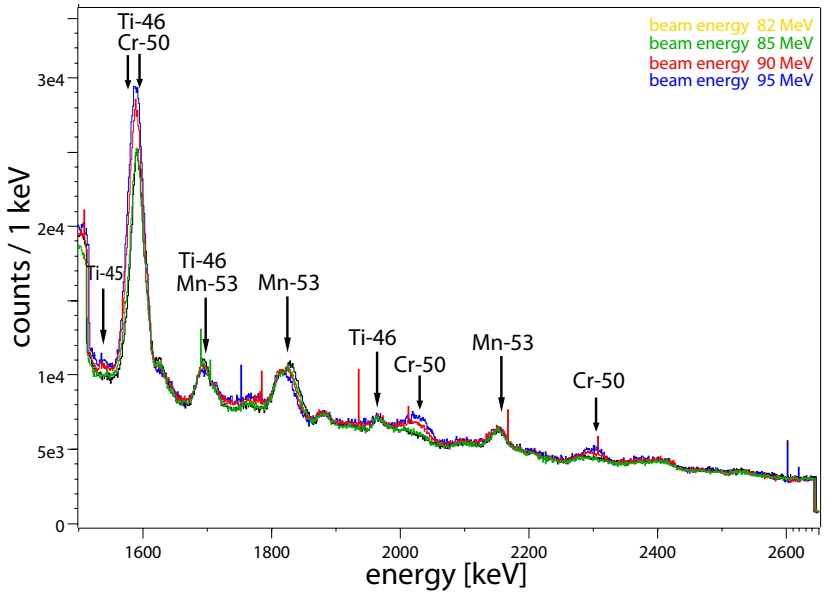

Figure 3.4.: *γ spectrum (1500-2650 keV) for the (^{32}S+^{24}Mg) reaction, obtained with a γ-γ trigger.*

Table 3.1.: *Energies, intensities, emitting evaporation residues and assigned transitions for the (^{32}S+^{24}Mg) reaction at a beam energy of 82 MeV , 85 MeV, 90 MeV and 95 MeV , with a γ-γ trigger condition.*

beam energy 82 MeV		beam energy 85 MeV		beam energy 90 MeV		beam energy 95 MeV			
energy (keV)	intensity	energy (keV)	intensity	energy (keV)	integral	energy (keV)	integral	nucleus	$J_{ini} \rightarrow J_{fin}$
76.21(50)	16546(978)	76.39(59)	21064(1619)	76.35(70)	17570(1593)	76.52(80)	9278(933)	^{208}Pb X-ray	$K_{\alpha 1}$
87.13(82)	10067(1113)	87.28(89)	8911(1026)	86.89(51)	6667(488)	87.02(52)	4853(353)	^{208}Pb X-ray	$K_{\beta 1}$
196.05(26)	1324(495)	196.31(14)	7782(1758)	197.80(46)	14506(3132)	194.24(21)	17501(6852)	^{50}Cr	$11^+ \rightarrow 10^+$
236.4(9)	120793(2446)	236.5(8)	94537(2439)	236.2(9)	88560(2941)	236.8(9)	42529(2756)	^{51}Mn	$\frac{7}{2}^- \rightarrow \frac{5}{2}^-$
272.9(7)	51030(1470)	273.1(9)	43390(1537)	272.8(8)	46682(1667)	272.7(7)	28846(1456)	^{50}Cr	$14^+ \rightarrow 13^+$
286.8(9)	22368(1555)	286.8(9)	17994(1407)	286.3(8)	11118(1185)	286.8(9)	4394(831)	^{53}Fe	$\frac{15}{2}^- \rightarrow \frac{13}{2}^-$
290.2(9) → DP**: 292	21862(1503)	290.6(9)	21821(1680)	290.1(9)	31623(2538)	290.1(9)	20720(1784)	^{45}Ti	$\frac{3}{2}^+ \rightarrow \frac{3}{2}^-$
346(1)	41257(1510)	346(1)	32248(1536)	345(1)	46961(5791)	345(1)	21017(2085)	^{51}Mn	$\frac{11}{2}^- \rightarrow \frac{9}{2}^-$
355.5(9) → DP**: 358	10439(1438)	354.4(9)	10606(1560)	355.1(9)	22328(5208)	356.8(9)	13181(2140)	^{45}Ti	$\frac{15}{2}^- \rightarrow \frac{13}{2}^-$
378(1) → DP**: 383	211218(2114)	378(1)	139676(2007)	378(1)	99296(2182)	378(1)	38188(1375)	^{46}Ti	$4^- \rightarrow 3^-$
"	"	"	"	"	"	"	"	^{53}Mn,	$\frac{5}{2}^- \rightarrow \frac{7}{2}^-$
"	"	"	"	"	"	"	"	^{52}Mn	$2^+ \rightarrow 6^+$
410(1) → DP**: 414	37767(1579)	411(1)	35652(1869)	411(1)	41242(2503)	411(1)	28012(2084)	^{45}Ti	$\frac{5}{2}^+ \rightarrow \frac{3}{2}^+$
419(1) → DP**: 422	67691(1508)	419(1)	54022(1693)	419(1)	47254(2138)	419(1)(14)	18871(1625)	^{46}V	$5^+ \rightarrow 3^+$
430(1)	65042(1354)	430(1)	41046(1384)	430(1)	60431(2037)	430(1)	40183(2013)	^{51}Mn	$\frac{17}{2}^- \rightarrow \frac{15}{2}^-$
458(1)	55848(1355)	458(1)	46146(1363)	458(1)	42190(1287)	458(1)	17220(867)	^{51}Mn	$\frac{19}{2}^- \rightarrow \frac{17}{2}^-$
" → DP**: 461	"	"	"	"	"	"	"	^{46}V	$\rightarrow 3^+$
470.5(9)	106857(1646)	470.7(9)	95027(1800)	470.4(9)	100196(1696)	470.6(9)	47134(1244)	^{53}Mn	$\frac{23}{2}^- \rightarrow \frac{21}{2}^-$

*due to the peak shape

**Doppler correction for the (^{32}S+^{16}O) reaction

Table 3.1.: *Energies, intensities, emitting evaporation residues and assigned transitions for the (^{32}S+^{24}Mg) reaction at a beam energy of 82 MeV , 85 MeV, 90 MeV and 95 MeV , with a γ-γ trigger condition.*

beam energy 82 MeV		beam energy 85 MeV		beam energy 90 MeV		beam energy 95 MeV			
energy (keV)	intensity	energy (keV)	intensity	energy (keV)	integral	energy (keV)	integral	nucleus	$J_{ini} \rightarrow J_{fin}$
480(2)	not fittable*	480(2)	not fittable*	480(2)	not fittable*	480(2)	not fittable*	^{45}Ti	$\frac{7}{2}^+ \rightarrow \frac{5}{2}^+$
→ DP**: 482									
509.5(5)	59552(832)	509.6(4)	58104(784)	509.6(5)	48213(760)	509.3(4)	30951(646)	511	
526.6(8)	218611(1157)	526.9(9)	176218(1093)	527.5(9)	167645(1151)	528.1(5)	99484(1045)	511 DP	
584(2)	55636(4394)	587(2)	63855(7595)	585(2)	74844(9440)	584(2)	53273(8863)	^{45}Ti	$\frac{17}{2}^- \rightarrow \frac{15}{2}^-$
→ DP**: 586									
609.8(9)	141399(2878)	609.9(9)	147736(2548)	609.7(9)	222299(2577)	609.7(9)	170828(2109)	^{50}Cr	$11^+ \rightarrow 10^+$
661.3(9)	102681(2151)	661.5(9)	112613(2258)	661.5(9)	193626(2672)	661.6(9)	156925(2244)	^{50}Cr	$12^+ \rightarrow 11^+$
682(2)	not fittable*	682(2)	not fittable*	682(2)	not fittable*	682(2)	not fittable*	^{53}Fe	$\frac{5}{2}^- \rightarrow \frac{3}{2}^-$
701(2)	not fittable*	701(2)	not fittable*	701(2)	not fittable*	701(2)	not fittable*	^{53}Fe	$\frac{19}{2}^- \rightarrow \frac{11}{2}^-$
723(1)	76657(13040)	723(1)	67904(20388)	723(1)	38084(6438)	724(1)	13289(2561)	^{51}Mn	$\frac{27}{2}^- \rightarrow \frac{23}{2}^-$
740.3(9)	177530(2591)	740.5(9)	138004(2759)	739.3(9)	135295(2959)	738.3(9)	75142(2773)	^{53}Mn	$\frac{15}{2}^- \rightarrow \frac{15}{2}^-$
”	”	”	”	”	”	”	”	^{45}Ti	$\frac{19}{2}^- \rightarrow \frac{17}{2}^-$
→ DP**: 743									
783.1(9)	475469(3100)	783.2(9)	429906(3336)	783.0(9)	558279(3475)	783.1(9)	377742(2978)	^{50}Cr	$2^+ \rightarrow 0^+$
834(2)	43248(6211)	834(1)	11531(3250)	833(1)	6893(386)	834(1)	not fittable*	^{53}Fe	$\frac{13}{2}^- \rightarrow \frac{11}{2}^-$
”	”	”	”	”	”	”	not fittable*	^{51}Mn	$\frac{23}{2}^- \rightarrow \frac{21}{2}^-$
868(2)	46155(1560)	868(2)	54050(1467)	868(2)	58629(1581)	867(2)	53353(1614)	^{52}Mn	$7^+ \rightarrow 6^+$
884.8(9)	814140(2116)	884.8(9)	538578(1946)	884.8(9)	372277(1928)	884.4(9)	156812(1626)	^{46}Ti	$2^+ \rightarrow 0^+$
→ DP**: 889									
910(2)	not fittable*	910(2)	not fittable*	910(2)	not fittable*	910(2)	not fittable*	^{46}V	$2^+ \rightarrow 0^+$
→ DP**: 914									
920(2)	not fittable*	920(2)	not fittable*	920(2)	not fittable*	920(2)	not fittable*	^{53}Mn	$\frac{21}{2}^- \rightarrow \frac{19}{2}^-$

*due to the peak shape

**Doppler correction for the (^{32}S+^{16}O) reaction

Table 3.1.: *Energies, intensities, emitting evaporation residues and assigned transitions for the (^{32}S+^{24}Mg) reaction at a beam energy of 82 MeV , 85 MeV, 90 MeV and 95 MeV , with a γ-γ trigger condition.*

beam energy 82 MeV		beam energy 85 MeV		beam energy 90 MeV		beam energy 95 MeV			
energy (keV)	intensity	energy (keV)	intensity	energy (keV)	integral	energy (keV)	integral	nucleus	$J_{ini} \rightarrow J_{fin}$
943.7(8)	129244(4971)	943.9(9)	100189(4489)	943.8(9)	95000(5284)	943.8(9)	31408(2280)	^{53}Mn	$\frac{17}{2}^- \rightarrow \frac{15}{2}^-$
959(1)	80853(2845)	959(1)	69305(2716)	958(1)	68470(3170)	958(1)	24547(1459)	^{53}Mn	$\frac{25}{2}^- \rightarrow \frac{23}{2}^-$
1010(1)	24095(2252)	1011(1)	21876(6207)	1011(1)	16912(5274)	1011(1)	5543(1599)	^{53}Fe	$\frac{11}{2}^- \rightarrow \frac{9}{2}^-$
1044(1)	198436(11617)	1044(1)	120137(8586)	1044(2)	121472(16708)	1045(2)	57737(11411)	^{46}Ti	$3^- \rightarrow 4^+$
$\rightarrow$ DP**: 1049									
1097(1)	426728(2375)	1097(1)	388232(2417)	1097(1)	526771(3263)	1097(1)	356630(3079)	^{50}Cr	$4^+ \rightarrow 2^+$
1116.3(9)	912133(2815)	1116.4(9)	614423(2601)	1116.6(9)	459590(2554)	1117(1)	193287(1805)	^{46}Ti	$4^+ \rightarrow 2^+$
$\rightarrow$ DP**: 1121									
								^{53}Mn	$\frac{13}{2}^- \rightarrow \frac{11}{2}^-$
1182(2)	not fittable*	1182(2)	not fittable*	1182(2)	not fittable*	1182(2)	not fittable*	^{45}Ti	$\frac{7}{2}^+ \rightarrow \frac{5}{2}^-$
$\rightarrow$ DP**: 1188									
1229(1)	99468(1738)	1230(1)	80479(1817)	1229(1)	85365(1781)	1230(1)	49356(1604)	^{53}Mn	$\frac{19}{2}^- \rightarrow \frac{17}{2}^-$
1251.1(9)	308942(3097)	1251.8(8)	230401(3271)	1250.8(8)	213855(2926)	1251.4(8)	104800(2636)	^{53}Mn	$\frac{15}{2}^- \rightarrow \frac{11}{2}^-$
"	"	"	"	"	"	"	"	^{51}Mn	$\frac{11}{2}^- \rightarrow \frac{7}{2}^-$
1283.0(8)	692084(3188)	1283.0(9)	554912(3408)	1282.5(8)	597531(4194)	1282.6(9)	369345(3828)	^{50}Cr	$6^+ \rightarrow 4^+$
"	"	"	"	"	"	"	"	^{46}Ti	$6^+ \rightarrow 4^+$
$\rightarrow$ DP**: 1289									
1338(2)	358376(2104)	1338(1)	267229(2105)	1337.8(2)	222523(2121)	1338(2)	105986(1742)	^{46}Ti	$10^+ \rightarrow 8^+$
$\rightarrow$ DP**:									
1440(1)	337859(3577)	1440(2)	243135(3531)	1440(2)	234713(3673)	1441(1)	114067(2887)	^{53}Mn	$\frac{11}{2}^- \rightarrow \frac{7}{2}^-$
1462(2)	not fittable*	1462(2)	not fittable*	1462(2)	not fittable*	1462(2)	not fittable*	^{45}Ti	$\frac{11}{2}^- \rightarrow \frac{7}{2}^-$
$\rightarrow$ DP**: 1468									
1541(2)	not fittable*	1541(2)	not fittable*	1541(2)	not fittable*	1541(2)	not fittable*	^{45}Ti	$\frac{15}{2}^- \rightarrow \frac{11}{2}^-$
$\rightarrow$ DP**: 1547									

*due to the peak shape

**Doppler correction for the (^{32}S+^{16}O) reaction

Table 3.1.: *Energies, intensities, emitting evaporation residues and assigned transitions for the (^{32}S+^{24}Mg) reaction at a beam energy of 82 MeV , 85 MeV, 90 MeV and 95 MeV , with a γ-γ trigger condition.*

beam energy 82 MeV		beam energy 85 MeV		beam energy 90 MeV		beam energy 95 MeV			
energy (keV)	intensity	energy (keV)	intensity	energy (keV)	integral	energy (keV)	integral	nucleus	$J_{ini} \rightarrow J_{fin}$
1591(1)	369007(2274)	1590(1)	336936(2467)	1589(1)	434427(2888)	1588.8(9)	299298(2518)	^{50}Cr	$8^+ \rightarrow 6^+$
"	"	"	"	"	"	"	"	^{50}Cr	$10^+ \rightarrow 8^+$
"	"	"	"	"	"	"	"	^{46}Ti	$8^+ \rightarrow 6^+$
$\rightarrow$ DP**: 1598									
1694(1)	83038(2286)	1694(1)	68778(2303)	1694(1)	56309(2433)	1694(1)	35152(3266)	^{53}Mn,	$\frac{17}{2}^- \rightarrow \frac{15}{2}^-$
"	"	"	"	"	"	"	"	^{46}Ti	$11^+ \rightarrow 10^+$
$\rightarrow$ DP**: 1700									
1819(2)	54890(2476)	1819(2)	49124(3755)	1819(2)	42898(2303)	1819(2)	26279(3318)	^{53}Mn	$\frac{17}{2}^- \rightarrow \frac{13}{2}^-$
1965(1)	15411(1963)	1964(1)	11266(1857)	1964(1)	8810(1581)	1962(1)	4022(1286)	^{46}Ti	$12^+ \rightarrow 10^+$
$\rightarrow$ DP**: 1977									
2028(1)	not fittable*	2028(1)	not fittable*	2028(1)	not fittable*	2028(2)	not fittable*	^{50}Cr	$13^+ \rightarrow 12^+$
2152(2)	25492(2891)	2152(2)	23120(2934)	2154(3)	51329(16650)	2150(2)	19032(6908)	^{53}Mn	$\frac{21}{2}^- \rightarrow \frac{17}{2}^-$
2301(3)	not fittable*	2301(3)	not fittable*	2299(3)	40905(12884)	2302(3)	28959(7113)	^{50}Cr	$14^+ \rightarrow 12^+$

*due to the peak shape

**Doppler correction for the (^{32}S+^{16}O) reaction

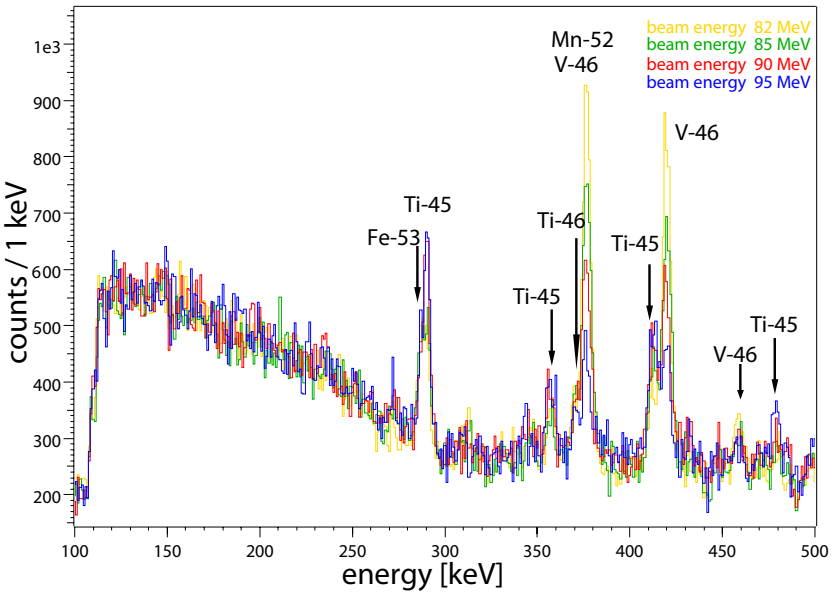

Figure 3.5.: *γ spectrum (100-500 keV) for the (^{32}S+^{24}Mg) reaction at a beam energy of 82 MeV (yellow), 85 MeV (green), 90 MeV (red) and 95 MeV (blue), obtained with a n-γ trigger.*

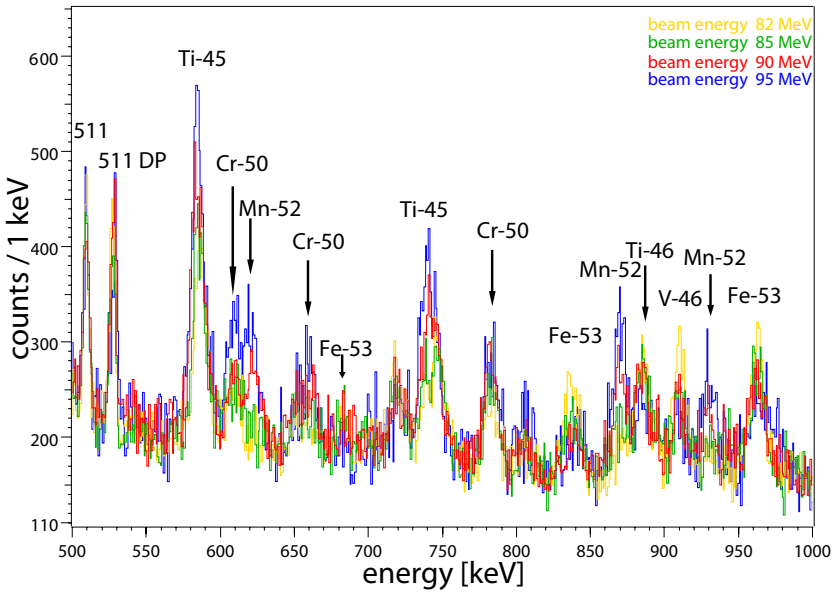

Figure 3.6.: *γ spectrum (500-1000 keV) for the (^{32}S+^{24}Mg) reaction, obtained with a n-γ trigger.*

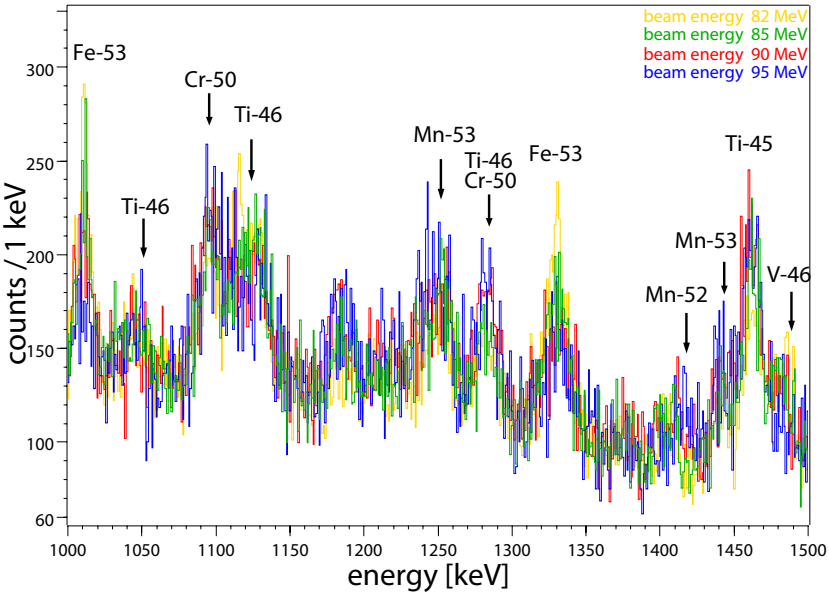

Figure 3.7.: *γ spectrum (1000-1500 keV) for the (^{32}S+^{24}Mg) reaction, obtained with a n-γ trigger.*

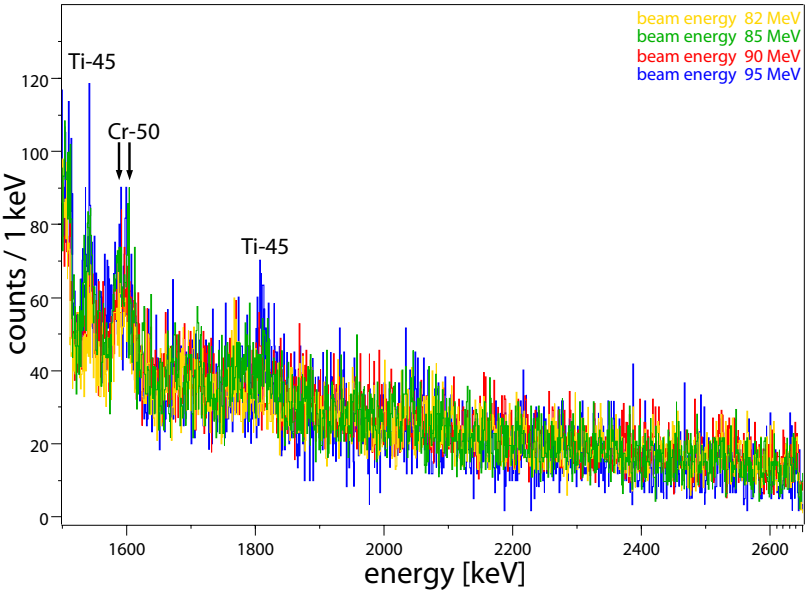

Figure 3.8.: *γ spectrum (1500-2650 keV) for the (^{32}S+^{24}Mg) reaction, obtained with a n-γ trigger.*

Table 3.2.: *Energies, intensities, emitting evaporation residues and assigned transitions for the (^{32}S+^{24}Mg)-reaction at a beam energy of 82 MeV , 85 MeV, 90 MeV and 95 MeV , with a n-γ trigger.*

beam energy 82 MeV		beam energy 85 MeV		beam energy 90 MeV		beam energy 95 MeV			
energy (keV)	intensity	energy (keV)	intensity	energy (keV)	integral	energy (keV)	integral	nucleus	$J_{ini} \rightarrow J_{fin}$
286.9 (9)	815 (97)	286.8 (7)	708 (77)	286.6 (8)	352 (195)	287.2 (9)	591 (96)	^{53}Fe	$\frac{15}{2}^- \rightarrow \frac{13}{2}^-$
289.0 (9) → DP**: 292	786 (96)	289.3 (9)	862 (86)	289.8 (9)	1471 (255)	290.4(9)	908(24)	^{45}Ti	$\frac{3}{2}^+ \rightarrow \frac{3}{2}^-$
356 (1) → DP**: 358	587 (62)	357 (1)	388 (61)	356 (1)	589 (60)	357 (1)	385 (50)	^{45}Ti	$\frac{15}{2}^- \rightarrow \frac{13}{2}^-$
377.2 (8) → DP**: 383	3603 (88)	376.7 (8)	2989 (84)	376.5 (9)	1804 (86)	376.4 (8)	531 (56)	^{46}V, ^{52}Mn	$7^+ \rightarrow 5^+$ $2^+ \rightarrow 6^+$
412.7 (8) → DP**: 414	806 (60)	412.6 (9)	1065 (64)	412.3 (8)	1100 (62)	413.0 (8)	805 (52)	^{45}Ti	$\frac{5}{2}^+ \rightarrow \frac{3}{2}^+$
420.3 (9) → DP**: 422	3225 (87)	420.2 (8)	2504 (80)	419.5 (8)	1689 (70)	420.2 (9)	656 (49)	^{46}V	$5^+ \rightarrow 3^+$
458.6 (9) → DP**: 461	608 (72)	459.0(9)	442 (58)	458.6 (8)	216 (53)			^{46}V	$\rightarrow 3^+$
479.8 (8) → DP**: 482	120 (63)					479.4 (9)	371 (44)	^{45}Ti	$\frac{7}{2}^+ \rightarrow \frac{5}{2}^+$
587.1 (8) → DP**: 586	1663 (80)	585.8 (9)	2053 (188)	584.9 (7)	2583 (88)	585.3 (8)	2204 (79)	^{45}Ti	$\frac{17}{2}^- \rightarrow \frac{15}{2}^-$
608 (1)	424 (71)	608 (1)	438 (90)	609 (1)	561 (68)	609 (1)	822 (68)	^{50}Cr	$11^+ \rightarrow 10^+$
				622 (1)	617 (68)	621 (2)	768 (67)	^{52}Mn	$9^+ \rightarrow 8^+$
						662 (1)	593 (57)	^{50}Cr	$12^+ \rightarrow 11^+$
		683 (3)	292 (81)					^{53}Fe	$\frac{5}{2}^- \rightarrow \frac{3}{2}^-$
738.4 (9) → DP**: 743	500 (98)	737.6 (9)	773 (98)	738 (1)	823 (204)	738 (1)	1086 (140)	^{45}Ti	$\frac{19}{2}^- \rightarrow \frac{17}{2}^-$
783 (1)	722 (71)	783 (1)	1067 (98)	782 (1)	980 (65)	783 (2)	665 (57)	^{50}Cr	$2^+ \rightarrow 0^+$

*due to the peak shape

**Doppler correction for the (^{32}S+^{16}O) reaction

Table 3.2.: *Energies, intensities, emitting evaporation residues and assigned transitions for the (^{32}S+^{24}Mg)-reaction at a beam energy of 82 MeV , 85 MeV, 90 MeV and 95 MeV , with a n-γ trigger.*

beam energy 82 MeV		beam energy 85 MeV		beam energy 90 MeV		beam energy 95 MeV			
energy (keV)	intensity	energy (keV)	intensity	energy (keV)	integral	energy (keV)	integral	nucleus	$J_{ini} \rightarrow J_{fin}$
837 (1)	1042 (81)	837 (1)	586 (67)	839 (2)	154 (55)	840 (1)	246 (62)	^{53}Fe	$\frac{13}{2}^- \rightarrow \frac{11}{2}^-$
		869 (1)	520 (63)	870 (1)	934 (63)	870 (1)	1131 (79)	^{52}Mn	$7^+ \rightarrow 6^+$
885 (2)	1298 (74)	885 (2)	1229 (73)	885 (2)	1012 (64)	886 (2)	542 (72)	^{46}Ti	$2^+ \rightarrow 0^+$
$\rightarrow$ DP**: 889									
911.9 (9)	1301 (73)	910.1 (9)	895 (68)	909 (1)	678 (60)			^{46}V	$2^+ \rightarrow 0^+$
$\rightarrow$ DP**: 914									
				929 (1)	651 (60)	930 (1)	370 (52)	^{52}Mn	$11^+ \rightarrow 9^+$
963.1 (9)	1563 (76)	963.1 (9)	1220 (74)	962.2 (9)	1155 (66)	962.6 (9)	479 (100)	^{53}Fe	$\frac{25}{2}^- \rightarrow \frac{21}{2}^-$
1011 (1)	1049 (74)	1011 (1)	483 (67)	1010 (1)	560 (60)	1011 (1)	409 (83)	^{53}Fe	$\frac{11}{2}^- \rightarrow \frac{9}{2}^-$
1045 (2)	298 (70)	1041 (2)	103 (68)	1046 (3)	122 (75)	104 (2)	286 (69)	^{46}Ti	$3^- \rightarrow 4^+$
$\rightarrow$ DP**: 1049									
1096 (4)	939 (70)	1096 (3)	962 (76)	1094 (3)	1156 (92)	1098 (4)	898 (90)	^{50}Cr	$4^+ \rightarrow 2^+$
1115 (3)	1196 (80)	1116 (3)	763 (132)	1111 (3)	739 (84)	1112 (4)	547 (76)	^{46}Ti	$4^+ \rightarrow 2^+$
$\rightarrow$ DP**: 1121									
1251 (2)	889 (103)	1251 (2)	1060 (68)	1249 (2)	937 (77)	1245 (2)	822 (64)	^{53}Mn	$\frac{15}{2}^- \rightarrow \frac{11}{2}^-$
1283 (1)	747 (94)	1283 (1)	545 (239)	1283 (1)	877 (78)	1282 (1)	699 (60)	^{50}Cr,	$6^+ \rightarrow 4^+$
$\rightarrow$ DP**: 1289								^{46}Ti	$6^+ \rightarrow 4^+$
1329.5 (9)	1726 (130)	1330 (1)	1189 (68)	1329 (1)	548 (77)	1329 (1)	268 (61)	^{53}Fe	$\frac{9}{2}^- \rightarrow \frac{7}{2}^-$
						1416.99 (30)	254 (79)	^{52}Mn	$8^+ \rightarrow 7^+$
1441 (1)	573 (96)	1442 (1)	382 (59)	1443 (1)	655 (80)	1441 (2)	362 (64)	^{53}Mn	$\frac{11}{2}^- \rightarrow \frac{7}{2}^-$
1463.1 (8)	1367 (96)	1462.3 (9)	1404 (75)	1461.8 (9)	502 (90)	1462 (1)	1130 (92)	^{45}Ti	$\frac{11}{2}^- \rightarrow \frac{7}{2}^-$
$\rightarrow$ DP**: 1468									

*due to the peak shape

**Doppler correction for the (^{32}S+^{16}O) reaction

Table 3.2.: *Energies, intensities, emitting evaporation residues and assigned transitions for the (^{32}S+^{24}Mg)-reaction at a beam energy of 82 MeV , 85 MeV, 90 MeV and 95 MeV , with a n-γ trigger.*

beam energy 82 MeV		beam energy 85 MeV		beam energy 90 MeV		beam energy 95 MeV			
energy (keV)	intensity	energy (keV)	intensity	energy (keV)	integral	energy (keV)	integral	nucleus	$J_{ini} \rightarrow J_{fin}$
1483 (1)	924 (94)	1481 (1)	714 (63)			1481 (1)	141 (61)	^{46}V	$9^+ \rightarrow 7^+$
				1541.9 (7) → DP**: 1547	328 (58)			^{45}Ti	$\frac{15}{2}^- \rightarrow \frac{11}{2}^-$
				1586.5 (8)	352 (61)			^{50}Cr	$8^+ \rightarrow 6^+$
				1601 (2)	292 (69)			^{50}Cr	$10^+ \rightarrow 8^+$
						1811(2) → DP**: 1818	not fittable*	^{45}Ti	$\frac{23}{2}^- \rightarrow \frac{19}{2}^-$

*due to the peak shape

**Doppler correction for the (^{32}S+^{16}O) reaction

Besides the fusion-evaporation channels from the (^{32}S+^{24}Mg) reaction also the reaction products of the fusion evaporation of the (^{32}S+^{16}O) reaction appear and ^{45}Ti and ^{46}Ti as well as ^{46}V are visible. These reactions are caused by the reaction of the beam with an oxide layer on the Mg target, which as an earth alkali metal oxides rapidly. The transitions from (^{32}S+^{16}O) reactions are visible in the γ spectra, which are Doppler corrected for the (^{32}S+^{24}Mg) reaction, at too small energies. For these transitions in tables 3.1 and 3.2, below the fitted energies, also the Doppler-corrected energies for the oxygen reactions are listed.
To compare the population of the different reactions channels for the four different beam energies some selected transitions per nucleus are analyzed and their intensities are determined. These transitions are listed in table 3.3.

Table 3.3.: *Selection of transitions to determine the relative intensities for the different beam energies.*

nucleus	energy [73] (keV)	transition ($J_i \rightarrow J_f$)	evaporation channel
^{51}Mn	237.3(2)	$\frac{7}{2}^- \rightarrow \frac{5}{2}^-$	α1p
^{45}Ti	292.77(5)	$\frac{3}{2}^+ \rightarrow \frac{3}{2}^-$	2p1n
^{46}V	423.5(1)	$5^+ \rightarrow 3^+$	1p1n
^{50}Cr	783.32(3)	$2^+ \rightarrow 0^+$	α 2p
^{52}Mn	869.9(2)	$7^+ \rightarrow 6^+$	3p1n
^{46}Ti	889.277(3)	$4^+ \rightarrow 2^+$	2p
^{53}Mn	1441.2(1)	$\frac{11}{2}^- \rightarrow \frac{7}{2}^-$	3p
^{53}Fe	1328.2(3)	$\frac{9}{2}^- \rightarrow \frac{7}{2}^-$	2p1n
(or)	1011.2(2)	$\frac{11}{2}^- \rightarrow \frac{9}{2}^-$	

The nuclei ^{50}Cr ($\alpha 2p$), ^{51}Mn ($\alpha 1p$), ^{53}Mn (3p) and ^{46}Ti(2p) are populated either by the evaporation of only protons or by the evaporation of alpha particles and protons. ^{45}Ti (2p1n), ^{46}V (1p1n), ^{52}Mn (3p1n) and ^{53}Fe (2p1n) are also produced by the evaporation of at least one single neutron.

For this reason the intensities of transitions in ^{50}Cr (α2p), ^{51}Mn (α1p), ^{53}Mn (3p) and ^{46}Ti(2p) are determined in the spectra generated by the γ-γ trigger, while for ^{45}Ti (2p1n), ^{46}V (1p1n), ^{52}Mn (3p1n) and ^{53}Fe (2p1n) they are determined in the spectra triggered by a neutron-γ trigger. For each transition in table 3.3 the relative intensity of a transition measured with the respective beam energy is calculated with respect to the highest intensity obtained with a specific beam energy. Table 3.4 shows the relative intensities for these transitions in the normalized γ spectra for the four beam energies. In the upper part of the table the intensities with the γ-γ trigger are specified for the nuclei ^{50}Cr, ^{51}Mn, ^{53}Mn and ^{46}Ti. In the lower part the relative intensities for the nuclei ^{45}Ti, ^{46}V , ^{52}Mn and ^{53}Fe are determined in the γ spectra triggered by a neutron-γ trigger .

The relative intensities for the different reaction channels are displayed in figure 3.9. The figure shows a part of the chart of nuclides for the region of interest. Marked in yellow are the two compound nuclei, ^{56}Ni for the reaction (^{32}S+^{24}Mg) and ^{48}Cr for the reaction (^{32}S+^{16}O). In shades of magenta the observed reaction products of the fusion evaporation of the beam with the target (^{32}S+^{24}Mg) are illustrated and in green the products of the fusion evaporation of the beam with the oxide layer on the target (^{32}S+^{16}O). The colour depth is correlated to the intensities of the transitions listed in table 3.3. The darker the colouration the higher is the relative intensity I_r of these transitions in the normalized spectra. A trend in the intensities of the observed reaction channel is obvious. The higher the beam energy of ^{32}S the more intense is the population of the lighter reaction products, like ^{50}Cr or ^{51}Mn. Decreasing the beam energy heavier particles like ^{53}Fe are populated stronger. The same trend is observed for the products of the (^{32}S+^{16}O) reaction. ^{45}Ti shows a higher intensity for a high beam energy, like 95 MeV, whereas the relative intensity of ^{46}V is smaller.
The main disadvantage of the ^{24}Mg target is the immediate oxidation in contact with air. An alternative reaction to the reaction of a ^{32}S beam on a ^{24}Mg target is the fusion-evaporation reaction between a ^{28}Si beam and a ^{28}Si target. The investigation of the excitation function of this alternative reaction is described in the next section.

Table 3.4.: *Determination of the relative intensities, in the upper part with a γ-γ trigger, in the lower part with a n-γ trigger.*

with γ-γ trigger

beam energy 82 MeV				**beam energy 85 MeV**				
energy (keV)	intensity I	$I * 1$	$I_{relative}$	energy (keV)	intensity I	$I * 1.21$	$I_{relative}$	nucleus
236.4(9)	120793(2446)	120793	100%	236.5(8)	94537(2439)	114389	95%	^{51}Mn
783.1(9)	475469(3100)	475469	61%	783.2(9)	429906(3336)	520186	67%	^{50}Cr
884.8(9)	814140(2116)	814140	100%	884.8(9)	538578(1946)	651679	80%	^{46}Ti
1440(1)	337859(3577)	337859	100%	1440(2)	243135(3531)	294193	87%	^{53}Mn
beam energy 90 MeV				**beam energy 95 MeV**				
energy (keV)	intensity I	$I * 1.21$	$I_{relative}$	energy (keV)	intensity I	$I * 2.07$	$I_{relative}$	nucleus
236.2(9)	88560(2941)	107158	89%	236.8(9)	42529(2756)	88035	73%	^{51}Mn
783.0(9)	558279(3475)	675518	86%	783.1(9)	377742(2978)	781926	100%	^{50}Cr
884.8(9)	372277(1928)	450456	55%	884.4(9)	156812(1626)	324601	40%	^{46}Ti
1440(2)	234713(3673)	284003	84%	1441(1)	114067(2887)	229275	68%	^{53}Mn

with neutron-γ trigger

beam energy 82 MeV				**beam energy 85 MeV**				
energy (keV)	intensity I	$I * 1$	$I_{relative}$	energy (keV)	intensity I	$I * 1$	$I_{relative}$	nucleus
289.0 (9)	786 (96)	786	52%	289.3 (9)	862 (86)	862	57%	^{45}Ti
420.3 (9)	3225 (87)	3225	100%	420.2 (8)	2504 (80)	2504	78%	^{46}V
870	0	0	0%	869 (1)	520 (63)	520	28%	^{52}Mn
1329.5 (9)	1726 (130)	1726	100%	1330 (1)	1189 (68)	1189	69%	^{53}Fe
beam energy 90 MeV				**beam energy 95 MeV**				
energy (keV)	intensity I	$I * 1$	$I_{relative}$	energy (keV)	intensity I	$I * 1.67$	$I_{relative}$	nucleus
289.9 (9)	1471 (255)	1471	97%	290.4 (9)	908(24)	1516	100%	^{45}Ti
419.5 (8)	1689 (70)	1689	52%	420.2 (9)	656 (49)	1096	34%	^{46}V
870 (1)	934 (63)	934	49%	870 (1)	1131 (79)	1889	100%	^{52}Mn
1329 (1)	548 (77)	548	32%	1329 (1)	268 (61)	448	26%	^{53}Fe

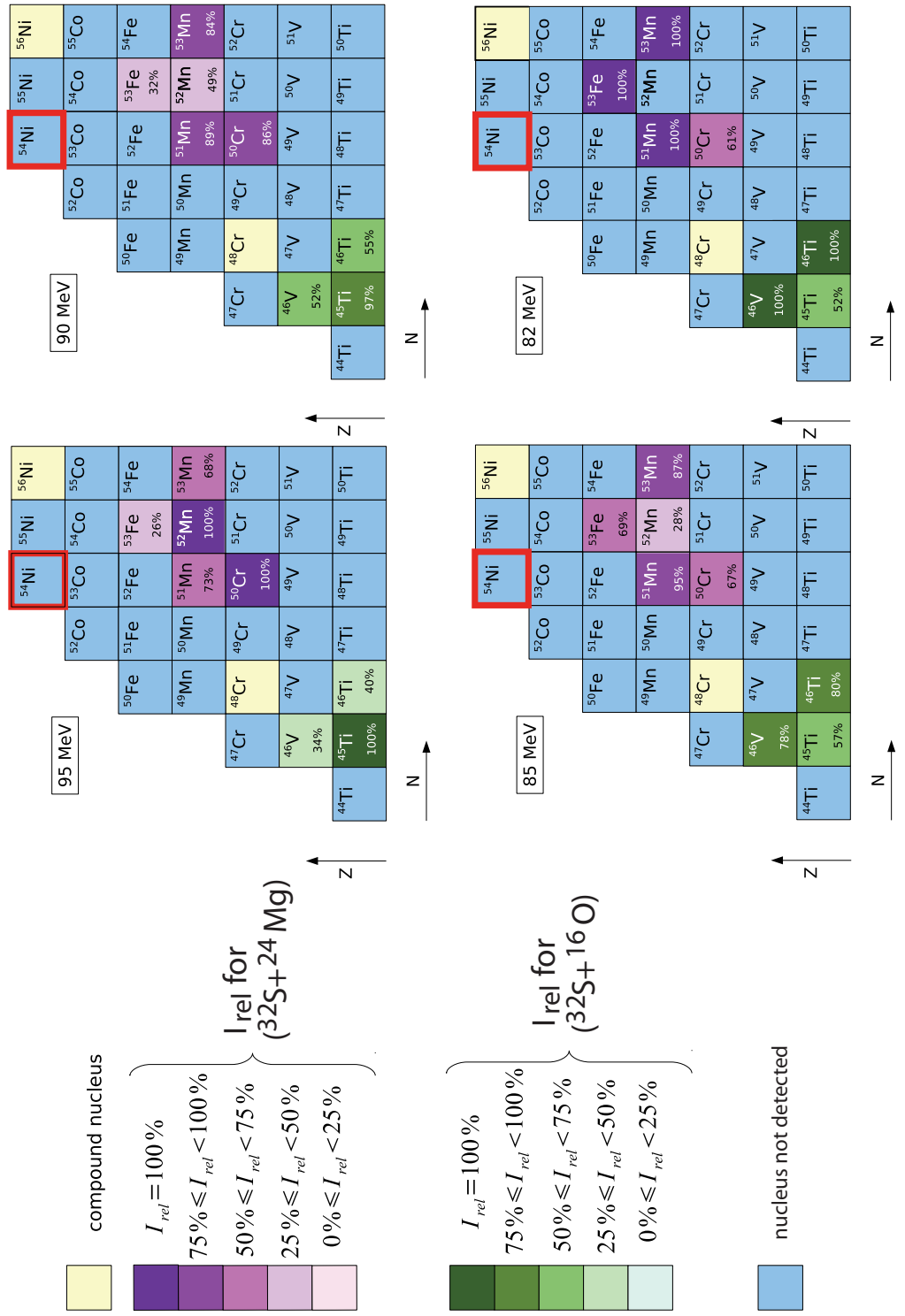

Figure 3.9.: *Part of the chart of nuclides with the products of fusion evaporation between beam and target (^{32}S+^{24}Mg) and also between beam and oxidation layer (^{32}S+^{16}O). The color depth is chosen with respect to the intensities of the transitions listed in table 3.3. The relative intensities are given in table 3.4.*

3.2. The (^{28}Si+^{28}Si) Reaction

For the (^{32}S+^{24}Mg) reaction a major background contribution was caused by reactions with the fast oxidizing target material Mg. In order find an alternative reaction the fusion evaporation with a ^{28}Si beam on a ^{28}Si target was investigated. This reaction forms the same compound nucleus. To understand the final distribution of evaporation channels another excitation function measurement was performed in order to identify the reaction channels close to ^{54}Ni. For this experiment the 4π Horus array [64] at the Cologne Tandem accelerator was employed to detect the emitted γ rays. Horus, ((H)igh efficiency (O)bservatory For γ-(R)ay (U)nique (S)pectroscopy) consists of 14 HPGe detectors with BGO shields and has an efficiency of 1.8% at an energy of 1332 keV. Figure 3.10 shows on the left side a view with respect to the beam direction into the Horus array. The right part of Figure 3.10 indicates the position of the 14 HPGe detectors.

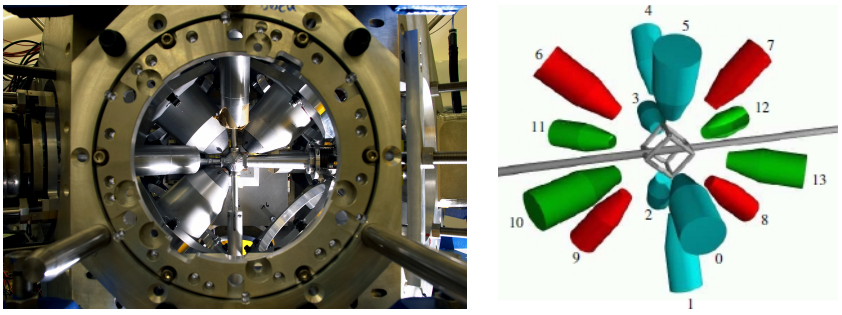

Figure 3.10.: *HORUS array at the Institut für Kernphysik (IKP), Cologne. left: the side view into the array with the target chamber in the center; right: position of the 14 HPGe detectors; figures taken from reference [64].*

Four different energies were used for the ^{28}Si beam with a charge state of 8^+: 66 MeV (effective beam time: 22 h 20 min), 70 MeV (22 h 30 min), 74 MeV (25 h 30 min) and 80 MeV (18 h). The thickness of the self-supporting ^{28}Si target was $0.096\frac{\text{mg}}{\text{cm}^2}$. The γ spectra are normalized to a common background level. The intensities of the peaks are compared between the four different runs.

The resulting γ-ray spectra are shown in figures 3.11 to 3.14. The peak energies, intensities and related transitions are summarized in table 3.2 (without normalization factors).

In the (^{32}S+^{24}Mg) experiment the exit channel ^{52}Mn was detected and no evidence for ^{54}Fe was found. In the (^{28}Si+^{28}Si) experiment the ^{54}Fe channel is observed especially at smaller beam energy but the ^{52}Mn channel is not identified.

The relative intensities of the selected transitions, see table 3.3, are compared for the four different beam energies in the same way as described in section 3.1 for the (^{32}S+^{24}Mg) experiment. To compare the population of ^{54}Fe, two-proton-evaporation channel, the transition $2^+ \rightarrow 0^+$ at an energy of 1408.1(2) keV [73] is chosen. The relative intensities are listed in table 3.6 and the results are displayed in figure 3.15. The color code is the

same as in figure 3.9 but in this experiment no fusion-evaporation reactions with an oxide layer occur.
Similar tendencies as in the previous experiment are observed: A smaller beam energy like 66 MeV enables the population of more proton-rich reaction channels like ^{53}Fe and even ^{54}Fe, while for higher beam energies like 80 MeV the evaporation of nucleons is favored populating lighter isotopes like ^{50}Cr.

The most relevant difference and improvement by using (^{28}Si+^{28}Si) reactions is that the resulting γ spectrum shows no impurities from the reaction with oxygen, like the population of $^{45,\,46}$Ti.

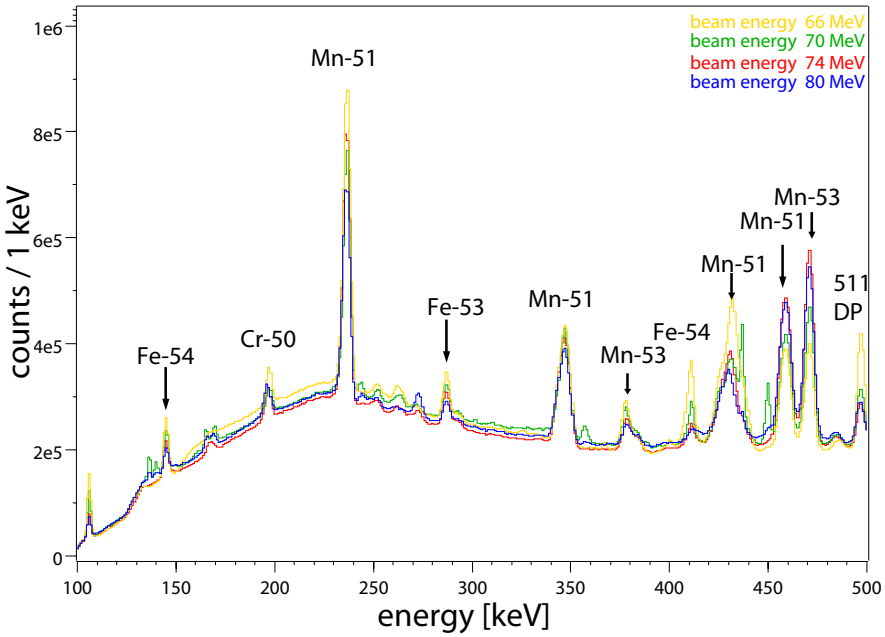

Figure 3.11.: *γ spectrum (100-500 keV) for the (^{28}Si+^{28}Si) reaction at a beam energy of 66 MeV (yellow), 70 MeV (green), 74 MeV (red) and 80 MeV (blue).*

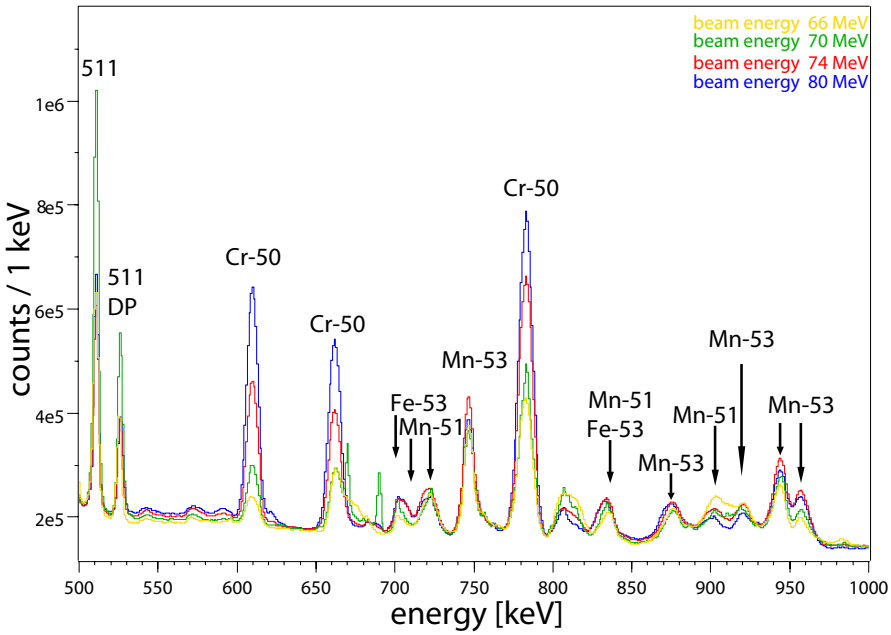

Figure 3.12.: *γ spectrum (500-1000 keV) for the (^{28}Si+^{28}Si) reaction.*

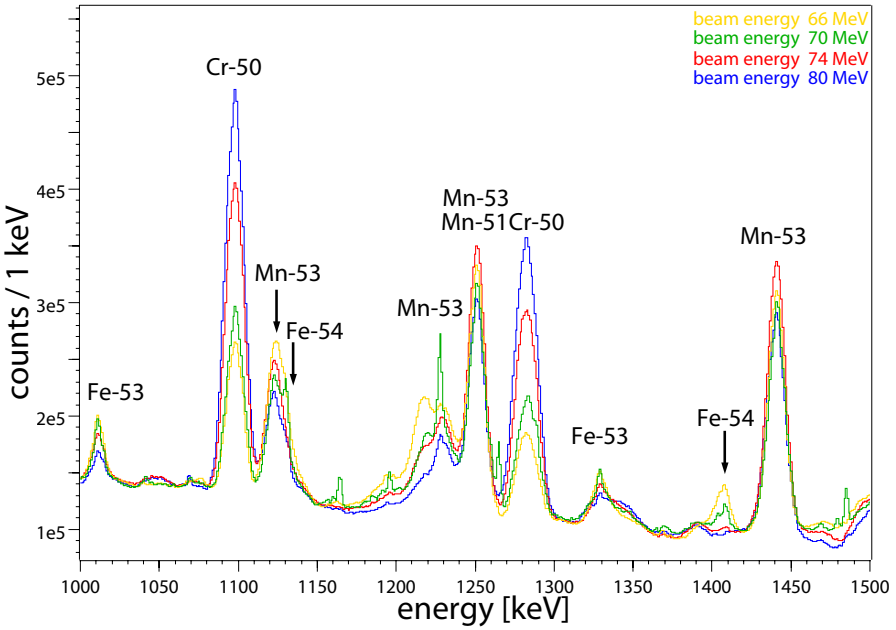

Figure 3.13.: *γ spectrum (1000-1500 keV) for the (^{28}Si+^{28}Si) reaction.*

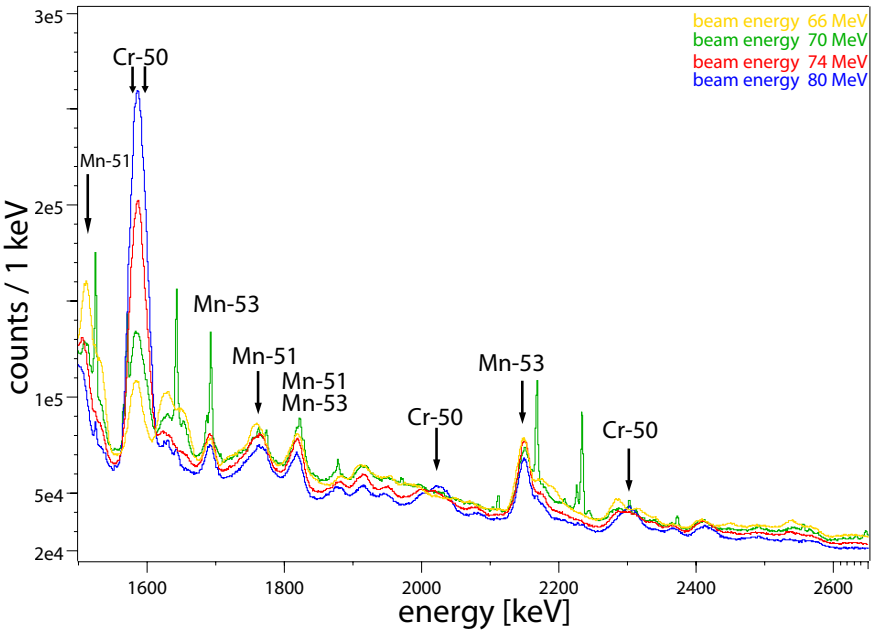

Figure 3.14.: *γ spectrum (1500-2650 keV) for the (^{28}Si+^{28}Si) reaction.*

Table 3.5.: *Energies, intensities and assigned transitions for the (^{28}Si+^{28}Si) reaction at a beam energy of 66 MeV , 70 MeV, 74 MeV and 80 MeV.*

beam energy 66 MeV		beam energy 70 MeV		beam energy 74 MeV		beam energy 80 MeV			
energy (keV)	intensity	energy (keV)	intensity	energy (keV)	integral	energy (keV)	integral	nucleus	$J_{ini} \rightarrow J_{fin}$
144.95(75)	304524(3491)	145.22(94)	168556(2332)	145.00(11)	214163(3493)	145.06(18)	97320(2597)	^{54}Fe	$10^+ \rightarrow 8^+$
197.14(12)	176717(3783	197.17(21)	109300(4084	196.62(15)	227944(6438)	196.17(19)	178165(6996)	^{50}Cr	$11^+ \rightarrow 10^+$
236.56(23)	2001539(3426)	236.60(28)	1328976(2855)	236.37(22)	2276009(3665)	236.31(32)	1321175(3124	^{51}Mn	$\frac{7}{2}^- \rightarrow \frac{5}{2}^-$
286.99(12)	229433(3102)	287.01(18)	159030(3416	286.97(15)	211803(3624)	286.96(29)	96511(3283)	^{53}Fe	$\frac{15}{2}^- \rightarrow \frac{13}{2}^-$
346.92(73)	1521029(6882)	346.94(71)	936653(3970)	346.69(69)	1677779(7029)	346.59(95)	1058107(6242	^{51}Mn	$\frac{11}{2}^- \rightarrow \frac{9}{2}^-$
378.61(16)	762687(3180)	379.71(32)	570886(4406)	379.26(18)	617059(3091)	379.25(32)	313910(2644)	^{53}Mn	$\frac{5}{2}^- \rightarrow \frac{7}{2}^-$
410.33(14)	883791(3433)	410.55(33)	567503(5666)	411.24(35)	326639(2698)	412.94(64)	166110(2238)	^{54}Fe	$6^+ \rightarrow 4^+$
431.17(63)	2426459(5759)	431.97(12)	2065153(11497)	429.97(75)	1771330(4498)	429.50(12)	969998(3747)	^{51}Mn	$\frac{17}{2}^- \rightarrow \frac{15}{2}^-$
458.81(52)	806071(2200)	458.96(56)	790117(2456)	458.80(37)	1678026(3524)	458.79(49)	1110017(3094)	^{51}Mn	$\frac{19}{2}^- \rightarrow \frac{17}{2}^-$
470.76(52)	776495(1939	470.92(46)	963151(2213)	470.72(31)	2019975(3028)	470.69(40)	1328498(2646)	^{53}Mn	$\frac{23}{2}^- \rightarrow \frac{21}{2}^-$
497.22(46)	856230(2036)	497.16(95)	402355(1748)	497.36(11)	464351(2081)	496.97(13)	337131(1822)	511DP	
609.33(22)	585459(2570)	609.69(12)	846235(2455)	609.70(41)	2546132(2875)	609.71(33)	3013033(2753)	^{50}Cr	$11^+ \rightarrow 10^+$
665.04(12)	1127178(2775)	661.96(90)	522650(1665)	662.01(49)	2071955(2487)	661.88(39)	2457464(2366)	^{50}Cr	$12^+ \rightarrow 11^+$
704.19(77)	167134(2340)	702.58(21)	182518(1337)	704.69(17)	522898(2001)	704.48(18)	416327(1698)	^{53}Fe	$\frac{19}{2}^- \rightarrow \frac{11}{2}^-$
								^{51}Mn	$\frac{27}{2}^- \rightarrow \frac{23}{2}^-$
721.69(21)	656196(3010)	722.30(13)	314793(1502)	720.88(12)	777391(2192)	720.74(16)	466767(1799)	^{51}Mn	$\frac{17}{2}^- \rightarrow \frac{13}{2}^-$
747.24(75)	1294721(2733)	747.19(78)	1134339(2442)	747.00(51)	2244580(3084)	746.95(69)	1453560(2567)	^{53}Mn	$\frac{15}{2}^- \rightarrow \frac{15}{2}^-$
782.62(50)	2166846(2809)	782.87(46)	2174012(2626)	782.86(28)	5223039(3539)	782.83(28)	4806608(3217)	^{50}Cr	$2^+ \rightarrow 0^+$
834.38(29)	295360(2014)	834.20(20)	390973(1890)	833.04(15)	685838(2303)	832.64(18)	507297(1990)	^{53}Fe	$\frac{13}{2}^- \rightarrow \frac{11}{2}^-$
								^{51}Mn	$\frac{23}{2}^- \rightarrow \frac{21}{2}^-$
877.04(22)	829012(3795)	877.34(25)	626485(3275)	876.68(17)	992336(3540)	875.39(21)	751878(3504)	^{53}Mn	$\frac{15}{2}^- \rightarrow \frac{13}{2}^-$
902.33(20)	1204754(4324)	901.80(28)	677617(3364)	901.12(18)	956795(3519)	899.93(28)	552822(3333)	^{51}Mn	$\frac{9}{2}^- \rightarrow \frac{7}{2}^-$
919.63(24)	1048761(4504)	919.50(24)	786459(3920)	920.37(17)	1061246(3906)	921.29(24)	668574(3717)	^{53}Mn	$\frac{21}{2}^- \rightarrow \frac{19}{2}^-$
942.85(20)	1261023(6420)	943.38(18)	1201671(5652)	943.37(11)	2038494(5451)	943.25(16)	1391443(5272)	^{53}Mn	$\frac{17}{2}^- \rightarrow \frac{15}{2}^-$

*due to the peak shape

Table 3.5.: *Energies, intensities and assigned transitions for the (^{28}Si+^{28}Si) reaction at a beam energy of 66 MeV , 70 MeV, 74 MeV and 80 MeV.*

beam energy 66 MeV		beam energy 70 MeV		beam energy 74 MeV		beam energy 80 MeV			
energy (keV)	intensity	energy (keV)	intensity	energy (keV)	integral	energy (keV)	integral	nucleus	$J_{ini} \rightarrow J_{fin}$
958.33(66)	486181(5665)	959.30(52)	557590(4478)	958.27(23)	1217357(4456)	958.26(32)	895947(4209)	^{53}Mn	$\frac{25}{2}^- \rightarrow \frac{23}{2}^-$
1011.34(24)	512853(2097)	1011.46(32)	356333(1943)	1011.45(31)	443249(2299)	1012.17(63)	194639(1959)	^{53}Fe	$\frac{11}{2}^- \rightarrow \frac{9}{2}^-$
1097.93(10)	1352742(2428)	1098.11(87)	1516503(2431)	1097.90(48)	3823652(3203)	1097.75(48)	3679565(2956)	^{50}Cr	$4^+ \rightarrow 2^+$
1124.78(92)	1535748(2727)	1125.22(12)	1092745(2417)	1123.36(10)	1560201(2682)	1123.52(15)	917934(2209)	^{53}Mn	$\frac{13}{2}^- \rightarrow \frac{11}{2}^-$
		1130.37(17)	120836(2588)					^{54}Fe	$4^+ \rightarrow 2^+$
1231.02(20)	818932(2532)	1228.53(24)	859369(3497)	1229.87(22)	1089489(3511)	1228.62(27)	776062(4031)	^{53}Mn	$\frac{19}{2}^- \rightarrow \frac{17}{2}^-$
1250.64(67)	2082975(2893)	1251.41(80)	1717312(2979)	1250.78(59)	3122778(3776)	1250.66(88)	2007113(4104)	^{51}Mn	$\frac{11}{2}^- \rightarrow \frac{7}{2}^-$
								^{53}Mn	$\frac{15}{2}^- \rightarrow \frac{11}{2}^-$
1283.08(14)	817682(2219)	1283.43(12)	1040556(2586)	1282.56(62)	2874432(3655)	1282.31(62)	3065927(4152)	^{50}Cr	$6^+ \rightarrow 4^+$
1329.07(29)	366113(3660)	1329.18(32)	205423(2353)	1329.37(43)	296120(4631)	1327.65(21)	254680(25947)	^{53}Fe	$\frac{9}{2}^- \rightarrow \frac{7}{2}^-$
1407.59(39)	226027(5427)	1408.03(51)	78755(2271)	1408.21(14)	20376(1676)			^{54}Fe	$2^+ \rightarrow 0^+$
1440.76(63)	2206993(3230)	1441.20(76)	1853689(3290)	1440.75(55)	3338222(4135)	1440.47(78)	2017601(3530)	^{53}Mn	$\frac{11}{2}^- \rightarrow \frac{7}{2}^-$
								^{51}Mn	$\frac{21}{2}^- \rightarrow \frac{19}{2}^-$
1583.64(40)	678289(5712)	1585.42(12)	2444278(37794)	1585.84(19)	4032447(17593)	1586.40(20)	4932841(23362)	^{50}Cr	$8^+ \rightarrow 6^+$
								^{50}Cr	$10^+ \rightarrow 8^+$
		1692.61(96)	198175(884)					^{53}Mn	$\frac{17}{2}^- \rightarrow \frac{15}{2}^-$
1761.15(60)	487592(5113)	1762.98(33)	120591(2900)	1763.21(49)	669712(4036)	1764.32(65)	494093(3539)	^{51}Mn	$\frac{15}{2}^- \rightarrow \frac{11}{2}^-$
1818.06(55)	511001(7315)	1820.98(55	356379(5165)	1817.23(47)	695940(4701)	1816.06(70)	467787(3997)	^{51}Mn	$\frac{3}{2}^- \rightarrow {}_{5}^{-}2^-$
								^{53}Mn	$\frac{17}{2}^- \rightarrow \frac{13}{2}^-$
				2028.00(50)	not fittable*	2028.00(50)	not fittable*	^{50}Cr	$13^+ \rightarrow 12^+$
2147.50(48)	539690(7262)			2149.10(40)	678163(7828)	2148.63(53)	388319(5797)	^{53}Mn	$\frac{21}{2}^- \rightarrow \frac{17}{2}^-$
		2302.31(87)	266872(2188)	2302.65(50)	230897(1185)	2302.69(26)	436768(23936)	^{50}Cr	$14^+ \rightarrow 12^+$

*due to the peak shape

Table 3.6.: *Relative intensities.*

beam energy 66 MeV				**beam energy 70 MeV**				
energy (keV)	intensity I	$I * 1.23$	$I_{relative}$	energy (keV)	intensity I	$I * 1.37$	$I_{relative}$	nucleus
236.56(23)	2001539(3426)	2462694	100%	236.60(28)	1328976(2855)	1823355	74%	^{51}Mn
782.62(50)	2166846(2809)	2665221	41%	782.87(46)	2174012(2626)	2978396	46%	^{50}Cr
1011.34(24)	512853(2097)	631014	100%	1011.46(32)	356333(1943)	488889	77%	^{53}Fe
1407.59(39)	226027(5427)	226027	100%	1408.03(51)	78755(2271)	78755	35%	^{54}Fe
1440.76(63)	2206993(3230)	2715484	81%	1441.20(76)	1853689(3290)	2543261	76%	^{53}Mn

beam energy 74 MeV				**beam energy 80 MeV**				
energy (keV)	intensity I	$I * 1$	$I_{relative}$	energy (keV)	intensity I	$I * 1.36$	$I_{relative}$	nucleus
236.3749(22)	2276009(3665)	2276009	92%	236.31(32)	1321175(3124)	1797987	73%	^{51}Mn
782.86(28)	5223039(3539)	5223039	80%	782.83(28)	4806608(3217)	6536987	100%	^{50}Cr
1011.45(31)	443249(2299)	443249	70%	1012.17(63)	194639(1959)	264884	42%	^{53}Fe
1408.21(14)	20376(1676)	20376	9%	1408	0	0	0%	^{54}Fe
1440.75(55)	3338222(4135)	3338222	100%	1440.47(78)	2017601(3530)	2745753	82%	^{53}Mn

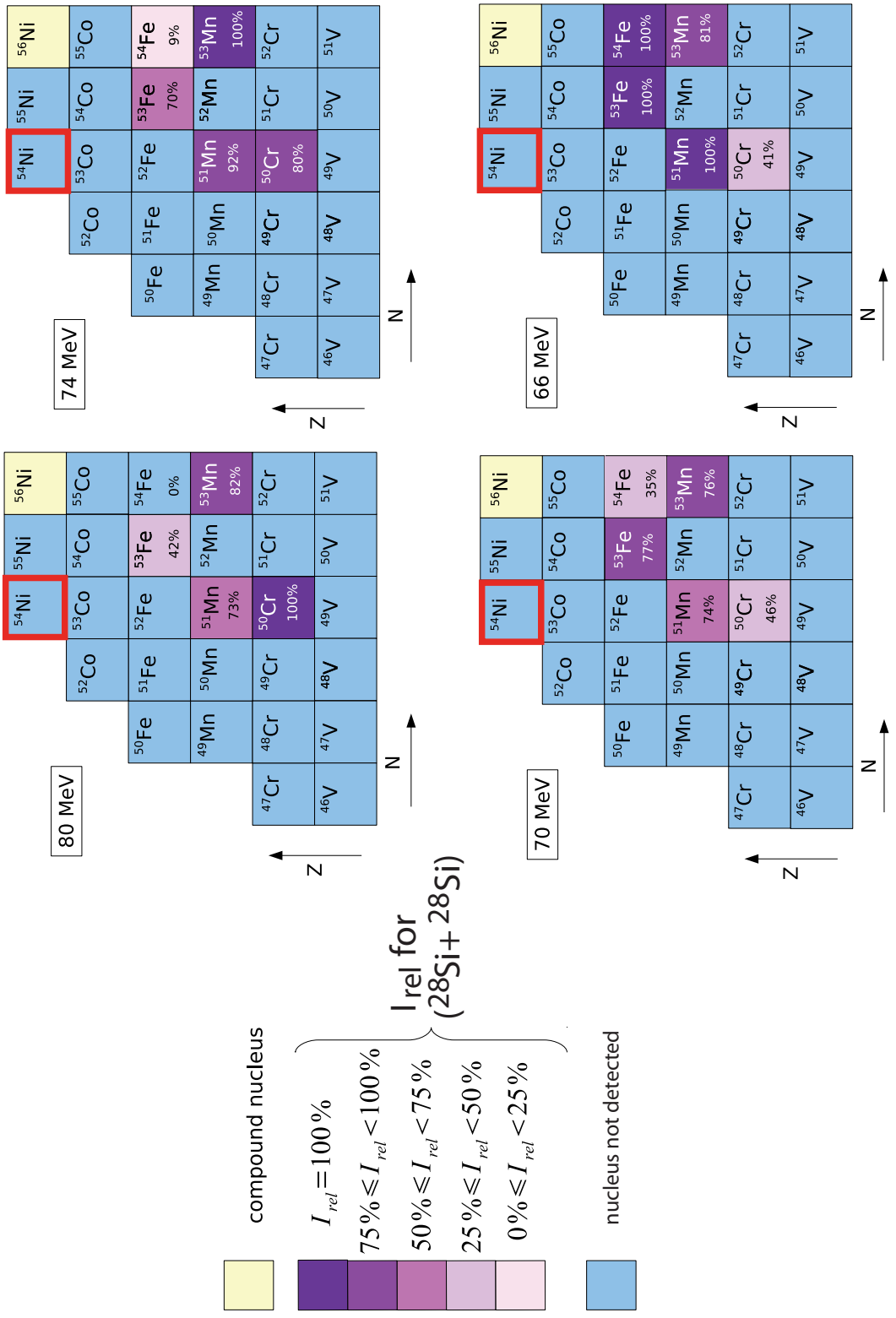

Figure 3.15.: *Part of the chart of nuclides with the products of fusion-evaporation reaction formed by the symmetric beam and target combination (^{28}Si+^{28}Si). The color depth is chosen with respect to the intensities of the transitions in table 3.3. The calculation of the relative intensities is illustrated in table 3.6.*

4. Final Experiment for the Search of Proton Emission of ^{54}Ni

4.1. Preparation of the Final Experiment

After the investigation of the reactions (^{32}S+^{24}Mg) and (^{28}Si+^{28}Si) at four different beam energies the decision was made to perform the final experiment for the search of the proton emission with the (^{28}Si+^{28}Si) reaction. This reaction has shown only small impurities of oxygen reactions and populates the nuclei close to the compound nucleus for low beam energies. Especially the verification of the ^{54}Fe population made this kind of reaction even more promising.

To estimate the optimal beam energy the cross sections were calculated with the program Cascade [78]. Figure 4.1 shows the calculated cross sections for ^{54}Ni with the reaction (^{28}Si+^{28}Si) for beam energies from 67 MeV to 79 MeV.

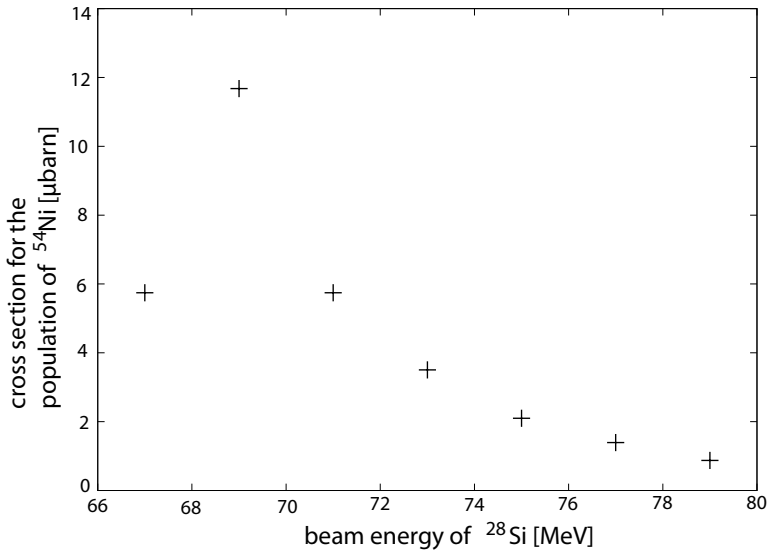

Figure 4.1.: *Cross section for the population of ^{54}Ni in dependence of different beam energies. The cross sections are calculated with the program Cascade [78].*

It was important to find a compromise between a low beam energy due to the results of section 3.2 and an energy which ensures the population of the 10^+ state of ^{54}Ni at around 6.5 MeV.

This compromise was found with a beam energy of 70 MeV. Considering the energy loss of the beam on its way to the center of the target, which is calculated to be approximately 2 MeV, and the local maximum of the cross section of $\sigma = 11.7\mu$barn for the population of ^{54}Ni around 69 MeV, this seems to be an appropriate choice.
The excitation energy of the compound nucleus ^{56}Ni was estimated with the program Pace, which is part of Lise++ [65] as $E_{ex} = 45.9$ MeV in the laboratory system. The assumption was used that the neutron separation energies of $S_n(^{56}\text{Ni}) = 16.6$ MeV and $S_n(^{55}\text{Ni}) = 14.2$ MeV are an upper energy limit to emit two neutrons from the compound nucleus. Additionally each separated neutron carries away an average kinetic energy of 2 MeV to 4 MeV. This leads to a total energy loss of $E_{loss} = 34.8 - 38.8$ MeV from the excitation energy E_{ex}, so that the remaining excitation energy of the two neutron evaporation channel ^{54}Ni is still $E_{ex,rest} = 6.5 - 10.5$ MeV and thereby high enough for populating the 10^+ level.

The second advantage of choosing a (^{28}Si+^{28}Si) reaction was the collision of two nuclei of the same mass, with a large transferred angular momentum to reach higher spin population.

The final experiment for the direct observation of proton emission out of ^{54}Ni took place in April 2009 and the effective beam time was $t = 240h = 8.64 \cdot 10^5$ s. The setup operated with a ^{28}Si beam of 70 MeV in a charge state of 9^+ and a beam intensity of $I = 1.37 \times 10^{10} \frac{1}{s}$. A pulsed beam was provided with a pulse length of 5 ns and a periodic time of 800 ns. The idea was to measure the proton emission of the isomeric 10^+ state with a lifetime of $\tau = 152(4)$ ns in the beam pauses with only low background. The beam impinged on a ^{28}Si target with the thickness of $0.33 \frac{\text{mg}}{\text{cm}^2}$. The recoils passed with a velocity of $v/c = 3.663\%$ the degrader foil in the CD chamber, made of $4.7 \frac{\text{mg}}{\text{cm}^2}$ thick tantalum and were implanted in a depth of $0.468 \frac{\text{mg}}{\text{cm}^2}$ into the catcher foil made of Al with a thickness of $1.2 \frac{\text{mg}}{\text{cm}^2}$. When proton emission took place the protons were supposed to be re-emitted out of the catcher foil and be detected by the silicon-strip detector (see section 4.3-1).

4.2. Peculiarities of an Experimental Setup for Reactions with Microbarn Cross Section

The main difficulty and challenge in this setup was to verify a reaction with a cross section in the order of a few microbarn. This required a setup, which was shielded from any mechanical perturbation. The influence of parasitic electronic induction had to be suppressed. This was realized as follows:

Vacuum

The vacuum system consisted of two pumping stations, one in front of the target chamber and the second one next to the end cup. Both were equipped with booster-, turbo- and getter pumps. When a vacuum of 10^{-6} mbar was reached, the booster- and turbo-pumps were switched off. The vacuum were only stabilized by the getter pumps which do not vibrate and do not emit high-frequency signals. To keep a vacuum only by getter pumps, the setup needed to be sealed very well.
Due to the thin foils which were used in the experiment a nitrogen ventilation system had to be created which prevented the destruction of the foils. The nitrogen gas reduced secondary reactions with air molecules. This was of high importance especially for the usage of alkali or earth alkali metal targets, like Mg [37, 101].

Electrical Grounding

The most important experimental condition was a low-noise electrical environment. There are two philosophies about efficient grounding. The first method is two provide one, very strong ground for the whole setup including all electronic modules and to separate it from external influences by using isolation transformers. The second idea is to isolate the reaction area (i.e. the target ladder in the first chamber and the DSSSD suspension, the catcher foil as well as the target wheel in the second chamber) and to allocate a different ground to the rest of the devices. This second way was realized in the setup and good resolutions of the signals could be achieved [37].

4.3. Detectors

4.3-1. Double-Sided Silicon-Strip Detector DSSSD

The most crucial device of the experiment was the CD-shaped double-sided silicon-strip detector (DSSSD), produced by RADCON [79], which was used to detect the emitted protons. The DSSSD is on the one side subdivided into 32 ring segments and in the other side into 64 strip segments. This allows a position determination with 2048 segments. The inner diameter of the detector is 32 mm, the outer is 85.04 mm. The thickness of the detector is 310 μm. The DSSSD was processed with a voltage of 60 V.

4.3-2. Neutron Detectors

Because ^{54}Ni is produced in the two-neutron-evaporation-channel of the compound nucleus ^{56}Ni, the neutron detection became an important tool for gating on the correct reaction. Five neutron detectors of the NORDBALL-array [46] were installed with focus on the CD chamber, at an angle of 37° to the beam line in forward direction. The efficiency of the neutron detector array is 9.75%. The detectors are filled with organic liquid scintillator (type BC-501). The inner side of the stainless steel container is coated with TiO_2 paint for a better reflection property. The backside of the scintillator is optically connected with a pyrex window to a photomultiplier (XP2041). They worked with voltages of ±3000 to 4500 V. As well as to the neutron signals the detectors were also sensitive to γ signals. But because of the different pulse shapes of γ and neutron signals the two types could be separated well. For this purpose neutron-γ discrimination modules were developed by the electronics workshop of the IKP, Cologne, [82].

4.3-3. HPGe Detectors

To observe the γ energies at the target and CD chamber, 6 standard High purity Germanium detectors (HPGe) were used. Four detectors monitored the reactions at the target and another two detectors were placed next to the DSSSD to measure the isomeric decays. The operational voltage was 4500-5000 V.

4.4. Electronics

4.4-1. Signal Processing

- A charge pulse from the DSSSD was transformed, shaped and amplified by preamplifiers, which were constructed in the electronics workshop of the IKP, Cologne. As main amplifier Mesytec modules Type STM-16 [70] were used, which provided the energy, time and multiplicity signals of the DSSSD.

- Only the time signals from the neutron detectors are of interest. After they were separated from the γ signals, which were also detected by the NORDBALL counters, they were used for the trigger conditions (see below) and are also digitized.

- Energy and time signals from the HPGe detectors are needed. The energy channels were connected with the main amplifier ORTEC modules [74]. The time signals were processed by the time-to-amplitude converter (TAC) and the constant-fraction discriminator (CFD). The logic OR from the time signals were also used for the trigger.

All analog signals were digitized by V785 ADC or a V775 TDC, produced by CAEN [13]. They were driven by a VME based CPU together with the trigger module (Triva5) [96]. The data acquisition program and the analysis software is part of the program MARaBOU [67].

Figure 4.2 demonstrates the signal processing.

4.4-2. Trigger Processing

Based on the experience of the previous beam times a system of three different triggers turned out to be most promising:

- a single trigger from the DSSSD time signal: trigger 1

- a coincidence trigger from the neutron-time signals and the γ-time signals at the target chamber: trigger 2

- a coincidence trigger from the neutron-time signals and the γ-time signals at the CD chamber: trigger 3

To achieve a coincidence the fast neutron signals were delayed and broadened, so that the slower γ signals could match into the coincidence gate.

In figure 4.3 the circuit diagram for the trigger processing is shown.

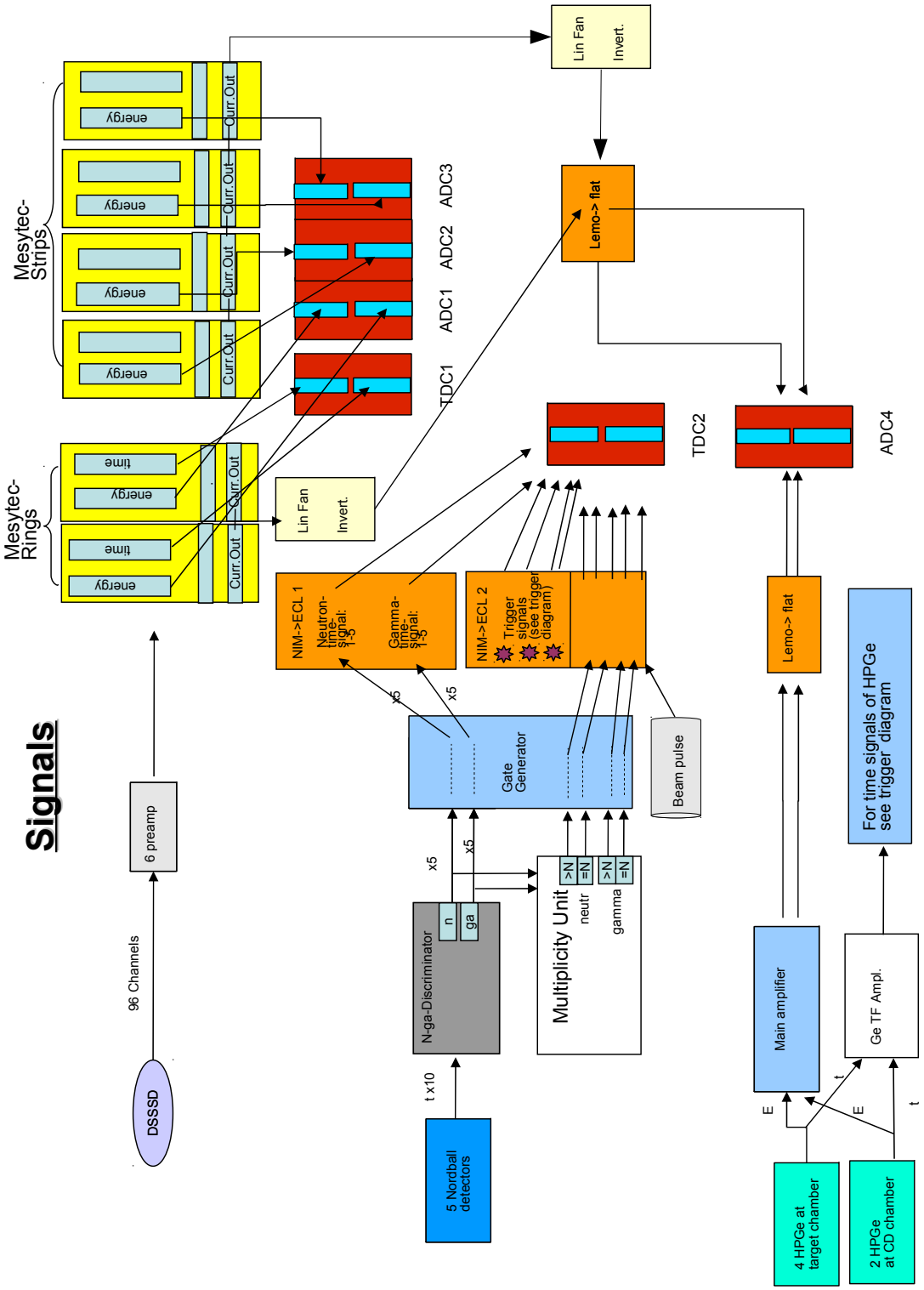

Figure 4.2.: *Diagram of signal circuit.*

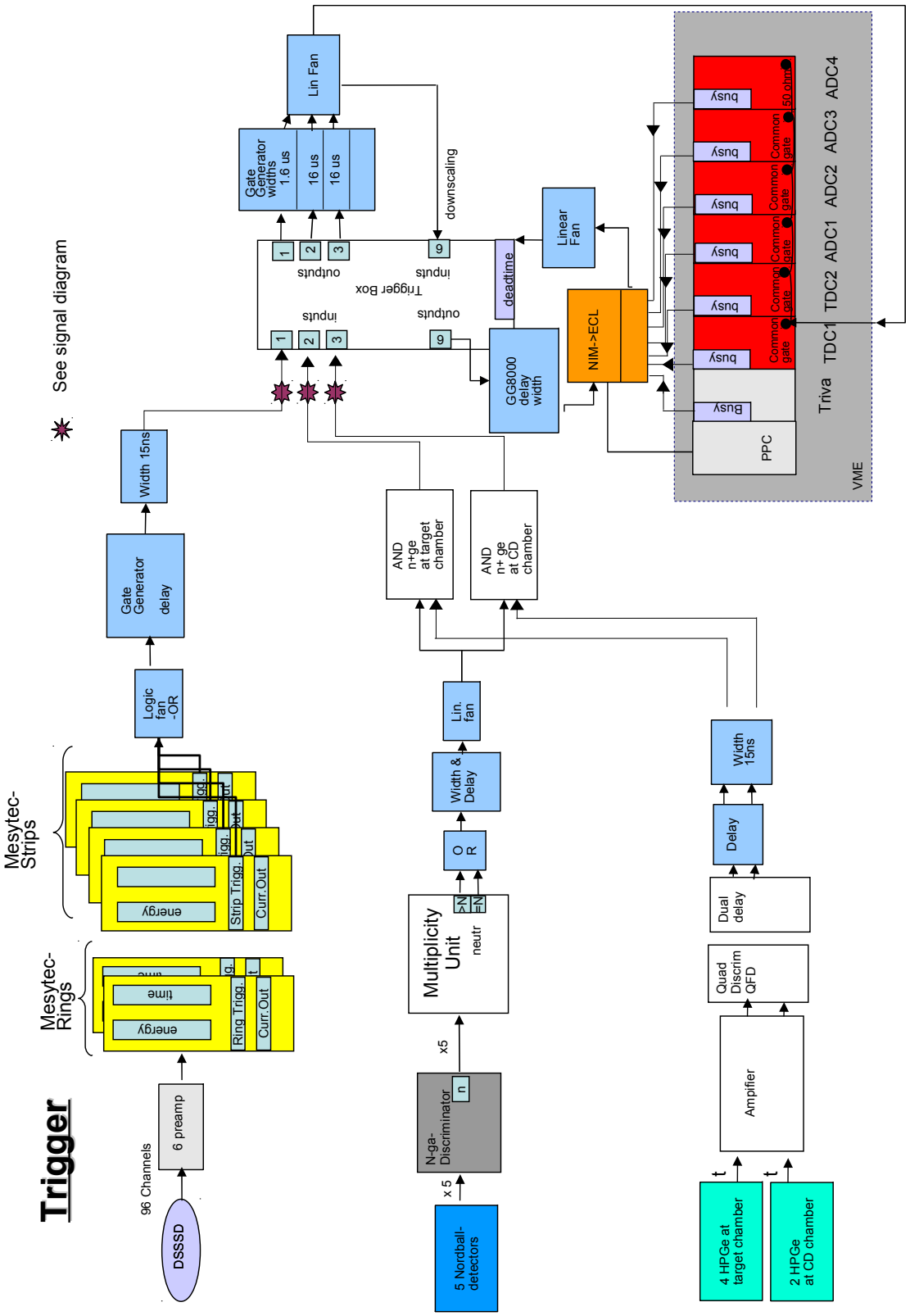

Figure 4.3.: *Diagram of trigger circuit.*

4.5. Analysis

In the sections 4.5-1 to 4.5-4 the analysis of the final beam time in April 2009 is described.

4.5-1. γ Spectra

In this section the γ spectra of the HPGe detectors at the target chamber as well as at the CD chamber are investigated to screen the population of the reaction channels during the beam time. They were triggered by a neutron-γ trigger and calibrated with a ^{226}Ra source, respectively ^{152}Eu, before and after the beamtime.

γ Spectra at the Target Chamber

Figures 4.4 to 4.7 illustrate the γ spectra of the HPGe detectors around the target chamber (here as an example from the two HPGe at 90° to the beam axis). They show the well-known recoils of the compound reaction with a large amount of ^{53}Fe, which confirms the dominant population of heavier recoils close to the compound nucleus, compare section 3.2, and the enrichment of the neutron-evaporation channel due to neutron-γ discrimination. Table 4.1 lists the energies, intensities, the transitions and the half-life of the related states. Besides the additional observation of ^{181}Ta and ^{27}Al energies the γ spectra demonstrate consistency with the results of section 3.2.

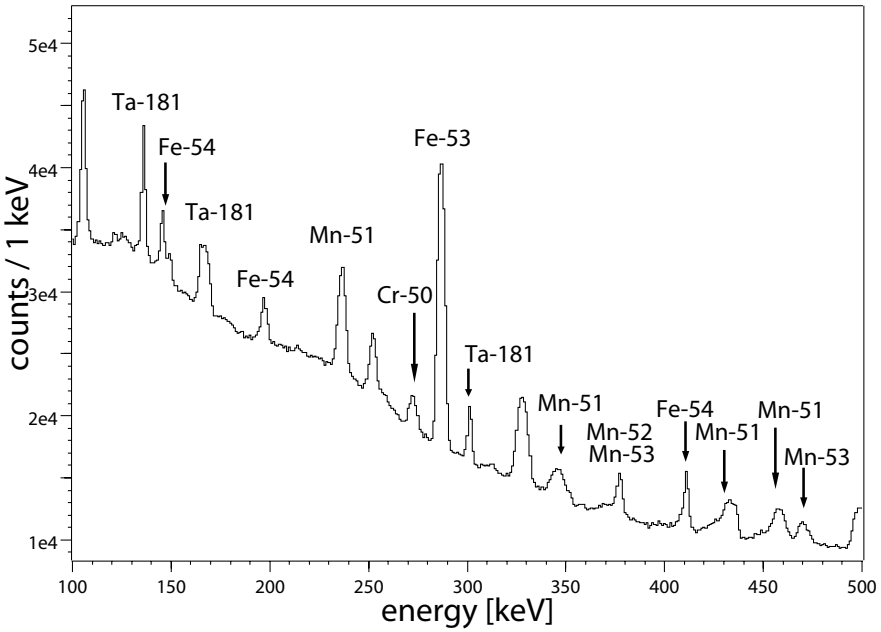

Figure 4.4.: *γ spectrum (100-500 keV) at the target chamber.*

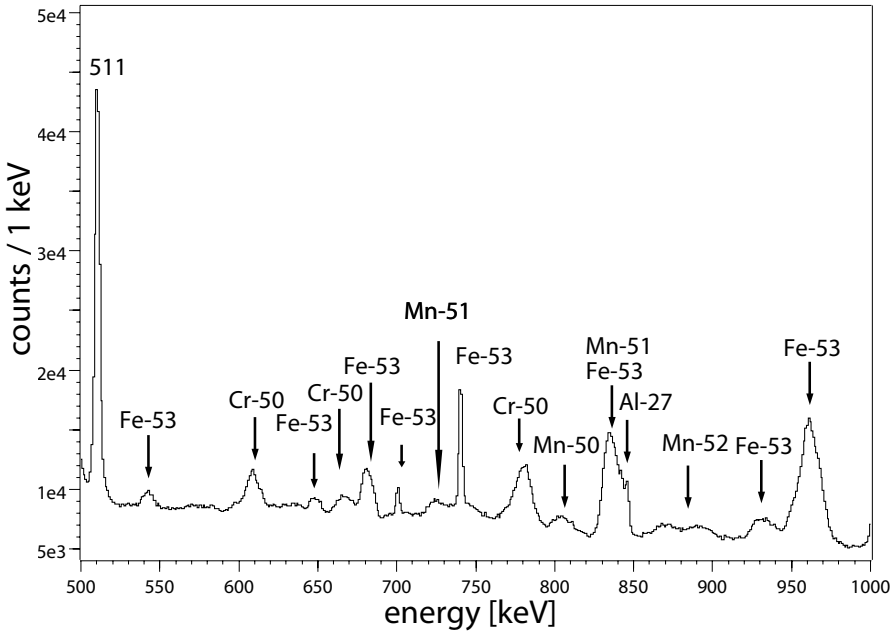

Figure 4.5.: *γ spectrum (500-1000 keV) at the target chamber.*

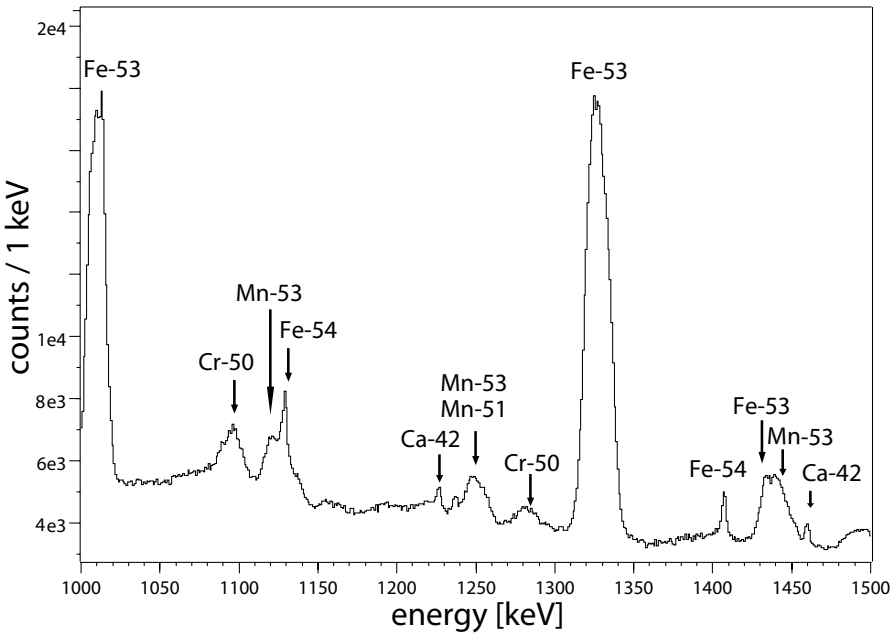

Figure 4.6.: *γ spectrum (1000-1500 keV) at the target chamber.*

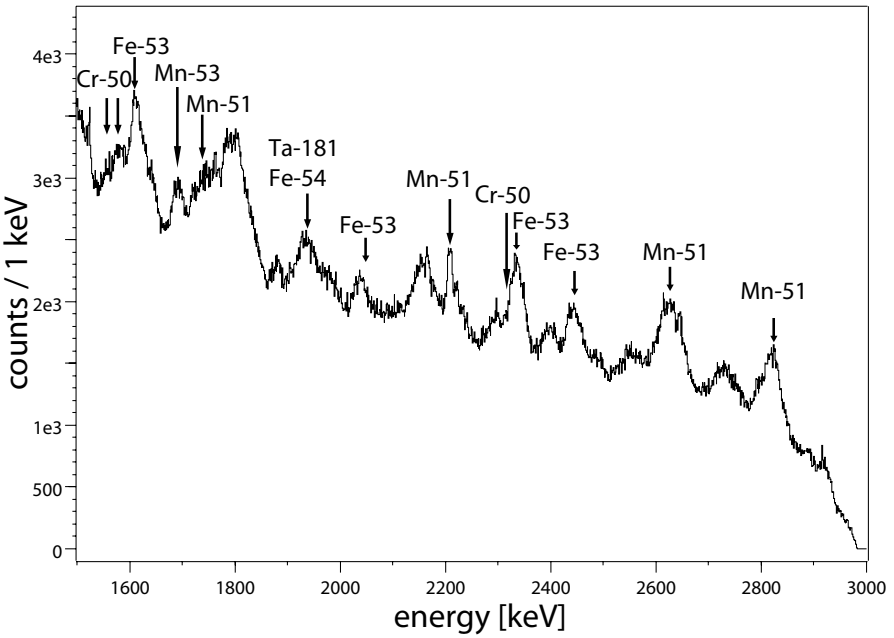

Figure 4.7.: *γ spectrum (1500-3000 keV) at the target chamber.*

Table 4.1.: *Energies, intensities, transitions and half-lives for the γ spectra at the target chamber.*

energy (keV)	intensity	nucleus	$J_{ini} \rightarrow J_{fin}$	$T_{\frac{1}{2}}$
56.49(40)	17039(823)	^{181}Ta X-rays	$K_{\alpha 1}$	
74.24(32)	46514(1598)	^{208}Pb X-rays	$K_{\alpha 1}$	
136.0(5)	20957(593)	^{181}Ta	$\frac{9}{2}^+ \rightarrow \frac{7}{2}^+$	39.5 ps
145.7(5)	9623(900)	^{54}Fe	$10^+ \rightarrow 8^+$	364 ns
166(2)	36690(2226)	^{181}Ta	$\frac{11}{2}^+ \rightarrow \frac{9}{2}^+$	16 ps
197.1(7)	10670(899)	^{54}Fe	$9^+ \rightarrow 10^+$	41 ps
236(1)	41508(1602)	^{51}Mn	$\frac{7}{2}^- \rightarrow \frac{5}{2}^-$	14.1 ps
272.4(8)	17601(4627)	^{50}Cr	$14^+ \rightarrow 13^+$	0.26 ps
286.7(5)	111655(1203)	^{53}Fe	$\frac{15}{2}^- \rightarrow \frac{13}{2}^-$	
301.2(3)	10794(514)	^{181}Ta	$\frac{11}{2}^+ \rightarrow \frac{7}{2}^+$	16 ps
346(1)	29553(5119)	^{51}Mn	$\frac{11}{2}^- \rightarrow \frac{9}{2}^-$	0.5 ps
377.2(9)	10054(1135)	^{53}Mn,	$\frac{5}{2}^- \rightarrow \frac{7}{2}^-$	117 ps
”	”	^{52}Mn	$2^+ \rightarrow 6^+$	21 min
411.0(3)	12478(470)	^{54}Fe	$6^+ \rightarrow 4^+$	1.215 ns
433(2)	27559(1902)	^{51}Mn	$\frac{17}{2}^- \rightarrow \frac{15}{2}^-$	1.43 ns

*due to the peak shape
*with Doppler correction

Table 4.1.: *Energies, intensities, transitions and half-lives for the γ spectra at the target chamber.*

energy (keV)	intensity	nucleus	$J_{ini} \rightarrow J_{fin}$	$T_{\frac{1}{2}}$
457(2)	18335(2426)	^{51}Mn	$\frac{19}{2}^- \rightarrow \frac{17}{2}^-$	< 0.7 ps
542.2(8)	11785(2821)	^{53}Fe	$\frac{17}{2}^- \rightarrow \frac{13}{2}^-$	
608.8(9)	30639(2644)	^{50}Cr	$11^+ \rightarrow 10^+$	0.49 ps
648.3(8)	19076(10276)	^{53}Fe	$\frac{5}{2}^- \rightarrow \frac{1}{2}^-$	2.8 ps
663(1)	8717(1106)	^{50}Cr	$12^+ \rightarrow 11^+$	0.111 ps
681.4(9)	37527(1021)	^{53}Fe	$\frac{5}{2}^- \rightarrow \frac{3}{2}^-$	2.8 ps
700.8(5)	5737(478)	^{53}Fe	$\frac{19}{2}^- \rightarrow \frac{11}{2}^-$	2.54 min
722(2)	18981(4296)	^{51}Mn	$\frac{17}{2}^- \rightarrow \frac{13}{2}^-$	1.43 ns
740.42(12)	27681(361)	^{53}Fe	$\frac{3}{2}^- \rightarrow \frac{7}{2}^-$	63 ns
780(2)	56533(1233)	^{50}Cr	$2^+ \rightarrow 0^+$	9.08 ps
804(2)	24433(7762)	^{50}Mn	$7^+ \rightarrow 5^+$	
834(1)	106093(11669)	^{53}Fe,	$\frac{13}{2}^- \rightarrow \frac{11}{2}^-$	<132 fs
”	”	^{51}Mn	$\frac{23}{2}^- \rightarrow \frac{21}{2}^-$	
845(2)	130041(8405)	^{27}Al	$\frac{1}{2}^+ \rightarrow \frac{5}{2}^+$	
870(2)	20069(2783)	^{52}Mn	$7^+ \rightarrow 6^+$	0.12 ps
932(1)	31427(1090)	^{53}Fe	$\frac{13}{2}^- \rightarrow \frac{11}{2}^-$	
961(1)	168268(1269)	^{53}Fe	$\frac{25}{2}^- \rightarrow \frac{21}{2}^-$	
1010(1)	177071(1268)	^{53}Fe	$\frac{11}{2}^- \rightarrow \frac{9}{2}^-$	53 fs
1096(1)	18564(2082)	^{50}Cr	$4^+ \rightarrow 2^+$	2.22 ps
1120(1)	8553(403)	^{53}Mn	$\frac{13}{2}^- \rightarrow \frac{11}{2}^-$	10.7 ps
1129.4(8)	14509(459)	^{54}Fe	$4^+ \rightarrow 2^+$	4 ps
1226.7(9)	2052(368)	^{42}Ca	$4^+ \rightarrow 0^+$	3 fs
1247(2)	54225(6308)	^{51}Mn,	$\frac{11}{2}^- \rightarrow \frac{7}{2}^-$	0.5 ps
”	”	^{53}Mn	$\frac{15}{2}^- \rightarrow \frac{11}{2}^-$	2.7ps
1281(2)	8647(2502)	^{50}Cr	$6^+ \rightarrow 4^+$	0.69 ps
1328(1)	265132(1470)	^{53}Fe	$\frac{9}{2}^- \rightarrow \frac{7}{2}^-$	17 ps
1407.1(9)	4537(341)	^{54}Fe	$2^+ \rightarrow 0^+$	0.8 ps
1434(2)	19582(1209)	^{53}Fe	$\frac{13}{2}^- \rightarrow \frac{11}{2}^-$	
1443(2)	15629(931)	^{53}Mn	$\frac{11}{2}^- \rightarrow \frac{7}{2}^-$	0.6 ps
1459.7(9)	1955(291)	^{42}Ca	$6^+ \rightarrow 4^+$	85 fs
1523.1(9)	1129(266)	^{42}Ca	$2^+ \rightarrow 0^+$	0.82 ps
1580(2)	not fittable*	^{50}Cr	$8^+ \rightarrow 6^+$	0.28 ps
1595(2)	not fittable*	^{50}Cr	$10^+ \rightarrow 8^+$	0.76 ps
1612(2)	16183(2837)	^{53}Fe	$\frac{11}{2}^- \rightarrow \frac{7}{2}^-$	
1689(2)	9764(841)	^{53}Mn	$\frac{17}{2}^- \rightarrow \frac{15}{2}^-$	0.16 ps

*due to the peak shape

*with Doppler correction

Table 4.1.: *Energies, intensities, transitions and half-lives for the γ spectra at the target chamber.*

energy (keV)	intensity	nucleus	$J_{ini} \rightarrow J_{fin}$	$T_{\frac{1}{2}}$
1768(2)	7418(775)	^{51}Mn	$\frac{23}{2}^- \rightarrow \frac{21}{2}^-$	
1931(2)	16722(2109)	^{181}Ta	$\rightarrow 7^+$	
1936(3)	7540(1392)	^{54}Fe	$3^+ \rightarrow 2^+$	
2041(2)	9362(2982)	^{53}Fe	$\frac{3}{2}^- \rightarrow \frac{7}{2}^-$	0.24 ps
2208.2(9)	5640(423)	^{51}Mn	$\frac{19}{2}^- \rightarrow \frac{15}{2}^-$	
2299(1)	7107(821)	^{50}Cr	$14^+ \rightarrow 12^+$	0.26 ps
2335(1)	22547(1230)	^{53}Fe	$\frac{11}{2}^- \rightarrow \frac{7}{2}^-$	53 fs
2443(2)	12520(1384)	^{53}Fe	$\frac{13}{2}^- \rightarrow \frac{9}{2}^-$	
2626(4)	26401(2835)	^{51}Mn	$\frac{7}{2}^- \rightarrow \frac{3}{2}^-$	
2821(4)	27357(2283)	^{51}Mn	$\frac{3}{2}^- \rightarrow \frac{5}{2}^-$	

*due to the peak shape
*with Doppler correction

γ spectra at the CD chamber

Figures 4.8 to 4.11 show the γ spectra from the two HPGe detectors around the CD chamber. They show the isomeric states which were already expected from the γ spectra at the target chamber, with ^{53}Fe as a dominant reaction channel. Also ^{181}Ta, the material of the degrader foil, contributes to the γ spectra especially in the low energy part, and ^{27}Al, of which the catcher foil is made, is detected. Table 4.2 lists the details of the the detected nuclei, i.e. the energies, intensities, transitions and half-lives.
Besides these reactions also the Doppler-shifted γ rays deriving from the target can be observed in the γ spectra. Because the spectra in figures 4.8 to 4.11 are not Doppler corrected these transitions occur at too high energies. The corresponding Doppler-corrected energies are also listed in table 4.2 for these transitions.
The most interesting question is whether it is possible to find an evidence for the population of isomeric ^{54}Ni, which should be implanted into the catcher foil.

If the 10^+ state just de-excites by γ decay to the ground state of ^{54}Ni the transition $2^+ \rightarrow 0^+$ should be visible in the γ spectrum at an energy of 1392 keV. But no hint of a peak at this energy can be found. If a proton emission has taken place an indirect evidence of this proton emission could be the detection of the $\frac{9}{2}^- \rightarrow \frac{7}{2}^-$ transition in ^{53}Co as it was observed in the RISING experiment at GSI, see section 1.3. However, on the one hand ^{53}Co also could have been populated directly by the fusion-evaporation itself and on the other hand this transition at 1327 keV is similar to the $\frac{9}{2}^- \rightarrow \frac{7}{2}^-$ transition in the mirror nucleus ^{53}Fe, which in this spectrum is populated intensively. Hence, the evidence for the population of ^{54}Ni is not given.

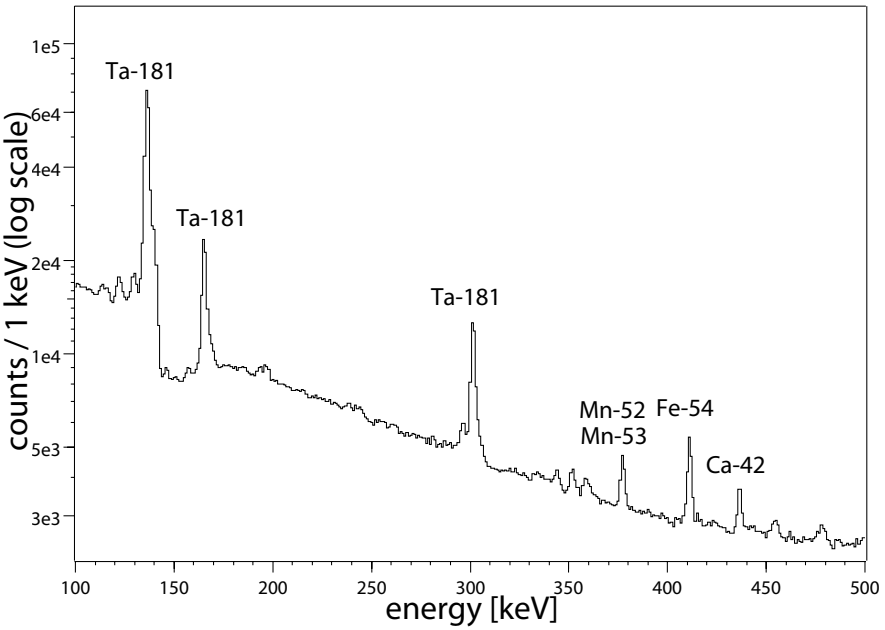

Figure 4.8.: *γ spectrum (100-500 keV) at the CD chamber.*

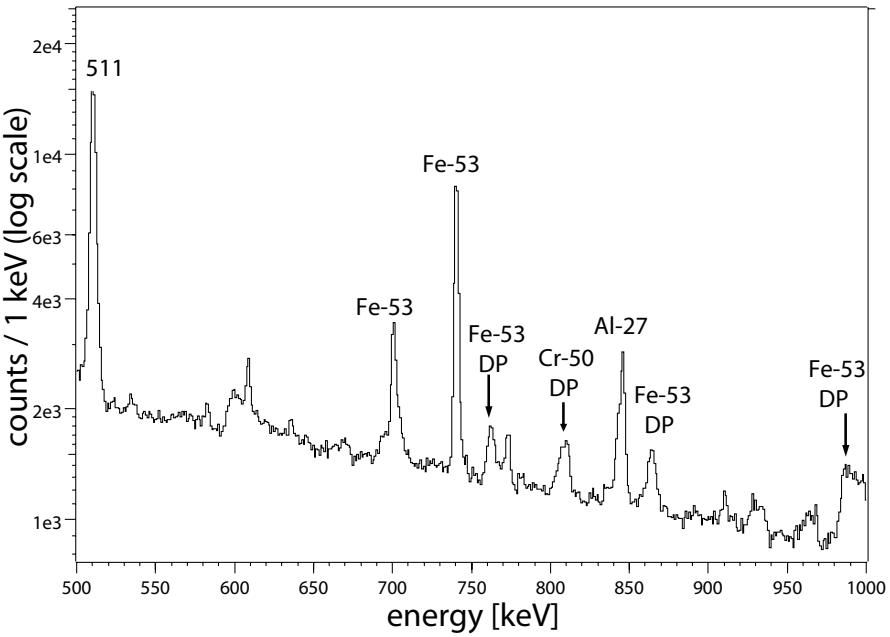

Figure 4.9.: *γ spectrum (500-1000 keV) at the CD chamber.*

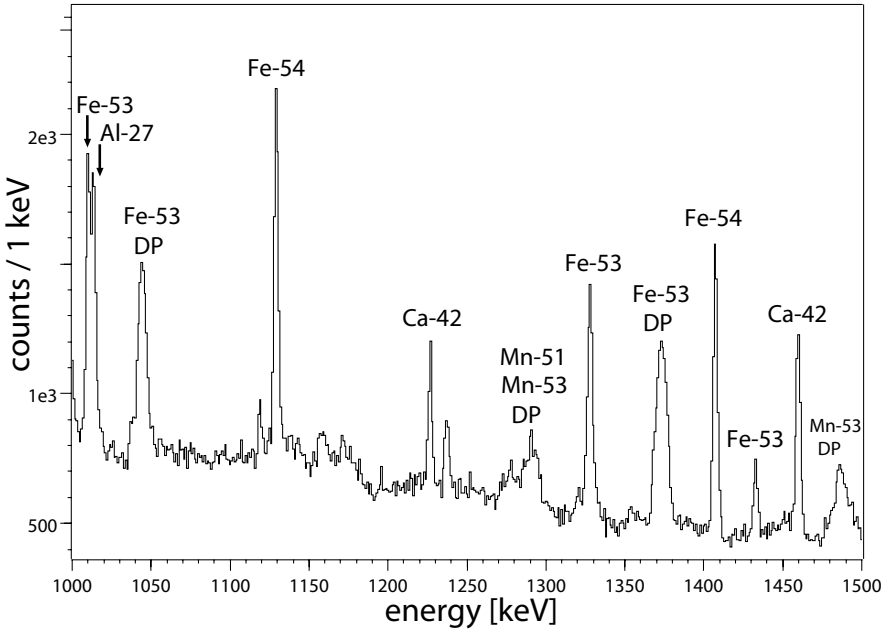

Figure 4.10.: *γ spectrum (1000-1500 keV) at the CD chamber.*

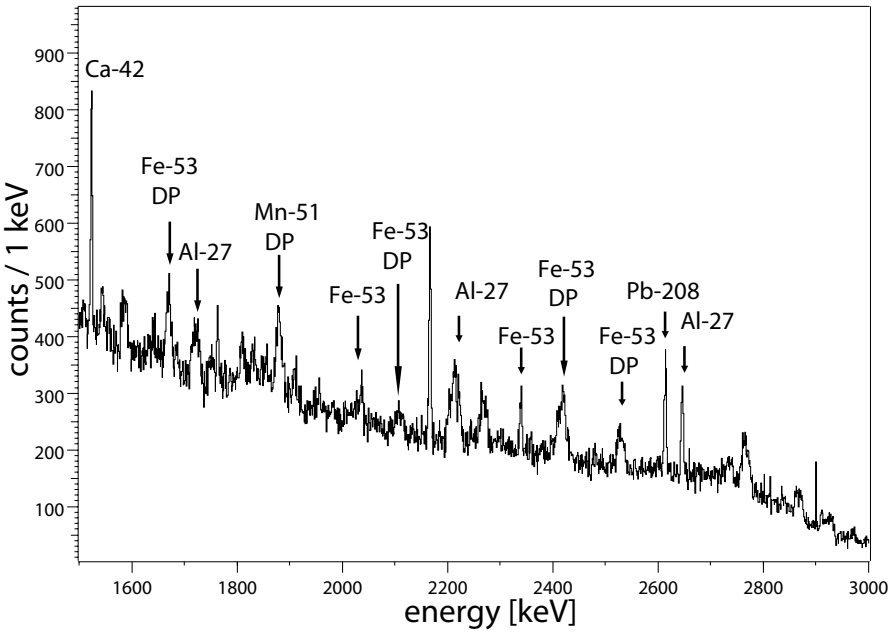

Figure 4.11.: *γ spectrum (1500-3000 keV) at the CD chamber.*

Table 4.2.: *Energies, intensities, transitions and half-lives for the γ spectra at the CD chamber.*

energy (keV)	intensity	nucleus	transition $J_{ini} \rightarrow J_{fin}$	$T_{\frac{1}{2}}$
56.71(11)	93515(935)	^{181}Ta, X-ray	$K_{\alpha 1}$	
136.35(45)	155417(653)	^{181}Ta	$\frac{9}{2}^+ \rightarrow \frac{7}{2}^+$	39.5 ps
165.38(10)	38376(399)	^{181}Ta	$\frac{11}{2}^+ \rightarrow \frac{9}{2}^+$	16 ps
301.50(14)	20425(328)	^{181}Ta	$\frac{11}{2}^+ \rightarrow \frac{7}{2}^+$	16 ps
377.21(46)	3738(199)	^{52}Mn	$2^+ \rightarrow 6^+$	21 min
”	”	^{53}Mn	$\frac{5}{2}^- \rightarrow \frac{7}{2}^-$	117 ps
411.15(30)	6231(219)	^{54}Fe	$6^+ \rightarrow 4^+$	1.215 ns
436.48(61)	2631(212)	^{42}Ca	$6^+ \rightarrow 4^+$	5.36 ns
700.86(38)	5894(181)	^{53}Fe	$\frac{19}{2}^- \rightarrow \frac{11}{2}^-$	2.54 min
740.45(11)	20183(206)	^{53}Fe	$\frac{3}{2}^- \rightarrow \frac{7}{2}^-$	63 ns
762.53(13) → DP**:741	3184(173)	^{53}Fe	$\frac{3}{2}^- \rightarrow \frac{7}{2}^-$	63 ns
808.84(13) → DP**:783	3009(152)	^{50}Cr	$2^+ \rightarrow 0^+$	9.08 ps
845.36(52)	7162(322)	^{27}Al	$\frac{1}{2}^+ \rightarrow \frac{5}{2}^+$	35 ps
864.31(15) → DP**:836	2611(241)	^{53}Fe	$\frac{13}{2}^- \rightarrow \frac{11}{2}^-$	<132 fs
996.90(31) → DP**:963	4366(416)	^{53}Fe	$\frac{25}{2}^- \rightarrow \frac{21}{2}^-$	
1011.77(10)	3187(127)	^{53}Fe	$\frac{11}{2}^- \rightarrow \frac{9}{2}^-$	53 fs
1013.61(57)	3065(120)	^{27}Al	$\frac{3}{2}^+ \rightarrow \frac{5}{2}^+$	1.49 ps
1044.36(91) → DP**:1011	4765(212)	^{53}Fe	$\frac{11}{2}^- \rightarrow \frac{9}{2}^-$	53 fs
1129.22(35)	4200(143)	^{54}Fe	$4^+ \rightarrow 2^+$	4 ps
1226.79(69)	1403(96)	^{42}Ca	$4^+ \rightarrow 0^+$	3 fs
1291.60(38) → DP**:1250	1865(378)	^{51}Mn,	$\frac{11}{2}^- \rightarrow \frac{7}{2}^-$	0.5 ps
		^{53}Mn	$\frac{15}{2}^- \rightarrow \frac{11}{2}^-$	2.7 ps
1327.95(61)	3156(194)	^{53}Fe	$\frac{9}{2}^- \rightarrow \frac{7}{2}^-$	17 ps
1373.19(11) → DP**:1328	6980(365)	^{53}Fe	$\frac{9}{2}^- \rightarrow \frac{7}{2}^-$	17 ps
1407.30(36)	3752(103)	^{54}Fe	$2^+ \rightarrow 0^+$	0.8 ps
1432.83(11)	892(89)	^{53}Fe	$\frac{13}{2}^- \rightarrow \frac{11}{2}^-$	
1459.74(51)	2659(117)	^{42}Ca	$6^+ \rightarrow 4^+$	85 fs
1486.83(28) → DP**:1441	2147(251)	^{53}Mn	$\frac{11}{2}^- \rightarrow \frac{7}{2}^-$	0.6 ps
1523.72(77)	1294(94)	^{42}Ca	$2^+ \rightarrow 0^+$	0.82 ps
1669.81(40) → DP**:1614	1466(218)	^{53}Fe	$\frac{9}{2}^- \rightarrow \frac{7}{2}^-$	17 ps
1720.00(50)	not fittable*	^{27}Al	$4^+ \rightarrow 2^+$	130 fs
1879.90(71) → DP**:1818	1938(706)	^{51}Mn,	$\frac{3}{2}^- \rightarrow \frac{5}{2}^-$	>0.7 ps
2036.81(47)	248(91)	^{53}Fe	$\frac{3}{2}^- \rightarrow \frac{7}{2}^-$	0.24 ps
2108.80(24) → DP**:2039	19(20)	^{53}Fe	$\frac{3}{2}^- \rightarrow \frac{7}{2}^-$	0.24 ps
2214.70(20)	9194(1823)	^{27}Al	$\frac{7}{2}^+ \rightarrow \frac{5}{2}^+$	26.6 fs

*due to the peak shape

**DP: with Doppler correction

Table 4.2.: *Energies, intensities, transitions and half-lives for the γ spectra at the CD chamber.*

energy (keV)	intensity	nucleus	transition $J_{ini} \rightarrow J_{fin}$	$T_{\frac{1}{2}}$
2339.48(26)	515(78)	^{53}Fe	$\frac{11}{2}^- \rightarrow \frac{7}{2}^-$	53 fs
2418.09(88) $\rightarrow$ DP**:2339	2120(699)	^{53}Fe	$\frac{11}{2}^- \rightarrow \frac{7}{2}^-$	53 fs
2527.80(14) $\rightarrow$ DP**:2445	1491(797)	^{53}Fe	$\frac{13}{2}^- \rightarrow \frac{9}{2}^-$	
2614.02(13)	911(81)	^{208}Pb	$3^- \rightarrow 0^+$	16.7 ps
2646.22(16)	809(86)	^{27}Al	$\frac{9}{2}^- \rightarrow \frac{7}{2}^+$	<14 fs

*due to the peak shape

**DP: with Doppler correction

4.5-2. DSSSD Spectra

Calibration and Dead-Layer Correction

The most important and interesting spectra are the energy spectra from the DSSSD, where the proton emission with an energy of 1280 keV should be visible. For a proton decay into the ground state of ^{53}Co also the energy of 2607 keV could be expected. The DSSSD spectra were calibrated with the triple-alpha source consisting of ^{239}Pu, ^{241}Am and ^{244}Cm before and after the beam time, see table 4.3.

In the next step it is important to consider the energy loss of the particles in the passive layers of the detector, shortly named 'dead-layer correction'. The dead-layer correction was developed in the diploma thesis of A. Wendt [101]. In figure 4.12 the composition of the DSSSD is sketched. Before a particle is detected in the active material, it crosses layers of SiN_4 or SiO_2, Al and p-type silicium.

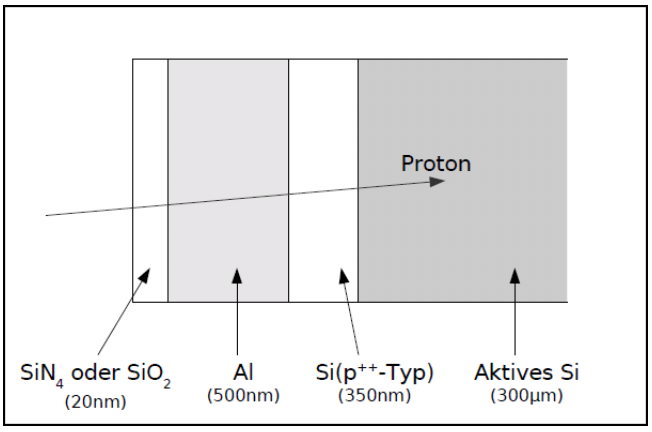

Figure 4.12.: *Dead layers of the DSSSD, before a charged particle is detected in the active silicium material, it looses a part of its energy in the passive layers of SiN_4 or SiO_2, Al and p-type Si, figure taken from [101].*

Not only the expected proton thereby loose part of its energy in the passive layers, but also the particles of the calibration source are decelerated. The dead-layer correction is processed in two steps: The first step is the calculation of the energy loss of the alpha

energy	$FWHM_{rel}$			
	Ring 0 (inner ring)		Ring 31 (outer ring)	
	before	after	before	after
5.155 MeV	1.60(2)%	1.44(1)%	1.70(2)%	1.80(1)%
5.486 MeV	1.42(2)%	1.30(1) %	1.64(2)%	1.7(1) %
5.805 MeV	1.32(2)%	1.26(1)%	1.55(3)%	1.46(1)%
$FWHM_{rel,RMS}$	1.45(2)%	1.33(1)%	1.63(2)%	1.65(1)%

Table 4.3.: *Relative FWHM, measured with a triple alpha-source, for the inner and outer ring segments of the DSSSD before and after beam time.*

particles in the passive layer; the second one considers the energy loss of the expected protons in the dead layer.

1. The energy loss of the alpha particles from the calibration source for every ring is estimated, after this a linear function in dependence of the measured energy E_{meas} is fitted:
$$E = a * E_{meas} + b \tag{4.1}$$
With this function every ring is recalibrated.

2. The expected protons loose their energy in the passive layer during beam time. Therefore it is important to calculate the kinematics of the ^{54}Ni particles, which is performed with Lise++ [65] as follows:
   - energy loss of ^{28}Si with an energy of 70 MeV to the center of the ^{28}Si target (total thickness $0.33\frac{\text{mg}}{\text{cm}^2}$), at a depth of $0.165\frac{\text{mg}}{\text{cm}^2}$ is 2.0147 MeV
   - resulting residual energy E_{rest} of ^{28}Si is 67.99 MeV
   - the compound nucleus energy at the target center: 33.995 MeV
   - energy loss of ^{54}Ni through $0.165\frac{\text{mg}}{\text{cm}^2}$ ^{28}Si: 4.648 MeV
     remaining energy of ^{54}Ni $E_{rest} = 29.346$ MeV
   - energy loss of ^{54}Ni in ^{181}Ta degrader (thickness $4.7\frac{\text{mg}}{\text{cm}^2}$): 26.766 MeV
     residual energy $E_{rest} = 2.5804$ MeV
   - ^{54}Ni intrudes into the ^{27}Al catcher: $0.468\frac{\text{mg}}{\text{cm}^2}$ which equates to $1.73 \pm 0.03 \mu$ m

   When protons are emitted from ^{54}Ni they have to move out of the ^{27}Al catcher and cross the dead layer of the DSSSD. The effective path length through the dead layer depends on the entrance angle into the DSSSD corresponding to the ring number.
   Now for every angle of the 32 different rings the energy loss for a proton with 7 different initial energies (0.5, 1, 2, 3, 4, 5 and 6 MeV) is calculated.

   The initial energy E_{ini} of the proton is fitted with following function in dependence of the measured energy E_{meas} for every ring:
$$E_{ini} = a * (E_{meas} + d) + b + \frac{c}{E_{meas} + d} \tag{4.2}$$

This dead-layer correction is not useful for the strip side of the DSSSD, because a strip segment is hit by the particles at diverse angles and so the energy loss varies accordingly. This is the motivation for using only the calibrated energy information of the ring side of the detector.

To demonstrate the operational reliability of the dead-layer correction three alpha spectra of the same ring are shown in figure 4.13:

1. The upper figure is the uncorrected spectrum of an alpha calibration; the three energies of the source are expected to be at 5.155 MeV, 5.486 MeV and 5.805 MeV.

2. The figure in the middle includes the energy loss of the alpha particles in the dead layer. The measured energy is decreased and the spectrum is shifted to lower energies.

3. In the lowest figure the correction for the energy loss of the protons during the beam time is considered. The initial energy of the protons will be reduced by crossing the dead layer of the DSSSD. To determine the energy before the energy loss the measured energy has to be shifted to higher energies.

For the expected proton of about 1 MeV also the deviation of the dead-layer correction is estimated. The dead-layer correction can vary between 20 and 40 keV depending on where the compound nucleus was produced in the target and on which ring was hit.

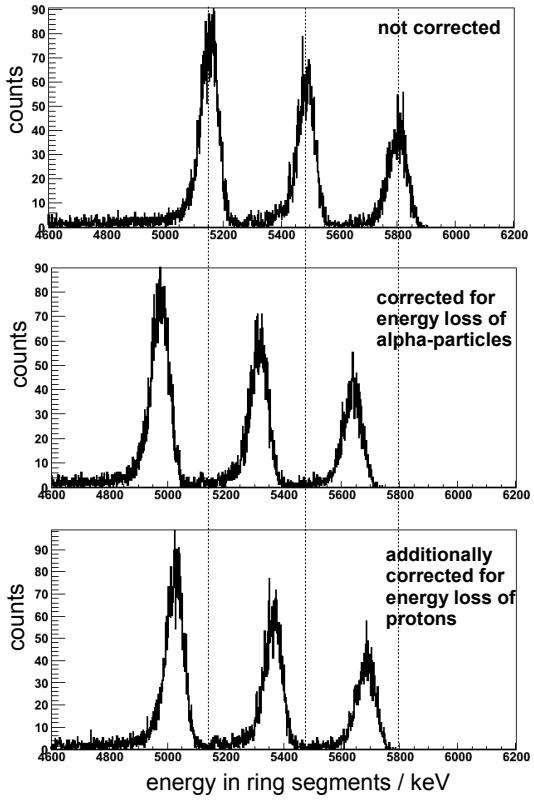

Figure 4.13.: *Spectrum of DSSSD ring segment, at the top: calibrated spectrum of triple alpha source, in the middle: correction for the energy loss of the alpha-calibration particles in the dead layer, at the bottom: additionally considering the energy loss of the protons during beam time.*

Analysis of Beam-Time DSSSD Spectra

After calibration and dead-layer correction in the next steps the events in the DSSSD are analyzed, which were detected during the beam time.
A reasonable physical event - in contrast to electronic noise for example - is supposed to be detected once on the ring side as well as once on the strip side of the DSSSD. For this reason the multiplicity of the signals on the strip side and the ring side of the DSSSD is defined as $\vec{M}$(strip signals, ring signals)^T. As a condition for a useful event $\vec{M} = (1,1)^T$ is claimed.
As explained in section 4.5-2 only the exact energy information of the events in the ring side of the DSSSD is of interest and will be used in the next analysis steps. In figure 4.14 the energies detected in the strip segments on the y-axis versus the calibrated energies of the ring segments are shown, which are corrected for the passive layers with the condition $\vec{M} = (1,1)^T$ imposed. On the diagonal line the correlation between physically reasonable events on the ring and strip side are obvious. These are the events which deposited nearly the same amount of energy in the front and the back side of the detector.
For the further analysis those events are investigated which derive from the field in figure 4.14 bordered by the two brown, diagonal lines.

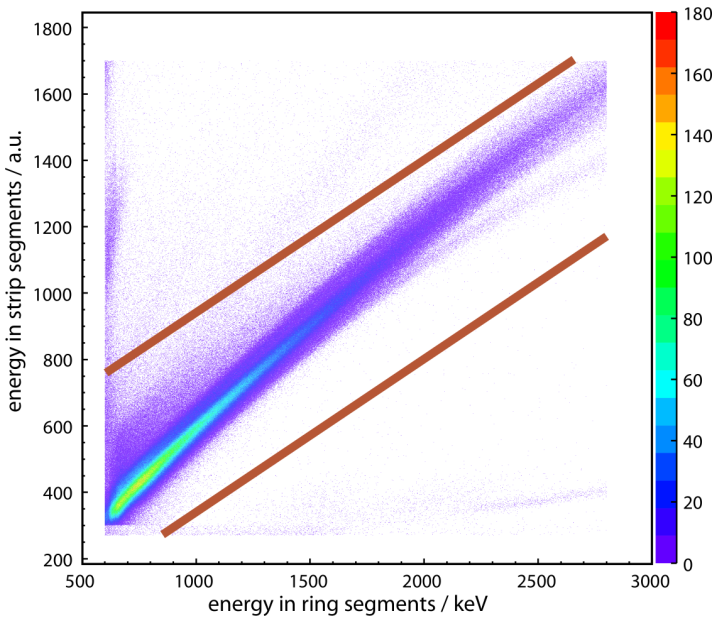

Figure 4.14.: *Correlation between the energy signals of the strip segments (y-axis) and the ring segments (x-axis). The signals of the ring side are corrected for the energy loss in the dead layer. Additionally the condition $\vec{M} = (1,1)^T$ is imposed. The brown, diagonal lines mark a region of interest where the required energetic relation between ring and strip segments are evident.*

Figure 4.15 shows the projection of the spectrum 4.14 for the marked region between the brown lines. This spectrum contains all events from the ring side of the DSSSD after

calibration and dead-layer correction, with the condition $\vec{M} = (1, 1)^T$ and additionally a reasonable, energetic relation between the front and the back side of the DSSSD is claimed. Due to the huge amount of background it is necessary to find additional, proper analysis conditions.

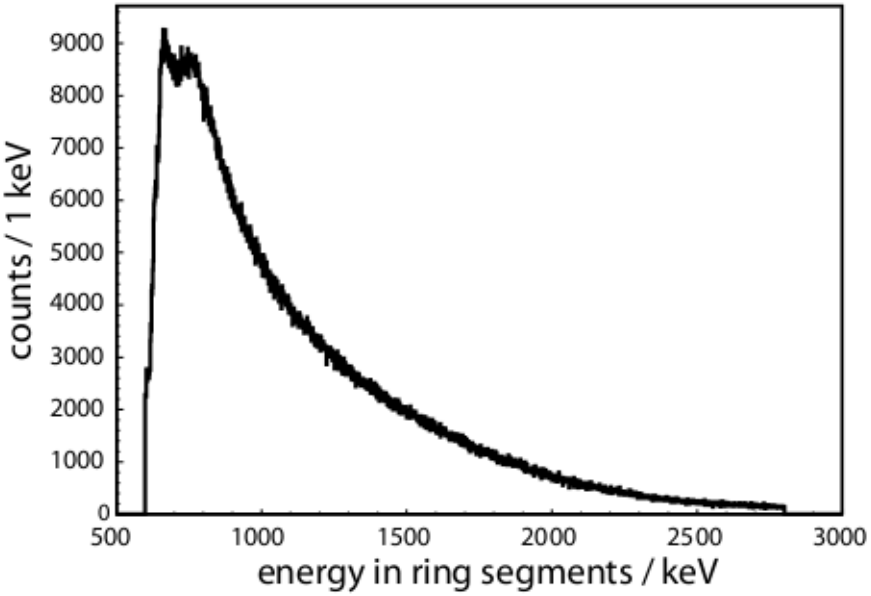

Figure 4.15.: *Resulting energy spectrum for rings with the conditions from figure 4.14.*

4.5-3. Investigation of the Time Conditions

The investigation of an isomeric event, like the 10^+ state of ^{54}Ni benefits from time correlations in the data.
The experiment was performed with a pulsed beam with a pulse width of 5 ns and a periodicity of 800 ns. During the beam gaps, prompt events should not be detectable. Isomeric events are supposed to be measured distinctly. In order to analyze the isomeric events the time information between the beam pulse and the measured events in the detectors is needed. A useful time information is given by the time difference between the trigger signals (see section 4.4-2) and the delayed beam pulse. The time signal of the beam pulse is used as delayed stop signal, because a trigger signal starts the data acquisition and cannot be applied as stop signal. Figure 4.16 shows on the y-axis the time difference between the trigger signals and the beam pulse. On the x-axis the energy signal of the DSSSD ring segments is plotted. For the energy signal all former conditions, mentioned in section 4.5-2, are considered. Additionally, the detection of at least one neutron is required to be more sensitive to the two-neutron-evaporation channel, which leads to ^{54}Ni. In this spectrum two accumulations of events are visible.

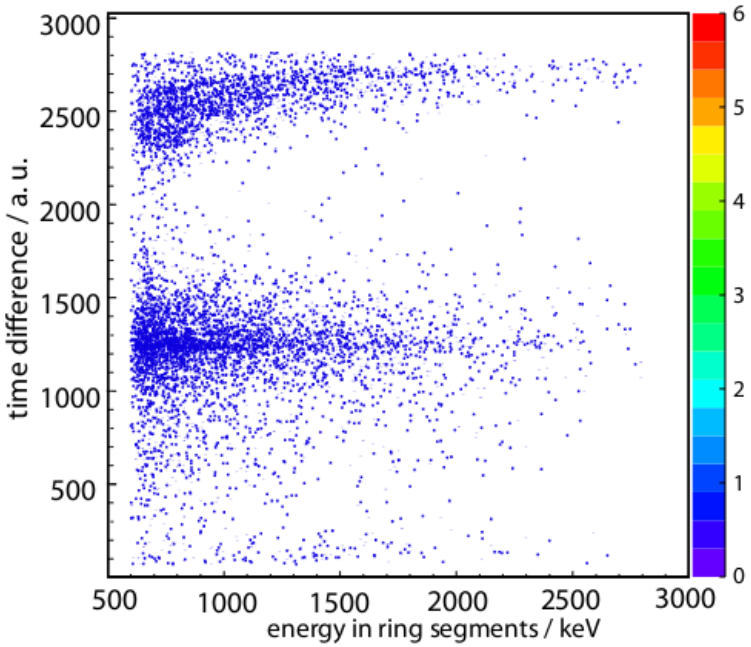

Figure 4.16.: *The time difference between triggers and beam pulse versus the energy in DSSSD-ring segments is shown; additionally, the detection of at least one neutron is required.*

In order to understand this structure, the time spectrum has to be investigated in detail. Three different triggers are applied, see section 4.4-2. These are a single trigger from the DSSSD-time signal (trigger 1), a coincidence trigger from the neutron-time signals and the γ-time signals at the target chamber (trigger 2) and a coincidence trigger generated by the neutron-time signals and the γ-time signals at the CD chamber (trigger 3).
Trigger 1 provides the time information of the particles, especially of the expected

protons, in the DSSSD . The time between the trigger-1 signal and the delayed beam pulse signal is shown in figure 4.17. This spectrum is most important. It describes the time difference between the beam, measured just before the reaction with the target, and the detection of an event in the DSSSD. It is characterized by a broad distribution at channel 2300-2800, which indicates the prompt events in the DSSSD.

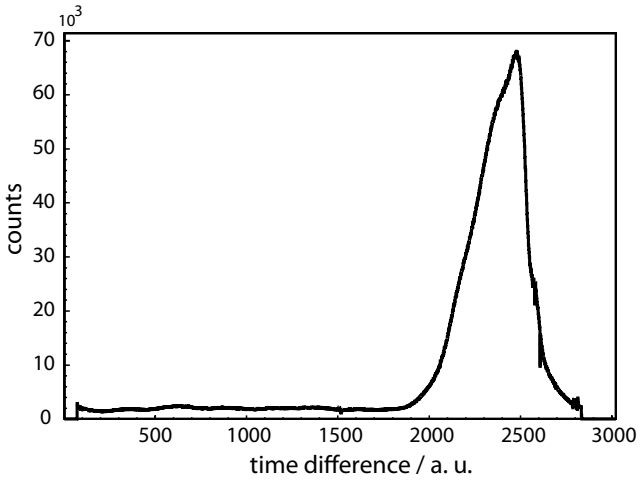

Figure 4.17.: *Time difference between trigger 1 (time signal from the DSSSD) and delayed beam pulse. The broad distribution at channel 2000-2800 are produced by prompt events.*

The time spectra in figures 4.18 and 4.19 are started by the neutron-γ coincidence trigger and stopped by the delayed beam-pulse signal. The spectrum in figure 4.18, which is generated with trigger 2, shows two peaks. The double-peak structure arises from the cases that either the neutron started the trigger or the γ event. The time signals of the four HPGe detectors signals around the target chamber had the same delays. This is the reason why only one double peak is observed. In the time spectrum started by trigger 3, see figure 4.19, two of those double peaks are visible. The two HPGe-detector signals at the CD chamber did not have the same delays. Hence, the effect, that the trigger is started by the neutron or the γ signal, occurs twice.

Trigger 2 and 3 were used for the analysis of the γ spectra. For the further analysis of the DSSSD spectra only the time information of the beam pulse in combination with trigger 1 is needed (figure 4.17).

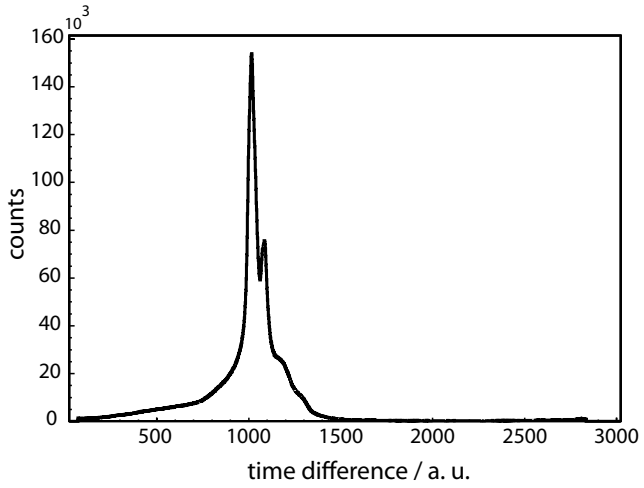

Figure 4.18.: *Time difference between trigger 2 (γ event at the target chamber in coincidence with a neutron) and beam pulse. The two peaks are caused by the effect that either the γ ray or the neutron started the trigger.*

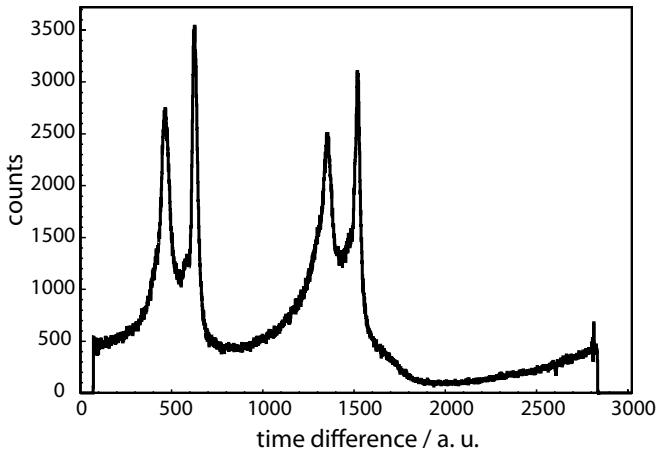

Figure 4.19.: *Time difference between trigger 3 (γ event at the CD chamber in coincidence with a neutron) and beam pulse. The double-peak structure is caused by the effect that either the γ ray or the neutron started the trigger. Due to the different delays of the two HPGe detector signals, this effect occurs twice.*

The spectrum in figure 4.16 is reproduced requiring that trigger 1 started the data acquisition, see figure 4.20 (a). The time spectrum is calibrated, considering that the

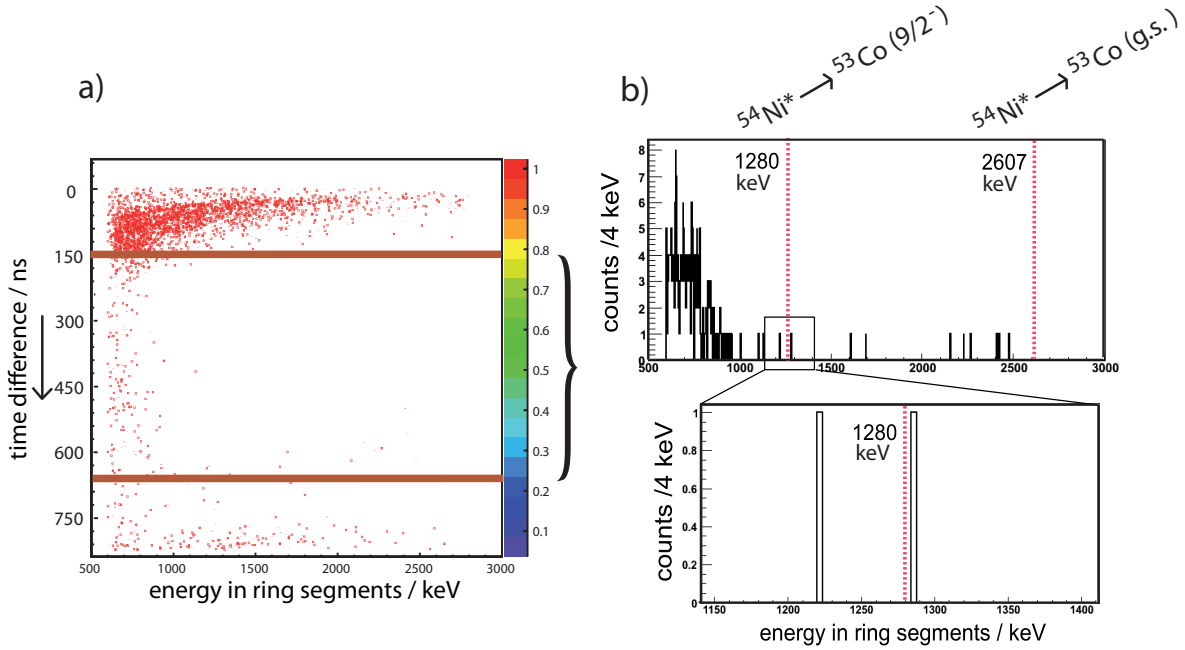

Figure 4.20.: *(a) Time difference between trigger 1 and beam pulse versus the energy in DSSSD-ring segments; additionally, the detection of at least one neutron is required. (b) Projection of figure (a) onto the x axis for the time interval Δt =150 ns - 660 ns. No significant events either at the energy of 1280 keV for a proton emission into the first excited state of ^{53}Co - or at the energy of 2607 keV - for a proton emission into the ground state of ^{53}Co - are detected (see figure 1.2).*

prompt signals are detected at $\Delta t = 0$ ns and the TDC range of 4096 channels equates to 1.2μs. The DSSSD is shielded against the primary beam. Nevertheless a large number of prompt events is measured. A possible explanation for this background are scattered particles. At about 150 ns after the beam pulse, after one half-life of the 10^+ state of ^{54}Ni, still around half of the ^{54}Ni nuclei are supposed to be detectable. The short-living background of the beam pulse has disappeared.
Figure 4.20 (b) shows the projection of the time spectrum onto the x-axis for the time interval between 150 ns and 660 ns. The background in the DSSSD spectrum is reduced very well by 4 orders of magnitude in comparison with the initial DSSSD spectrum in figure 4.15. No significant events either at the energy of 1280 keV - which would verify the proton emission into the first excited state of ^{53}Co - or at the energy of 2607 keV - which would be a hint for the proton emission into the ground state of ^{53}Co - are detected. The isomeric 10^+ state in ^{54}Ni is not or too weakly populated in this fusion-evaporation reaction. The predicted cross section for the population of ^{54}Ni, see section 4.1, has to be downscaled, which is done in the next section.

4.5-4. Estimation of the Upper Limit of the Cross Section for the Production of the isomeric 10^+ State in ^{54}Ni

Based upon the results of section 4.5-3 the upper cross section for the proton emission out of the isomeric 10^+ state of ^{54}Ni is determined:
With respect to the background events the number of the collected protons C_p in the energy spectrum of the DSSSD in figure 4.20(b) is ($C_p \leq 3 \pm 1$). This spectrum is a projection from figure 4.20 (a) and is taken between 150 ns and 660 ns after the fusion-evaporation reaction. The life time of the 10^+ state in ^{54}Ni is $\tau = 218(4)$ ns. Hence, in this chosen time interval 45% of the events are supposed to decay and in the entire time spectrum for the number of emitted protons $C_p \leq (6.7 \pm 2.2)$ is expected. The cross section for the proton emission out of the 10^+ state in ^{54}Ni, $\sigma(^{54}\mathrm{Ni}(10^+)\mathrm{p})$, is calculated as follows:

$$\sigma(^{54}\mathrm{Ni}(10^+)\mathrm{p}) \leq \frac{C_p}{I \cdot N \cdot \epsilon_N \cdot \epsilon_{DSSSD} \cdot \Omega \cdot t} \tag{4.3}$$

with

- counts of the measured protons in the DSSSD: $C_p \leq (6.7 \pm 2.2)$
- beam intensity: $I = (20 \pm 1)nA = (2.2 \pm 0.1)pnA = (1.39 \pm 0.07) \cdot 10^{10} \frac{1}{s}$
- surface density of the target:

$$N = \frac{\mathrm{d(cm)} * \rho(\frac{\mathrm{mg}}{\mathrm{cm}^3}) \cdot A_Z}{M} \tag{4.4}$$

$$= \frac{(0.33 \pm 0.01)^{-3}(\frac{\mathrm{g}}{\mathrm{cm}^2}) \cdot 6.022 \cdot 10^{23} \frac{1}{\mathrm{mol}}}{28.09 \frac{\mathrm{g}}{\mathrm{mol}}} = (7.1 \pm 0.2) \cdot 10^{18} \frac{1}{\mathrm{cm}^2} \tag{4.5}$$

- efficiency of neutron detectors: $\epsilon_N = (9.75 \pm 1)\%$ see [101]
- efficiency of DSSSD: $\epsilon_{DSSSD} = 93\%$
- solid angle of the DSSSD with respect to the catcher foil: $\Omega = 17\%$ see [101]
- beam time: $t = (243.5 \pm 4)\mathrm{h} = (8.766 \pm 0.144) \cdot 10^5 \mathrm{s}$

The upper limit of the cross section for the proton emission from the isomeric 10^+ state is:

$$\boxed{\rightarrow \sigma(^{54}\mathrm{Ni}(10^+)\mathrm{p}) \leq (5.0 \pm 2.8)\mathrm{nbarn}} \tag{4.6}$$

With the proton-γ branching ratio of $\frac{I_p}{I_\gamma} = 36(2)\%$ [84] the upper limit of the cross section for the population of the 10^+ state of ^{54}Ni is:

$$\boxed{\sigma(^{54}\text{Ni}(10^+)) \leq (13.9 \pm 7.8)\text{nbarn}} \tag{4.7}$$

The errors are calculated with Gaussian error propagation.
In comparison to the results of the diploma thesis of A. Wendt [101] the cross sections $(^{54}Ni(10^+)\text{p})$ and $\sigma(^{54}Ni(10^+))$ could be downscaled by a factor of seven, see table 4.4.

	diploma thesis A.Wendt [101]	final experiment April 2009
$\sigma(^{54}Ni(10^+)p) \leq$	$(36.6 \pm 13.4)nbarn$	$(5.0 \pm 2.8)nbarn$
$\sigma(^{54}Ni(10^+)) \leq$	$(101.7 \pm 37.2)nbarn$	$(13.9 \pm 7.8)nbarn$

Table 4.4.: *Upper limits of the cross sections $\sigma(^{54}Ni(10^+)p)$ and $\sigma(^{54}Ni(10^+))$ compared for the different experiments*

As it is shown in section 4.1 the cross section for the population of the ground state of ^{54}Ni, calculated with the program Cascade, is about $10 - 12\mu$barn and by this about 3 orders of magnitude higher than the determined cross section $\sigma(^{54}\text{Ni}(10^+))$ of the isomeric 10^+ state.
The program Pace, which is part of of Lise++ [65], predicts for the population of ^{54}Ni a higher cross section of $\sigma = 155\mu$barn. So the difference between the experimentally determined cross section for the population of the isomeric 10^+ state and the theoretically predicted cross section for the population of the ground state of ^{54}Ni is about four orders of magnitude.

5. Conclusion and Outlook

The efforts and results of the series of experiments between 2006 and 2009 with the aim to observe the proton emission of the isomeric 10^+ state in ^{54}Ni, underscore the difficulties to provide evidence for a physical event with a predicted cross section of a few microbarn.

In order to maximise the sensitivity of the setup particular attention was paid to a clean electrical grounding of the experimental setup. While the first experiments still had to struggle with a high beam-correlated background in the DSSSD spectra, the enhancement of the experimental setup and of the analysis conditions enabled it to obtain background-free DSSSD spectra in the last experiment. The most important improvements were the choice of a pulsed beam, light material (aluminium) for the catcher foil and the development of the 'dead-layer correction'.
Two experiments were performed to determine the best reaction partners and the optimal beam energy.

The final experiment used the (^{28}Si+^{28}Si) reaction at 70 MeV. The γ spectra confirm the population of the expected reaction channels and demonstrate the operational reliability of the neutron-γ discrimination. To distinguish physical events from electronic noise in the DSSSD, correlations between the signals of the front and the back side of the detector are required for further use.
The additional condition of the detection of at least one neutron in the NORDBALL detectors makes the DSSSD spectra sensitive to the two-neutron-evaporation channel ^{54}Ni. The time correlation between beam pulse and DSSSD events is necessary to select the isomeric events in the DSSSD spectra. Especially after a time of 150 ns the short-living nuclei do not contribute to the DSSSD spectrum, while the isomeric events like an proton from the 10^+ state of ^{54}Ni with a half-life of $T_{1/2} = 152(4)$ ns are supposed to be visible. The resulting DSSSD spectrum in figure 4.20 (c) is very clean, but does not provide evidence for the detection of the emitted protons of ^{54}Ni at an energy of 1280 keV for the proton emission into the first excited state of ^{53}Co or at an energy of 2607 keV for the proton emission into the ground state of ^{53}Co. The isomeric 10^+ state in ^{54}Ni is not or too weakly populated in this kind of fusion-evaporation reactions.
The upper limit of the cross section for the proton emission of the 10^+ state is determined as $\sigma(^{54}Ni(10^+)p) \leq (5.0 \pm 2.8)$ nbarn. With the branching ratio of $\frac{I_p}{I_\gamma} = 36(2)\%$ the upper cross section limit for the population of the 10^+ state in ^{54}Ni is calculated as $\sigma(^{54}Ni(10^+)) \leq (13.9 \pm 7.8)$ nbarn.
In comparison to the former experiment of A. Wendt [101] both cross sections could be downscaled by a factor of seven.

One possibility to increase the efficiency is a higher detector efficiency, for example with a 4π-neutron-detector array or a silicon-detector array. The other option is to increase the production rate with a higher beam intensity like it is supported in large research facilities. But in comparison to the life time of the 10^+ state in ^{54}Ni with $\tau = 218(4)$ ns the lengths of the flight paths in most of the facilities are too long. The most promising option to increase the population of ^{54}Ni and to investigate the isomeric 10^+ state in ^{54}Ni is, to perform this kind of experiment with a fragment separator, like the FRS at GSI, as it had already been done in the former experiment of Rudolph et al. [84].

Part II.

Multi-Nucleon Transfer Reactions in the Actinide Region

6. Introduction

Studies in the actinide region ($89 \leq Z \leq 103$) are extremely challenging due to a lack of targets and a significant background from fission, which is dominating all nuclear reactions with excitation energies above the fission barrier. Neutron-deficient nuclei are producible by fusion-evaporation reactions and information even close to the proton dripline can be gathered. However neutron-rich heavy nuclei were, for a very long time, only accessible by decay studies. The investigations of these hard-to-reach nuclei have become practicable only with the development of new highly-selective experimental techniques and sophisticated experimental setups [11]. Gäggeler et al.[36] managed to populate light actinides with the ^{48}Ca+^{248}Cm deep-inelastic transfer reaction in 1986 [19] and this technique was favoured to study neutron-rich nuclei for low lying states as well as for high-spin states, [93, 107]. Therefore since the early 1990s the focus of heavy-ion transfer reactions also moved towards to neutron-rich nuclei. Investigating the influence of isospin effects on the nuclear potential and on the effective interactions promised insights into shell effects and magic numbers [11]. While at that time those experiments were performed with gamma-detector arrays in combination with one particle detector like a parallel-plates avalanche counter (PPAC), the development and improvement of large-acceptance spectrometers like PRISMA at LNL (Laboratori Nazionali di Legnaro, Italy) or VAMOS (VAriable MOde Spectrometer) at GANIL (Grand Accélérateur National d'Ions Lourds, France) combined with the construction of highly-efficient gamma-detection arrays made this kind of research much more versatile especially for nuclear structure investigations [22].
In the second part of this thesis two multi-nucleon transfer (MNT) experiments, that took place at the LNL in Legnaro in 2007 and 2008, are analyzed and compared for the target-like fragments. In both experiments ^{238}U was used as target, in the first measurement a ^{70}Zn beam with 460 MeV and in the second experiment a ^{136}Xe beam of 926 MeV was delivered. Primarily, both experiments were designed for the investigations of the beam-like fragments and the analyses for the beam-like particles were already performed by Jose Javier Valiente Dobon [98] and Francesco Recchia [83]. Usually MNT experiments are used to populate the neutron-rich, beam-like fragments because of the tendency to create N/Z equilibrium (see 7.2). However, the results of this extended analysis for the target-like nuclei demonstrate that this reaction type is also suitable to obtain information on target-like fragments in the region of neutron-rich actinides. In particular, the analysis of the data for neutron-rich uranium and thorium isotopes provides interesting, new results.

7. Multi-Nucleon Transfer Reactions

A transfer reaction is a direct process, in which one or more nucleons are exchanged between two nuclei [69]. If more than one nucleon is transferred, the process is called 'multi-nucleon transfer' (MNT). In contrast to indirect reactions, direct reactions are characterized by very small transition time scales ($t_{trans} \leq 10^{-22}s$) with a minimum of rearrangement processes within the nuclei. Typical features of transfer reactions are asymmetric angular distributions and increasing intensities in forward directions showing a diffraction pattern.

If a nucleon is transferred from the projectile to the target, a 'stripping' reaction has taken place. A 'pickup' reaction has occurred, if a nucleon is received by the projectile from the target. There is a crucial difference between transfer reactions with light and heavy ions. Whereas light ions with rather simple reaction mechanisms are well-suited to study particle-particle interactions in the nuclear matter, reactions with heavy ions show more complexity. These reactions are subject of ongoing investigations in order to understand reaction mechanisms, especially the transition between the quasi-elastic and deep-inelastic regimes and fusion [22].

7.1. Classification of Reactions with Heavy Ions

To distinguish between the different reaction types with heavy ions, the following classification is typically used.

Within the optical model the total reaction cross section for the reaction can be defined as [69]:

$$\sigma_r = \pi \left(\frac{\lambda}{2\pi}\right)^2 \sum_l (2l+1) \cdot T_l \tag{7.1}$$

with
λ: wave length of the incident particle
l: angular momentum
T: transmission coefficient (the probability for absorption of the partial waves).
As a first-order approximation T is equal to 1 for all reactions except for those at the surfaces of the nuclei:

$$T = \begin{cases} 1 & for \quad l \leq l_s \\ 0 & for \quad l > l_s \end{cases}$$

with the angular momentum at the surface l_s.

The angular momentum allows a classification of heavy ion reactions :

- Complete Fusion (CF): For small angular momenta, i.e. more or less central collisions, accretion of the reaction partners occurs and the identity of the original nuclei disappears. This system can generate an evaporation residue (ER) or in the case of higher angular momentum can be fissioned symmetrically (SF). This angular momentum is restricted to values smaller than the critical angular momentum l_{cr}, where the fission barrier is strongly suppressed.
- Deep Inelastic Collision (DIC): For $l_{cr} < l < l_g$ (with l_g the grazing angular momentum) the centrifugal forces are dominant and no long-lived reaction product is possible. The nuclei interpenetrate their surface zones. The kinetic energy is transformed into inner excitation energy. Because of the overlap parts of the masses can be transferred.
- Quasi Elastic Collision (QEC): For angular momenta higher than the grazing angular momentum ($l > l_g$) the kinetic energy of the reaction partners remains nearly the same. Transfer of one or more nucleons as well as Coulomb excitation occurs.

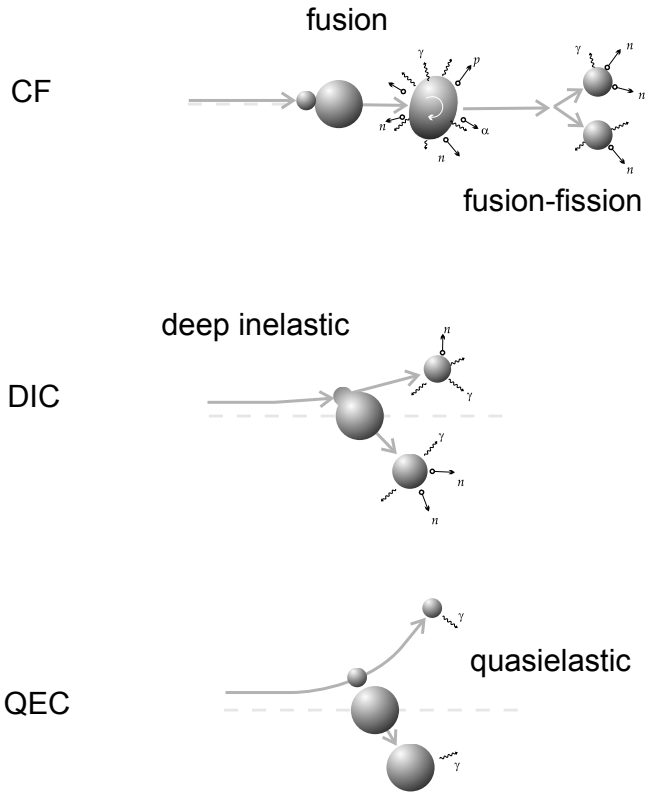

Figure 7.1.: *Reaction mechanisms with heavy ions at energies above the Coulomb barrier: complete fusion (CF), deep inelastic collision (DIC) and quasi elastic collision (QEC) (figures modified from reference [11]).*

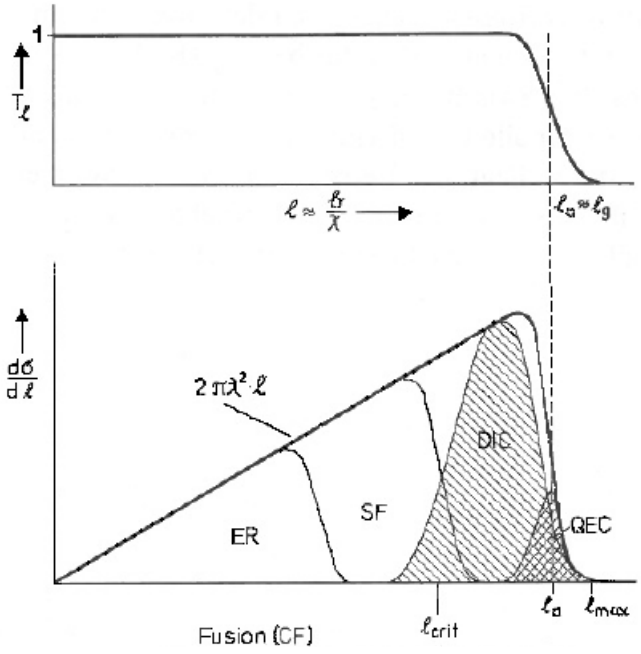

Figure 7.2.: *Dependence of the transmission coefficient and differential cross section on the angular momentum. The heavy-ion reactions can be classified according to the angular momentum, ER = evaporation residue, SF = symmetric fission, DIC = deep inelastic collision, QEC = quasi elastic collision (figure from reference [69]).*

7.2. N/Z Equilibration

To populate neutron-rich nuclei, it is important to understand the mechanism of transfer concerning the N/Z ratio [11]. In the work of Freiesleben and Kratz [30] the results of the research on this topic are summarized extensively. In transfer reactions an equilibration between the two N/Z ratios of the projectile and target is always preferred. That means lighter reaction partners, which have a small N/Z ratio, tend to pick up some neutrons while heavier nuclei, with a higher N/Z ratio, show the tendency to pick up protons. Using an U target with a light projectile (like Zn or Xe) - as it was done in the two analyzed experiments - the population of neutron-rich Cu and Ni isotopes is expected for the Zn beam and neutron-rich I, Te and Sb isotopes for the Xe beam. Consequently, for the target-like reaction products significant cross sections for Np and Pu isotopes are anticipated. The results of the analysis of the experiments will be shown in chapter 11. Swiatecki et al. [92] describe the equilibration process as minimization of the liquid drop energy of two touching spherical nuclei. Further investigations of Krolas et al. [61] explained the process with the assumption of two distant, non-touching nuclei. The reaction is supposed to be affected by strong dynamical deformation at the scission point.
The process of charge equilibration is quite complex. Several studies were performed to understand the mechanism in order to find the proper conditions for new experiments populating very neutron-rich isotopes [11]. Iwata et al. [53] point out the influence of the

velocity of the reaction partners at the collision. To suppress the charge equilibration the velocity of the two nuclei must be above the velocity corresponding to the proton or neutron Fermi momenta, so that there is less time for rearrangement processes during the collision. This can be achieved by increasing the beam energy. Also the importance of a small mass asymmetry between the two nuclei A_1/A_2 for the suppression of the N/Z equilibration is described.

8. Collective Properties of Actinide Nuclei

The actinides are the elements with $89 \leq Z \leq 103$, which follow the element actinium in the periodic table. They are unstable, though the lifetimes of the isotopes ^{232}Th, ^{235}U, ^{238}U and ^{244}Pu are long enough to show natural abundance of these nuclei in nature. Other isotopes which occur naturally are the Pa isotopes. They are members of the decay chain of ^{235}U and ^{238}U.
Neutron-rich actinide nuclei are located far away from shell closures and are therefore characterized by effects of strong collectivity. Most notably vibration effects, like octupole vibrations and the interplay of vibration and rotation are the focus of interest like in the lanthanide region.

8.1. Theoretical Descriptions and Predictions for the Actinide Region

Based on the liquid-drop model Bohr and Mottelson [9, 10] found an expression for the radius of a vibrating nucleus in dependence of the angles θ and ϕ:

$$R(\Theta, \phi) = R_0[1 + \sum_{\lambda>=1} \sum_{\mu=-\lambda}^{+\lambda} a_{\lambda\mu} Y_{\lambda\mu}(\Theta, \phi)] \tag{8.1}$$

with the standard deformation parameter $a_{\lambda\mu}$ and with $Y_{\lambda\mu}(\Theta, \phi)$ as normalized spherical harmonics. The order of the excitation is given by the parameter λ, with $\lambda = 1$ for the translation of the centre of mass, $\lambda = 2$ for the quadrupole excitation and $\lambda = 3$ for the octupole excitation. μ describes the different vibration modes. For shapes of axial symmetry all deformation parameters with $\mu \neq 0$ disappear. The remaining deformation parameters $a_{\lambda 0}$ are defined as $\beta_\lambda \equiv a_{\lambda 0}$. A typical level scheme of an octupole-vibrating nucleus features a low-lying band of negative parity, which characterizes the asymmetric shape under reflection, next to the rotational band of the ground state. This is also known from rotational spectra of reflection-asymmetric molecules like HCl. The stronger the octupole coupling forces are the more collective the vibration is. This causes a low lying excitation energy of the first negative-parity band. When the states of the ground-state rotational band and the octupole band alternate, the system has a permanent intrinsic octupole deformation.
In search of appropriate indicators for octupole vibration/deformation Ahmad et al.

found strong E1 transitions as experimental evidence [2]. But E1 transitions are also sensitive to single-particle states. Therefore a clear distinction of the source of the E1 strength is difficult. A better indicator for octupole collectivity is the E3 moment and respectively the E3 transition strength. In the region $N \approx 88$ and $N \approx 134$ an E3 transition strength of 30 to 50 Weisskopf units is supposed to be the result from octupole collectivity [59].
A wealth of theoretical predictions regarding the different shapes of nuclei in the actinide region are available:

Microscopic-Macroscopic Approach

With microscopic-macroscopic calculations Sobiczweski et al. [88] make detailed predictions about the region of heavy and superheavy nuclei for $88 \leq Z \leq 112$ and $134 \leq N \leq 170$. The probability for α decay, the deformation energy and the excitation energy of the 2^+ states are also calculated for $^{226\text{-}236}$Th and $^{226\text{-}238}$U isotopes. The maximum of deformation energy and the minima of excitation energy of the first 2^+ states within the respective isotopic chain are predicted for ^{236}Th and ^{238}U. Also moments of inertia, assuming the nuclei as ideal rotors, are calculated in the cranking approximation.

Cluster Model

Shneidman et al. [85, 86, 87] interpret the low-lying alternative parity bands in the actinide region in the cluster model. They assume that reflection-asymmetric shape is a consequence of cluster effects in the nuclei. The reflection-asymmetric shapes are produced by the collective motion of nucleons between the two clusters or as the motion in the mass asymmetry coordinate. The mass asymmetry coordinate is given by $\eta = \frac{A_1 - A_2}{A_1 + A_2}$ with A_1 and A_2 as the mass number of the heavy and the light nucleus of the dinuclear system consisting of two touching nuclei or clusters. Due to Shneidman et al. only the α cluster contributes significantly to low-energy states. For the α-clustering configuration is $|\eta^\alpha| = \frac{A-2A_1}{A} = 1 - \frac{8}{A}$ (with $A_1 + A_2 = A$ and $A_1 = 4$).
Predictions for the low-lying alternating parity bands in the heaviest nuclei are made for the first time within this cluster model. The parity splitting and electric dipole, quadrupole and octupole transition moments are calculated. Especially for the lightest N=148 isotones including ^{240}U detailed results for the ground-state rotational band and the vibrational band of negative parity are listed.
A first comparison of the predictions in [86] with experimental results on ^{240}U is given in chapter 12.

Mean-field and beyond Mean-Field

Delaroche et al. [25] make extended predictions with mean-field and beyond mean-field methods for about 55 even-even actinides from Th to No. As part of the analysis the structural properties of $^{226\text{–}236}$Th and $^{228\text{–}242}$U of normal and isomeric potential

deformations are investigated and tensors of inertia and potential energy landscapes were calculated with Hartree–Fock–Bogolyubov (HFB) mean field methods. Figures 8.1(a) and 8.1(b) show the kinetic moments of inertia for even $^{226–236}$Th and $^{228–242}$U isotopes as a function of the rotational frequency ω for normal elongations. The results of the cranking HFB calculations in black dots are compared with collective model calculations, which are based on adiabatic approximation, marked with red circles. In both isotopic chains an increase of the moments of inertia with increasing rotational frequency are theoretically predicted. These upbending and even backbending effects are due to the gradual decoupling of nucleon pairs by coriolis forces and are for the $^{226–236}$Th and $^{228–242}$U isotopes expected at rotational frequencies between 0.15 MeV and 0.3 MeV.

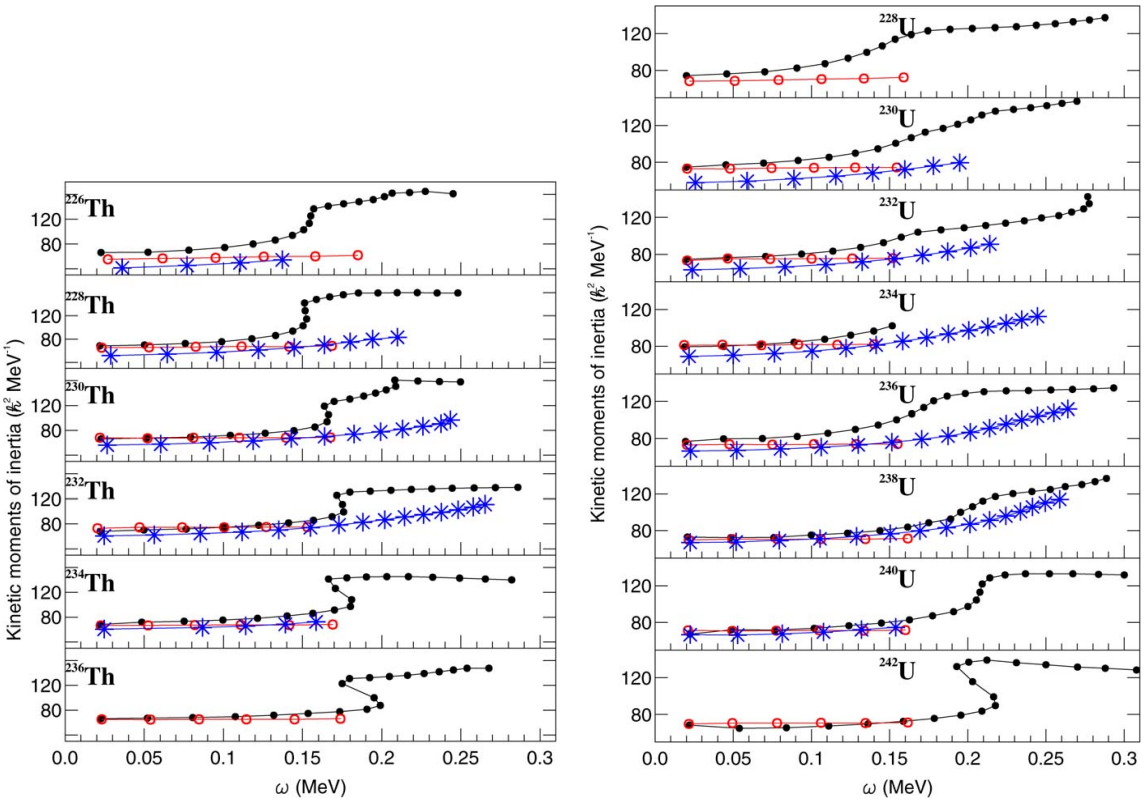

(a) for even-even $^{226–236}$Th-isotopes (b) for even-even $^{228–242}$U-isotopes

Figure 8.1.: *Theoretical predictions for some even-even Th isotopes (a) and U isotopes (b) from Delaroche et al. [25]. Kinetic moments of inertia in dependence of the rotational frequency are shown: cranking HFB calculations in black curves are compared with calculations within a collective model in red circles and experimental data (obtained from [29, 50, 51]) in blue stars.*

The comparison with experimental results [29, 50, 51], plotted as blue stars, is performed up to the limit where experimental data have been available. The results of the two experiments, analyzed in section 11, will extend this limit and the kinetic moments of inertia will be compared in section 12 with the new experimental insights in ^{240}U .

Relativistic Mean-Field

With relativistic mean-field methods Vretenar et al. [99] make predictions for the isotopic chains of Th, U, Pu, Cm, Cf, Fm, and No. The binding energies, ground-state quadrupole and hexadecapole moments are calculated with a nuclear energy density functional in relativistic Hartree-Bogoliubov (RHB) calculations.

Jian-You Guo et al. [43] describe shape evolution from spherical to octupole deformed shapes with the reflection asymmetric relativistic mean-field theory in even-even Th isotopes. The details of the method can be obtained from Geng et al. [39]. Deformations, matter-density distributions and potential-energy surfaces are calculated. It is predicted that Th isotopes undergo two types of shape transition:
In figure 8.2 the potential energy landscape for the even-even Th isotopes $^{218\text{-}246}$Th is plotted versus the quadrupole deformation parameter β_2 and the octupole deformation parameter β_3. The isotopes evolve from spherical shape in ^{218}Th to octupole deformed shape in ^{230}Th and finally to quadrupole deformed shape in ^{246}Th.

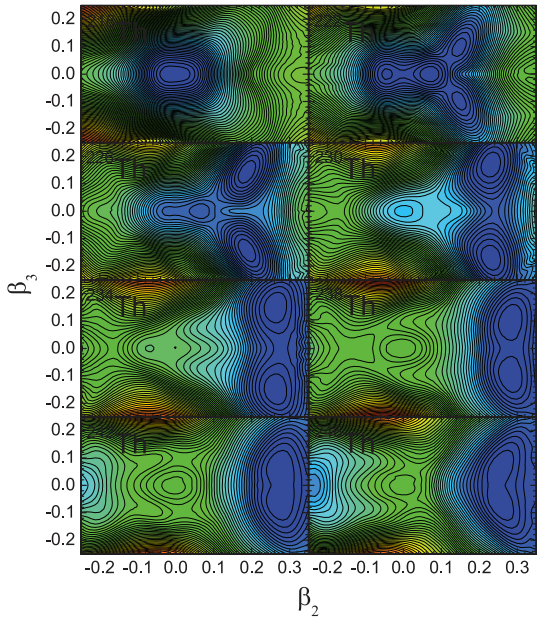

Figure 8.2.: *The potential energy surface of even-even Th isotopes from $^{218\text{-}246}$Th versus the quadrupole deformation parameter β_2 and the octupole deformation parameter β_3. Shape transitions from spherical shape in ^{218}Th to octupole shape in ^{230}Th and finally to quadrupole shape in ^{246}Th are predicted by [43].*

8.2. Actual Status of Experimental Results in U and Th nuclei

Cocks et al. [20] investigated the high-spin structure of Rn, Ra and Th isotopes via multi-nucleon-transfer reactions of ^{136}Xe+^{232}Th at 833 MeV successfully. The aim was to verify the interleaving bands with opposite parity which was demonstrated up to high spins ($I \approx 28$) with high quality Gammasphere spectra for ^{218,220,222}Rn, ^{222,224,226,228}Ra and ^{228,230,234}Th isotopes. A trend from octupole vibration to deformation was observed for Ra, Rn and Th. These investigations demonstrate the feasibility of this kind of transfer experiments.

In 2005 Ishii et al. [51] managed to populate neutron-rich uranium nuclei via grazing reactions with an ^{18}O beam at an energy of 200 MeV on a ^{238}U target. The experiment was performed at the tandem booster of the Japan Atomic Energy Research facility (JAEA).

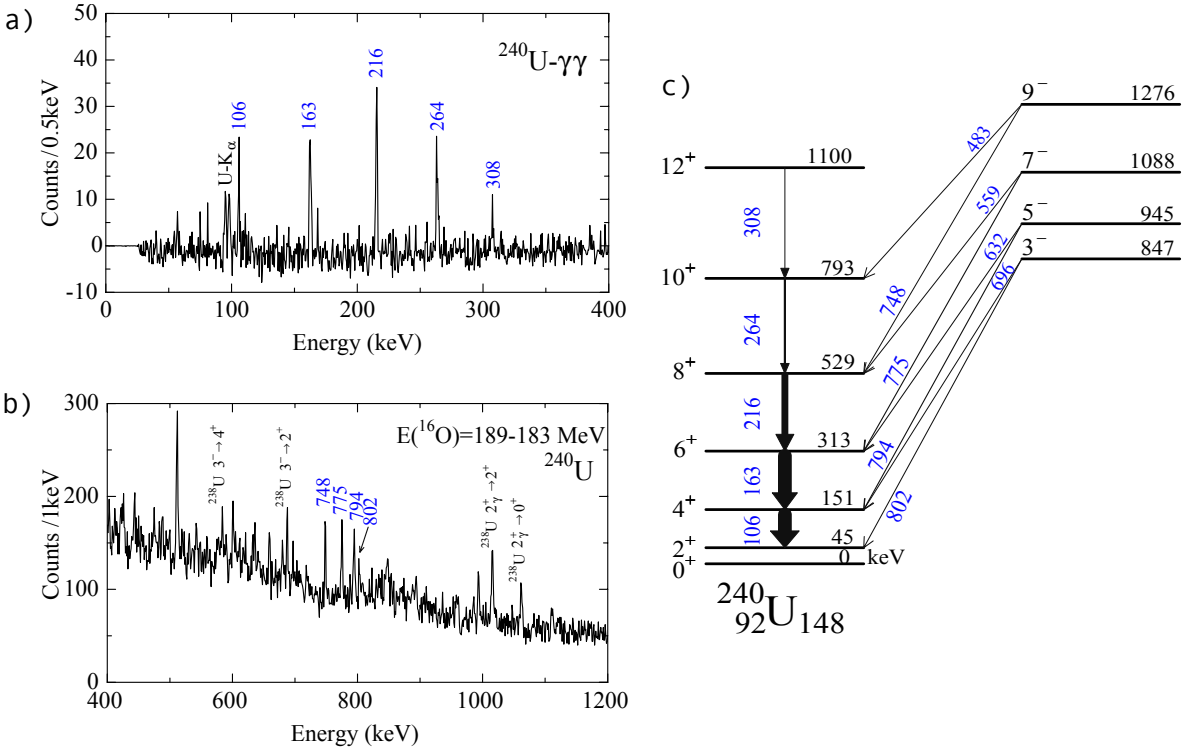

Figure 8.3.: *a) Sum of γ-γ coincidence spectra, which are gated on transitions (at 163 keV, 216 keV and 264 keV) of the ground state rotational band b) γ-singles spectrum of the negative-parity band of ^{240}U, obtained by gating on the total energy of ^{16}O $E(^{16}O) = 189 - 183$ MeV; c) resulting level scheme for ^{240}U (figures taken from reference [51]).*

By gating on high, deposited energy of the projectile-like particles in a Si $\Delta E - E$-detector, the population of ^{240}U was proven. By coincidence gating on the 163-, 216-, and 264-keV energies the ground-state rotational band was established up to the 12^+ state at 1100 keV, see figure 8.3 a). Even the first negative parity band could be observed up to the 9^- state at 1276 keV, see figure 8.3 b). The transitions with 748-, 775-, 483-, and 559-keV γ energies could only be confirmed to be coincident with the ground-state band transitions and not with intraband transitions due to low statistics. Figure 8.3 c) shows the resulting levelscheme for ^{240}U.
The same group [52] observed γ-singles spectra of ^{236}Th and ^{242}U at the JAEA facility with an (^{18}O, ^{20}Ne) reaction. To populate ^{236}Th an ^{238}U target was bombarded at an beam energy of 200 MeV. For ^{242}U the ^{18}O beam at 162 MeV impinged on a ^{244}Pu target. They discovered for the first time possible transitions in the ground-state rotational band of ^{236}Th up to the 10^+ state (see figure 8.4) and in the ground state rotational band of ^{242}U up to the 8^+ state. The γ-singles spectra were obtained by setting gates in the $\Delta E - E$ spectra of the projectile-like nuclei measured in a Si detector as it was already done in the previous experiment [51]. Figure 8.4 a) shows a ^{236}Th γ-singles spectrum by setting a gate on the kinetic energy of 5-11 MeV in the two-proton-transfer channel ^{20}Ne. In figure 8.4 b) the resulting, preliminary level scheme of ^{236}Th is pictured.
Using the results of a series of their experimental studies Ishii et al. [52] investigate

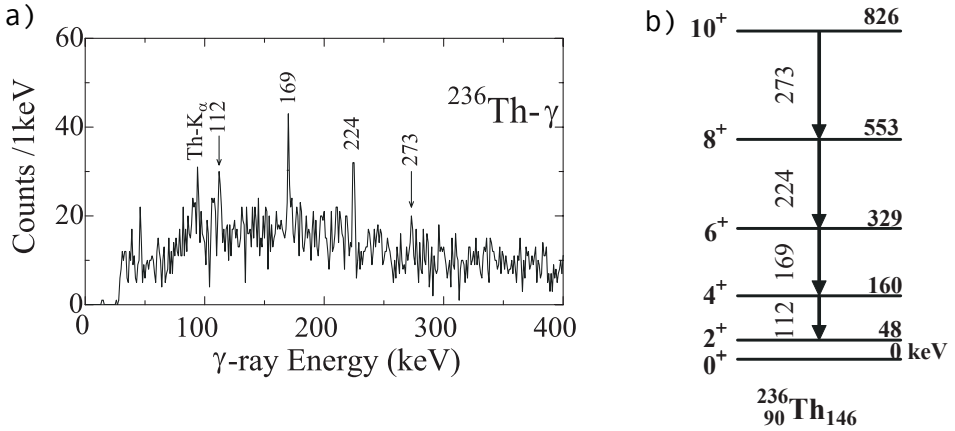

Figure 8.4.: *a) γ-singles spectrum for ^{236}Th, obtained by gating on the kinetic energy of 5-11 MeV in the $\Delta E - E$ spectrum of ^{20}Ne; b) resulting level scheme of ^{236}Th, figures from [52].*

the excitation energy of the 2^+ state in the ground-state bands of Th, U, Pu and Cm in dependence of the neutron number N. Local minima of the excitation energy of the 2^+ state at $N \approx 146$ for U and Pu isotopes and possibly for Th and Cm isotopes are regarded. With the assumption that mid-shell nuclei are characterized by strong collectivity, a spherical shell closure in the neutron shell at N=166 is expected (N=126 marks the shell closure at small N). Regarding the proton numbers Z the $h_{\frac{9}{2}}$ orbital is fully occupied at Z=92 and hence a subshell closure at Z=92 may exist. A doubly magic shell closure for ^{256}U with Z=92 and N=164 is predicted by this group.

9. Experimental Setup

To study the feasibility of multi-nucleon reactions for actinide spectroscopy two experiments have been analyzed and their results have been compared. The experiments were performed at the Laboratori Nazionali di Legnaro (LNL) in Italy using the Tandem-ALPI and the Piave-ALPI complex. The Tandem accelerator is a van-de-Graaff accelerator with a terminal voltage of 15 MV. The ions delivered by the tandem can be re-accelerated by the superconducting resonant cavity post-accelerator, called ALPI [66]. For heavier ions the tandem is replaced by another injector, the Piave positive-ion injector, which is based on superconducting radio-frequency quadrupoles. Piave is designed to accelerate ions with $A/Q \leq 8.5$ up to an energy of 1.2 MeV/u.[77].
The first experiment, performed in the year 2007, was a multi-nucleon transfer experiment with a ^{70}Zn beam impinging on an ^{238}U target. The ^{70}Zn beam, delivered by Tandem-ALPI, had a beam energy of 460 MeV. The second multi-nucleon-transfer experiment, which took place in 2008, ran with a ^{136}Xe beam, provided by Piave-ALPI. The ^{136}Xe beam with an energy of 926 MeV was also directed on an ^{238}U target.

The details of the experimental setups can be found in table 9.1. The beam of light ions reacts with the heavier target and transfer reaction take place. The beam-like light particles enter the magnetic spectrometer, PRISMA (see section 9.2), which is placed at the grazing angle of the reaction. The HPGe-detector array CLARA measures the γ rays at the target position. Typically, MNT experiments at the LNL have been designed for the investigation for the beam-like fragments. Also the former analyses of these two experiments, performed by J.J. Valiente Dobon and F. Recchia, were done concerning the beam-like nuclei around ^{70}Zn [98] and ^{136}Xe [83].
In this analysis the target-like fragments around ^{238}U, are the focus of interest.

With the information on the beam-like particles in PRISMA, knowledge about the binary reaction partners, the target-like nuclei, is obtained. The velocity vector deduced from PRISMA allows a proper Doppler correction of the γ spectra for the moving target-like nuclei. These γ spectra, Doppler corrected for the target-like fragments, are analyzed.

In the following sections the different components of the experimental setup are described.

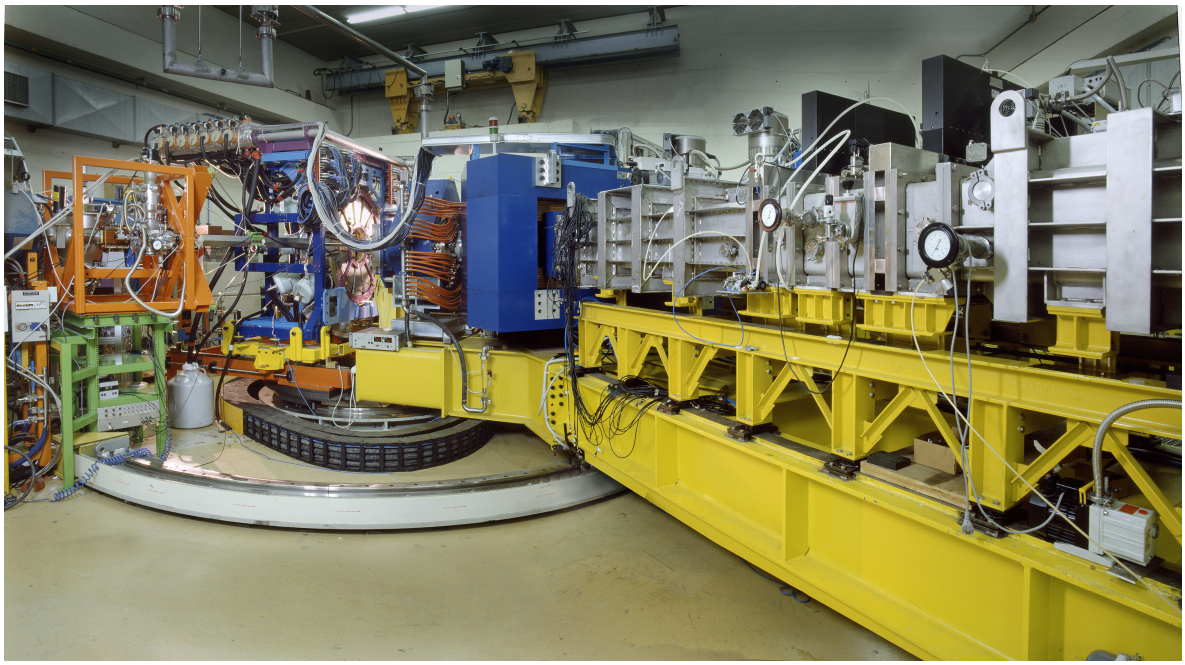

Figure 9.1.: *PRISMA Spectrometer with CLARA, figure taken from reference [17].*

	1^{st} experiment ^{70}Zn +^{238} U	2^{nd} experiment ^{136}Xe +^{238} U
accelerator	Tandem+ALPI	Piave+ALPI
beam	^{70}Zn	^{136}Xe
beam energy / MeV	460	926
current/pnA	2-2.5	2.5-3.5
duration/h	192	120
target	$1\frac{\text{mg}}{\text{cm}^2}$ ^{238}U	$0.5\frac{\text{mg}}{\text{cm}^2}$ ^{238}U
PRISMA angle / °	64 / 61	47
Dipole magnetic field strength / T	0.715/ 0.726	0.836
Quadrupole magnetic field strength/ T	0.652 / 0.663	0.768
MWPPAC gas	C_4H_{10}	C_4H_{10}
MWPPAC gas pressure / mbar	7	6.5
IC gas	CH_4	CH_4
IC gas pressure / mbar	79.6	74.0

Table 9.1.: *Parameters and settings of the two performed experiments at the LNL, Legnaro.*

9.1. The CLover ARrAy- CLARA

To observe the γ rays emitted after the reactions at the target position the CLover ARrAy, CLARA, was used. From March 2004 to 2008 CLARA consisted of 25 Euroball Clover HPGe detectors. It was mounted around the target position where afterwards in May 2011 the AGATA demonstrator was installed. Each Clover detector was anti-Compton shielded with Bismut-Germanium-Oxalat (BGO) and consisted of 4 HPGe crystals. Each of the crystals had a diameter of 5 cm. The efficiency of CLARA was about 3% for $E_\gamma = 1.3\,\mathrm{MeV}$, the ratio of peak-to-total approximately 45%. The energy resolution was around 1% for $v/c = 10\%$ [31]. A Doppler correction is performed for the γ spectra of the target-like fragments using the velocity vectors provided by PRISMA.

9.2. The PRISMA Spectrometer

PRISMA is a large-acceptance magnetic spectrometer designed for heavy ions. A schematic drawing is shown in figure 9.2. PRISMA is placed at the grazing angle of the reaction, so that the beam-like particles after multi-nucleon reactions are analyzed in PRISMA. PRISMA provides for the beam-like projectiles the mass (A), atomic number (Z), energy, charge state (q) and the trajectory.
Following the trajectory of the ions the beam-like projectile first pass a micro channel plate (MCP) detector at the entrance of the PRISMA spectrometer. Then the nucleons are focused and deflected by two magnets (a quadrupole and a dipole). At the focal plane the ions are detected by the multi wire parallel plates avalanche counter (MWPPAC) and an ionisation chamber (IC). The distance between the start detector and the focal plane is 6.5 m. PRISMA covers a solid angle of 80 msr ($\Delta\Theta = 12°$ in plane and $\Delta\Theta = 22°$ out of plane). It is characterized by the following quantities [6]:

- first order resolving power $\frac{p}{\Delta p} = 2000$
- dispersion $\approx \frac{4cm}{\%}\frac{\Delta p}{p}$
- energy resolution $\approx \frac{1}{1000}$
- nuclear charge (Z) resolution $\approx \frac{1}{60}$
- mass resolution $\approx \frac{1}{300}$
- rate capability ≈ 100 kHz

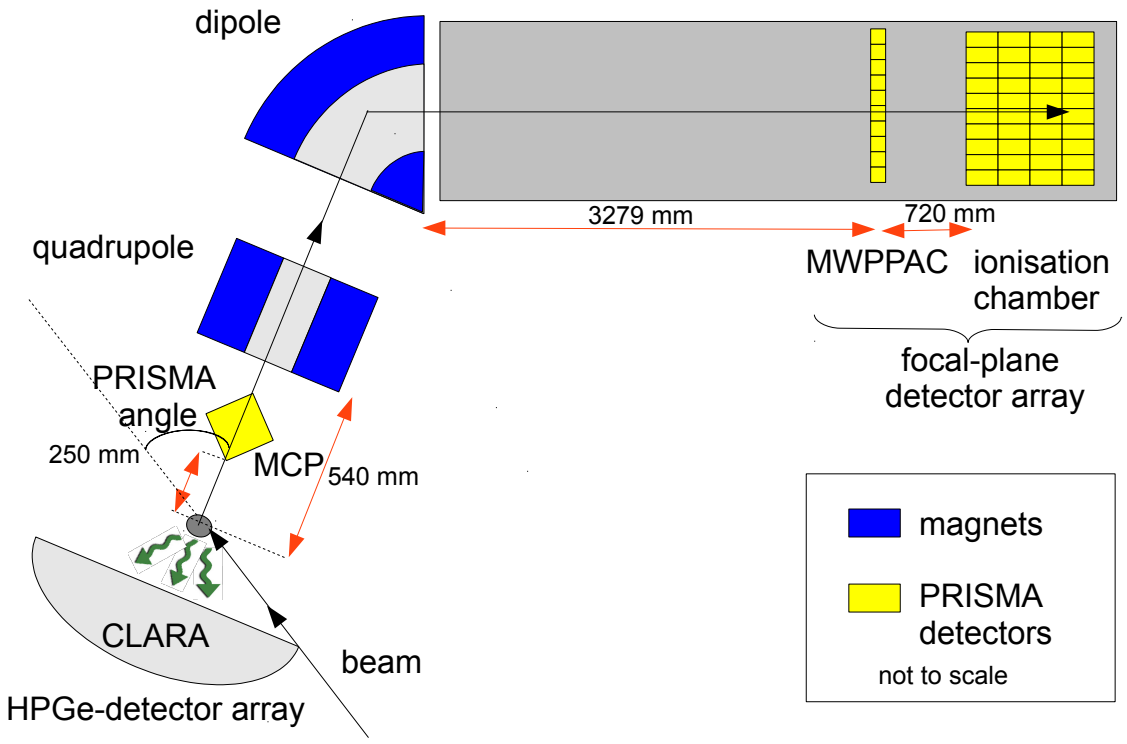

Figure 9.2.: *Schematic drawing of the PRISMA Spectrometer with CLARA.*

9.2-1. Micro Channel Plate (MCP) Detector

A position-sensitive entrance detector is placed 25 cm downstream the target. It consists of 2-dimensional rectangular micro channel plates ($80 \times 100\,\mathrm{mm}^2$), mounted in a chevron configuration [71]. It provides a timing resolution of less than 400 ps; its fast time signal serves for time-of-flight (TOF) measurements and it is used as the delayed TOF stop signal. The entrance angle resolution is smaller than 0.5° in the dispersion plane. The x (along the PRISMA dispersion plane) and y coordinates give a position resolution of 1 mm in each axis. In typical experiments with heavy-ion beams the efficiency reaches nearly 100% [71].

9.2-2. Magnets

Behind the MCP magnetic lenses, a quadrupole singlet (Q) and a dipole magnet (D), are located. The quadrupole lens is placed 50 cm behind the target for focussing the ejectiles. Its aperture diameter is 32 cm, while its effective length is 50 cm. 60 cm behind the quadrupole the dipole is installed with 60° bending angle and 1.2 m curvature radius [72]. The incoming charged particles are bent on different trajectories by the dipole due to their magnetic rigidity.

9.2-3. Focal Plane Detectors

Multi Wire Parallel Plates Avalanche Counter (MWPPAC) In the focal plane (327.9 cm behind the dipole) the isobutane gas-filled multi-wire parallel plates avalanche counter (MWPPAC) is mounted [6]. The detector needs to cover a large area because of the large solid angle and a large optical dispersion of the ions. The total active area in the focal plane is $13 \times 100\,\mathrm{cm}^2$. On their way through the MWPPAC the ions cross a three electrode structure composed of gold plated tungsten wires: at the entrance a x-position sensitive anode, which is divided in 10 sections, in the center a cathode, also subdivided into 10 sections, and at the end of the detector a y-position sensitive anode, which covers the entire width of the MWPPAC .
The tasks for the MWPPAC are to give information about the x and y positions of the ions and to provide a timing signal. The timing signal is used as start signal for the time-of-flight measurements (with a delayed stop signal from the MCP). Due to its sharp shaping time (300-400 ps resolution) it also serves as trigger signal for the data acquisition.

Ionisation Chamber (IC) 60 cm behind the MWPPAC the ions are completely stopped in the ionisation chamber (IC) and their energy and energy loss ΔE on their way through the ionisation chamber are detected. The active volume of the IC is $120 \times 120 \times 13\,\mathrm{cm}^3$ (depth $\times$ width $\times$ height respectively). It consists of 68 pads (10 sections $\times$ 4 pads + 28 side pads), which all work as independent ΔE sections [6]. The entrance window is made of 1.5 μm thick Mylar foil, which is constructed to hold pressures of 100 mbar with a maximum deformation of 3 mm. The detector is filled with methane gas of 99.9% purity, because methane has a high electron drift velocity.

9.3. PRISMA Data Analysis

In this paragraph the path of processing data, which derive from the PRISMA detectors, is shortly described. The PRISMA data analysis has already been performed by Jose Javier Valiente Dobon and Francesco Recchia from the LNL for the analysis of the beam-like reaction products for the two experiments. It is used as a starting point for the analysis of the target-like nuclei (see chapter 11).

9.3-1. Trajectory

The first analysis step after the calibration of the MCP and the alignment of the MWPPAC is the reconstruction of the trajectories (with length D) of the ions in PRISMA. The ions follow bent trajectories due to the Lorentz force with

$$qvB_{dipole} = \frac{Av^2}{R} \tag{9.1}$$

where q is the charge, v the velocity, B_{dipole} the magnetic field strength of the dipole, A the mass and R the radius of the circular path.
The reconstruction is performed by an iterative process, supposing that the radius R=120 cm as a first guess. The velocity v is calculated as $v = \frac{D}{TOF}$ of the assumed trajectory. The values of v, A/q and R are varied until the difference of the calculated position in the MWPPAC to the experimentally determined position is smaller than 1 mm and reasonable values of v, A/q and R and thus D are found.

9.3-2. Atomic Number Z

The ions are stopped in the IC and the total kinetic energy E_{kin} is deposited in the IC. The energy E_{IC} and the energy loss ΔE_{IC} of the particles are measured.

The energy loss in dependence of the path length of the trajectory, z, is given by the Bethe-Bloch-formula:

$$\frac{dE(z)}{dz} \propto \frac{AZ^2}{E(z)} \tag{9.2}$$

where A is the mass and Z the atomic number of the particle in PRISMA. The relation between energy loss and the energy respectively and Z^2 is used to graphically determine Z by setting polygon gates in two-dimensional plots. There are three methods to select Z:

1. Z can be derived from the $\Delta E_{IC} - E_{IC}$-matrix.
2. Z can be obtained by using the relation between energy loss ΔE_{IC} and the range r of the ions in the IC. The range is calculated with

$$r(E) = \int_0^E (-\frac{dE}{dz})^{-1} dE. \tag{9.3}$$

In this case Z is selected in a $\Delta E-$range plot.

3. The third method combines 1. and 2. The deposited energy E_{IC} is plotted versus the calculated range, see equation (9.3). Again a separation of Z is visible and polygon gates are set. Two of these plots are shown in figures 11.1 for the (^{70}Zn+^{238}U) experiment and 11.2 for the (^{136}Xe+^{238}U) experiment.

9.3-3. Charge State q

When the projectile-like particle is stopped in the IC the entire kinetic energy is deposited and is given by

$$E_{kin} = \frac{1}{2}Av^2 = E_{IC}. \tag{9.4}$$

Together with equation (9.1) a correlation between the deposited energy E_{IC} and the charge state q of the particle is exploited:

$$E_{IC} \propto qRv \tag{9.5}$$

with R, the radius of the trajectory , and v, the velocity of the particle. In the 2d plot of the energy E_{IC} versus Rv the different charge states are separated and can be selected with polygon gates.

9.3-4. Mass A

Rewriting equation 9.1 results in

$$A = qB_{dipole}\frac{R}{v}. \tag{9.6}$$

Now the velocity v, the radius of the trajectory R and the charge state q of the projectile-like particles in PRISMA are known to calculate the mass A and to create mass spectra. Figures 11.3 and 11.4 show the mass distributions for the (^{70}Zn+^{238}U) experiment and for the (^{136}Xe+^{238}U) experiment.

Further information about the PRISMA data analysis can, for example, be found in Ref. [90].

10. Calculations

10.1. Q value

For a nuclear reaction A(a,b)B the sum of the kinetic energies T_i before and after the reaction can vary due to different binding energies of the reaction partners [44].
The Q value is defined as the difference of the kinetic energies in the initial and the final state:

$$Q = (T_B + T_b) - (T_A + T_a) \tag{10.1}$$

Due to the conservation of energy the Q value is also the difference of the rest energies before and after the reaction:

$$Q = [(m_{0A} + m_{0a}) - (m_{0B} + m_{0b})]c^2 \tag{10.2}$$

with the rest masses m_{0i}.

The reaction is exothermic, characterized by a net energy release, when $Q > 0$. In this case the sum of the rest masses of the reactants is larger than those of the products. For $Q < 0$ the reaction is endothermic and requires additional energy.

Table 10.1 lists the calculated Q values for the proton and neutron-transfer channel for the (^{70}Zn+^{238}U) reaction and for the (^{136}Xe+^{238}U) reaction. The Q values are calculated with the mass information from the atomic mass data center [3]. The calculation covers the experimentally observed nuclei, see section 11.2 up to the limit where the mass information for the very neutron-rich nuclei is available.
Figures 10.1(a) to 10.1(e) picture the calculated Q values from table 10.1.

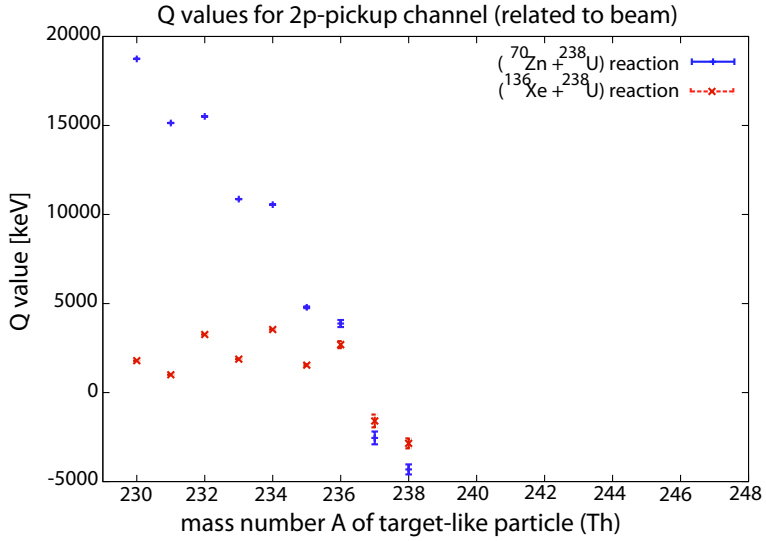
Q values for 2p-pickup channel (related to beam)
(70Zn + 238U) reaction
(136Xe + 238U) reaction
Q value [keV]
mass number A of target-like particle (Th)

(a)

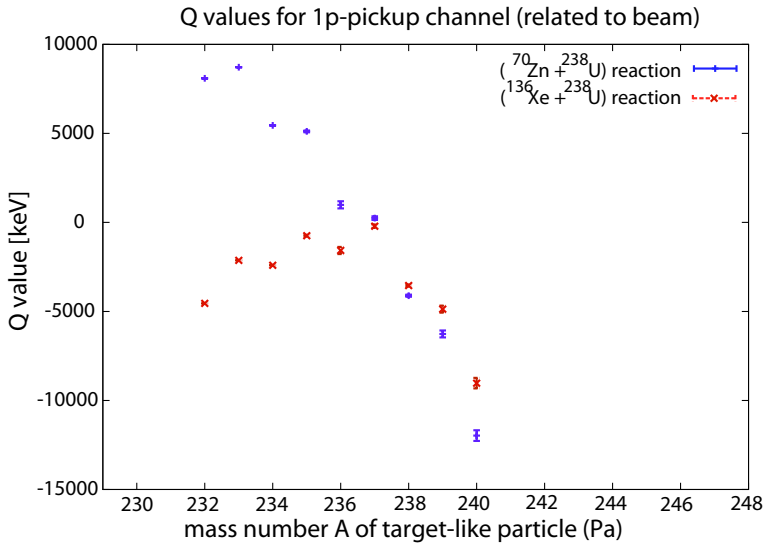
Q values for 1p-pickup channel (related to beam)
(70Zn + 238U) reaction
(136Xe + 238U) reaction
Q value [keV]
mass number A of target-like particle (Pa)

(b)

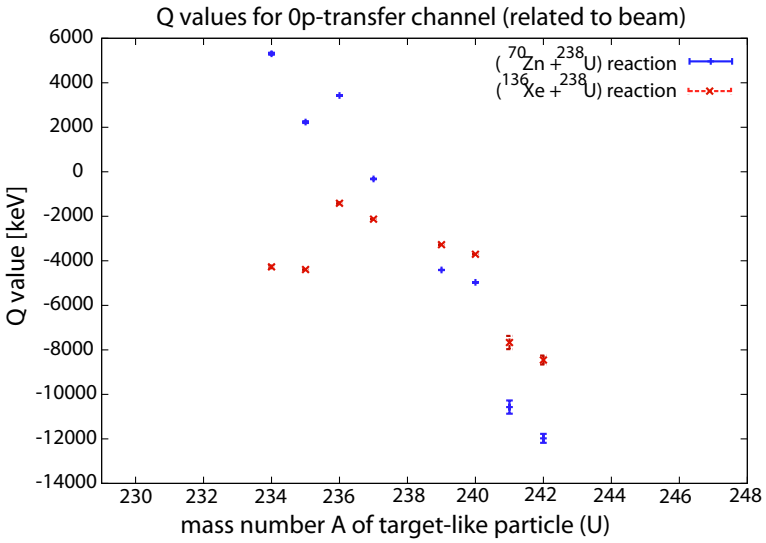
Q values for 0p-transfer channel (related to beam)
(70Zn + 238U) reaction
(136Xe + 238U) reaction
Q value [keV]
mass number A of target-like particle (U)

(c)

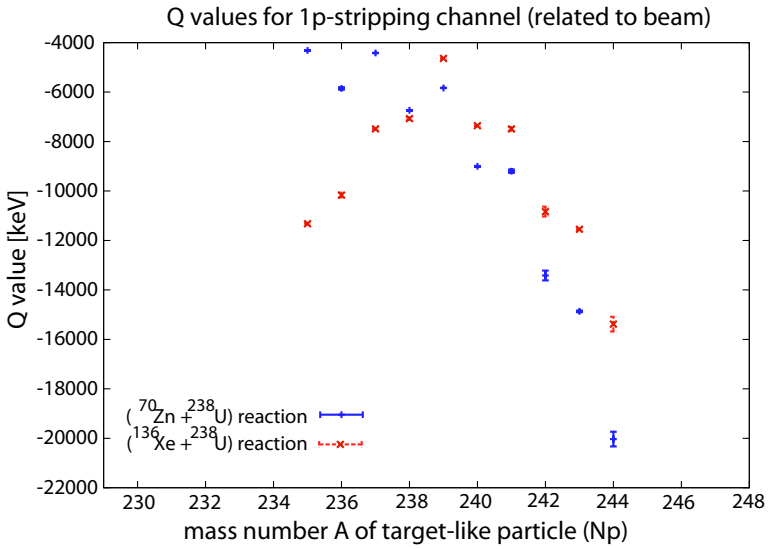

(d)

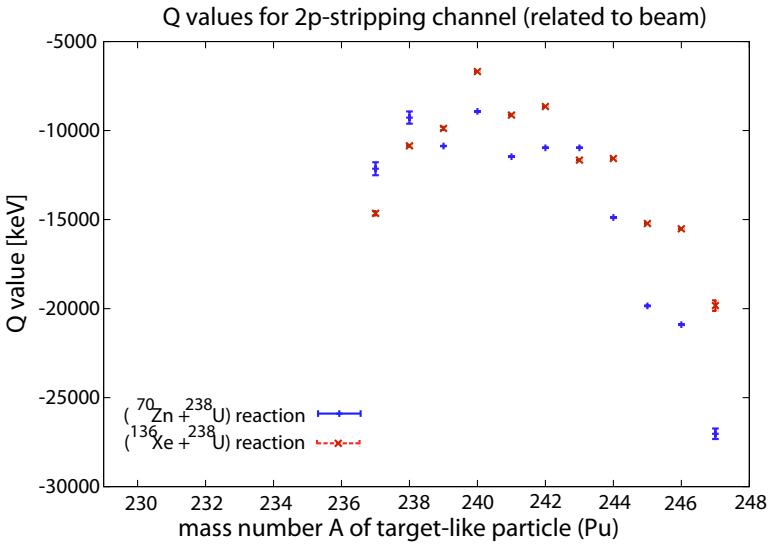

(e)

Figure 10.1.: *Calculated Q values due to table 10.1 for the (^{70}Zn+^{238}U) reaction in blue and for the (^{136}Xe+^{238}U) reaction in red color.*

Table 10.1.: *Q values for the (^{70}Zn+^{238}U) reaction and for the (^{136}Xe+^{238}U) reaction.*

	(^{70}Zn+^{238}U) reaction		(^{136}Xe+^{238}U) reaction	
transferred nucleons (related to beam)	products	Q value [keV]	products	Q value [keV]
+2p-2n	^{238}Th+^{70}Ge	-4318(283)	^{238}Th+^{136}Ba	-2854(283)
+2p-1n	^{237}Th+^{71}Ge	-2550(359)	^{237}Th+^{137}Ba	-1597(359)
+2p	^{236}Th+^{72}Ge	3876(196)	^{236}Th+^{138}Ba	2691(196)
+2p+1n	^{235}Th+^{73}Ge	4787(50)	^{235}Th+^{139}Ba	1542(51)
+2p+2n	^{234}Th+^{74}Ge	10552(5)	^{234}Th+^{140}Ba	3541(11)
+2p+3n	^{233}Th+^{75}Ge	10867(4)	^{233}Th+^{141}Ba	1876(11)
+2p+4n	^{232}Th+^{76}Ge	15509(4)	^{232}Th+^{142}Ba	3259(10)
+2p+5n	^{231}Th+^{77}Ge	15141(4)	^{231}Th+^{143}Ba	1002(15)
+2p+6n	^{230}Th+^{78}Ge	18743(5)	^{230}Th+ ^{144}Ba	1789(15)
+1p-3n	^{240}Pa+^{68}Ga	-11973(298)	^{240}Pa+^{134}Cs	-9028(298)
+1p-2n	^{239}Pa+^{69}Ga	-6265(196)	^{239}Pa+^{135}Cs	-4871(196)
+1p-1n	^{238}Pa+^{70}Ga	-4115(60)	^{238}Pa+^{136}Cs	-3546(61)
+1p	^{237}Pa+^{71}Ga	243(100)	^{237}Pa+^{137}Cs	-212(100)
+1p+1n	^{236}Pa+^{72}Ga	987(200)	^{236}Pa+^{138}Cs	-1575(200)
+1p+2n	^{235}Pa+^{73}Ga	5113(50)	^{235}Pa+^{139}Cs	-746(51)
+1p+3n	^{234}Pa+^{74}Ga	5453(7)	^{234}Pa+^{140}Cs	-2406(12)
+1p+4n	^{233}Pa+^{75}Ga	8719(4)	^{233}Pa+^{141}Cs	-2129(13)
+1p+5n	^{232}Pa+^{76}Ga	8093(8)	^{232}Pa+^{142}Cs	-4549(15)
-4n	^{242}U+^{66}Zn	-11976(201)	^{242}U+^{132}Xe	-8456(201)
-3n	^{241}U+^{67}Zn	-10572(298)	^{241}U+^{133}Xe	-7670(298)
-2n	^{240}U+^{68}Zn	-4964(6)	^{240}U+^{134}Xe	-3707(9)
-1n	^{239}U+^{69}Zn	-4412(3)	^{239}U+^{135}Xe	-3273(9)
+1n	^{237}U+^{71}Zn	-321(11)	^{237}U+^{137}Xe	-2129(10)
+2n	^{236}U+^{72}Zn	3429(7)	^{236}U+^{138}Xe	-1412(44)
+3n	^{235}U+^{73}Zn	2234(40)	^{235}U+^{139}Xe	-4393(22)
+4n	^{234}U+^{74}Zn	5307(47)	^{234}U+^{140}Xe	-4272(61)
-1p-5n	^{244}Np+^{64}Cu	-20033(298)	^{244}Np+^{130}I	-15386(298)
-1p-4n	^{243}Np+^{65}Cu	-14867(32)	^{243}Np+^{131}I	-11546(33)
-1p-3n	^{242}Np+^{66}Cu	-13416(200)	^{242}Np+^{132}I	-10835(200)
-1p-2n	^{241}Np+^{67}Cu	-9199(71)	^{241}Np+^{133}I	-7491(71)
-1p-1n	^{240}Np+^{68}Cu	-9003(16)	^{240}Np+^{134}I	-7358(19)
-1p	^{239}Np+^{69}Cu	-5832(4)	^{239}Np+^{135}I	-4639(11)
-1p+1n	^{238}Np+^{70}Cu	-6736(4)	^{238}Np+^{136}I	-7073(51)
-1p+2n	^{237}Np+^{71}Cu	-4418(4)	^{237}Np+^{137}I	-7487(29)
-1p+3n	^{236}Np+^{72}Cu	-5852(51)	^{236}Np+^{138}I	-10165(97)
-1p+4n	^{235}Np+^{73}Cu	-4314(5)	^{235}Np+^{139}I	-11323 (32)

Table 10.1.: *Q values for the (^{70}Zn+^{238}U) reaction and for the (^{136}Xe+^{238}U) reaction.*

	(^{70}Zn+^{238}U) reaction		(^{136}Xe+^{238}U) reaction	
transferred nucleons (related to beam)	products	Q value [keV]	products	Q value [keV]
-2p-7n	^{247}Pu+^{61}Ni	-27031(298)	^{247}Pu+^{127}Te	-19831(298)
-2p-6n	^{246}Pu+^{62}Ni	-20904(16)	^{246}Pu+^{128}Te	-15519(17)
-2p-5n	^{245}Pu+^{63}Ni	-19849(15)	^{245}Pu+^{129}Te	-15219(16)
-2p-4n	^{244}Pu+^{64}Ni	-14885(6)	^{244}Pu+^{130}Te	-11570(9)
-2p-3n	^{243}Pu+^{65}Ni	-10967(4)	^{243}Pu+^{131}Te	-11662(8)
-2p-2n	^{242}Pu+^{66}Ni	-10968(4)	^{242}Pu+^{132}Te	-8652(10)
-2p-1n	^{241}Pu+^{67}Ni	-11470(4)	^{241}Pu+^{133}Te	-9128(26)
-2p	^{240}Pu+^{68}Ni	-8919(4)	^{240}Pu+^{134}Te	-6684(13)
-2p+1n	^{239}Pu+^{69}Ni	-10867(5)	^{239}Pu+^{135}Te	-9878(90)
-2p+2n	^{238}Pu+^{70}Ni	-9271(346)	^{238}Pu+^{136}Te	-10856(46)
-2p+3n	^{237}Pu+^{71}Ni	-12145(368)	^{237}Pu+^{137}Te	-14648(123)

10.2. Cross Section

The cross sections σ for the reactions (^{70}Zn+^{238}U) at 460 MeV and (^{136}Xe+^{238}U) at 926 MeV are determined using the GRAZING code.

The GRAZING code calculates cross sections for the reaction of two colliding heavy nuclei at moderate energies concerning mass, charge, kinetic and excitation energy and angular momentum [105]. The GRAZING model treats the two reaction partners as nuclei with independent nucleons [103, 104, 22]. For the reaction between the two nuclei the Coulomb forces and strong interaction are considered. Surface vibrations are taken into account via macroscopic approximation. The transfer of nucleons is described as successive mechanism and is calculated in microscopic approximation: single-particle states of the two colliding nuclei are characterized with microscopic form factors. The single-particle states which contribute to the exchange process are described by average single particle level densities. The trajectories of the particles are calculated solving the system of classical, coupled equations for variables of relative motion and deformation parameters [21]. The entire formalism, which forms the basis for the GRAZING code, can be found in references [103, 104].

Figures 10.2(a) to 10.2(j) illustrate the results of the GRAZING calculations for the target-like nuclei with $90 \leq Z \leq 94$ for (^{70}Zn+^{238}U) at 460 MeV and the (^{136}Xe+^{238}U) experiment at 926 MeV. Table 10.2 lists the calculated cross sections on the left side in blue color for the (^{70}Zn+^{238}U) reaction and on the right side in red color for the (^{136}Xe+^{238}U) reaction. This calculation considers the evaporation of nucleons. From former experimental experiences with PRISMA [32] an approximate sensitivity limit of σ =0.1 mbarn for the detection of the beam-like fragments in PRISMA is deduced. In order to determine the lower sensitivity limit for the detection of the target-like fragments with CLARA by gating on the beam-like fragments in PRISMA one has to consider the efficiency of CLARA. Assuming kinematic coincidences and supposing the CLARA efficiency to be approx 3%, the lower sensitivity limit for the detection of target-like fragments is $\sigma \geq \frac{0.1\text{mbarn}}{3\%}$=3 mbarn. The assumed sensitivity limit is marked in the figures as dashed lines. The results of the analysis of the γ spectra in section 11.4 will be discussed with respect to these GRAZING calculations and the Q-value calculations of section 10.1.

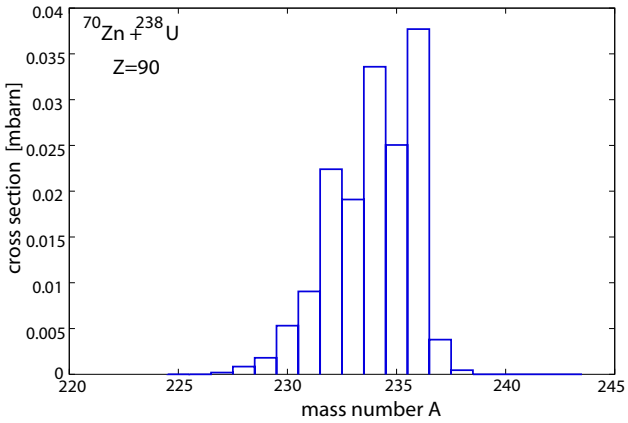

(a) σ for $_{90}$Th

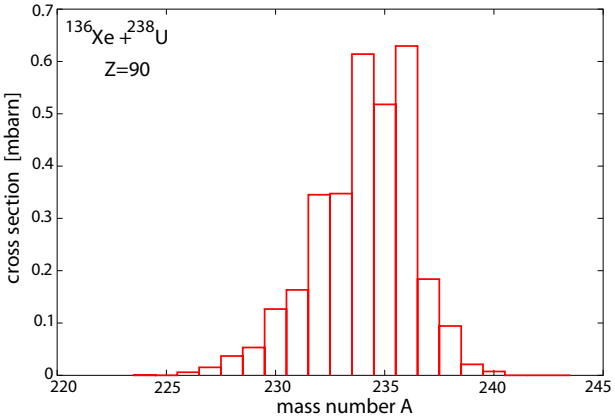

(b) σ for $_{90}$Th

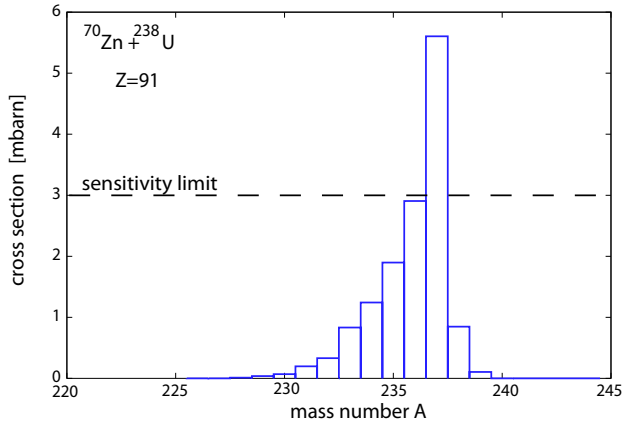

(c) σ for $_{91}$Pa

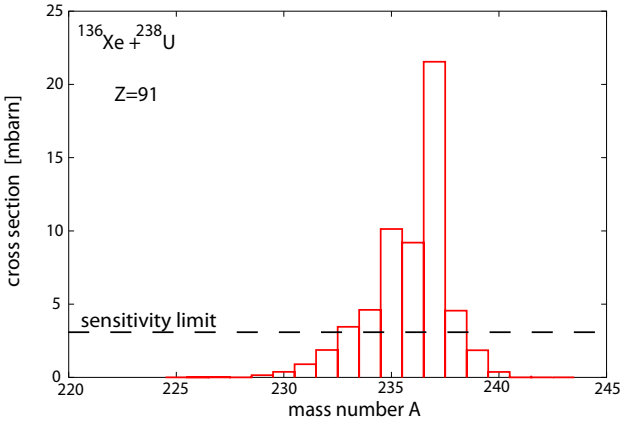

(d) σ for $_{91}$Pa

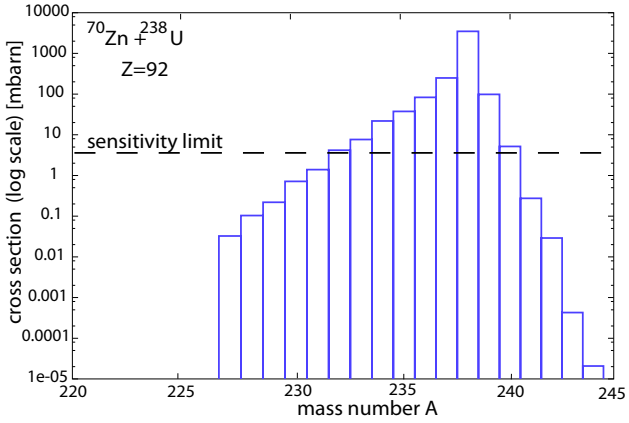

(e) σ (log scale) for $_{92}$U

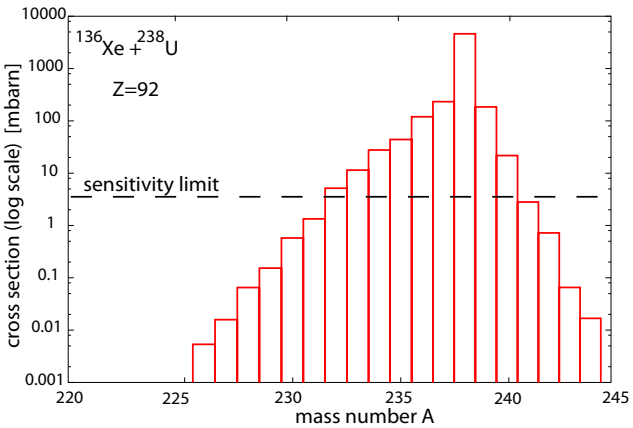

(f) σ (log scale) for $_{92}$U

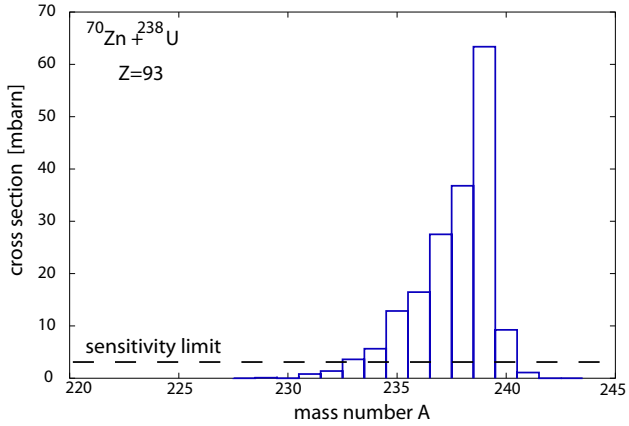

(g) σ for $_{93}$Np

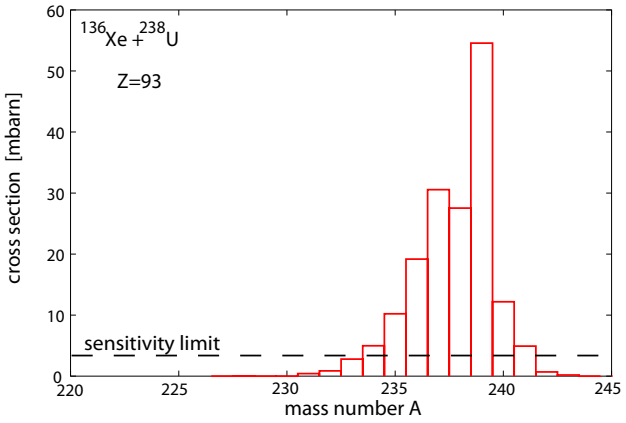

(h) σ for $_{93}$Np

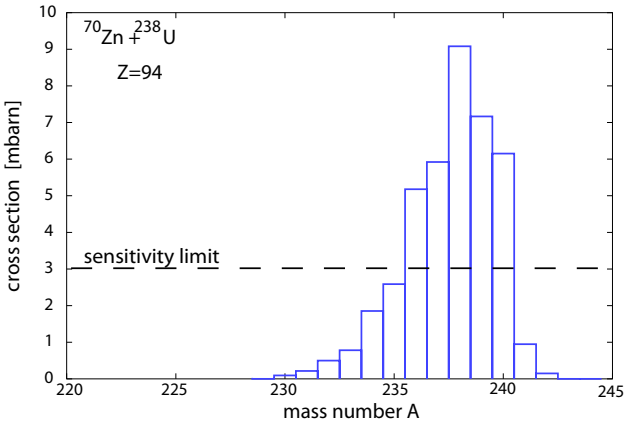

(i) σ for $_{94}$Pu

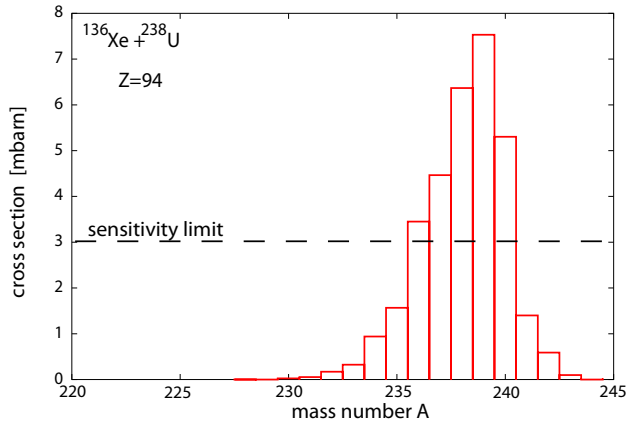

(j) σ for $_{94}$Pu

Figure 10.2.: *Calculated cross sections on the left side in blue for the (^{70}Zn+^{238}U) reaction at 460 MeV beam energy and on the right side in red for the (^{136}Xe+^{238}U) reaction at 926 MeV. The calculation are performed with the GRAZING code [105] for the isotopic chains of $90 \leq Z \leq 94$. The assumed lower sensitivity limit of $\sigma \geq 3$ mbarn for the detection of the target-like fragments are marked with dashed lines.*

Table 10.2.: *Cross sections of the target-like nuclei for the (^{70}Zn+^{238}U) reaction with 460 MeV beam energy and for the (^{136}Xe+^{238}U) reaction with 926 MeV beam energy. Calculated with the GRAZING code [105].*

	(^{70}Zn+^{238}U) reaction	(^{136}Xe+^{238}U) reaction
target-like nucleus	σ (mbarn)	σ (mbarn)
^{244}Th		$1.31 \cdot 10^{-08}$
^{243}Th		$1.41 \cdot 10^{-06}$
^{242}Th		$6.36 \cdot 10^{-05}$
^{241}Th		$7.95 \cdot 10^{-04}$
^{240}Th		$7.43 \cdot 10^{-03}$
^{239}Th		$2.10 \cdot 10^{-02}$
^{238}Th	$4.49 \cdot 10^{-04}$	$9.43 \cdot 10^{-02}$
^{237}Th	$3.78 \cdot 10^{-03}$	$1.83 \cdot 10^{-01}$
^{236}Th	$3.77 \cdot 10^{-02}$	$6.29 \cdot 10^{-01}$
^{235}Th	$2.50 \cdot 10^{-02}$	$5.17 \cdot 10^{-01}$
^{234}Th	$3.35 \cdot 10^{-02}$	$6.14 \cdot 10^{-01}$
^{233}Th	$1.90 \cdot 10^{-02}$	$3.47 \cdot 10^{-01}$
^{232}Th	$2.24 \cdot 10^{-02}$	$3.45 \cdot 10^{-01}$
^{231}Th	$9.05 \cdot 10^{-03}$	$1.63 \cdot 10^{-01}$
^{230}Th	$5.31 \cdot 10^{-03}$	$1.26 \cdot 10^{-01}$
^{229}Th	$1.80 \cdot 10^{-03}$	$5.31 \cdot 10^{-02}$
^{228}Th	$8.41 \cdot 10^{-04}$	$3.69 \cdot 10^{-02}$
^{227}Th	$1.88 \cdot 10^{-04}$	$1.53 \cdot 10^{-02}$
^{226}Th	$5.00 \cdot 10^{-05}$	$5.82 \cdot 10^{-03}$
^{225}Th	$5.54 \cdot 10^{-06}$	$2.05 \cdot 10^{-03}$
^{224}Th		$5.81 \cdot 10^{-04}$
^{247}Pa		$2.48 \cdot 10^{-10}$
^{246}Pa		$4.22 \cdot 10^{-07}$
^{245}Pa		$2.46 \cdot 10^{-05}$
^{244}Pa		$4.32 \cdot 10^{-04}$
^{243}Pa		$2.82 \cdot 10^{-03}$
^{242}Pa		$1.22 \cdot 10^{-02}$
^{241}Pa	$5.92 \cdot 10^{-04}$	$1.13 \cdot 10^{-01}$
^{240}Pa	$7.01 \cdot 10^{-03}$	$3.68 \cdot 10^{-01}$
^{239}Pa	$1.04 \cdot 10^{-01}$	1.85
^{238}Pa	$8.47 \cdot 10^{-01}$	4.55
^{237}Pa	5.60	$2.15 \cdot 10^{+01}$
^{236}Pa	2.90	9.20
^{235}Pa	1.89	$1.01 \cdot 10^{+01}$
^{234}Pa	1.24	4.61
^{233}Pa	$8.33 \cdot 10^{-01}$	3.45
^{232}Pa	$3.31 \cdot 10^{-01}$	1.87

Table 10.2.: *Cross sections of the target-like nuclei for the (^{70}Zn+^{238}U) reaction with 460 MeV beam energy and for the (^{136}Xe+^{238}U) reaction with 926 MeV beam energy. Calculated with the GRAZING code [105].*

	(^{70}Zn+^{238}U) reaction	(^{136}Xe+^{238}U) reaction
target-like nucleus	σ (mbarn)	σ (mbarn)
^{231}Pa	$1.97{\cdot}10^{-01}$	$9.01{\cdot}10^{-01}$
^{230}Pa	$6.96{\cdot}10^{-02}$	$3.78{\cdot}10^{-01}$
^{229}Pa	$3.73{\cdot}10^{-02}$	$1.50{\cdot}10^{-01}$
^{228}Pa	$1.12{\cdot}10^{-02}$	$6.02{\cdot}10^{-02}$
^{227}Pa	$5.62{\cdot}10^{-03}$	$2.67{\cdot}10^{-02}$
^{226}Pa	$1.49{\cdot}10^{-03}$	$6.38{\cdot}10^{-03}$
^{225}Pa		$2.0248{\cdot}10^{-03}$
^{244}U	$2.07{\cdot}10^{-05}$	$1.67{\cdot}10^{-02}$
^{243}U	$4.27{\cdot}10^{-04}$	$6.54{\cdot}10^{-02}$
^{242}U	$2.90{\cdot}10^{-02}$	$7.20{\cdot}10^{-01}$
^{241}U	$2.74{\cdot}10^{-01}$	2.81
^{240}U	5.17	$2.16{\cdot}10^{+01}$
^{239}U	$9.86{\cdot}10^{+01}$	$1.84{\cdot}10^{+02}$
^{238}U	$3.48{\cdot}10^{+03}$	$4.61{\cdot}10^{+03}$
^{237}U	$2.48{\cdot}10^{+02}$	$2.33{\cdot}10^{+02}$
^{236}U	$8.31{\cdot}10^{+01}$	$1.19{\cdot}10^{+02}$
^{235}U	$3.74{\cdot}10^{+01}$	$4.40{\cdot}10^{+01}$
^{234}U	$2.19{\cdot}10^{+01}$	$2.76{\cdot}10^{+01}$
^{233}U	7.64	$1.14{\cdot}10^{+01}$
^{232}U	4.18	5.15
^{231}U	1.39	1.33
^{230}U	$7.17{\cdot}10^{-01}$	$5.75{\cdot}10^{-01}$
^{229}U	$2.19{\cdot}10^{-01}$	$1.53{\cdot}10^{-01}$
^{228}U	$1.03{\cdot}10^{-01}$	$6.51{\cdot}10^{-02}$
^{227}U	$3.24{\cdot}10^{-02}$	$1.58{\cdot}10^{-02}$
^{226}U		$5.34{\cdot}10^{-03}$
^{249}Np		$6.77{\cdot}10^{-08}$
^{248}Np		$3.32{\cdot}10^{-06}$
^{247}Np		$4.88{\cdot}10^{-05}$
^{246}Np		$4.01{\cdot}10^{-04}$
^{245}Np	$2.29{\cdot}10^{-06}$	$5.80{\cdot}10^{-03}$
^{244}Np	$1.87{\cdot}10^{-04}$	$2.39{\cdot}10^{-02}$
^{243}Np	$6.17{\cdot}10^{-03}$	$1.92{\cdot}10^{-01}$
^{242}Np	$9.46{\cdot}10^{-02}$	$6.95{\cdot}10^{-01}$
^{241}Np	1.08	4.91
^{240}Np	9.24	$1.21{\cdot}10^{+01}$
^{239}Np	$6.33{\cdot}10^{+01}$	$5.45{\cdot}10^{+01}$

Table 10.2.: *Cross sections of the target-like nuclei for the (^{70}Zn+^{238}U) reaction with 460 MeV beam energy and for the (^{136}Xe+^{238}U) reaction with 926 MeV beam energy. Calculated with the GRAZING code [105].*

	(^{70}Zn+^{238}U) reaction	(^{136}Xe+^{238}U) reaction
target-like nucleus	σ (mbarn)	σ (mbarn)
^{238}Np	$3.67{\cdot}10^{+01}$	$2.75{\cdot}10^{+01}$
^{237}Np	$2.75{\cdot}10^{+01}$	$3.05{\cdot}10^{+01}$
^{236}Np	$1.64{\cdot}10^{+01}$	$1.91{\cdot}10^{+01}$
^{235}Np	$1.28{\cdot}10^{+01}$	$1.02{\cdot}10^{+01}$
^{234}Np	5.63	4.97
^{233}Np	3.60	2.79
^{232}Np	1.37	$8.69{\cdot}10^{-01}$
^{231}Np	$7.98{\cdot}10^{-01}$	$4.12{\cdot}10^{-01}$
^{230}Np	$3.02{\cdot}10^{-01}$	$1.19{\cdot}10^{-01}$
^{229}Np	$1.02{\cdot}10^{-01}$	$5.23{\cdot}10^{-02}$
^{228}Np	$3.31{\cdot}10^{-02}$	$1.24{\cdot}10^{-02}$
^{227}Np		$4.24{\cdot}10^{-03}$
^{250}Pu		$1.28{\cdot}10^{-11}$
^{249}Pu		$1.10{\cdot}10^{-08}$
^{248}Pu		$1.36{\cdot}10^{-06}$
^{247}Pu		$2.80{\cdot}10^{-05}$
^{246}Pu		$5.86{\cdot}10^{-04}$
^{245}Pu	$6.97{\cdot}10^{-06}$	$3.11{\cdot}10^{-03}$
^{244}Pu	$4.88{\cdot}10^{-04}$	$2.88{\cdot}10^{-02}$
^{243}Pu	$9.28{\cdot}10^{-03}$	$9.75{\cdot}10^{-02}$
^{242}Pu	$1.49{\cdot}10^{-01}$	$5.88{\cdot}10^{-01}$
^{241}Pu	$9.47{\cdot}10^{-01}$	1.39
^{240}Pu	6.15	5.30
^{239}Pu	7.16	7.53
^{238}Pu	9.08	6.36
^{237}Pu	5.92	4.46
^{236}Pu	5.17	3.45
^{235}Pu	2.58	1.56
^{234}Pu	1.85	$9.40{\cdot}10^{-01}$
^{233}Pu	$7.81{\cdot}10^{-01}$	$3.23{\cdot}10^{-01}$
^{232}Pu	$4.98{\cdot}10^{-01}$	$1.71{\cdot}10^{-01}$
^{231}Pu	$2.15{\cdot}10^{-01}$	$5.45{\cdot}10^{-02}$
^{230}Pu	$9.30{\cdot}10^{-02}$	$2.56{\cdot}10^{-02}$
^{229}Pu	$2.58{\cdot}10^{-02}$	$6.63{\cdot}10^{-03}$
^{228}Pu		$2.42{\cdot}10^{-03}$

11. Data Analysis for Target-Like Nuclei

The aim of the analysis was to compare the two experiments (^{70}Zn+^{238}U) with a beam energy of 460 MeV and (^{136}Xe+^{238}U) with a beam energy of 926 MeV and to determine which measurement yields the best results to populate neutron-rich nuclei in the actinide region. A crucial question is, how the measurements are affected by the indirect identification of the reaction products by a spectrometer like PRISMA.

11.1. Selection of Z

Already from the selection of the atomic number Z, an impression about the response in PRISMA and the quality of the data is gained. Z is determined graphically with the analysis of the two-dimensional plot of released energy in the ionisation chamber (IC) versus the range of the beam-like particles in the IC (see section 9.3-2). These plots are shown in figure 11.1 for the data of the (^{70}Zn+^{238}U) experiment and in figure 11.2 for the (^{136}Xe+^{238}U) experiment. The main difference between the two experiments is the number of selectable elements. With a beam of ^{136}Xe ($Z = 54$) reaction products with isotopes of $Z < 54$ as well as $Z > 54$ are observed, implying proton-stripping as well as proton-pickup reactions. With the ^{70}Zn beam ($Z = 30$) only ejectiles with $Z \leq 30$ are populated with reasonable statistics. The pickup channels $Z > 30$ are disfavoured.

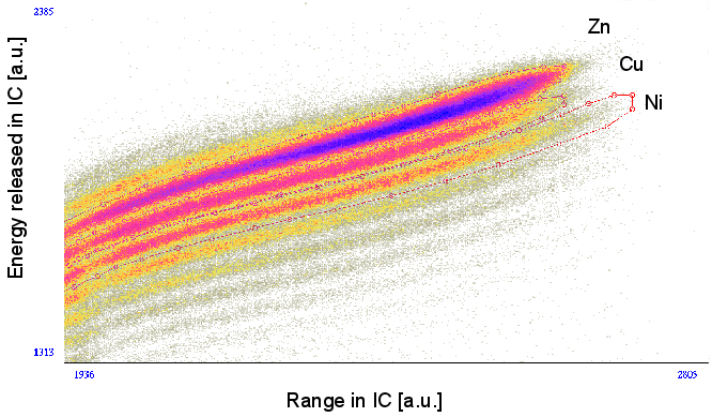

Figure 11.1.: *Distribution of released energy in the IC versus the range of the ions in the IC for the (^{70}Zn +^{238} U) experiment, with logarithmic numbers of entries (provided by J.J. Valiente Dobon). Polygon gates for Zn, Cu and Ni are set.*

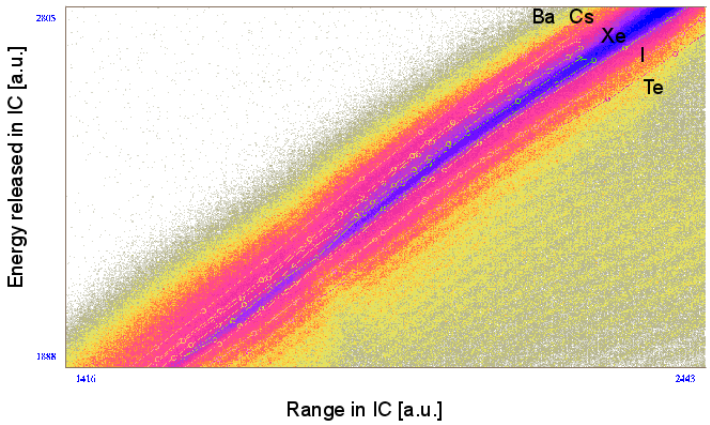

Figure 11.2.: *Distribution of released energy in the IC versus the range of the ions in the IC for the ($^{136}Xe + ^{238}$ U) experiment, with logarithmic numbers of entries (provided by F. Recchia). Polygon gates for Ba, Cs, Xe, I and Te are set.*

Table 11.1.: *Selection of Z from figures 11.1 and 11.2*

analyzed Z in the IC (^{70}Zn + ^{238} U) exp.	(^{136}Xe + ^{238} U) exp.	p-transfer channel (related to beam)	corresponding Z in the actinide region
$_{30}$Zn	$_{54}$Xe	elastic	$_{92}$U
$_{29}$Cu	$_{53}$I	1p-stripping	$_{93}$Np
$_{28}$Ni	$_{52}$Te	2p-stripping	$_{94}$Pu
	$_{55}$Cs	1p-pickup	$_{91}$Pa
	$_{56}$Ba	2p-pickup	$_{90}$Th

For the (^{70}Zn+^{238}U) experiment three different gates in Z, Zn ($Z = 30$), Cu ($Z = 29$) and Ni ($Z = 28$), are set. In the (^{136}Xe+^{238}U) experiments five different gates for Z, Xe ($Z = 54$), I ($Z = 53$), Te ($Z = 52$), Cs ($Z = 55$) and Ba ($Z = 56$) are used with proper statistics. Assuming the ideal case of kinematic coincidences, when the nucleons which are stripped by one reaction partner are picked up by the second reaction partner, the reaction channels lead to the target-like nuclei U ($Z = 92$), Np ($Z = 93$) and Pu ($Z = 94$) in the (^{70}Zn+^{238}U) experiment and to U ($Z = 92$), Np ($Z = 93$), Pu ($Z = 94$), Pa ($Z = 91$) and Th ($Z = 90$) in the case of the (^{136}Xe + ^{238} U) experiment. Table 11.1 summarizes the IC selected elements and the expected corresponding elements in the actinide region.

11.2. Mass Distributions

With the procedure described in section 9.3-4 the mass spectra of the beam-like nuclei are generated. Figures 11.3 and 11.4 show the mass distributions for the (^{70}Zn +^{238} U) experiment and for the (^{136}Xe +^{238} U) experiment. Due to the selection of Z, see section 11.1, in the case of the (^{70}Zn +^{238} U) experiment three mass spectra for Z=28 to Z=30 are determined. For the (^{136}Xe +^{238} U) experiment five mass spectra for Z=52 to Z=56 are produced.

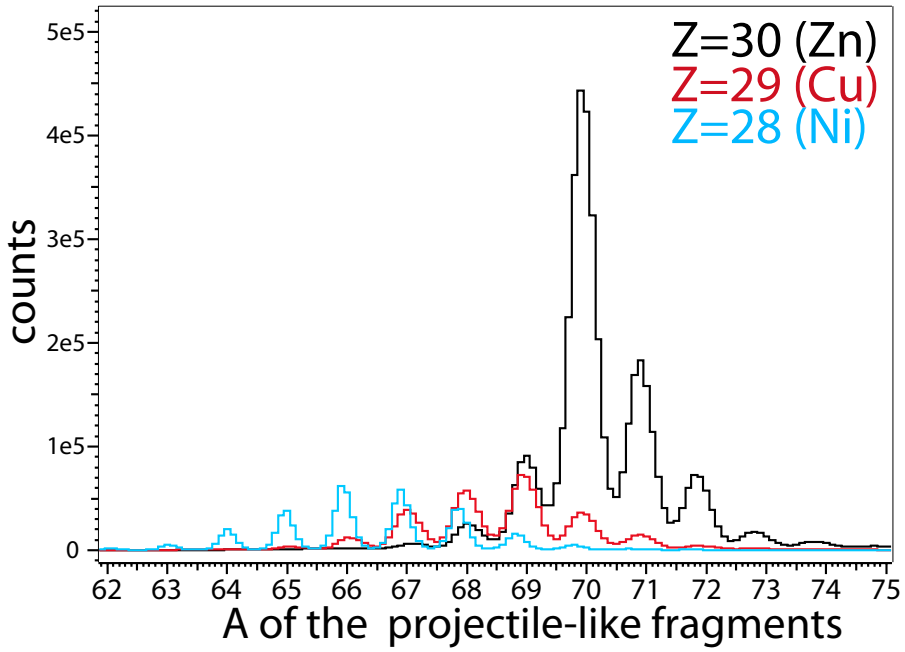

Figure 11.3.: *Mass distributions for $Z = 28 - 30$, from the (^{70}Zn+^{238}U) experiment*

The mass distributions show the following characteristics:

Intensity

Table 11.2 lists the intensities of the mass distributions shown in figures 11.3 and 11.4. There is - corresponding to the duration of the beam time and the thickness of the targets - more statistics in the resulting mass spectrum of the (^{70}Zn+^{238}U) experiment than of the (^{136}Xe+^{238}U) experiment. The beam particles ^{70}Zn and ^{136}Xe occur in the mass distributions with the highest intensities respectively. The intensity of the ^{70}Zn mass peak is about 6.9 times higher in than the intensity of the ^{136}Xe mass peak. The relative intensities of the mass peaks from the other nuclei are determined with respect to the intensity of the beam-mass peaks. Figure 11.5 shows parts of the chart of nuclides in the regions around the employed beams. The beam nuclei are colored in black. The relative intensities are illustrated in steps of grey color due to the RGB-color code.
In the case of kinematic coincidences a population of the corresponding target-like

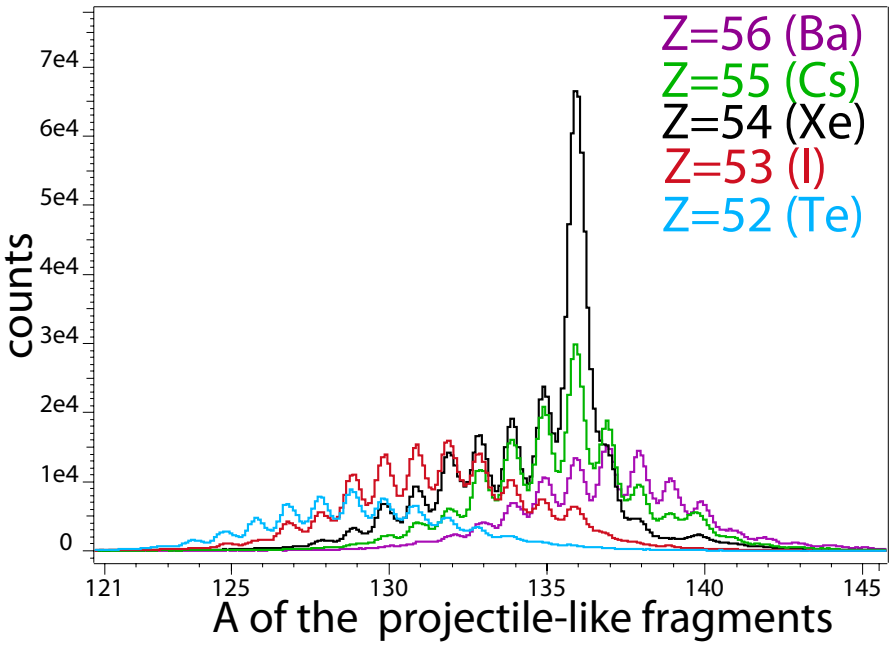

Figure 11.4.: *Mass distributions for $Z = 52 - 56$, from the (^{136}Xe+^{238}U) experiment*

nuclei is expected as it is shown in figure 11.6: The area of nuclei bordered by red color shows the - in the ideal case- possible population in the (^{70}Zn+^{238}U) experiment, the area bordered in blue marks the possible population of actinides in the (^{136}Xe+^{238}U) experiment. Both areas cover nuclei, which are still unknown and which are labeled in grey in figure 11.6. The cross section calculations in section 10.2 predict the limits for the population of very neutron-rich actinides. However, the successful analysis of the two-neutron-evaporation channel of the (^{70}Zn+^{238}U) experiment, see section 11.4-1, will show, that neutron-rich nuclei very close to the region of still unknown nuclei are populated.

Table 11.2.: *Intensities and relative intensities of the mass distributions in figures 11.3 and 11.4.*

(^{70}Zn+^{238}U) experiment			(^{136}Xe+^{238}U) experiment		
mass A	intensity I	relative I	mass A	intensity I	relative I
Z=28			**Z=52**		
61	1532 (140)	0,08%	123	536 (143)	0,16%
62	4787 (135)	0,24%	124	3287 (361)	0,99%
63	16809 (215)	0,85%	125	7902 (708)	2,39%
64	62162 (327)	3,14%	126	12914 (950)	3,91%
65	123632 (423)	6,24%	127	18607 (677)	5,63%
66	209356 (547)	10,57%	128	20067 (1095)	6,07%
67	191549 (516)	9,67%	129	25469 (1497)	7,71%
68	139918 (491)	7,06%	130	18088 (1129)	5,47%
69	52846 (531)	2,67%	131	15235 (1140)	4,61%
70	15417 (281)	0,78%	132	8404 (744)	2,54%
71	4033 (401)	0,20%	133	4597 (519)	1,39%
			134	3497 (1244)	1,06%
Z=29			**Z=53**		
64	2747 (678)	0,14%	125	2364 (378)	0,72%
65	13068 (430)	0,66%	126	1783 (753)	0,54%
66	47642 (564)	2,40%	127	12374 (690)	3,74%
67	165993 (970)	8,38%	128	9725 (729)	2,94%
68	234828 (1191)	11,85%	129	34116 (1139)	10,32%
69	331916 (1671)	16,76%	130	37533 (902)	11,36%
70	151915 (1365)	7,67%	131	41314 (1831)	12,50%
71	59707 (1185)	3,01%	132	41470 (1388)	12,55%
72	11045 (420)	0,56%	133	31276 (1482)	9,46%
73	3807 (751)	0,19%	134	20766 (942)	6,28%
			135	13172 (1328)	3,99%
			136	17220 (1000)	5,21%
Z=30			**Z=54**		
67	15679 (649)	0,79%	128	7559 (5594)	2,29%
68	90940 (1137)	4,59%	129	6956 (689)	2,10%
69	307861 (2979)	15,54%	130	19968 (864)	6,04%
70	**1980972(3117)**	**100,00%**	131	28121 (1513)	8,51%
71	753053 (3343)	38,01%	132	38461 (1217)	11,64%
72	310212 (3291)	15,66%	133	41583 (1437)	12,58%
73	61599 (1376)	3,11%	134	50278 (963)	15,21%
74	26927 (1495)	1,36%	135	52018 (1349)	15,74%
			136	**330532(1735)**	**100,00%**

Table 11.2.: *Intensities and relative intensities of the mass distributions in figures 11.3 and 11.4.*

(^{70}Zn+^{238}U) experiment			(^{136}Xe+^{238}U) experiment		
mass A	intensity I	relative I	mass A	intensity I	relative I
			Z=55		
			129	904 (446)	0,27%
			130	3639 (466)	1,10%
			131	10036 (90)	3,04%
			132	10791 (704)	3,26%
			133	35612 (1812)	10,77%
			134	47204 (1244)	14,28%
			135	57202 (1146)	17,31%
			136	103147 (1580)	31,21%
			137	50939 (1496)	15,41%
			138	19884 (1150)	6,02%
			139	4392 (573)	1,33%
			140	3560 (727)	1,08%
			141	2538 (553)	0,77%
			142	386 (173)	0,12%
			Z=56		
			131	1085 (237)	0,33%
			132	6070 (3405)	1,84%
			133	17819 (6529)	5,39%
			134	17341 (1110)	5,25%
			135	30344 (1193)	9,18%
			136	38558 (1213)	11,67%
			137	45844 (1342)	13,87%
			138	41643 (1515)	12,60%
			139	23885 (1354)	7,23%
			140	18141 (1631)	5,49%
			141	5211 (1111)	1,58%
			142	4411 (1424)	1,33%
			143	3244 (1329)	0,98%
			144	2644 (834)	0,80%

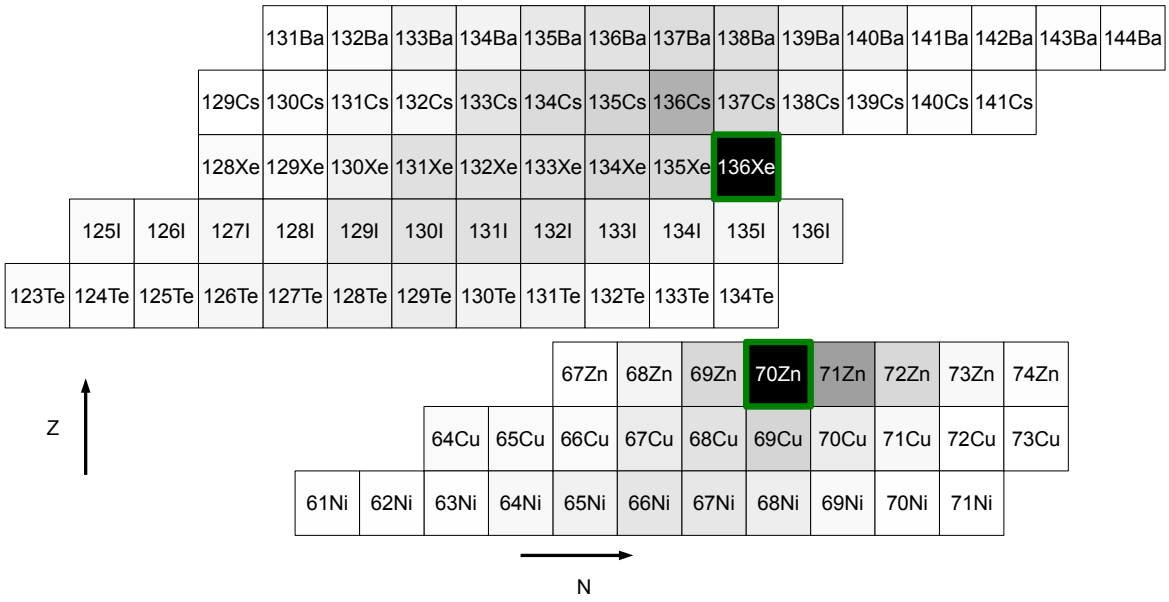

Figure 11.5.: *Excerpts of the chart of nuclides around the employed beam nuclei* ^{70}Zn *and* ^{136}Xe *in black colour. The relative intensities, related to the intensity of the beam-mass peaks, are illustrated in steps of grey color.*

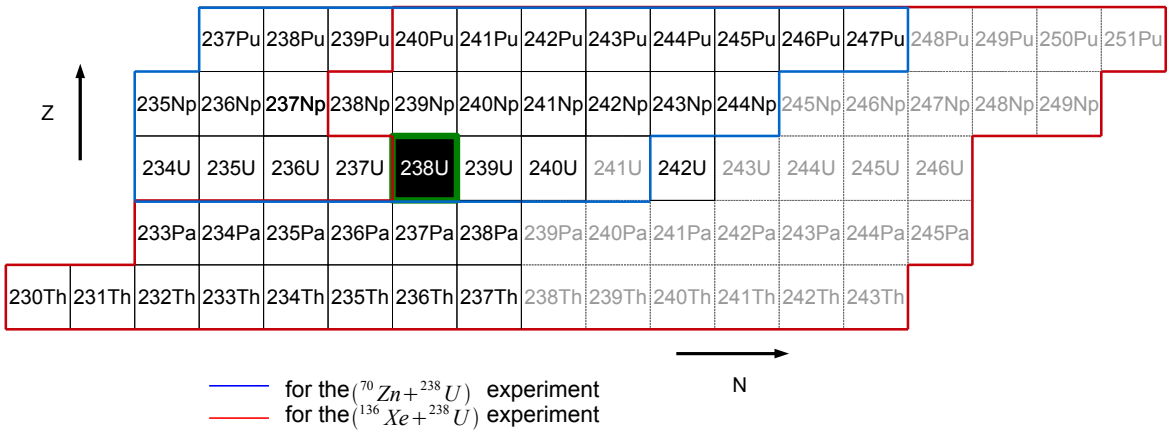

Figure 11.6.: *Regions in the chart of nuclides for the corresponding actinide nuclei, which are supposed to be populated in case of kinematic coincidences; bordered with blue color for the* ($^{70}Zn+^{238}U$) *experiment, surrounded by a red line for the* ($^{136}Xe+^{238}U$) *experiment. Unknown nuclei are labeled in grey.*

Upper mass limit of detected isotopes

In transfer reactions it is expected that the lighter projectile tends to strip protons and to pick up some neutrons, as discussed in section 7.2. In the (^{70}Zn+^{238}U) experiment this tendency is confirmed. In the mass distribution for $Z = 30$ nuclei heavier than the beam up to ^{74}Zn are found, coming from neutron-pickup reactions. The same is true for the Cu isotopes ($Z = 29$), where the isotopes heavier than ^{69}Cu up to ^{73}Cu are observed and for the Ni isotopes ($Z = 28$), where nuclei heavier than ^{68}Ni, i.e. ^{71}Ni, are detected. In the (^{136}Xe+^{238}U) experiment the tendency to pick up neutrons only occurs to a limited extent: In the mass distribution of the Xe isotopes there is no distinctive mass peak for nuclei heavier than the beam. In the mass spectrum of Z=53 neutron pickup occurs because nuclei heavier than ^{135}I, i.e. ^{136}I, are detected. The mass distribution of the Te spectrum is limited by ^{134}Te. Hence, the neutron-pickup reactions are strongly suppressed.
Striking is the evidence for the proton-pickup channels (Cs, Ba), because these reaction channels usually are expected to be populated only weakly. Neutron pickup occurs is indicated by the fact that Cs isotopes heavier than ^{137}Cs (up to ^{141}Cs) and also heavier than ^{138}Ba (even up to ^{144}Ba) are found.
All the pickup reactions of the beam-like nuclei in both experiments indicate that stripping reactions from the target and a transfer reaction to the projectile have taken place. Otherwise nuclei, which are heavier than the beam, could not have been populated. Further insights will be gained by the analysis of the γ spectra in section 11.

Resolution in mass

As an indicator for the quality of the mass spectra the relative mass resolutions in figures 11.3 and 11.4 for both experiments are determined. Table 11.3 lists the masses m with the full-width-at-half maximum (FWHM) and $\frac{m}{\Delta m}$ for $Z = 28$ to $Z = 30$ for the (^{70}Zn+^{238}U) experiment and for $Z = 52$ to $Z = 56$ for the (^{136}Xe+^{238}U) experiment. Because of the differing errors of $\frac{m}{\Delta m}$, the weighted averages of $\frac{m}{\Delta m}$ are calculated and shown in figure 11.7. The relative mass resolutions for the (^{70}Zn+^{238}U) experiment between are $\frac{m}{\Delta m} = 134.18 \pm 0.09$ and $\frac{m}{\Delta m} = 160.72 \pm 0.04$. For the (^{136}Xe+^{238}U) experiment they range from $\frac{m}{\Delta m} = 202.03 \pm 0.17$ to $\frac{m}{\Delta m} = 284.79 \pm 0.28$. These are reasonable values in comparison with the specification of PRISMA with $\frac{m}{\Delta m} = 300$ [6]. Although PRISMA works at its limits with a ^{136}Xe beam, the relative resolution is remarkably good.

Table 11.3.: *Relative mass resolution obtained for the (^{70}Zn+^{238}U) experiment and the (^{136}Xe+^{238}U) experiment*

(^{70}Zn+^{238}U) experiment			(^{136}Xe+^{238}U) experiment		
m (channel)	Δ m (FWHM) (channel)	$\frac{m}{\Delta m}$	m (channel)	Δ m (FWHM) (channel)	$\frac{m}{\Delta m}$
Z=28			**Z=52**		
61.16 (1)	0.39 (3)	155 (11)	122.98 (26)	0.35 (7)	351 (74)
62.08 (3)	0.33 (8)	186(5)	123.98 (12)	0.47 (4)	259 (21)
63.04 (1)	0.31 (4)	202(2)	124.97 (87)	0.54 (3)	231(14)
64.00 (1)	0.31 (2)	205.4 (9)	125.99 (7)	0.49 (2)	255 (12
64.97 (1)	0.31 (1)	206.4(6)	127.01 (4)	0.49 (1)	258 (7)
65.94 (1)	0.32 (1)	204.3 (5)	128.01 (5)	0.48 (2)	265 (9)
66.90 (1)	0.32 (1)	205.1(5)	129.01 (5)	0.52 (2)	249 (9)
67.86 (1)	0.33 (1)	202.6(7)	130.04 (6)	0.52 (2)	251(10)
68.82 (1)	0.33 (2)	204 (1)	131.03(7)	0.53 (3)	250 (12)
69.78 (2)	0.34 (5)	205(3)	132.05 (9)	0.49 (3)	271 (16)
70.74 (9)	0.44 (3)	162(10)	133.03 (11)	0.43 (4)	308 (25)
			133.99 (32)	0.59 (11)	227 (42)
weighted $\varnothing(\frac{m}{\Delta m})$= 160.72 ± 0.04			weighted $\varnothing(\frac{m}{\Delta m})$=264.99 ± 0.16		
Z=29			**Z=53**		
64.18 (2)	0.49(7)	129 (19)	125.06 (2)	0.50 (5)	249 (26)
65.08 (4)	0.44(1)	149 (4)	126.02 (3)	0.48 (12)	263 (66)
66.04 (2)	0.42(4)	154 (1)	127.00 (6)	0.55 (2)	232 (9)
67.01 (8)	0.45(2)	149 (1)	128.02 (7)	0.42 (2)	303 (15)
67.97 (7)	0.44(2)	153 (1)	129.04 (4)	0.52 (1)	249 (5)
68.95 (6)	0.47(2)	146 (1)	130.05 (3)	0.49 (1)	263 (5)
69.93 (10)	0.46(3)	149 (1)	131.06 (4)	0.51 (1)	257 (7)
70.90 (2)	0.48(6)	146 (2)	132.08 (3)	0.51 (1)	259 (6)
71.90 (4)	0.43(13)	165 (5)	133.07 (4)	0.48 (2)	277 (8)
72.89 (2)	0.52(6)	140 (16)	134.08 (5)	0.48 (2)	279 (9)
			135.07 (8)	0.46 (3)	295 (18)
			136.10 (6)	0.56 (2)	241 (9)
weighted $\varnothing(\frac{m}{\Delta m})$= 134.18 ± 0.09			weighted $\varnothing(\frac{m}{\Delta m})$=261.78 ± 0.14		
Z=30			**Z=54**		
67.07 (4)	0.42 (1)	162 (5)	127.93 (4)	0.65 (17)	197 (51)
68.01 (1)	0.42 (4)	162 (1)	128.95 (1)	0.45 (3)	285 (21)
68.97 (1)	0.41 (3)	168 (1)	129.94 (2)	0.50 (2)	260 (8)
69.93 (1)	0.45 (1)	155 (1)	130.96 (5)	0.52 (2)	252 (8)
70.99 (1)	0.45 (1)	156 (1)	131.99 (3)	0.51 (1)	261 (6)
71.85 (1)	0.47 (3)	153 (1)	132.97 (3)	0.47 (1)	284 (7)
72.92 (2)	0.47 (7)	154 (2)	133.99 (2)	0.45 (7)	298 (4)

Table 11.3.: *Relative mass resolution obtained for the (^{70}Zn+^{238}U) experiment and the (^{136}Xe+^{238}U) experiment*

(^{70}Zn+^{238}U) experiment			(^{136}Xe+^{238}U) experiment		
m (channel)	Δ m (FWHM) (channel)	$\frac{m}{\Delta m}$	m (channel)	Δ m (FWHM) (channel)	$\frac{m}{\Delta m}$
74.00 (5)	0.52 (2)	143 (5)	134.99 (2)	0.43 (8)	312 (6)
			136.04 (1)	0.59 (3)	232 (1)
weighted ∅($\frac{m}{\Delta m}$)= 150.39 ± 0.02			weighted ∅($\frac{m}{\Delta m}$)=202.03 ± 0.18		
			Z=55		
			129.08 (3)	0.44 (14)	293 (93)
			129.99 (1)	0.48 (4)	269 (24)
			130.99 (5)	0.55 (3)	240 (14)
			131.99 (3)	0.47 (2)	280 (13)
			132.98 (4)	0.52 (2)	254 (8)
			133.99 (3)	0.50 (9)	267 (5)
			134.99 (2)	0.47 (7)	287 (4)
			136.00 (2)	0.50 (6)	271 (3)
			137.02 (3)	0.49 (1)	279 (5)
			138.04 (5)	0.48 (2)	290 (11)
			138.98 (1)	0.37 (4)	377 (36)
			139.85 (1)	0.65 (5)	215 (15)
			140.99 (5)	0.60 (19)	
			142.17 (5)	0.38 (14)	235 (74)
			weighted ∅($\frac{m}{\Delta m}$)=284.79 ± 0.29		
			Z=56		
			131.09 (2)	0.35 (6)	380 (64)
			132.11 (3)	0.65 (17)	203 (53)
			133.03 (2)	0.79 (13)	168 (28)
			134.02 (2)	0.54 (2)	250 (10)
			135.02 (4)	0.52 (1)	259 (7)
			136.03 (3)	0.51 (1)	269 (6)
			137.02 (3)	0.52 (1)	266 (5)
			138.02 (4)	0.51 (1)	271 (6)
			139.03 (5)	0.49 (2)	283 (10)
			140.02 (7)	0.54 (3)	259 (13)
			141.06 (3)	0.56 (12)	252 (54)
			142.06 (2)	0.61 (11)	233 (42)
			143.09 (13)	0.77 (8)	186 (19)
			144.11 (3)	0.60 (15)	240(60)
			weighted ∅($\frac{m}{\Delta m}$)=221.16 ± 0.33		

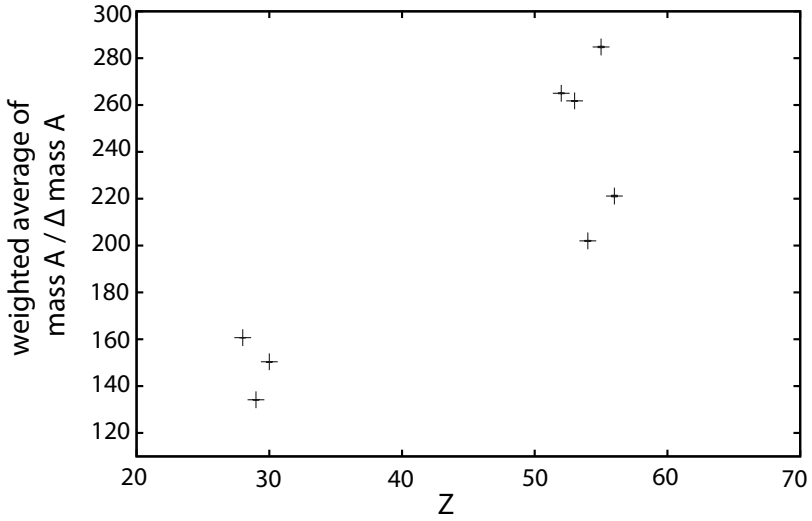

Figure 11.7.: *Weighted averages of $\frac{m}{\Delta m}$ for the different Z values. Around Z=30 for the mass spectra from the (^{70}Zn+^{238}U) experiment, around Z=54 from the (^{136}Xe+^{238}U) experiment.*

11.3. Analysis Conditions for Background Suppression

The PRISMA spectrometer provides information on the beam-like nuclei, in particular the trajectory, the time-of-flight (the velocity respectively), the energy loss ΔE and the total deposited energy E_{IC} in the ionisation chamber, the atomic number Z, the charge state q and the mass A. Based on the information on the particle-like nuclei conclusions about the target-like nuclei need to be drawn. By selecting the atomic number Z and the mass A, see section 11.2, the isotopes of interest are extracted assuming kinematic coincidences. This means the ideal case, when all stripped nucleons in a reaction are transferred onto the reaction partner. But in addition the evaporation of nucleons is possible. Consequently, the selection of the mass or Z of the beam-like particle does not lead to the corresponding target-like reaction channel. Thus, an analysis condition is helpful to suppress the evaporation channel sufficiently.
The evaporation of nucleons requires the separation energy. Hence, for high excitation energies after MNT the probability for nucleon evaporation increases. However, gating on small excitation energies suppresses the nucleon evaporation channel in the analysis. In both experiments U is used as target material, which becomes unstable against fission at excitation energies above the fission barrier. A high background is caused by fission fragments. Gating on small excitation energies also suppresses the fission reaction channels.
The excitation energy is a selective quantity to find the reaction channels of kinematic coincidences. But the excitation energy after MNT cannot exactly be determined from the values coming from PRISMA, because this requires the knowledge about the energies or the masses of all particles before and after the reaction. The numbers and the energies of the evaporated nucleons are not measured.
However, there are different possibilities to obtain a gating condition which is related to the excitation energy: An equivalent quantity is the time-of-flight (TOF) of the beam-like particles [89]. The higher the velocity of a beam-like particle in PRISMA, the less energy has been transferred in the reaction. Beam-like particles originating from reactions of kinematic coincidences have on average a higher velocity than those deriving from reactions including nucleon evaporation.

Also the energy difference between the initial beam energy and the energy of the beam-like particles measured in the IC is a good indicator for the reaction. This energy difference (less the energy loss in material) is equivalent to the lower energy limit of the Q value. This energy difference is named 'ε'. ε is given in arbitrary units because the deposited energy in the IC is calibrated only relatively.

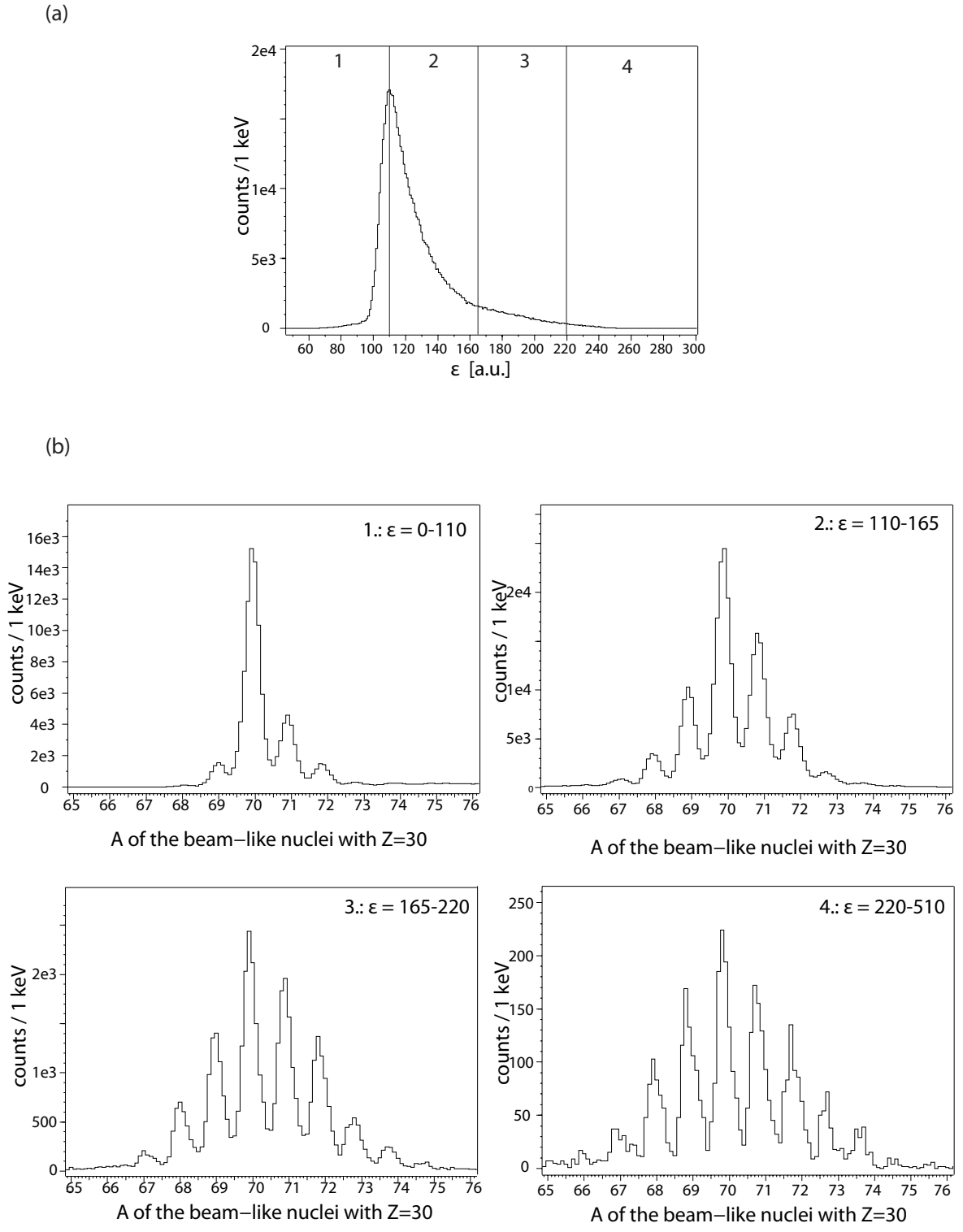

Figure 11.8.: *(a) ε spectrum with Z=30 for the data of the (^{70}Zn+^{238}U) experiment; the spectrum is divided in 4 sections, which are used to generate the mass distributions in (b).*

Figure 11.8 (a) shows an example for an ε spectrum for the (^{70}Zn+^{238}U) experiment for Z=30. In figure 11.8 (b) the effect of ε gating on the mass spectra is demonstrated. By gating on 4 different regions in the ε spectrum, marked with the lines in figure 11.8, the mass distributions vary significantly. For high ε the mass distribution is broad and more isotopes appear. This indicates the evaporation of neutrons.
The effect of ε gating on the γ spectra is shown as well. Figure 11.9 contains an ε spectrum for a gate on ^{68}Zn. This is the two-neutron-transfer channel of the (^{70}Zn+^{238}U) reaction. The corresponding target-like nucleus is ^{240}U.

The effect of the three different ε gates on the γ-singles spectra for ^{68}Zn, Doppler corrected for the target-like nuclei, are shown in figure 11.10. A gate on high ε only contributes to the background in the γ spectrum (for ε >200 in magenta). The peak-to-total ratio improves using low energetic ε gates (for ε=140-200 in green and ε <140 in black).

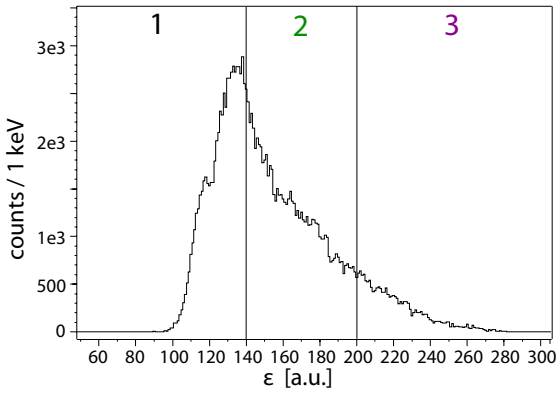

Figure 11.9.: *ε spectrum for the gate on ^{68}Zn. 3 different gating regions are marked for 1. ε <140, 2. ε=140-200 and 3. ε >200.*

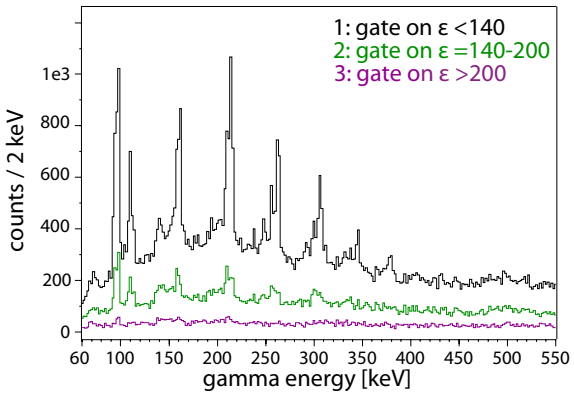

Figure 11.10.: *γ-singles spectra for the gate on ^{68}Zn, Doppler corrected for the target-like nuclei. The γ spectra are obtained from the three different gates in the ε spectrum in figure 11.9.*

In conclusion, ε emerges as a useful gating condition to obtain the reaction channels of interest. It is applied for the analysis of the γ spectra in section 11.4. Each γ spectrum in section 11.4 is gated on small values of ε.

11.4. Analysis of the γ Spectra

For the investigation of the γ spectra of the target-like reaction products, the PRISMA information about the corresponding beam-like nuclei is used. Kinematic coincidences are assumed, meaning that, nucleons which are stripped / picked up by the beam are supposed to be picked up / stripped by the target. For example, by detecting ^{68}Zn, the two-neutron-stripping channel of the ^{70}Zn beam, ^{240}U is expected, the two-neutron-pickup channel of the target. In this way the γ spectra, Doppler corrected for the target-like nuclei, are gated on the data of the beam-like particles including gates on (i) the atomic number Z, see section 11.1, (ii) the mass, see section 11.2, and (iii) low values of ε, see section 11.3. For the Doppler correction, the velocity vectors of the target-like fragments are determined using two-body kinematics. The γ spectra are obtained by the GASP Data Analysis Program Package [5] and displayed with the program TV [95].

11.4-1. Analysis of Uranium Spectra

The γ transitions in the U isotopes ^{237}U, ^{238}U and ^{239}U are well known [73]. The investigation of γ spectra for the respective mass gates of these isotopes grants the possibility to survey the reliability of the analytical procedure.

Elastic-Reaction Channel: ^{238}U

The γ spectrum for the gate on ^{70}Zn is analyzed with a Doppler correction for the target-like nuclei. The most dominant γ rays originate from the Coulomb excitation of the target material ^{238}U. Figure 11.11 shows the highly excited ground-state rotational band of ^{238}U in blue for the (^{70}Zn+^{238}U) experiment and in red for the data of the (^{136}Xe+^{238}U) experiment. The second spectrum is multiplied by a factor of 4.8 in order to normalize both spectra to the same background level in the region of the X-rays and γ rays of low energies. The transition energies and intensities from both experiments and also from reference [73] are listed in table 11.4. It is obvious that the target is higher excited with the heavier ^{136}Xe beam than with the ^{70}Zn beam: In the (^{70}Zn+^{238}U) experiment the excitation to the 20^+ state is visible, the γ-γ spectrum shows coincidences up to the 18^+ level. For the data of the (^{136}Xe+^{238}U) experiment the γ-ray energies in the singles and the coincidence spectrum are observed up to the 22^+ state.
In both reactions the energies of the first negative-parity band are only assumed in the background and cannot unambiguously be distinguished from transitions of ^{74}Ge(n,n') reactions. However, it is demonstrated that a Doppler correction for the target-like nuclei provide γ spectra of the ground-state rotational band of ^{238}U .

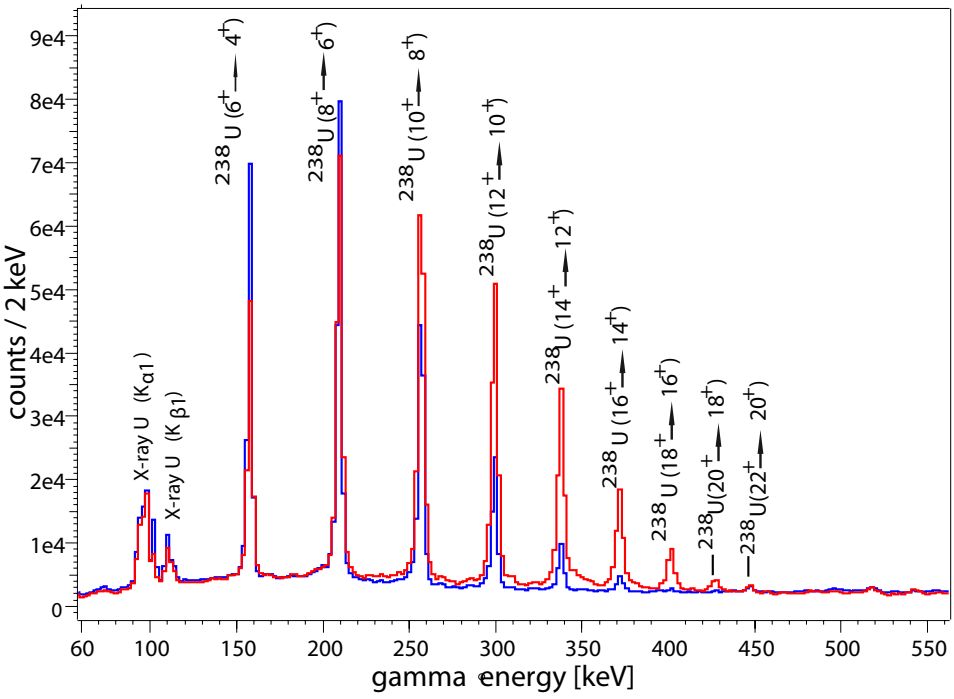

Figure 11.11.: *^{238}U -singles spectra, without background subtraction, in blue for data of the (^{70}Zn+^{238}U) experiment and in red for the (^{136}Xe+^{238}U) experiment. In the second case the intensity is multiplied with a factor 4.8 in order to normalize the low-energy part of the two spectra.*

Table 11.4.: *Doppler corrected γ-ray energies and intensities for the target-like products and observed transitions for the gate on ^{70}Zn and ^{136}Xe, which correspond to the ^{238}U-reaction channel. Additionally, the transitions from reference [73] are listed for comparison.*

(^{70}Zn+^{238}U) exp.		(^{136}Xe+^{238}U) exp.		literature [73]	
γ energy (keV)	I	γ energy (keV)	I*4.8	γ energy (keV)	transition ($J_{init} \rightarrow J_{fin}$)
158.8(8)	96877(356)	157.8(6)	71871(708)	158.80(3)	$6^+ \rightarrow 4^+$
210.6(5)	131971(393)	209.5(5)	127648(933)	211.0(3)	$8^+ \rightarrow 6^+$
257.8(4)	88946(329)	256.8(6)	129719(968)	257.8(4)	$10^+ \rightarrow 8^+$
300.5(4)	38905(252)	299.5(4)	102795(848)	300.6(9)	$12^+ \rightarrow 10^+$
338.8(4)	12516(224)	337.8(5)	65341(724	338.8 (4)	$14^+ \rightarrow 12^+$
373.2(6)	4651(180)	371.8(7)	32781(630)	372.9(13)	$16^+ \rightarrow 14^+$
403.3(6)	712(151)	401.5(7)	14375(498)	402.6 (4)	$18^+ \rightarrow 16^+$
427.7(5)	401(224)	427.0(7)	4375(631)	427.9 (4)	$20^+ \rightarrow 18^+$
		447.3(8)	2181(608)	448.9(4)	$22^+ \rightarrow 20^+$

One-Neutron-Pickup Channel: ^{237}U

For the one-neutron-pickup channels (related to the beam) the population of ^{237}U is expected assuming kinematic coincidences.
Figure 11.12 shows the γ-singles spectra with a gate on ^{71}Zn for the (^{70}Zn+^{238}U) experiment.

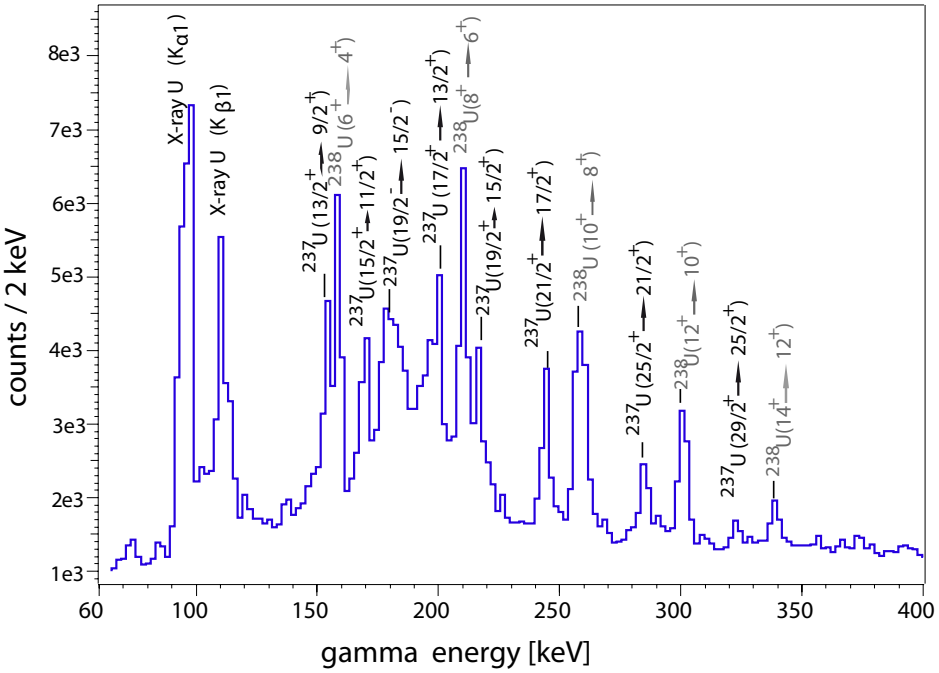

Figure 11.12.: *^{237}U-singles spectra for data of the the (^{70}Zn+^{238}U) experiment. Transitions of the ground-state rotational band of ^{238}U are labeled in grey.*

A strong contribution from the excitation of the target, ^{238}U, up to the 14^+ state of the ground-state rotational band is visible. The transitions of ^{238}U are labeled in grey. Besides these transitions the ground-state rotational band of ^{237}U is observed. This band consists of two signature partner bands.

Figure 11.13 contains the γ spectrum of the band with signature $\alpha = \frac{1}{2}$. It is generated by adding the coincidence spectra, gated on the energies 155 keV, 201 keV, 245 keV and 286 keV. This band is verified up to the $\frac{29}{2}^+$ state. The 180 keV-peak derives from the $\frac{19}{2}^- \rightarrow \frac{15}{2}^-$ transition in the negative parity band, which decays into the ground-state band, see reference [108]. The second signature partner band with $\alpha = -\frac{1}{2}$ is verified by coincidence gating up to the $\frac{19}{2}^+$ state.
Table 11.5 lists the determined energies, intensities and transitions of ^{237}U for the singles spectrum.

In the (^{136}Xe+^{238}U) experiment for the gate on ^{137}Xe and in the case of kinematic coincidences the population of ^{237}U is expected. As explained in section 11.2, there is no distinct peak for A=137 in the mass distribution for Xe isotopes. The γ-singles spectrum shown in figure 11.14 is obtained by gating into the right edge of the ^{136}Xe

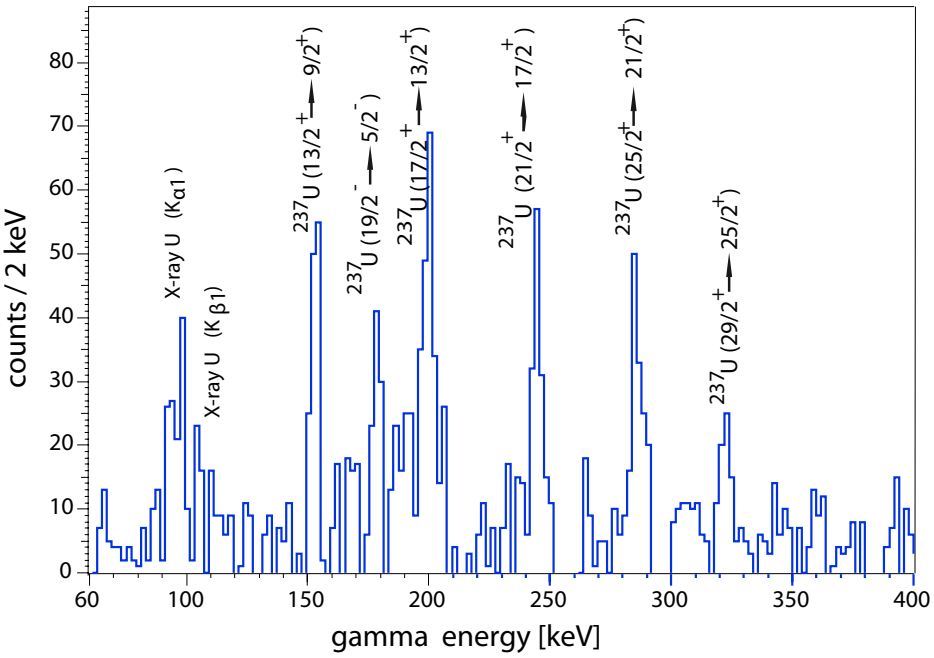

Figure 11.13.: *Signature partner band with $\alpha = -\frac{1}{2}$ of the ground-state rotational band of ^{237}U produced with addition of the gated spectra at the energies 155 keV, 201 keV, 245 keV and 286 keV.*

mass peak. The influence of ^{238}U in the singles spectrum in figure is strong. For this data-set γ-γ spectra are not significant due to low statistics. Transitions cannot be verified by coincidence gating. However, comparing the energies in figure 11.14 to those of figure 11.12 same transitions are found. The energies and intensities of these transitions are also listed in table 11.5.
The GRAZING calculations, see section 10.2, predict comparable cross sections for the population of ^{237}U in both experiments. With $\sigma \approx 249$ mbarn for the (^{70}Zn+^{238}U) experiment the cross section is slightly higher than $\sigma \approx 233$ mbarn for the (^{136}Xe+^{238}U) experiment. Also regarding the Q values for the one-neutron-pickup channel, section 10.1, the population of ^{237} is favoured in the (^{70}Zn+^{238}U) reaction.

With the investigation of the γ spectra of the one-neutron-pickup channel the successful accomplishment of the analysis procedure is demonstrated: Gating on the beam-like particles in PRISMA also selects the kinematically coincident target-like reaction channels in the γ spectra.

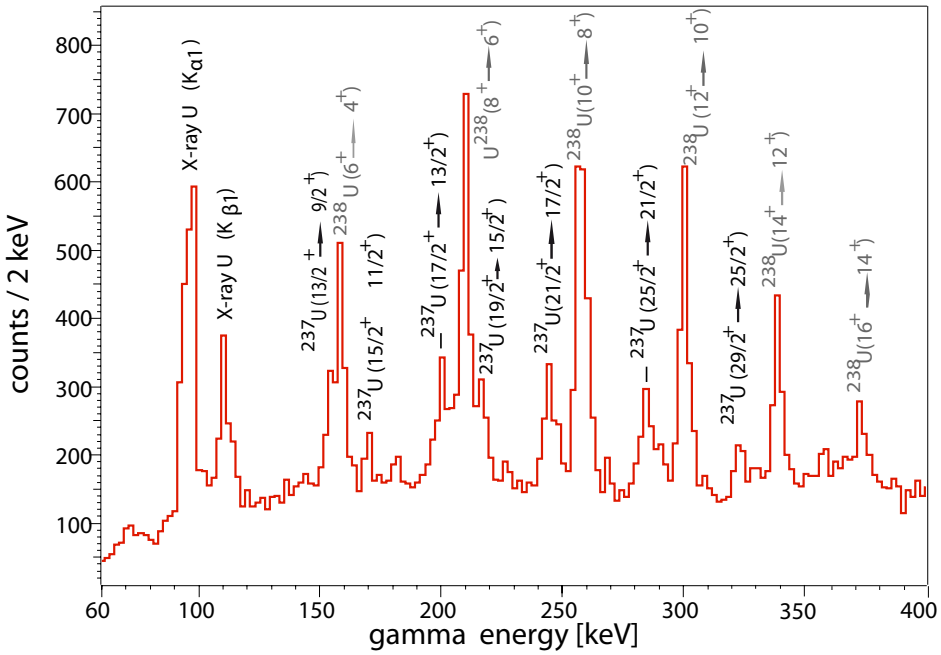

Figure 11.14.: *^{237}U-singles spectra in red for the (^{136}Xe+^{238}U) experiment. Transitions of the ground-state rotational band of ^{238}U are labeled in grey.*

Table 11.5.: *Observed energies and transitions of the ground-state band of ^{237}U in the γ-singles spectrum of figures 11.12 and 11.14.*

(^{70}Zn+^{238}U) exp.		(^{136}Xe+^{238}U) exp.		literature [73]	
γ energy (keV)	I	γ energy (keV)	I	γ energy (keV)	transition ($J_{init} \rightarrow J_{fin}$)
first signature partner band with $\alpha = \frac{1}{2}$					
154.6(5)	3943(126)	153.6(8)	361(36)	155	$\frac{13}{2}^+ \rightarrow \frac{9}{2}^+$
200.4(4)	2928(133)	200.3(8)	613(37)	201	$\frac{17}{2}^+ \rightarrow \frac{13}{2}^+$
244.9(6)	3402(130)	244.1(5)	450(73)	245	$\frac{21}{2}^+ \rightarrow \frac{17}{2}^+$
285.4(6)	1513(134)	284.3(4)	484(107)	286	$\frac{25}{2}^+ \rightarrow \frac{21}{2}^+$
322.5(7)	643(103)	322.7(5)	140(42)	322	$\frac{29}{2}^+ \rightarrow \frac{25}{2}^+$
second signature partner band with $\alpha = -\frac{1}{2}$					
170.5(5)	2622(139)	169.6(5)	339(57)	171	$\frac{15}{2}^+ \rightarrow \frac{11}{2}^+$
218.4(7)	2576(121)	216.2(7)	454(37)	217	$\frac{19}{2}^+ \rightarrow \frac{15}{2}^+$
negative parity band, see reference [108]					
180(1)	9976(1009)			181	$\frac{19}{2}^- \rightarrow \frac{15}{2}^-$

One-Neutron-Transfer Channel: ^{239}U

The same analysis as for the one-neutron-pickup channel (related to the beam), see section 11.4-1, is performed for the one-neutron-stripping channel with the aim to demonstrate the feasibility of the analysis procedure.
The corresponding target-like particle for the one-neutron-stripping channels, with the beam-like fragments ^{69}Zn and ^{135}Xe, is ^{239}U. Figure 11.15 shows the resulting γ-singles spectra for the (^{70}Zn+^{238}U) experiment with a gate on ^{69}Z in blue and for the (^{136}Xe+^{238}U) experiment with a gate on ^{135}Xe in red. The intensity of the γ spectrum of the (^{136}Xe+^{238}U) experiment is multiplied with a factor 2.8 to normalize the low-energy part of both spectra.

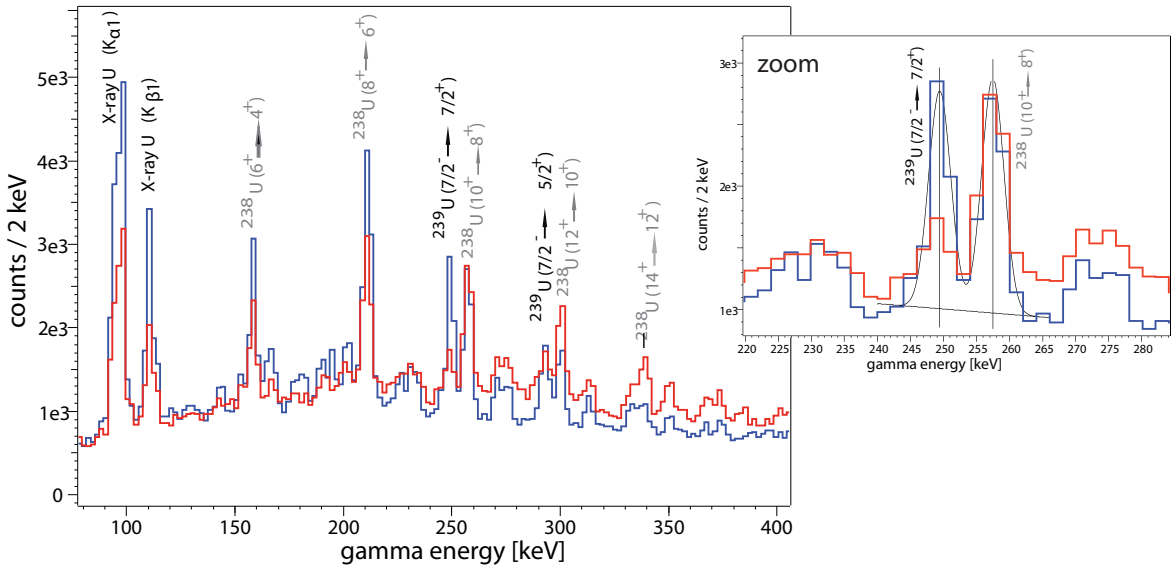

Figure 11.15.: *^{239}U-singles spectra, without background subtraction in blue for data of the (^{70}Zn+^{238}U) experiment and in red for data of the (^{136}Xe+^{238}U) experiment. The intensity of the second spectrum is multiplied with a factor 2.8 to normalize the low energy part of the two spectra. A zoom into the spectrum demonstrates the population of ^{239}U at the transition ($\frac{7}{2}^- \rightarrow \frac{7}{2}^+$) in comparison to the population of ^{238}U with the ($10^+ \rightarrow 8^+$) transition.*

The identification of γ rays from ^{239}U is difficult. ^{239}U as an even-odd nucleus is characterized by a multi-band structure with low-energetic transitions. Most intra-band transitions are expected in the X-ray region or at energies higher than 500 keV where the peak-to-total ratio in the spectra is very low. The only transitions which are a hint for ^{239}U are the transition $\frac{7}{2}^- \rightarrow \frac{7}{2}^+$ at an energy of 250.072(5) keV and the $\frac{7}{2}^- \rightarrow \frac{5}{2}^+$ transition at an energy of 292.587(2) keV [73], see also reference [51]. The striking difference between the spectra from the two experiments is the contamination by ^{238}U, which is detected up to the 14^+ state for these mass gates. Comparing the ($\frac{7}{2}^- \rightarrow \frac{7}{2}^+$) transition of ^{239}U to the ($10^+ \rightarrow 8^+$) transition of ^{238}U in the (^{70}Zn+^{238}U) experiment a ratio of 0.93 is calculated. In the spectrum from the (^{136}Xe+^{238}U) experiment the

Table 11.6.: *Energies and intensities of the two identified ^{239}U transitions. To investigate the influence of ^{238}U the intensity of the $(10^+ \rightarrow 8^+)$ transition in ^{238}U is compared to the intensity of the $(\frac{7}{2}^- \rightarrow \frac{7}{2}^+)$ transition in ^{239}U.*

(^{70}Zn+^{238}U) exp.		(^{136}Xe+^{238}U) exp.		literature [73]	
γ energy (keV)	I	γ energy (keV)	I*2.8	γ energy (keV)	transition ($J_{init} \rightarrow J_{fin}$)
250.4(8)	3721(107)	249.7(8)	1156(175)	250.072 (5)	^{239}U ($\frac{7}{2}^- \rightarrow \frac{7}{2}^+$)
292.4(9)	2249(83)	292.4(6)	862(55)	292.587(2)	^{239}U($\frac{7}{2}^- \rightarrow \frac{5}{2}^+$)
257.2(6)	4009(112)	257.3(7)	3855(244)	257.8 (4)	^{238}U ($10^+ \rightarrow 8^+$)

ratio is 0.29. The contamination of ^{238}U in ^{239}U data is in the (^{136}Xe+^{238}U) experiment about three times higher than in the (^{70}Zn+^{238}U) experiment.

There are two explanations for this effect: The first is the resolution in the mass distributions, figures 11.3 and 11.4. The mass peaks in figure 11.4 show an overlap between the isotopes. The expected contribution of the neighbouring isotopes in the mass gates of the (^{136}Xe+^{238}U) experiment is higher than the mass gates of the (^{70}Zn+^{238}U) experiment. The second possibility for the strong population of ^{238}U in this mass gate is the evaporation of neutrons. For the case that the neutron, which is stripped off the beam, is not transferred onto the target, the gates on ^{69}Zn and ^{135}Xe do not relate to ^{239}U but to ^{238}U.

The calculations of the cross sections in section 10.2 consider the evaporation of neutrons. However, the predicted cross sections for ^{239}U after nucleon evaporation is predicted to be two times higher in the (^{136}Xe+^{238}U) experiment ($\sigma_{^{239}U} \approx 185$ mbarn) than in the (^{70}Zn+^{238}U) experiment ($\sigma_{^{239}U} \approx 99$ mbarn). Also the Q value is higher in the (^{136}Xe+^{238}U) reaction than in (^{70}Zn+^{238}U) reaction. Thus, the predictions, including neutron evaporation, expect a higher population of ^{239}U for the (^{136}Xe+^{238}U) experiment. The ratio of the contribution of ^{239}U to the contribution of ^{238}U in these γ spectra is supposed to be better in the (^{136}Xe+^{238}U) experiment. Following the calculations leads to the conclusion that the contamination of ^{238}U is not caused by neutron evaporation but by other effects like for example the resolution in the mass distributions.

Two-Neutron-Transfer Channel: ^{240}U

For the gate on the two-neutron-stripping channel ^{68}Zn and ^{134}Xe respectively, corresponding to the ^{240}U-reaction channel of the target-like particle, the quality of the γ spectra between the two experiments differs a lot. Figure 11.16 shows the singles spectra of ^{240}U for both cases. The analysis of the gate on ^{68}Zn, corresponding to ^{240}U from

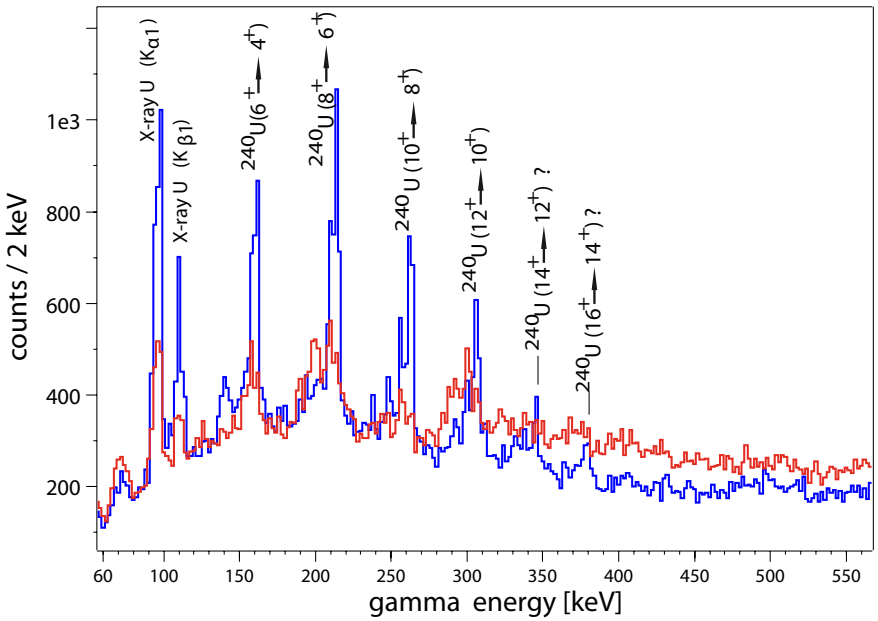

Figure 11.16.: *^{240}U-singles spectra in blue for data of the the (^{70}Zn+^{238}U) experiment and in red for the (^{136}Xe+^{238}U) experiment. The intensities of both spectra are very similar.*

the (^{70}Zn+^{238}U) experiment, is very successful: The known transitions of ^{240}U up to the 12^+ state are identified. Already in the γ-singles spectrum two new transitions at 345 keV and 380 keV are seen (compare figure 8.3).

Figure 11.17 shows the corresponding γ-γ spectrum. Besides the already observed peaks in the γ-singles spectrum another transition becomes visible at 407.9(13) keV. Furthermore a candidate for a fourth, new transition appears at 430.3(19) keV. The $4^+ \rightarrow 2^+$ and the $2^+ \rightarrow 0^+$ transitions at 105.6 keV and 45 keV [51, 4], are not observed. These decays occur via internal electron conversion. The high energy part from the γ-γ spectrum is shown in figure 11.18. The proposed transitions of Ishii et al. [52], see also figure 8.3 (b), for the negative parity band of ^{240}U are not observed.
Table 11.7 lists the γ energies and intensities from the γ-γ spectrum in figure 11.17. The known transitions and new transitions of ^{240}U are assigned to the observed γ energies.

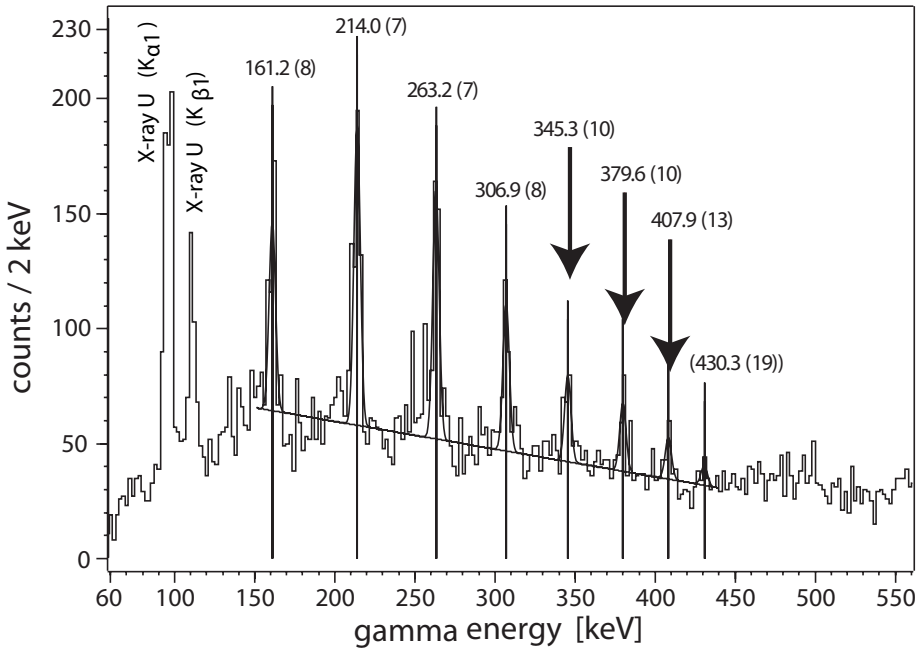

Figure 11.17.: *Projection of 2d-γ-γ spectrum for the mass gate on ^{68}Zn for the (^{70}Zn+^{238}U) experiment, Doppler corrected for the target-like nuclei. Three new transitions (marked with arrows) of the ground-state rotational band of ^{240}U are verified. A fourth peak at 430.3(19) keV is observed, but it cannot unambiguously be assigned by coincidence gating.*

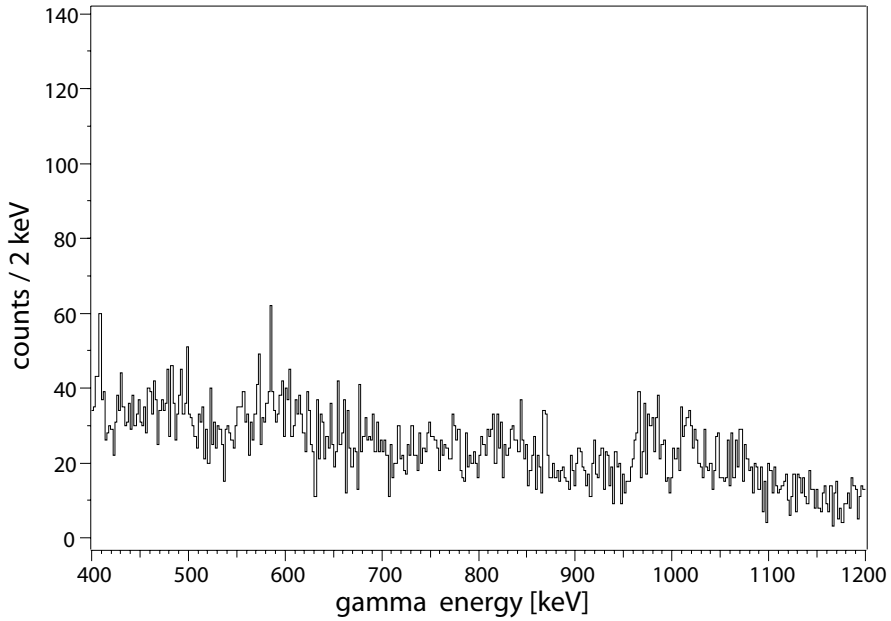

Figure 11.18.: *High-energy part of the spectrum in figure 11.17.*

Table 11.7.: *γ energies and intensities of the ^{240}U transitions in the γ-γ spectrum in figure 11.17.*

(^{70}Zn+^{238}U) exp. γ energy *(keV)*	intensity	transition *($J_{init} \rightarrow J_{fin}$)*
161.2(8)	205(23)	$6^+ \rightarrow 4^+$
214.0(7)	325(25)	$8^+ \rightarrow 6^+$
263.2(7)	272(23)	$10^+ \rightarrow 8^+$
306.9(8)	161(19)	$12^+ \rightarrow 10^+$
345.3(10)	94(16)	$14^+ \rightarrow 12^+$?
379.6(10)	74(15)	$16^+ \rightarrow 14^+$?
407.9(13)	45(14)	$18^+ \rightarrow 16^+$?
(430.3(19)	22(13)	$20^+ \rightarrow 18^+$?)

The transitions are proven to be members of the ground-state band by coincidence gating in the γ-γ spectrum. Figures 11.19 to 11.22 show the γ-γ spectra without background subtraction gated on known transitions of the ground-state rotational band [52]. The resulting spectrum for gating on the energy of 161 keV shows two distinct peaks (214 keV and 263 keV) and a high background which is due to a high Compton background. The gated spectra for the other known ground-state-band transitions in figures 11.20 to 11.22 from the 12^+ state to the 6^+ state show peaks around 345, 380 and 408 keV (with the exception of a 380-keV peak in figure 11.22). Moreover -the other way around- by gating on the unknown transitions at 345 keV, 380 keV and 408 keV, displayed in figures 11.23, 11.24 and 11.25, the already known ground-state band cascade, de-exciting to the 4^+-state, is observed (with exception of 307-keV peak in figure 11.24). The fourth peak at 430.3(19) keV is observed, but it cannot unambiguously be verified.

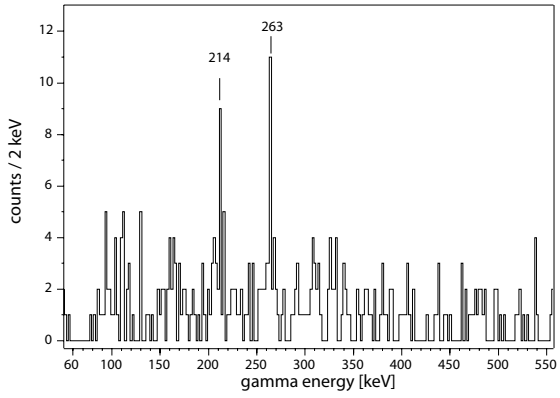

Figure 11.19.: *Coincidence spectrum for gate on the 161.2(8)-keV peak in the γ-γ spectrum of figure 11.17.*

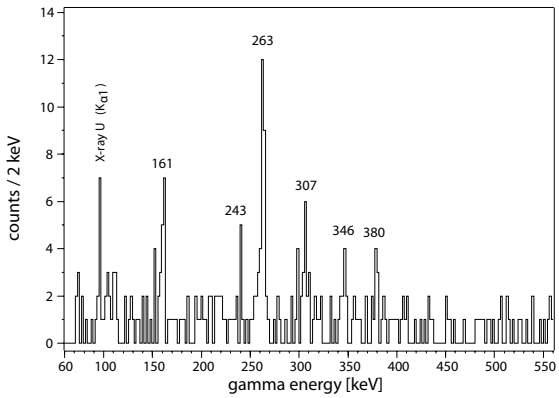

Figure 11.20.: *Coincidence spectrum for gate on the 214.0(7)-keV peak in the γ-γ spectrum of figure 11.17.*

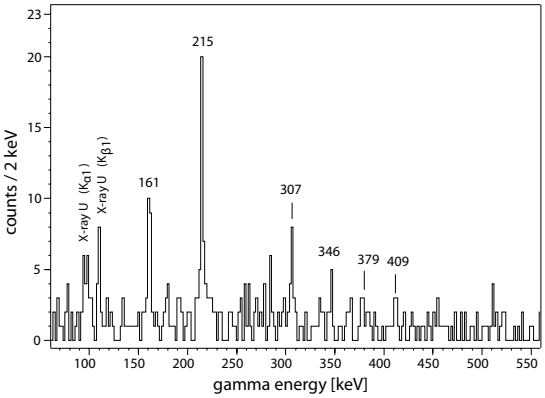

Figure 11.21.: *Coincidence spectrum for gate on the 263.2(7)-keV peak in the γ-γ spectrum of figure 11.17.*

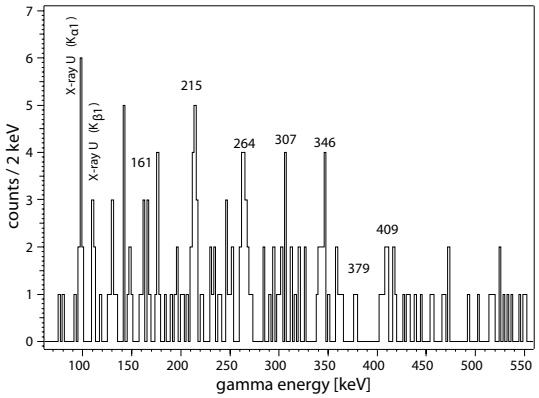

Figure 11.22.: *Coincidence spectrum for gate on the 306.9(8) keV-peak in the γ-γ spectrum of figure 11.17.*

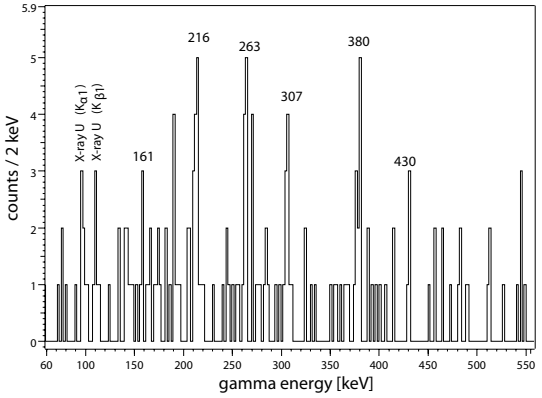

Figure 11.23.: *Coincidence spectrum for gate on the 345.3(10)-keV peak in the γ-γ spectrum of figure 11.17.*

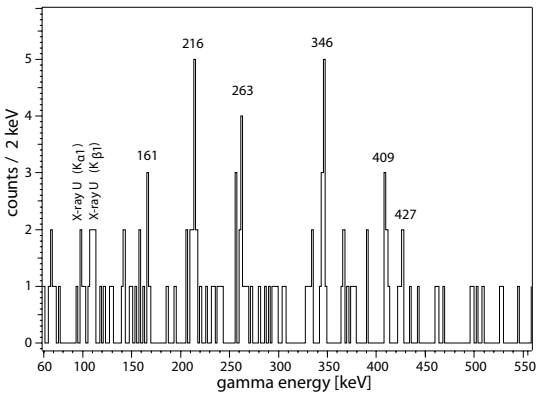

Figure 11.24.: *Coincidence spectrum for gate on the 379.6(10)-keV peak in the γ-γ spectrum of figure 11.17.*

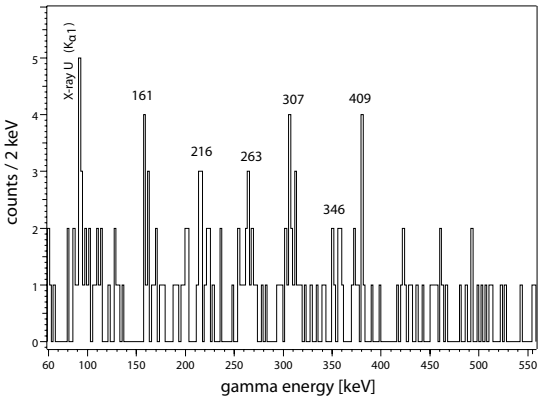

Figure 11.25.: *Coincidence spectrum for gate on the 407.9(19)-keV peak in the γ-γ spectrum of figure 11.17.*

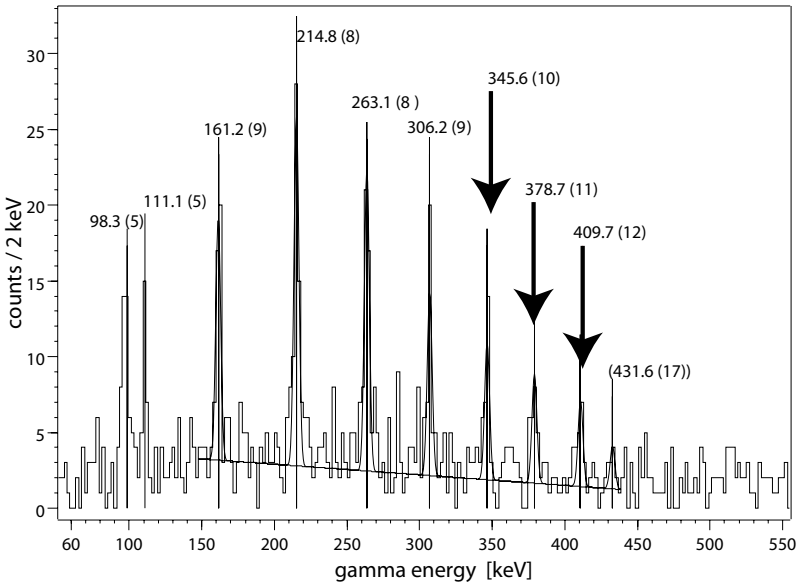

Figure 11.26.: *Sum of the coincidence spectra obtained by gating the 214 keV in figure 11.20 , 263 keV in figure 11.21 and 307 keV in figure 11.22. The new transitions are marked with arrows.*

Table 11.8.: γ *energies, intensities and transitions of the spectrum, shown in figure 11.26.*

observed γ energies *(keV)*	intensity	transition $(J_{init} \rightarrow J_{fin}$ *)*
161.2(9)	33.9(70)	$6^+ \rightarrow 4^+$
214.8(8)	48.8(78)	$8^+ \rightarrow 6^+$
263.1(8)	42.4(73)	$10^+ \rightarrow 8^+$
306.2(9)	25.5(58)	$12^+ \rightarrow 10^+$
345.6(10)	19.2(52)	$14^+ \rightarrow 12^+$
378.7(11)	15.3(46)	$16^+ \rightarrow 14^+$
409.7(12)	12.0(42)	$18^+ \rightarrow 16^+$
(431.6(17)	5.9(33)	$20^+ \rightarrow 18^+$)

The final spectrum in figure 11.26 contains the added γ spectra gated on the decay cascade of ^{240}U from the 12^+ state to 6^+ state. The spectrum shows the population of the ground-state rotational band of ^{240}U up to the 18^+. Table 11.8 contains the determined γ energies, intensities and assigned transitions. The new results on ^{240}U will be compared with theoretical predictions of Delaroche et al. [25] and Shneidman et al. [86] in chapter 12.

The γ spectrum of the (^{136}Xe+^{238}U) experiment, with a gate on ^{134}Xe, corresponding to ^{240}U, is dominated by the transition energies of the ground-state rotational band of ^{238}U. Even in the γ-singles spectrum the decays of ^{240}U are not visible. This is in contrast to the cross-section and Q-value calculations in section 10.2 and section 10.1. The predicted cross section for the population of ^{240}U is 4 times higher in the (^{136}Xe+^{238}U) experiment ($\sigma_{^{240}U} \approx$22 mbarn) than in the (^{70}Zn+^{238}U) experiment ($\sigma_{^{240}U} \approx$5 mbarn). Also the Q value is higher in the (^{136}Xe+^{238}U) reaction.

Conclusion of the Analysis of Uranium Isotopes

The investigation of the isotopic chain from ^{237}U to ^{240}U demonstrates the feasibility of the analysis procedure.

The γ spectra of the quasi-elastic reaction channel, with a Doppler correction for the target-like nuclei, see figure 11.11, show the ground-state rotational band of ^{238}U. Higher spins are observed for the (^{136}Xe+^{238}U) experiment than for the (^{70}Zn+^{238}U) experiment due to the heavier mass and higher Z of the beam.

Via the γ spectra of the one neutron-transfer channels, the population of ^{237}U and ^{239}U, respectively, is demonstrated. The investigation of ^{240}U data from the (^{70}Zn+^{238}U) experiment allows to discover three new transition energies up to the 18^+ state by coincidence gating. Furthermore a candidate for the ($20^+ \rightarrow 18^+$) transition in ^{240}U is found.
Investigations of ^{240}U have been very instructive, it suggests the analysis of the data for ^{241}U. However, the γ spectrum for the corresponding gates on ^{67}Zn and ^{133}Xe, only show the transitions of the ground-state rotational band from ^{238}U and a high background.

The γ spectra of the neutron-transfer channel of the (^{136}Xe+^{238}U) experiment are dominated by transitions of the ground-state rotational band of ^{238}U. The calculations in section 10.2 predict for the (^{136}Xe+^{238}U) experiment higher cross sections for the population of ^{239}U and ^{240}U than for the (^{70}Zn+^{238}U) experiment. The GRAZING calculation consider the evaporation of neutrons. With respect to these calculations the high contamination in the γ spectra by ^{238}U cannot be explained by neutron evaporation. It is interpreted as a consequence of the insufficient mass resolution, see figure 11.4.

11.4-2. Analysis of the Proton-Stripping Channel

One-Proton-Transfer Channel: Neptunium

The one-proton-stripping channels of the beam particles yield Cu isotopes in the (^{70}Zn+^{238}U) experiment and I isotopes in the (^{136}Xe+^{238}U) experiment. In kinematic coincidences these reaction channels are expected to populate Np isotopes as the target-like reaction products.

All Np spectra of the (^{70}Zn+^{238}U) experiment show clearly X-rays from Np ($K_{\alpha 1}$ at 101.059 keV, $K_{\alpha 2}$ at 97.069 keV and $K_{\beta 1}$ at 114.234 keV). Only the gates on the isotopes ^{67}Cu to ^{70}Cu provide γ-ray spectra for the target-like nuclei with enough statistics, compare figure 11.3. The two γ spectra gated on ^{67}Cu and ^{70}Cu, which correspond to $^{241-xn}$Np and $^{238-xn}$Np target-like isotopes, show the transitions of the ground-state rotational band of ^{238}U.
More interesting spectra are generated by gating on ^{68}Cu and ^{69}Cu, which correspond to the $^{240-xn}$Np and $^{239-xn}$Np reaction channels, see figures 11.27 and 11.28. Table 11.9 lists the energies and intensities of the observed peaks.

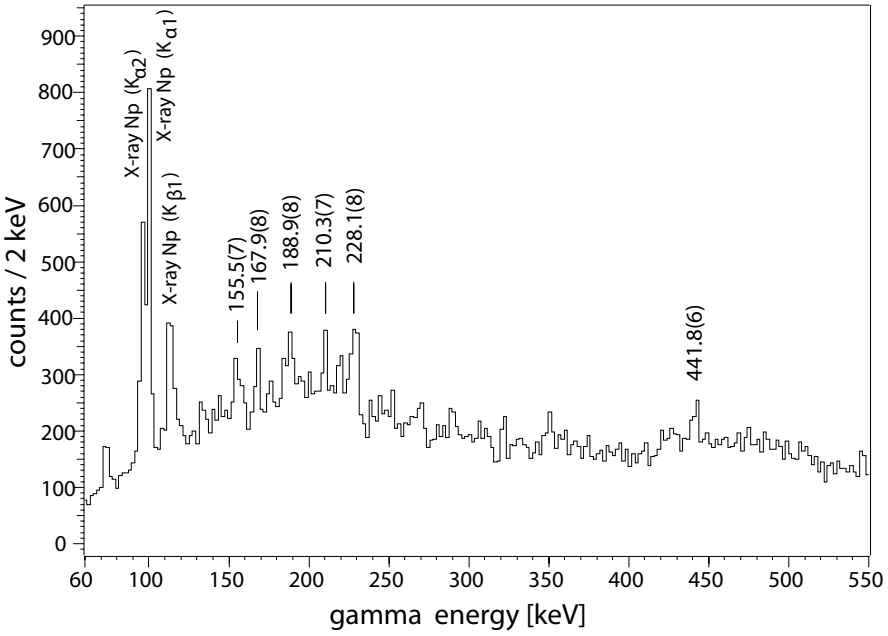

Figure 11.27.: *Singles-γ spectrum for ^{69}Cu Doppler corrected for target-like fragments, corresponding to $^{239-xn}$Np from the (^{70}Zn+^{238}U) experiment.*

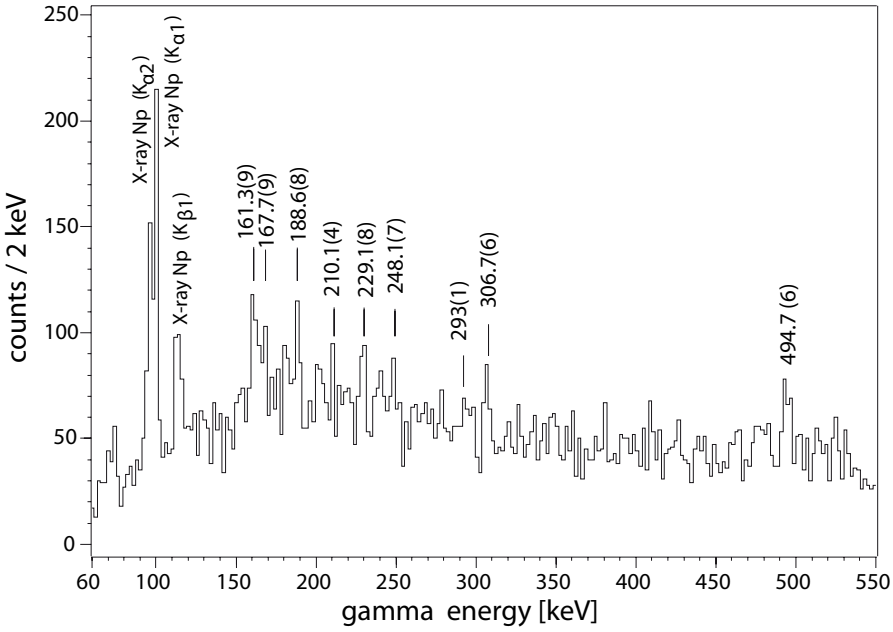

Figure 11.28.: *Singles-γ spectrum for ^{68}Cu Doppler corrected for target-like fragments, corresponding to $^{240-xn}$Np from the (^{70}Zn+^{238}U) experiment.*

The clear indication for peaks found in figures 11.27 and 11.28 cannot unambiguously be assigned to specific nuclei. The high background in the γ spectra does not allow coincidence gating in γ-γ matrices.
The grazing calculations, see section 10.2, predict for ^{239}Np the highest population in the isotopic chain. The level scheme of ^{239}Np is well known [73]. However the γ spectrum for $^{239-xn}$Np in figure 11.27 does not show these known transitions. Although the X-rays indicate the population of Np, the peaks cannot be assigned to any Np isotope. Coincidence gating is needed to understand the correlations between the found transitions.
Transitions in ^{240}Np are only known from the β^- decay of ^{240}U without any spin information [73]. In the γ spectrum for the gate on $^{240-xn}$Np in figure 11.28 four transitions are in agreement with transitions in ^{240}Np. Again coincidence gating is needed to gain unambiguous results.
In both spectra also contributions from U is possible. Peaks (at 161 keV and 210 keV respectively) around the typical energies of the ground-state rotational band of even-even U isotopes are observed. The analysis of this proton-stripping channel demonstrates the necessity to suppress the high background. In section 13 the realization of background suppression in a future experiment is discussed.

Table 11.9.: *Observed γ-ray energies and intensities in the γ-singles spectrum with gates on ^{68}Cu and ^{69}Cu, which correspond to $^{240-xn}$ and $^{239-xn}Np$ isotopes, from the (^{70}Zn+^{238}U) experiment. The transitions cannot unambiguously be identified, possible de-excitations are listed.*

(^{70}Zn+^{238}U) exp.		literature [73]	
γ energy (keV)	I	possible transition ($J_{init} \rightarrow J_{fin}$)	γ energy (keV)
gate on ^{69}Cu ($^{239-xn}$Np)			
155.5(7)	252(44)		
167.9(8)	241(35)		
188.9(8)	699(84)		
210.3(7)	546(70)	^{238}U ($8^+ \rightarrow 6+$)	211.0 (3)
228.1(8)	588(49)		
441.8(6)	142(37)		
gate on ^{68}Cu ($^{240-xn}$Np)			
161.3(9)	179(24)	^{238}U ($6^+ \rightarrow 4^+$)	158.8(3)
167.7(9)	119(21)	^{240}Np *	169.2 (1)
188.6(8)	80(19)	^{240}Np *	189.7(1)
210.1(4)	63(16)	^{238}U ($8^+ \rightarrow 6^+$) ^{240}Np *	211.0 (3) 212.3(5)
229.2(8)	147(21)		
248.2(7)	139(25)		
293(1)	84(25)	^{240}Np *	294.8 (3)
306.7(6)	80(17)		
494.7(6)	163(22)		

* see reference [73]:
originates from the β decay of ^{240}U, spins are not known

For the (^{136}Xe+^{238}U) experiment the γ spectra for each mass gate only show the transitions of the ground-state rotational band of ^{238}U. Neither γ-ray transitions deriving from Np nor Np X-rays are observed. The X-rays at 98 keV are identified as ^{238}U X-rays.

The GRAZING calculations predict for the population of Np isotopes for both experiments cross sections of the same order of magnitude, for example $\sigma_{^{239}Np}$ =63 mbarn and $\sigma_{^{240}Np}$ =9 mbarn in the (^{70}Zn+^{238}U) experiment and $\sigma_{^{239}Np}$ =55 mbarn and $\sigma_{^{240}Np}$ =12 mbarn in the (^{136}Xe+^{238}U) experiment.

The Q values of the transfer reactions with (^{136}Xe+^{238}U) leading to Np isotopes with $A \geq 239$ are higher than with (^{70}Zn+^{238}U) reactions. Due to this calculations comparable or even better results for the γ spectra for the (^{136}Xe+^{238}U) experiment are expected with respect to the (^{70}Zn+^{238}U) experiment. A possible explanation for the high contamination of ^{238}U in the γ spectra of the (^{136}Xe+^{238}U) experiment for the one-proton-stripping channel is the quality of the Z selection in figure 11.2. With

the heavy ^{136}Xe beam the PRISMA spectrometer reaches its limits. In the polygon gates for a specific Z in figure 11.2 contamination from neighbouring elements are visible.

Two-Proton-Transfer Channel: Plutonium

The gates on Ni and Te isotopes selects the two-proton-transfer channel. This corresponds to Pu isotopes for the target-like nuclei. All γ spectra for these gates, Doppler corrected for the target-like nuclei, do not show any peak structure, for the data of the (^{70}Zn+^{238}U) experiment and for the (^{136}Xe+^{238}U) experiment. No evidence for Pu is seen, although the calculations in section 10.2 predict for the population of Pu isotopes cross sections up to σ =10 mbarn.

11.4-3. Analysis of the Proton-Pickup Channels

As shown in figures 11.1 and 11.2, yield for the proton-pickup reactions of the beam-like particles is only available from the (^{136}Xe+^{238}U) experiment. The investigation of the expected Pa and Th spectra is therefore accomplished with the dataset of the (^{136}Xe+^{238}U) experiment.

One-Proton-Transfer Channel: Protactinium

The γ spectra for the target-like nuclei generated with a gate on Cs isotopes are supposed to contain data for Pa isotopes from one-proton-transfer channel. γ spectra for ^{133}Cs to ^{139}Cs are shown in figure 11.4 with a Doppler correction for the target-like nuclei. These gates correspond to target-like nuclei $^{236-xn}$Pa to $^{241-xn}$Pa.
In all γ spectra a strong contamination of ^{238}U is visible. The transition energies for the ground-state rotational band in ^{238}U are dominant. All spectra feature the same peak structure, as an example figure 11.29 shows the γ-singles spectrum for the mass $A = 135$ which is supposed to result in ^{239}Pa. However, the γ energies of the ground-state band of ^{238}U arise. It is interesting to observe that the dominant X-rays in all of the spectra for mass gates $A = 133$ to $A = 139$, see figure 11.30, are lower than the known X-ray energies of U (98.434 keV for the K_{α_1} X-rays and 111.298 keV for the K_{β_1} X-rays [29]). Table 11.10 lists the X-ray energies and intensities found in the γ spectra for gates on ^{133}Cs to ^{139}Cs. The X-rays around 95 keV and 108 keV are close to the X-ray energies of Pa which are 95.863 keV for K_{α_1} and 108.422 keV for K_{β_1} [29].

The GRAZING calculations in sections 10.2 predict for the population of Pa isotopes in the (^{136}Xe+^{238}U) experiment cross sections up to 22 mbarn. This is the same value as the predicted cross section for ^{240}U in the (^{70}Zn+^{238}U) experiment, where ^{240}U has

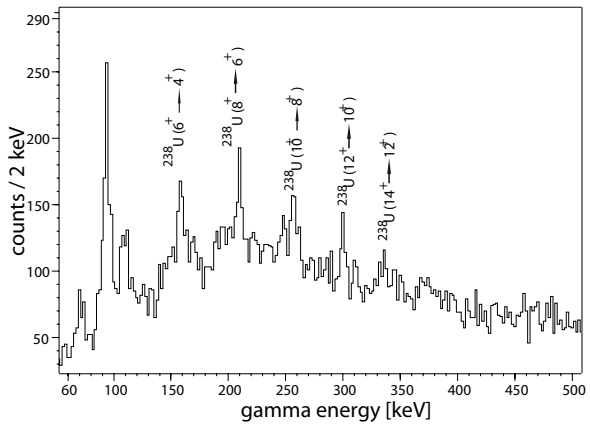

Figure 11.29.: *Singles γ spectrum for gate on ^{135}Cs, corresponding to ^{239}Pa, for the (^{136}Xe+^{238}U) experiment: ^{238}U energies are dominant*

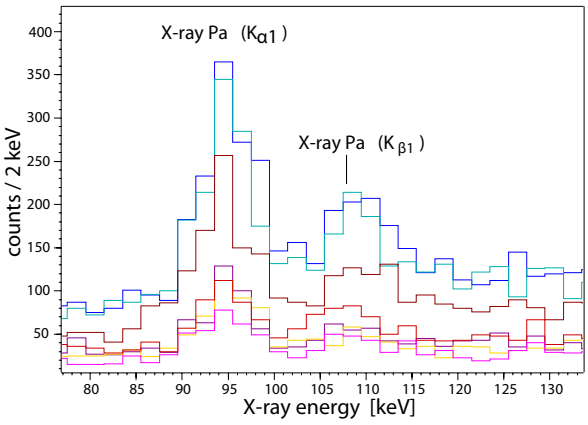

Figure 11.30.: *Singles-γ spectrum for gates on ^{133}Cs to ^{139}Cs, corresponding to $^{236-xn}$Pa to $^{241-xn}$Pa, for the (^{136}Xe+^{238}U) experiment; with zoom into the region of X-rays: typical X-rays of Pa occur*

Table 11.10.: *X-ray energies and intensities from the γ spectra gated on the beam-like fragments ^{133}Cs to ^{139}Cs, which correspond to the target-like nuclei $^{241-xn}Pa$ to $^{235-xn}Pa$. The X-ray energies of Pa are observed.*

beam-like nucleus	target-like nucleus	X-ray (K_α) energy(keV)	I	X-ray (K_β) energy(keV)	I
^{133}Cs	$^{241-xn}$Pa	94.7(8)	235(23)	107.4(8)	167(22)
^{134}Cs	$^{240-xn}$Pa	94.5(9)	200(28)	108.4(8)	87(27)
^{135}Cs	$^{239-xn}$Pa	94.3(8)	586(55)	109.4(8)	207(59)
^{136}Cs	$^{238-xn}$Pa	95.2(7)	872(62)	109.1(7)	382(65)
^{137}Cs	$^{237-xn}$Pa	94.8(8)	697(48)	108.6(6)	262(44)
^{138}Cs	$^{236-xn}$Pa	94.9(8)	231(24)	107.9(8)	63(20)
^{139}Cs	$^{235-xn}$Pa	95.2(7)	264(29)	108.8(9)	61(24)

been verified, see section 11.4-1.
These considerations lead to the conclusion that Pa has been populated. Pa isotopes are nuclei with odd Z. Odd-even or odd-odd nuclei are often characterized by a more complex decay scheme in comparison with even-even nuclei, see for example the γ spectrum of ^{239}U in figure 11.15. This may be another reason, why it is difficult to verify the detection of Pa isotopes. However, also the contamination by ^{238}U is high. A possible explanation for the observation of ^{238}U in the one-proton-pickup channel is also in this case the resolution in Z (figure 11.2) as it is already discussed for the one-proton-stripping channel in section 11.4-2.

Two-Proton-Transfer Channel: Thorium

The mass distribution for Z=56 in figure 11.4 shows a population of beam-like ejectiles for Ba isotopes between $A = 131$ and $A = 144$. The γ spectra for the gates on ^{134}Ba and ^{140}Ba contain enough statistics for an analysis corresponding to Th isotopes between ^{235}Th and ^{240}Th as target-like nuclei.
All Th γ spectra are characterized by a similar peak structure and a high, unresolved background level. As an example for the quality of the spectra figure 11.31 shows the γ-singles spectrum for the gate on ^{138}Ba, which corresponds to $^{236-xn}$Th for the target-like nuclei. ^{236}Th is the heaviest Th isotope for which experimental data of γ-ray transitions have been available, see reference [52]. For Th isotopes with $A > 236$ only the ground state is known.

In table 11.11 an overview of the observed γ energies and intensities in the different spectra for gates on ^{134}Ba to ^{139}Ba are given.

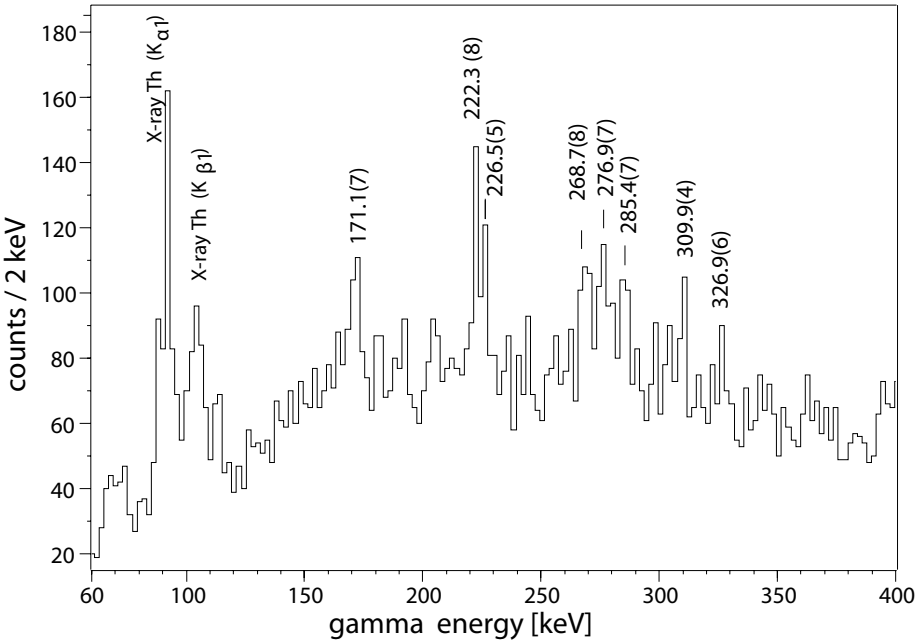

Figure 11.31.: *Singles-γ spectrum for ^{138}Ba, Doppler corrected for target-like fragments, corresponding to $^{236-xn}Th$, from the (^{136}Xe+^{238}U) experiment.*

Table 11.11.: *Observed energies in the γ-singles spectrum with gates on Ba isotopes, which correspond to Th isotopes, Doppler corrected for target-like nuclei.*

$^{235-xn}$Th		$^{236-xn}$Th		$^{237-xn}$Th		
γ energies *(keV)*	I	γ energies *(keV)*	I	γ energies *(keV)*	I	possible assignment
-	-	171.1(7)	135(27)	170.1(4)	131(23)	even Th($6^+ \rightarrow 4^+$)
-	-	222.3(8)	125(20)	222.5(6)	118(26)	even Th($8^+ \rightarrow 6^+$)
226.6(6)	48(20)	226.5(5)	84(18)	-		even Th($8^+ \rightarrow 6^+$)
-	-	268.7(8)	140(23)	266.0(8)	446(57)	even Th($10^+ \rightarrow 8^+$)
-	-	276.9(7)	147(24)	-		even Th($10^+ \rightarrow 8^+$)
-	-	285.4(7)	114(22)	-	-	
-	-	309.9(4)	66(16)	-		even Th($12^+ \rightarrow 10^+$)
-	-	326.9(6)	44(16)	-	-	
$^{238-xn}$Th		$^{239-xn}$Th		$^{240-xn}$Th		
γ energies	I	γ energies	I	γ energies	I	possible assignment
170.2(6)	65(13)	170(1)	26(12)	171.5(6)	31(14)	even Th($6^+ \rightarrow 4^+$)
220.8(8)	27(18)	-	-	-	-	even Th($8^+ \rightarrow 6^+$)
227.3(7)	30(15)	226.7(9)	31(12)	223(1)	55(22)	even Th($8^+ \rightarrow 6^+$)
-	-	271(1)	6(4)	271(1)	56(30)	even Th($10^+ \rightarrow 8^+$)
312.3(9)	41(14)	-	-	-	-	even Th($12^+ \rightarrow 10^+$)

In order to increase statistics, the γ spectra of the different gates are added and pictured in figure 11.32. The yellow spectrum shows the γ-singles spectrum of ^{134,135}Ba, which

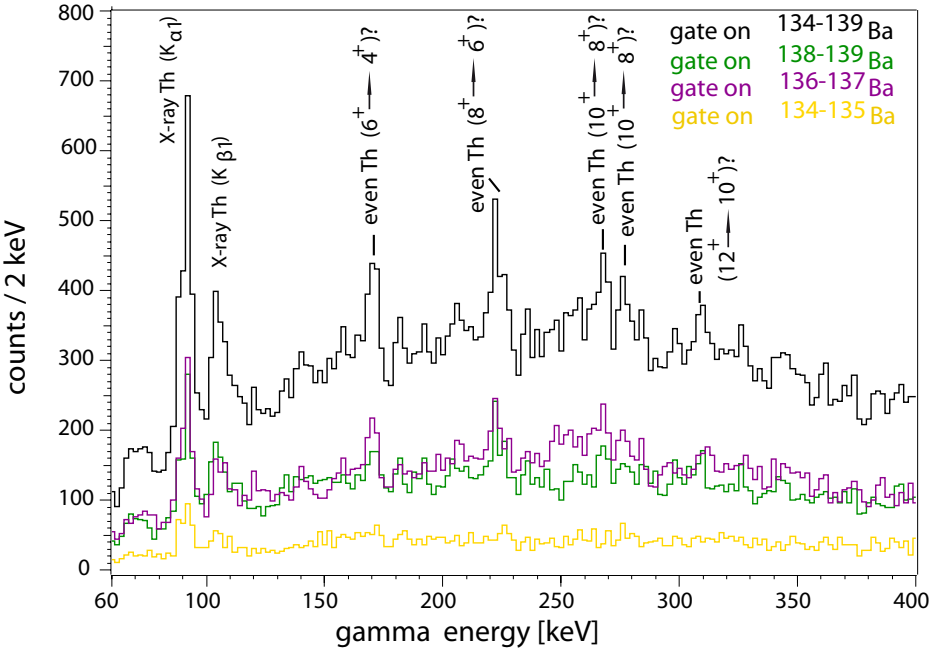

Figure 11.32.: *The yellow spectrum shows the γ-singles spectrum gated on ^{134,135}Ba, which corresponds to $^{240-xn,239-xn}$Th. The spectrum in magenta is produced by a gate on ^{136,137}Ba, corresponding to $^{238-xn,237-xn}$Th. The γ spectrum with gate on ^{138,139}Ba, corresponding to $^{236-xn,235-xn}$Th, is displayed in green. The resulting addition of the γ spectra for the three gates, in black, shows besides the strong Th X-rays candidates for transitions in the ground-state rotational band up to the 12^+ state of even-even Th isotopes.*

corresponds to $^{240-xn,239-xn}$Th. The spectrum in magenta contains the gate on ^{136,137}Ba, corresponding to $^{238-xn,237-xn}$Th. The spectrum gated on ^{138,139}Ba, corresponding to $^{236-xn,235-xn}$Th, is displayed in green colour. The resulting γ spectrum of all three gates, in black, includes the γ spectra of the isotopic chain from $^{240-xn}$Th to $^{235-xn}$Th. Besides strong Th X-rays significant γ transitions are visible. Table 11.12 lists the γ energies and intensities of this γ spectrum. Due to the high background, gating in γ-γ matrices is not applicable and thus it is not possible to assign the observed energies to a certain Th isotope.

Table 11.12.: *γ energies and intensities from the γ spectrum in figure 11.32 for the added gates on the isotopes $^{134-139}$Ba. The corresponding target-like nuclei are $^{235-xn}$Th to $^{240-xn}$Th.*

γ energy (keV)	I	possible assignment ($J_{init} \rightarrow J_{fin}$)
170.16(31)	386(50)	even Th($6^+ \rightarrow 4^+$)
222.62(36)	504(58)	even Th($8^+ \rightarrow 6^+$)
267.43(43)	398(51)	even Th($10^+ \rightarrow 8^+$)
276.96(53)	319(48)	even Th($10^+ \rightarrow 8^+$)
309.65(64)	334(58)	even Th($12^+ \rightarrow 10^+$)

In figure 11.33 the level schemes of the ground-state rotational band up to the 12^+ states of ^{232}Th, ^{234}Th [73] are plotted together with the proposed level scheme for ^{236}Th [52].

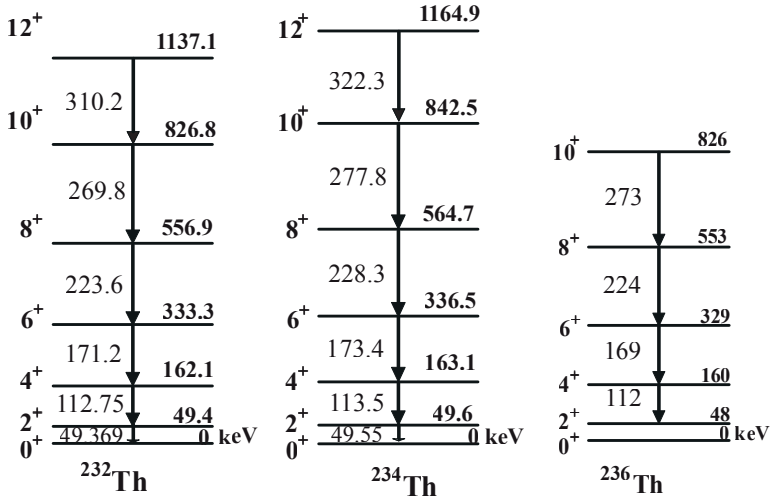

Figure 11.33.: *Level scheme of the even-even Th isotopes ^{232}Th, ^{234}Th up to the 12^+ state [73]. Also the proposed level scheme for ^{236}Th from Ishii et al. [52] up to the 10^+ state is shown.*

The comparison of these γ transitions with the peak structure in figure 11.32 provides strong evidence that even-even Th isotopes are observed. However, individual isotopes cannot be separated.
The probable population of Th isotopes is remarkable with respect to the GRAZING calculations in section 10.2. For the population of Th isotopes cross sections lower than 0.7 mbarn are calculated. This is about four times smaller than the assumed lower sensitivity limit for the target-like nuclei at $\sigma \approx 3$ mbarn, see section 10.2. The interpretation of the GRAZING calculations and the lower sensitivity limit with respect to the analysis have been consistent so far.

Following the Q-value calculations from section 10.1 the population of Th isotopes are the exothermic reaction channels of the (^{136}Xe+^{238}U) reactions and the population of Th isotopes may be favored.

In summary, the results of the two-proton-pickup-channel is promising for investigations of neutron-rich Th isotopes. It motivated another MNT experiment at the LNL in Legnaro for the investigation of these Th isotopes. The experiment is outlined in chapter 13.

12. Comparison with Theoretical Predictions

The analysis of the γ spectra for the two-neutron-transfer channel, described in section 11.4-1, yielded new transitions of the ground-state rotational band of ^{240}U. In this chapter these new results are compared with the latest theoretical predictions of Delaroche et al. [25] and Shneidman et al. [86] (see also section 8.1).

Moments of Inertia (MoI)

The moments of inertia (MoI) of the ground state of ^{240}U are calculated with the γ transitions of the ground-state rotational band. The kinetic MoI is given by the transition energies of the ground-state rotational band [26]:

$$J^{(1)} = \frac{\hbar^2(2I-1)}{E_\gamma(I \to I-2)} \tag{12.1}$$

The deviations in energy differences between the consecutive rotational transition energies are the basis to define also a dynamic MoI $J^{(2)}$:

$$J^{(2)} = \frac{\hbar^2 \Delta I}{\Delta E_\gamma} = \frac{\hbar^2(2I-1-(2(I-2)-1))}{\Delta E_\gamma} = \frac{4\hbar^2}{E_{\gamma 1} - E_{\gamma 2}} \tag{12.2}$$

with $E_{\gamma 1} = E(I \to I-2)$, $E_{\gamma 2} = E(I-2 \to I-4)$.

The rotational frequency for the kinetic MoI is calculated with $\hbar\omega_{kin} = \frac{E(I \to I-2)}{2}$ and for the dynamic MoI with $\hbar\omega_{dyn} = \frac{(E(I \to I-2))+(E(I-2 \to I-4))/2}{2}$.

For the γ transitions of ^{240}U, listed in table 11.7, the kinetic and dynamic MoI are determined for the entire cascade of the ground-state band between the proposed 20^+ and the 0^+ state.

As explained in section 11.4-1 the transitions below the 4^+ state are not visible in this experiment because the states decay by internal electron conversion. For these two unobserved transitions the level information from Ishii et al. [51] ($E_\gamma(4^+ \to 2^+) = 105.6\,\text{keV}$) and Back et al. [4] ($E_\gamma(2^+ \to 0^+) = 45.0\,\text{keV}$) are used. The results for the calculation of $J^{(1)}$ and $J^{(2)}$ are shown in table 12.1. The data points in figure 12.1 illustrate the kinetic MoI (in red) and the dynamic MoI (in blue).
With the following parametrization, which first was considered by Harris [45], the MoI, $J^{(1)}$ and $J^{(2)}$, are parametrized:

Table 12.1.: *Kinetic and dynamic MoI and spins for* ^{240}U

E_γ (keV)	I ($\hbar$)	ω_{kin} ($\frac{\text{MeV}}{\hbar}$)	ω_{dyn} ($\frac{\text{MeV}}{\hbar}$)	$J^{(1)}$ ($\frac{\hbar^2}{\text{MeV}}$)	$J^{(2)}$ ($\frac{\hbar^2}{\text{MeV}}$)	calc. I ($\hbar$)
45(1)*	2	0.0225 (5)		66.7(15)		1.95(4)
105.6(10)**	4	0.0528(1)	0.0377(3)	66.3(1)	66.0 (1)	3.95(4)
161.2(8)	6	0.0806(4)	0.0668(2)	68.2(3)	71.9 (10)	5.92(7)
214.0(7)	8	0.1070(3)	0.0938(3)	70.1(2)	75.7 (9)	7.96(9)
263.2(7)	10	0.1316(3)	0.1193(2)	72.2(2)	81.4 (11)	10.05(11)
306.9(8)	12	0.1535(4)	0.1425(3)	74.9(2)	91.5(16)	12.12(13)
345.3(10)	14	0.1727(5)	0.1631(3)	78.2(2)	104.1(26)	14.11(16)
379.6(10)	16	0.1898(5)	0.1812(3)	81.7(2)	116.6(34)	16.05(19)
407.9(13)	18	0.2040(6)	0.1969(4)	85.8(3)	141.0(62)	17.77(23)
(430.3(19)	20	0.215(1)	0.2096(6)	90.6(4)	179.2(152)	19.22 (27))

* from reference [51]
** from reference [4]

$$J^{(1)} = J_0 + J_1\omega^2 \tag{12.3}$$

$$J^{(2)} = J_0 + 3J_1\omega^2 \tag{12.4}$$

With the Harris parametrization a good indicator is given to compare the experimental MoI with the ideal slope of the MoI for the ground state rotational band without decoupling of nucleons. The Harris parametrization in figure 12.1 is performed up to the 16^+ state. The parameters are found to be $J_0 = (63.9\pm0.7)\frac{\hbar^2}{MeV}$ and $J_1 = (498\pm18)\frac{\hbar^4}{MeV^3}$. For the higher transitions beyond the 16^+ state an increasing deviation to the slope, an upbending effect, is observed.

In black stars the kinetic MoI are plotted, which are calculated by Delaroche et al. [25], see section 8.1. The absolute numbers of the kinetic MoI are consistently higher than the experimentally determined MoI but an increase of the kinetic MoI around a rotational frequency of 0.2 $\frac{MeV}{\hbar}$ is expected as well.

The spins for the ground-state rotational band are deduced, following the procedure described in reference [26] and the expression:

$$I = J_0\omega + J_1\omega^3 + \frac{1}{2} \tag{12.5}$$

The results are also listed in table 12.1. Up to the 16^+ state the calculated spins agree within the errorbars with the assigned even spins of the ground-state rotational band. For transitions above the 16^+ state small deviation of the spin values occur. This again is caused by the upbending effect.

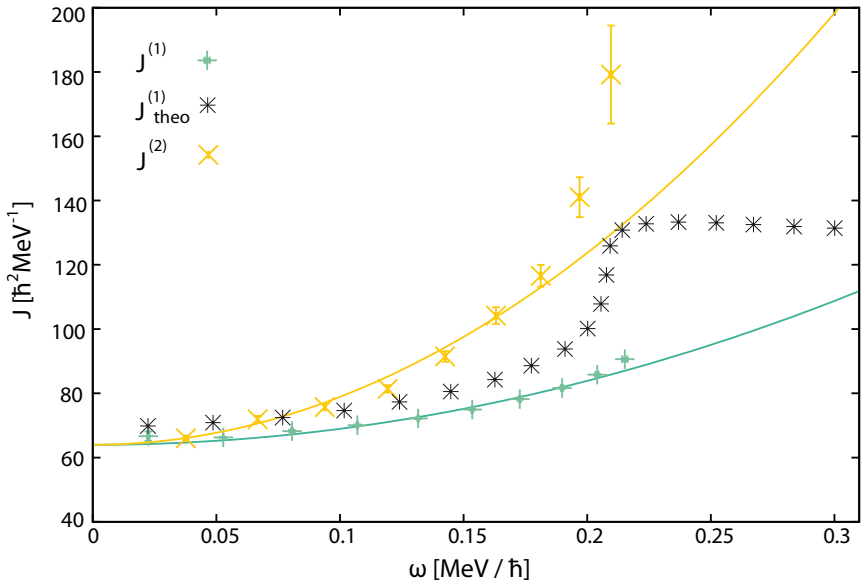

Figure 12.1.: *Kinetic MoI, $J^{(1)}$ in green, and dynamic MoI, $J^{(2)}$ in yellow, for the ground-state rotational band of ^{240}U. The lines are fits to the data points (up to 16+) with equations 12.3 and 12.4. The Harris parameters are $J_0 = (63.9 \pm 0.7)\frac{\hbar^2}{MeV}$ and $J_1 = (498 \pm 18)\frac{\hbar^4}{MeV^3}$. The kinetic MoI from the theoretical calculations of Delaroche et al. [25] are plotted as black stars.*

Comparison with Calculations in the Cluster Model

The experimental data are also compared to the predictions by the cluster model [86]: Figure 12.4 shows three level scheme of the ground-state rotational band of ^{240}U, on the left side the level scheme from Shneidman et al. [86], in the center the experimental data from this present analysis are given (deduced from table 11.7). The level scheme on the right shows the data from Ishii et al. [51]. The two experimental data sets are consistent. In figure 12.2 a comparison between the results of this analysis and the experimental data of Ishii et al. [51] is given in blue color. The transition energies only agree within 2 keV. In red color the difference in transition energies between the present results and the predictions of Shneidman et al. [86] are illustrated. The differences stays within 20 keV.
The difference in level energies in ^{240}U between the results of the present analysis and the experimental data of Ishii et al. [51] are illustrated in figure 12.3 in blue color.The difference between the level energies of the data of Ishii et al. [51] is smaller than 4 keV. The comparison to the calculations of Shneidman et al. [86], pictured in figure 12.3 in red, shows a difference in level energies up to 70 keV for the 18^+ state.
The calculations were performed before experimental data from ^{240}U were available. Concerning this fact, the deviation in the level energy of around 70 keV and the difference in transition energies within 20 keV at high spins are within very reasonable limits.

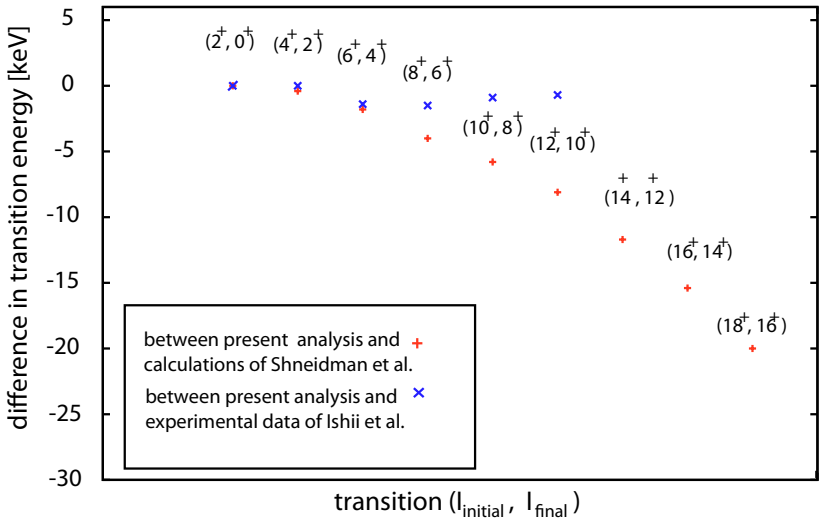

Figure 12.2.: *Difference of transition energies in the ground-state rotational band of* ^{240}U *between the result of the present analysis and (i) the calculations of Shneidman et al. [86] in red and (ii) the experimental data of Ishii et al. [51] in blue.*

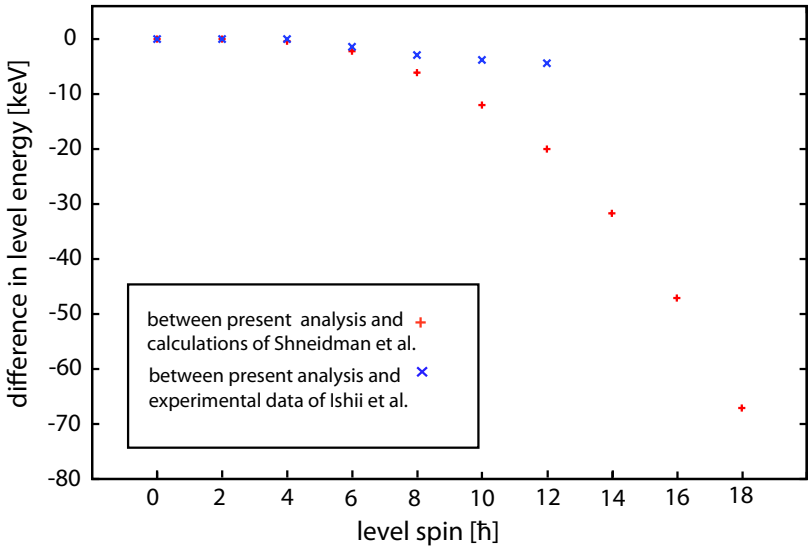

Figure 12.3.: *Difference of level energies in the ground-state rotational band of* ^{240}U *between the result of the present analysis and (i) the calculations of Shneidman et al. [86] in red and (ii) the experimental data of Ishii et al. [51] in blue.*

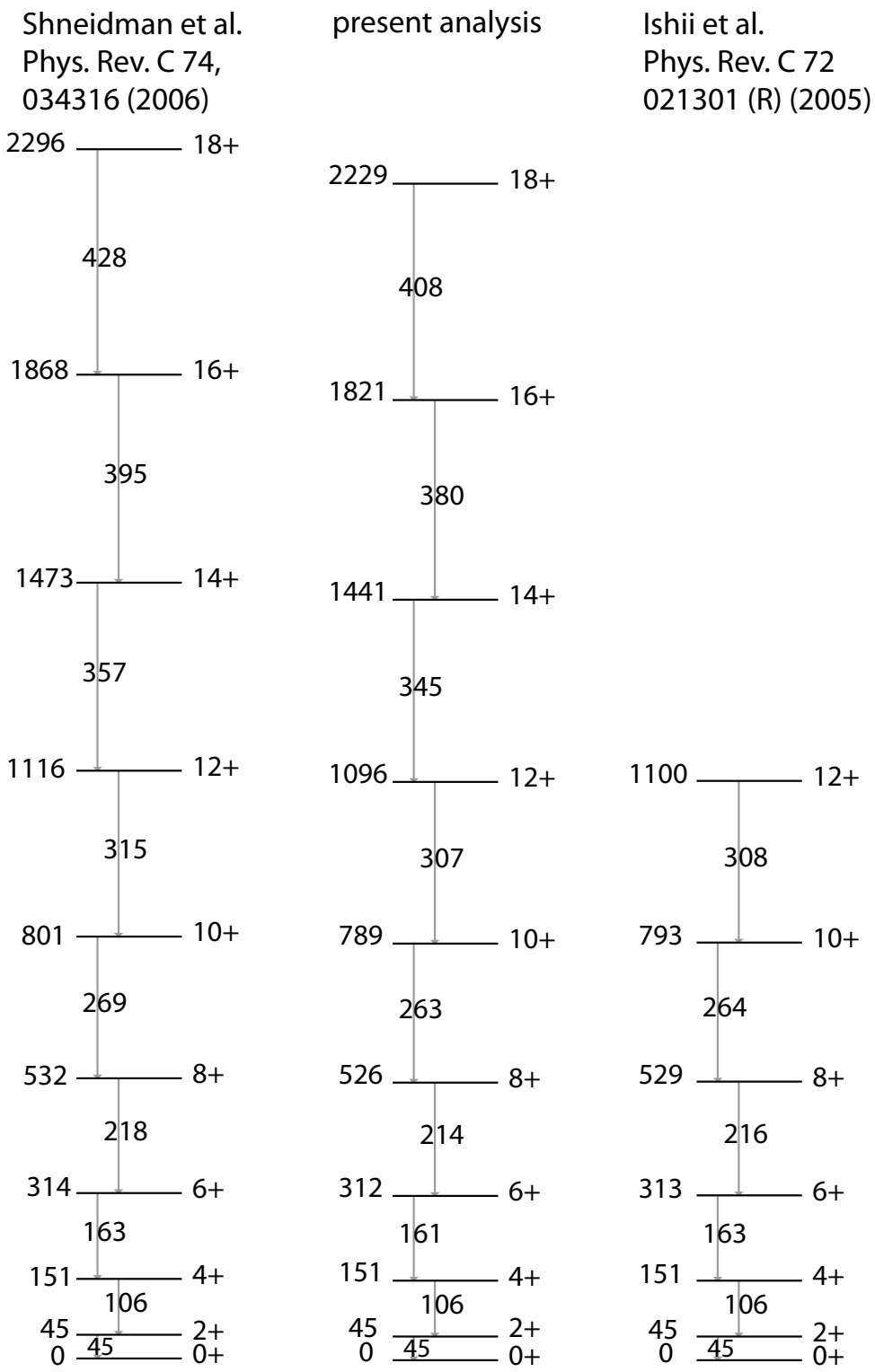

Figure 12.4.: *Level scheme of the ground-state rotational band of ^{240}U. On the left: theoretical predictions from Shneidman et al. [86] in the cluster model. In the center: the level scheme from the present analysis of the (^{70}Zn+^{238}U) experiment. On the right: level scheme from Ishii et al. [51].*

13. Conclusion and Outlook

The information on the beam-like reaction products for the (^{70}Zn+^{238}U) experiment at 460 MeV and the (^{136}Xe+^{238}U) experiment at 926 MeV from PRISMA is combined with a Doppler correction for the target-like nuclei. The resulting γ spectra were analyzed for neutron-rich U-, Pa-, Th-, Np- and Pu- isotopes. The investigation of the isotopic chain from ^{237}U to ^{240}U demonstrates the feasibility of the new analysis procedure.
With a ^{70}Zn beam on a ^{238}U target at 460 MeV it was possible to verify known energies of ^{237}U, ^{238}U , ^{239}U and ^{240}U. The level scheme of the ground-state rotational band of ^{240}U was extended up to the 18^+ state. New transitions at 345.3(10) keV, 379.6(10) keV and 407.9(13) keV are discovered and confirmed by coincidence gating in the γ-γ matrix. A candidate for the ($20^+ \rightarrow 18^+$) transition at 430.3(19) keV is found. With this new information on ^{240}U the kinetic and dynamic moments of inertia are determined. The kinetic moments of inertia are compared with the theoretical predictions from relativistic mean-field theory. They show an upbending effect at rotational frequencies at $0.2\frac{MeV}{\hbar}$ which is also theoretically predicted by Delaroche et al. [25]. The level and transition energies are also compared with predictions in the cluster model by Shneidman et al. [86]. The experimental data are consistent with the cluster model calculations within reasonable values.
The γ spectra of the neutron-transfer channels of the (^{136}Xe+^{238}U) experiment are dominated by transitions of the ground-state rotational band of ^{238}U. Although the GRAZING calculations predict higher cross sections for the population of ^{239}U and ^{240}U in the (^{136}Xe+^{238}U) experiment than in the (^{70}Zn+^{238}U) experiment, the population of ^{240}U could not be observed with the ^{136}Xe based reaction. PRISMA works with a ^{136}Xe beam at its limits. Though the relative mass resolution is within specifications, it is difficult to separate the ejectiles in the ionisation chamber.
The proton-pickup channels, corresponding to Np and Pu isotopes, are investigated for both experiments. The data of the (^{70}Zn+^{238}U) experiment contain with gates on the isotopes ^{68}Cu and ^{69}Cu, corresponding to $^{240-xn}$ and $^{239-xn}$Np isotopes, hints for transitions from Np isotopes The γ spectra from the (^{136}Xe+^{238}U) experiment again only show a contribution of ^{238}U, although the GRAZING calculations predict similar cross sections for the population of Np isotopes. A possible explanation is the limited Z selection, given e.g. by the $\Delta E-$range plot, see figure 11.2.

For the analysis of the proton-stripping reaction channel data from the (^{136}Xe+^{238}U) experiment are available. The γ spectrum of Pa isotopes show contributions of ^{238}U, which again might be caused by the quality of the Z selection. However, from the analysis of the X-ray region allows the conclusion that Pa isotopes were produced.
Ba isotopes correspond to the Th isotopes for the target-like fragments, for the (^{136}Xe+^{238}U) experiment. The γ spectra show all a similar peak structure with energies

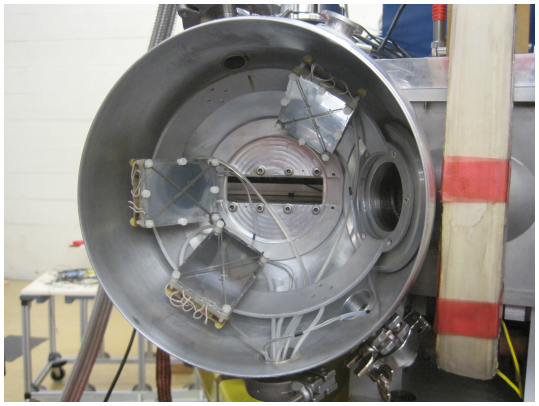

Figure 13.1.: *The target chamber with 3 DANTE detectors installed on a ring at an angle of* 58° *related to the beam axis. The opening on the right side of the chamber is the entrance into the PRISMA spectrometer.*

experimental features	
accelerator	Piave+ALPI
beam	^{136}Xe
beam energy	1 GeV
current	2 pnA
duration	97 h
target	0.5 & 1 $\frac{\text{mg}}{\text{cm}^2}$ ^{238}U
PRISMA angle	50 °

Table 13.1.: *Setup of the experiment 11.22 in October 2011 at the LNL, Legnaro.*

of the ground-state rotational band of even-even Th nuclei up to the 12^+ state. By adding the γ-singles spectra for all mass gates on the Ba isotopes, the γ energies of the ground-state band of even-even Th nuclei emerge. Coincidence gating is not feasible due to the low peak-to-total ratio.
In future a more selective experiment is needed to suppress the background and to trigger on the reaction channels of the target-like nuclei. This is achieved by an additional particle detector around the target, which detects the target-like nuclei. Requiring coincidences of the beam-like particles in PRISMA and of the target-like nuclei in the particle detector in the target chamber, the conditions for the analysis of the γ spectra are improved by gating on surviving evaporation residues and suppression of the fission reaction products.
An experiment was proposed [80] and performed in October 2011 at the LNL, Legnaro. It employs three MCPs from the DANTE (Detector Array for multi-Nucleon Transfer Ejectiles), [97] as additional particle detectors around the target, see figure 13.1.

The parameters of this experiment are listed in table 13.1. It has been optimized for the detection of Th isotopes. A ^{136}Xe beam with 1 GeV energy was delivered by the Piave-ALPI complex and directed onto an ^{238}U target. The target was backed with a niobium layer to be stable against heat.

The three DANTE detectors were placed at 58° with respect to the beam axis. This corresponds to the calculated grazing angle of the target-like nuclei. The beam-like particles are expected at an angle of 50°, where the PRISMA entrance is located. The experiment was performed successfully and the analysis is ongoing. New results for actinide nuclei, especially Th isotopes, are expected [100].

Bibliography

[1] Ahmad, I., and Butler, P.A.:
Octupole shapes in nuclei
Annual Review of Nuclear and Particle Science 43(1), Annual Reviews, USA, 71–116, 1993.

[2] Ahmad, I., Chasman, R.R., Gindler, J.E., and Friedman, A.M.:
Enhanced E1 Transition Rates and Octupole Deformation in ^{225}Ac
Physical Review Letters 52(7), APS, 503–506, 1984.

[3] Atomic Mass Data Center:
http://www.nndc.bnl.gov/amdc/, Brookhaven National Laboratory.

[4] Back, B.B., Flynn, E.R., Hansen, O., Casten, R.F., and Garrett, J.D.:
Energy levels in even actinide isotopes from (t, p) reactions
Nuclear Physics A 217(1), Elsevier, 116–124, 1973.

[5] Bazzacco, D., and Ur, C.A.:
GASP Data Analysis Program Package
http://www.lnl.infn.it/ gasp.

[6] Beghini, S., Corradi, L., Fioretto, E., Gadea, A., Latina, A., Montagnoli, G., Scarlassara, F., Stefanini, A.M., Szilner, S., Trotta, M., and others:
The focal plane detector of the magnetic spectrometer PRISMA
Nuclear Instruments and Methods in Physics Research Section A: Accelerators, Spectrometers, Detectors and Associated Equipment 551(2-3), Elsevier, 364–374, 2005.

[7] Bentley, M.A., and Lenzi, S.M.:
Coulomb energy differences between high-spin states in isobaric multiplets
Progress in Particle and Nuclear Physics 59(2), Elsevier, 497–561, 2007.

[8] Blank, B.:
One-and Two-Proton Radioactivity
The Euroschool Lectures on Physics with Exotic Beams, Vol. III, Springer, 153–201, 2009.

[9] Bohr, A.:
Mat. Fys. Medd. Dan Vid Selsk, Vol 26 No 14,1952.

[10] Bohr, A. and Mottelson B.R..:
Mat. Fys. Medd. Dan. Vid Selsk, Vol. 27, No 16, 1953.

[11] Broda, R.:
Spectroscopic studies with the use of deep-inelastic heavy-ion reactions
Journal of Physics G: Nuclear and Particle Physics 32, IOP Publishing, R151, 2006.

[12] Butler, P.A., and Nazarewicz, W.:
Intrinsic reflection asymmetry in atomic nuclei
Reviews of Modern Physics 68(2), APS, 349, 1996.

[13] CAEN GmbH: www.caen.it, Klingenstrasse 108, Solingen, D-42651.

[14] Casten, R.F.:
Nuclear structure from a simple perspective
Oxford University Press, USA, 1990.

[15] Cerny, J., Esterl, J.E., Gough, R.A., and Sextro, R.G.:
Confirmed proton radioactivity of $^{53}Co^{m}$
Physics Letters B 33(4), Elsevier, 284–286, 1970.

[16] Cerny, J., Gough, R. A., Sextro, R. G., and Esterl, J. E.:
Further results on the proton radioactivity of $^{53}Co^{m}$
Nuclear Physics A 188(3), Elsevier, 666–672, 1972.

[17] CLARA homepage: http://clara.lnl.infn.it/images.

[18] Cocks, J.F.C., Butler, P.A., Cann, K.J., Greenlees, P.T., Jones, G.D., Asztalos, S., Bhattacharyya, P., Broda, R., Clark, R.M., Deleplanque, M.A., and others:
Observation of Octupole Structures in Radon and Radium Isotopes and Their Contrasting Behavior at High Spin
Physical Review Letters 78(15), APS, 2920–2923, 1997.

[19] Cocks, J.F.C., Butler, P.A., Cann, K.J., Greenlees, P.T., Jones, G.D., Smith, J.F., Jones, P.M., Julin, R., Juutinen, S., Müller, D., and others:
Multi-nucleon transfer reactions as a tool for spectroscopy of heavy nuclei
Journal of Physics G: Nuclear and Particle Physics 26, IOP Publishing, 23, 2000.

[20] Cocks, J.F.C, Hawcroft, D., Amzal, N., Butler, P.A., Cann, K.J., Greenlees, P.T., Jones, G.D., Asztalos, S., Clark, R.M., Deleplanque, M.A., and others:
Spectroscopy of Rn, Ra and Th isotopes using multi-nucleon transfer reactions
Nuclear Physics A 645(1), Elsevier, 61–91, 1999.

[21] Corradi, L.:
The many facets of heavy ion transfer reactions
Nuclear Physics A 834(1-4), Elsevier, 129c–134c, 2010.

[22] Corradi, L., Pollarolo, G., and Szilner, S.:
Multinucleon transfer processes in heavy-ion reactions
Journal of Physics G: Nuclear and Particle Physics 36, IOP Publishing, 113101, 2009.

[23] Cresswell, A.J., Butler, P.A., Cline, D., Cunningham, R.A., Devlin, M., Hannachi, F., Ibbotson, R., Jones, G.D., Jones, P.M., Simon, M., and others:
Population of collective bands in Dy isotopes using heavy ion induced transfer reactions
Physical Review C 52(4), APS, 1934, 1995.

[24] de Angelis, G.:
The Structure of Neutron-rich Nuclei Studied by Deep Inelastic Reactions: Recent Results from LNL
Acta Physica Polonica B 42(3-4), 519, 2011.

[25] Delaroche, J.P., Girod, M., Goutte, H., and Libert, J.:
Structure properties of even-even actinides at normal and super deformed shapes analysed using the Gogny force
Nuclear Physics A 771, Elsevier, 103–168, 2006.

[26] Draper, J.E., Stephens, F.S., Deleplanque, M.A., Korten, W., Diamond, R.M., Kelly, W.H., Azaiez, F., Macchiavelli, A.O., Beausang, C.W., Rubel, E.C., and others:
Spins in superdeformed bands in the mass 190 region
Physical Review C 42(5), APS, 1791–1795, 1990.

[27] Duchêne, G., Beck, F.A., Twin, P.J., De France, G., Curien, D., Han, L., Beausang, C.W., Bentley, M.A., Nolan, P.J., and Simpson, J.:
The Clover: a new generation of composite Ge detectors
Nuclear Instruments and Methods in Physics Research Section A: Accelerators, Spectrometers, Detectors and Associated Equipment 432(1), Elsevier, 90–110, 1999.

[28] Farnea, E.:
Gamma spectroscopy of neutron-rich nuclei with the CLARA-PRISMA setup
The European Physical Journal-Special Topics 150(1), Springer, 103–106, 2007.

[29] Firestone, R.B., and Shirley, V.S.:
Table of Isotopes
8th Ed., John Wiley k, Sons, New York, 1996.

[30] Freiesleben, H., and Kratz, J.V.:
N/Z-equilibration and nucleon exchange in dissipative heavy-ion collisions
Physics Reports 106(1-2), Elsevier, 1–120, 1984.

[31] Gadea, A.:
The CLARA-PRISMA Setup Installed at LNL: Description, First Results and Perspectives
NUSTAR '05, University of Surrey, United Kingdom, 5-8 January 2005.

[32] Gadea, A., and Freeman, S. J.:
Investigation of Collective and Shell Model States in the ^{132}Sn Region
CLARA-PRISMA Proposal PAC 07, INFN-LNL , 2007.

[33] Gadea, A., Lenzi, S.M., Lunardi, S., Mărginean, N., Zuker, A.P., Angelis, G. De, Axiotis, M., Martinez, T., Napoli, D.R., Farnea, E., and others:
Observation of ^{54}Ni: Cross-Conjugate Symmetry in $f_{\frac{7}{2}}$ Mirror Energy Differences
Physical Review Letters 97(15), APS, 152501, 2006.

[34] Gadea, A., Marginean, N., Corradi, L., Lenzi, S.M., Ur, C.A., Farnea, E., Angelis, G. De, Fioretto, E., Napoli, D.R., Stefanini, A.M., and others:
The CLARA-PRISMA setup installed at LNL: first results
Journal of Physics G: Nuclear and Particle Physics 31, IOP Publishing, S1443, 2005.

[35] Gadea, A., Napoli, D.R., de Angelis, G., Menegazzo, R., Stefanini, A.M., Corradi, L., Axiotis, M., Berti, L., Fioretto, E., Kroell, T., and others:
Coupling a CLOVER detector array with the PRISMA magnetic spectrometer
The European Physical Journal A-Hadrons and Nuclei 20(1), Springer, 193–197, 2003.

[36] Gäggeler, H., Brüchle, W., Brügger, M., Schädel, M., Sümmerer, K., Wirth, G., Kratz, JV, Lerch, M., Blaich, T., Herrmann, G., and others:
Production of cold target-like fragments in the reaction of ^{48}Ca+^{248}Cm
Physical Review C: Nuclear physics 33(6), 1983, 1986.

[37] Geibel, K.:
Suche nach isomerem Protonenzerfall in ^{54}Ni
Diploma Thesis, Institut für Kernphysik, Universität zu Köln, 2007.

[38] Geissel, H., Armbruster, P., Behr, K.H., Brunle, A., Burkard, K., Chen, M., Folger, H., Franczak, B., Keller, H., Klepper, O., and others:
The GSI projectile fragment separator (FRS): a versatile magnetic system for relativistic heavy ions
Nuclear Instruments and Methods in Physics Research Section B: Beam Interactions with Materials and Atoms 70(1-4), Elsevier, 286–297, 1992.

[39] L. S. Geng, J. Meng, and H. Toki:
Reflection Asymmetric Relativistic Mean Field Approach and Its Application to the Octupole Deformed Nucleus ^{226}Ra
Chin. Phys. Lett. 24, 1865, 2007.

[40] Giovinazzo, J., Blank, B., Chartier, M., Czajkowski, S., Fleury, A., Jimenez, M.J. Lopez, Pravikoff, M.S., Thomas, J.C., Santos, F. de Oliveira, Lewitowicz, M., and others:
Two-Proton Radioactivity of ^{45}Fe
Physical review letters 89(10), APS, 102501, 2002.

[41] Goldanskii, V.I.:
Modes of Radioactive Decay Involving Proton Emission
Annual Review of Nuclear Science 16(1), Annual Reviews 4139 El Camino Way, PO Box 10139, Palo Alto, CA 94303-0139, USA, 1–30, 1966.

[42] Gregorich, K.E., Moody, K.J., Lee, D., Kot, W.K., Welch, R.B., Wilmarth, P.A., and Seaborg, G.T.:
Actinide production in ^{136}Xe bombardments of ^{249}Cf
Physical Review C 35(6), APS, 2117, 1987.

[43] Guo, J.Y., Jiao, P., and Fang, X.Z.:
Microscopic description of nuclear shape evolution from spherical to octupole-deformed shapes in relativistic mean-field theory
Physical Review C 82(4), APS, 047301, 2010.

[44] Hänsel, H., and Neumann, W.:
Physik. Atome, Atomkerne, Elementarteilchen
Spektrum, Akad. Verl., 1995.

[45] Harris, S.M.:
Higher order corrections to the cranking model
Phys. Rev. 138, APS, B509–B513, 1965.

[46] Herskind, B.:
The NORDBALL multidetector system for the study of nuclear structure
Nuclear Physics A 447, Elsevier, 395–412, 1986.

[47] Hofmann, S., Reisdorf, W., Münzenberg, G., Hessberger, F.P., Schneider, J.R.H., and Armbruster, P.:
Proton radioactivity of ^{151}Lu
Zeitschrift für Physik A Hadrons and Nuclei 305(2), Springer, 111–123, 1982.

[48] Hofmann, S., and Gesellschaft für Schwerionenforschung mbH:
Proton Radioactivity
Radiochimica Acta 70/71, 93–105, Oldenbourg Wissenschaftsverlag, 1995.

[49] Hoischen, R.:
An Isomer Study of the Nucleus ^{54}Ni Preparations, Simulations, and First Results
Master Thesis, 2006.

[50] Humphreys, R.D., Butler, P.A., Bastin, J.E., Greenlees, P.T., Hammond, N.J., Herzberg, R.D., Jenkins, D.G., Jones, G.D., Kankaanpää, H., Keenan, A., and others:
In-beam electron spectroscopy of ^{226}U and ^{254}No
Physical Review C 69(6), APS, 064324, 2004.

[51] Ishii, T., Shigematsu, S., Asai, M., Makishima, A., Matsuda, M., Kaneko, J., Hossain, I., Ichikawa, S., Kohno, T., and Ogawa, M.:
In-beam γ-ray spectroscopy of ^{240}U using the (^{18}O,^{16}O) reaction
Physical Review C 72(2), APS, 021301, 2005.

[52] Ishii, T., Makii, H., Asai, M., Koura, H., Shigematsu, S., Tsukada, K., Toyoshima, A., Matsuda, M., Makishima, A., Kaneko, J., and others:
Ground-state bands of neutron-rich ^{236} Th and ^{242}U nuclei and implication of spherical shell closure at $N = 164$
Physical Review C 76(1), APS, 011303, 2007.

[53] Iwata, Y., Otsuka, T., Maruhn, J.A., and Itagaki, N.:
Suppression of charge equilibration leading to the synthesis of exotic nuclei
Physical Review Letters 104(25), APS, 252501, 2010.

[54] Jianyou, G., Peng, J., and Xiangzheng, F.:
Microscopic description of nuclear shape evolution from spherical to octupole-deformed shapes in relativistic mean-field theory
Physical Review. C, Nuclear Physics 82(4), 2010.

[55] Jolos, R.V., and von Brentano, P.:
Angular momentum dependence of the parity splitting in nuclei with octupole correlations
Physical Review C 49(5), APS, 2301–2304, 1994.

[56] Jolos, R.V., and von Brentano, P.:
Rotational spectra and parity splitting in nuclei with strong octupole correlations
Nuclear Physics A 587(2), Elsevier, 377–389, 1995.

[57] Jolos, R.V. and von Brentano, P.:
Parity splitting in the alternating parity bands of some actinide nuclei
Physical Review C 60(6), APS, 064317, 1999.

[58] Junde, H., and Su, H.:
Nuclear Data Sheets for A= 54
Nuclear Data Sheets 107(6), Elsevier, 1393–1530, 2006.

[59] Kibedi, T., and Spear, R.H.:
Reduced electric-octupole transition probabilities, $B(E3; 0_1^+ \rightarrow 3_1^-)$ - An update
At. Data Nucl. Data Tables 80, 35, 2002.

[60] Kowal, M., and Skalski, J.:
Low-energy shape oscillations of negative parity in the main and shape-isomeric minima in actinides
Physical Review C 82(5), APS, 054303, 2010.

[61] Krolas, W., Broda, R., Fornal, B., Pawlat, T., Grawe, H., Maier, KH, Schramm, M., and Schubart, R.:
Gamma coincidence study of $^{208}Pb+$ 350 MeV ^{64}Ni collisions
Nuclear Physics A 724(3-4), Elsevier, 289–312, 2003.

[62] Lane, G.J., Broda, R., Fornal, B., Byrne, A.P., Dracoulis, G.D., Blomqvist, J., Clark, R.M., Cromaz, M., Deleplanque, M.A., Diamond, R.M., and others:
Structure of exotic nuclei near and above ^{208}Pb populated via deep-inelastic collisions
Nuclear Physics A 682, 71–71, 2001.

[63] Latina, A., Stefanini, A.M., Beghini, S., Behera, B..R, Corradi, L., Angelis, G. De, Rosa, A. De, Fioretto, E., Gadea, A., Gulmini, M., and others:
PRISMA - a magnetic spectrometer for heavy ions at LNL
Nuclear Physics A 734, Elsevier, E1–E4, 2004.

[64] Linnemann, A.:
Das HORUS-Würfelspektrometer und Multiphononenanregung in ^{106}Cd
Dissertation, Institut für Kernphysik, Universität zu Köln, 2005.

[65] The lise code, a simulation of fragment separators
http://groups.nscl.msu.edu/lise/lise.html.

[66] Homepage of Laboratori Nazionali di Legnaro (LNL):
www.lnl.infn.it.

[67] MARaBOU: Data Acquisition: www.bl.physik.tu-muenchen.de/marabou/html.

[68] Marsden, E., and Lantsberry, W.C.:
The passage of α particles through hydrogen
Philosophical Magazine Series 6 30(176), Taylor Francis, 240–243, 1915.

[69] Mayer-Kuckuk, T.:
Kernphysik
BG Teubner, Stuttgart, 1984.

[70] Mesytec main amplifier module: Stm-16: www.mesytec.com/silicon.html:stm-16+.

[71] Montagnoli, G., Stefanini, A.M., Trotta, M., Beghini, S., Bettini, M., Scarlassara, F., Schiavon, V., Corradi, L., Behera, B.R., Fioretto, E., and others:
The large-area micro-channel plate entrance detector of the heavy-ion magnetic spectrometer PRISMA
Nuclear Instruments and Methods in Physics Research Section A: Accelerators, Spectrometers, Detectors and Associated Equipment 547(2-3), Elsevier, 455–463, 2005.

[72] Montanari, D., Farnea, E., Leoni, S., Pollarolo, G., Corradi, L., Benzoni, G., Gadea, A., Fioretto, E., Latina, A., Montagnoli, G., and others:
Response function of the magnetic spectrometer PRISMA
The European Physical Journal A-Hadrons and Nuclei 47(1), Springer, 1–7, 2011.

[73] National Nuclear Data Center, http://www.nndc.bnl.gov/nudat2
Brookhaven National Laboratory.

[74] Ortec modules: http://www.ortec-online.com/solutions/index.aspx.

[75] Paul, E.S., Woods, P.J., Davinson, T., Page, R.D., Sellin, P.J., Beausang, C.W., Clark, R.M., Cunningham, R.A., Forbes, S.A., Fossan, D.B., and others:
In-beam γ-ray spectroscopy above ^{100}Sn using the new technique of recoil decay tagging
Physical Review C 51(1), APS, 78, 1995.

[76] Pfützner, M., Badura, E., Bingham, C., Blank, B., Chartier, M., Geissel, H., Giovinazzo, J., Grigorenko, LV, Grzywacz, R., Hellstrm, M., and others:
First evidence for the two-proton decay of ^{45}Fe
The European Physical Journal A-Hadrons and Nuclei 14(3), Springer, 279–285, 2002.

[77] Pisent, A., Bisoffi, G., Carlucci, D., Cavenago, M., Chiurlotto, F., Comunian, M., Fagotti, E., Galata, A., Poggi, M., Porcellato, A.M., and others:
Beam Commissioning of the Superconducting RFQS of the New LNL Injector Piave
Proceedings of the Particle Accelerator Conference, 2696–2698, 2005.

[78] Pühlhofer, F.:
On the interpretation of evaporation residue mass distributions in heavy-ion induced fusion reactions
Nuclear Physics A 280(1), Elsevier, 267–284, 1977.

[79] RADCON Ltd. Company, Zelenograd, Moscow Reg., Russia.

[80] Reiter, P., and others:
Spectroscopy of neutron rich Th and U nuclei after multi-nucleon reactions
AGATA Demonstrator Experimental Proposal, October 2011.

[81] Rohozinski, S.G.:
Octupole vibrations in nuclei
Reports on Progress in Physics 51, IOP Publishing, 541, 1988.

[82] Roth, J., Cleeman, L., Eberth, J., Heck, T., Neumann, W., and Nolte, M.:
A neutron multiplicity technique for in-beam gamma-spectroscopy on neutron deficient nuclei
4th International Conference on Nuclei Far from Stability, Helsingør, Denmark, 7 - 13 Jun 1981, pp.680-3, 1981.

[83] Recchia, F.: private communication.

[84] Rudolph, D., Hoischen, R., Hellström, M., Pietri, S., Podolyák, Z., Regan, P.H., Garnsworthy, A.B., Steer, S.J., Becker, F., Bednarczyk, P., and others:
Isospin symmetry and proton decay: Identification of the 10^+ *isomer in* ^{54}Ni
Physical Review C 78(2), APS, 021301, 2008.

[85] Shneidman, T.M., Adamian, G.G., Antonenko, N.V., Jolos, R.V., and Scheid, W.:
Cluster interpretation of properties of alternating parity bands in heavy nuclei
Physical Review C 67(1), APS, 014313, 2003.

[86] Shneidman, T.M., Adamian, G.G., Antonenko, N.V., and Jolos, R.V.:
Possible alternative parity bands in the heaviest nuclei
Physical Review C 74(3), 34316, 2006.

[87] Shneidman, T.M., Adamian, G.G., Antonenko, N.V., and Jolos, R.V.:
Cluster approach to the structure of nuclei with $Z \geq 96$
Physics of Atomic Nuclei 70(8), Springer, 1452–1456, 2007.

[88] Sobiczewski, A., Muntian, I., and Patyk, Z.:
Problem of 'deformed' superheavy nuclei
Physical Review C 63(3), APS, 034306, 2001.

[89] Söderström, P.A., Nyberg, J., Regan, P.H., Algora, A., De Angelis, G., Ashley, SF, Aydin, S., Bazzacco, D., Casperson, RJ, Catford, W.N. and others:
Spectroscopy of neutron-rich ^{168,170} *Dy: Yrast band evolution close to the* N_p N_n *valence maximum*
Physical Review C 81(3), APS, 034310, 2010.

[90] Söderström, P.A.:
Collective Structure of Neutron-Rich Rare-Earth Nuclei and Development of Instrumentation for Gamma-Ray Spectroscopy
Uppsala Universitet, Digital Comprehensive Summaries of Uppsala Dissertations from the Faculty of Science and Technology 818, 2011.

[91] Stefanini, A.M., Corradi, L., Maron, G., Pisent, A., Trotta, M., Vinodkumar, A.M., Beghini, S., Montagnoli, G., Scarlassara, F., Segato, G.F., and others:
The heavy-ion magnetic spectrometer PRISMA
Nuclear Physics A 701(1-4), Elsevier, 217–221, 2002.

[92] Swiatecki, W.J.:
Common features and differences between fission and heavy ion physics
J. Phys. Colloq 33 C5-45, 1972.

[93] Takai, H., Knott, C.N., Winchell, D.F., Saladin, J.X., Kaplan, M.S., de Faro, L., Aryaeinejad, R., Blue, R.A., Ronningen, R.M., Morrissey, D.J, and others:
Population of high spin states by quasi-elastic and deep inelastic collisions
Physical Review C 38(3), APS, 1247, 1988.

[94] Taylor, M.J., Hammond, G., Bentley, M.A., Becker, F., Grebosz, J., Banu, A., Barton, CJ, Beck, T., Bednarczyk, P., Bracco, A., and others:
Spectroscopy of nuclei approaching the proton drip-line using a secondary-fragmentation technique with the RISING detector array
Journal of Physics G: Nuclear and Particle Physics 31, IOP Publishing, S1527, 2005.

[95] Theuerkauf, J.:
Die Analyse von zwei- und mehrdimensionalen -Koinzidenzspektren an Beispielen aus Hochspinexperimenten in der Massengegend um ^{146}Gd
Dissertation, Institut für Kernphysik, Universität zu Köln, 1994.

[96] Triva 5, trigger module: www.gsi.de/informationen/wti/ee/elekt/entwicklung/triva5.html.

[97] Valiente-Dobón, J.J., Gadea, A., Brambilla, S., Kondratiev, N.A., Beghini, S., Corradi, L., de Angelis, G., Vedova, F. Della, Farnea, E., Fioretto, E., and others:
The new Heavy-ion MCP-based Ancillary Detector DANTE for the CLARA-PRISMA Setup
AIP Conference Proceedings, volume 853, 202, 2006.

[98] Valiente-Dobón, J.J., Lenzi, S.M., Freeman, S.J., Lunardi, S., Smith, J.F., Gottardo, A., Della Vedova, F., Farnea, E., Gadea, A., Napoli, D.R., and others:
Spectroscopy of neutron-rich $^{59-63}Mn$ *isotopes*
Physical Review C 78(2), APS, 024302, 2008.

[99] Vretenar D. , Niksic T. and Ring P.:
Relativistic nuclear energy density functionals Int. Journal of Mod. Phys. E Vol. 19, 548-557, 2010.

[100] Vogt. A.:
Teilchenidentifikation für In-Beam-Gammaspektroskopie neutronenreicher Aktinidenkerne
Bachelorarbeit, Institut für Kernphysik, Universität zu Köln, 2011.

[101] Wendt, A.:
Isomere Protonenzerfälle in der pf-Schale
Diploma Thesis, Institut für Kernphysik, Universität zu Köln, 2008.

[102] Wiedenhöver, I., Janssens, R.V.F, Hackman, G., Ahmad, I., Greene, J.P., Amro, H., Bhattacharyya, P.K., Carpenter, M.P., Chowdhury, P., Cizewski, J., and others:
Octupole Correlations in the Pu Isotopes: From Vibration to Static Deformation?
Physical review letters 83(11), APS, 2143–2146, 1999.

[103] Winther, A.:
Grazing reactions in collisions between heavy nuclei
Nuclear Physics A 572(1), Elsevier, 191–235, 1994.

[104] Winther, A.:
Dissipation, polarization and fluctuation in grazing heavy-ion collisions and the boundary to the chaotic regime
Nuclear Physics A 594(2), Elsevier, 203–245, 1995.

[105] Winther, A.: *The Grazing Code*, http://www.to.infn.it/ nanni/grazing.

[106] Woods, P.J., and Davids, C.N.:
Nuclei beyond the proton drip-line
Annual Review of Nuclear and Particle Science 47(1), USA, 541–590, 1997.

[107] Wu, C.Y., Liu, X.T., Sorensen, S.P., Kincaid, R.W., Guidry, M.W., Cline, D., Kernan, W.J., Vogt, E., Czosnyka, T., Kavka, A.E., and others:
Population of high-spin states in the actinide region by heavy-ion transfer reactions
Physics Letters B 188(1), Elsevier, 25–28, 1987.

[108] Zhu, S., Janssens, R.V.F., Lane, G.J., Wiedenhöver, I., Carpenter, M.P., Ahmad, I., Byrne, A.P., Chowdhury, P., Cline, D., Deacon, A.N., and others:
Strength of octupole correlations in the actinides: contrasting behavior in the isotones ^{237}U and ^{239}Pu
Physics Letters B 618(1), Elsevier, 51–59, 2005.

List of Tables

List of Figures

Danksagung / Acknowledgment

Zuerst möchte ich Prof. Dr. Peter Reiter für die Betreuung der Arbeit danken. Durch die Vielseitigkeit der Aufgabenstellung war es mir möglich ein breites Spektrum kernphysikalischen und technischen Wissens zu vertiefen. Ich bedanke mich für die Unterstützung und das hohe Maß an Diskussionsbereitschaft.

Ich danke Prof. Dr. Andreas Zilges für die Übernahme des Korreferats.

Desweiteren danke ich der gesamten Arbeitsgruppe sowie auch allen ehemaligen Mitgliedern der Gruppe für die angenehme und freundliche Arbeitsatmosphäre. Insbesondere möchte ich mich für die Unterstützung in den zahlreichen Strahlzeiten bedanken, die ohne die vielen Freiwilligen nicht realisierbar gewesen wären.

Besonderer Dank geht an Dr. Tanja Kotthaus, die mir stets mit Tatkraft und Fachwissen beratend zur Seite stand.

I would like to thank our swedish collaborators from the University of Lund, especially Prof. Dr. Dirk Rudolph, Prof. Dr. Claas Fahlander, Dr. Pavel Golubev, Dr. Robert Hoischen and Dr. Vladimir Avdeitchikov for their support and fruitful discussions.

I wish to thank Dr. Jose Javier Valiente Dobon from the Laboratori Nazionale di Legnaro, Italy, and Dr. Francesco Recchia from the University of Padua, Italy, for their great and constructive cooperation.

I am also grateful to Prof. Dr. Andres Gadea, Prof. Dr. Silvia Lenzi, Dr. Dino Bazzacho, Dr. Enrico Farnea, Caterina Michelagnoli , Dr. Eda Sahin, Dr. Suzana Szilner, Michael Bowry and Dr. Pär-Anders Söderström.

I would like to thank Dr. Jean-Paul Delaroche and Dr. Michel Girod for providing their calculations of the moments of inertia for ^{240}U.

Ein großer Dank geht an die Operateure des Tandembeschleunigers des IKP, Lothar Steinert, Otto Rudolph und Uwe Werner, die für einen reibungslosen Strahlbetrieb sorgten.

Ich danke Dr. Oskar Zell für die Herstellung der Targets.

Ich möchte auch besonders der Feinmechanikwerkstatt des IKP unter der Leitung von Stefan Thiel und der Elektronikwerkstatt des IKP unter der Leitung von Christoph Görgen danken, die sich durch hohe Einsatzfreude auszeichneten.

Für ihre stete Diskussionsbereitschaft und Unterstützung danke ich Dr. Nigel Warr, Dr. Andrey Blazhev und Dr. Jürgen Eberth.

Ich danke den Systemadministratoren Benedikt Birkenbach, Norbert Braun, Gunnar Frießner, Michael Pfeiffer, Nima Saed-Samii und Dr. Ralf Schulze für die Wartung der Rechner. Darüber hinaus bewiesen sie außerordentliche Geduld bei meiner rasant wachsenden Belegung des Plattenspeichers.

Ich möchte mich bei allen anderen Institutsmitgliedern für die sehr angenehme Zusammenarbeit und das hohe Maß an Kooperationsbereitschaft bedanken. Die Jahre in diesem Institut habe ich als große Bereicherung empfunden. Namentlich erwähnt seien Dr. Janis Endris und Desiree Radeck.

Ich danke meinen Freunden, insbesondere Susanne, Friederike, Stephan, Nico und Philip.

Herzlicher Dank geht an meine gesamte Familie, insbesondere meiner Mutter, für jedwede Unterstützung und alles Weitere.

Vielen Dank & Thank you all!

Erklärung

Ich versichere, dass ich die von mir vorgelegte Dissertation selbstständig angefertigt, die benutzten Quellen und Hilfsmittel vollständig angegeben und die Stellen der Arbeit – einschließlich Tabellen, Karten und Abbildungen –, die anderen Werken im Wortlaut oder dem Sinn nach entnommen sind, in jedem Einzelfall als Entlehnung kenntlich gemacht habe; dass diese Dissertation noch keiner anderen Fakultät oder Universität zur Prüfung vorgelegen hat; dass sie – abgesehen von unten angegebenen Teilpublikation – noch nicht veröffentlicht worden ist sowie, dass ich eine solche Veröffentlichung vor Abschluss des Promotionsverfahrens nicht vornehmen werde. Die Bestimmungen dieser Promotionsordnung sind mir bekannt. Die von mir vorgelegte Dissertation ist von Prof. Dr. Peter Reiter betreut worden.

Köln, den 7.Mai 2012 Kerstin Geibel

Teilveröffentlichungen: keine